ArgonCube – A Novel Concept for Liquid Argon Time Projection Chambers

Inauguraldissertation
der Philosophisch-naturwissenschaftlichen Fakultät
der Universität Bern

vorgelegt von

Roman Berner

von Spreitenbach

Leiter der Arbeit
Prof. Dr. I. Kreslo

Albert Einstein Center for Fundamental Physics
Laboratory for High Energy Physics
Physics Institute

ArgonCube – A Novel Concept for Liquid Argon Time Projection Chambers

Inauguraldissertation
der Philosophisch-naturwissenschaftlichen Fakultät
der Universität Bern

vorgelegt von

Roman Berner

von Spreitenbach

Leiter der Arbeit
Prof. Dr. I. Kreslo

Albert Einstein Center for Fundamental Physics
Laboratory for High Energy Physics
Physics Institute

Von der Philosophisch-naturwissenschaftlichen Fakultät
angenommen.

Bern, 1st October 2021

Der Dekan
Prof. Dr. Z. Balogh

Cosmic Gall

Neutrinos, they are very small.
They have no charge and have no mass
And do not interact at all.

The earth is just a silly ball
To them, through which they simply pass,
Like dustmaids down a drafty hall
Or photons through a sheet of glass.

They snub the most exquisite gas,
Ignore the most substantial wall,
Cold-shoulder steel and sounding brass,
Insult the stallion in his stall.

And, scorning barriers of class,
Infiltrate you and me! Like tall
And painless guillotines, they fall
Down through our heads into the grass.

At night, they enter at Nepal
And pierce the lover and his lass
From underneath the bed - you call
It wonderful; I call it crass.

John Updike
Telephone Poles and Other Poems
1963

Abstract

Neutrinos are elementary particles that allow for the study of some of the most fundamental questions in particle physics, e.g. the matter-antimatter asymmetry observed in the Universe. Current and future neutrino experiments are designed to measure the properties of these particles with unprecedented accuracy to answer those questions. For this purpose, large data samples collected with very sensitive and precise detectors are required.

The Liquid Argon Time Projection Chamber (LArTPC) is an ideal detector for neutrino experiments as it provides accurate particle tracking and calorimetric information, and it can be scaled to large active masses for the collection of high-statistics data samples. However, monolithic LArTPCs face the problem of large cathode bias voltages of several 100 kV and a large amount of stored energy in the drift field, posing the risk of severe damage in the case of electric breakdowns. Furthermore, traditional LArTPCs employ projective wire readout systems, which introduce ambiguities in the 3-dimensional (3D) event reconstruction. The event reconstruction using data acquired with a projective wire readout is particularly challenging in high-multiplicity environments where several particle interactions can overlap within the drift window of the LArTPC.

To address these problems, the ArgonCube collaboration developed a novel LArTPC design that segments the total detector volume into several electrically and optically isolated LArTPCs sharing a common cryostat. In this way, the cathode bias voltages and the stored energies within the detector's drift fields are reduced. Furthermore, the inactive volume of the ArgonCube detector is reduced using new technology to shape the electric field. This technology would slow down the energy released in the case of an electric breakdown.

The ArgonCube design furthermore employs a pixelated charge readout system that provides unambiguous particle tracking in 3D. In addition, a dielectric light detection system, sensitive to the Liquid Argon (LAr) scintillation light and with an excellent time resolution of $\mathcal{O}(1\,\mathrm{ns})$, was developed. These detectors enable a precise association of detached energy depositions to specific neutrino interaction vertices, enabling an improved accuracy of the LArTPC event reconstruction.

This thesis motivates the use of LArTPCs in neutrino experiments and describes the novel ArgonCube concepts and technologies. Furthermore, the design and results of several prototypes used to study the performance of the ArgonCube technologies are presented. For the detector calibration, neutral pions decaying within a LArTPC can be used as standard candles. A method based on machine-learning techniques to reconstruct neutral pion decays in a modular LArTPC environment is presented.

ArgonCube found application in the Near-Detector (ND) of the Deep Underground Neutrino Experiment (DUNE) and has been proposed for one of the Far-Detector (FD) units of the experiment.

Preface

In the Standard Model of Particle Physics (SM), neutrinos are massless elementary particles that interact only weakly with matter. Therefore, it is very challenging to detect neutrinos and measure their interactions. Although the neutrino is among the most abundant particle in the Universe, it took more than two decades from the postulation of this particle in 1930 to its first detection in 1956. In 2002, it was found that neutrinos can undergo flavour changes, a phenomenon called *neutrino oscillation*, which requires a non-zero neutrino mass. Since this is not predicted by the SM, the mysterious particles opened a door for physics beyond the SM. Measuring the properties of neutrinos and their oscillation parameters enable studying the fundamental properties of the Universe. They might shed light on the mechanism responsible for the observed matter-antimatter asymmetry in the Universe. DUNE is a next-generation neutrino-oscillation experiment designed to precisely measure neutrino oscillations to infer the oscillation parameters. Chapter 1 briefly discusses these topics and motivates the work done for this thesis. A summary of neutrino physics relevant to the scope of this thesis is given in Chapter 2.

The LArTPC is an ideal detector type to study neutrino interactions since it provides excellent calorimetric information and particle tracking. The technology of the LArTPC is described in Chapter 3. LArTPCs can be scaled to detectors with active masses of several thousand tonnes. Massive detectors are desired in neutrino physics to increase the probability of having one of the rare neutrino interactions happening within the detector. However, monolithic LArTPCs of such size often have long drift distances of typically several metres and consequently need huge cathode bias voltages of a few hundred kV. Such detectors usually store a considerably large amount of energy in the electric field of the Time Projection Chamber (TPC). These properties pose severe risks for damage in the case of an electric breakdown. To address those problems, the ArgonCube collaboration developed a novel design for large LArTPCs. The ArgonCube approach is to split the total detector into several identical modules, each hosting two independent LArTPCs with short drift distances and relatively small cathode bias voltages. For an improved sensitivity to particle interactions, the ArgonCube collaboration further developed a pixelated charge readout system intended to be operational in LAr, at cryogenic temperatures. The two-dimensional pixel readout provides unambiguous particle tracking in 3D. In addition, the Research and Development (R&D) program of ArgonCube leads to a large area-coverage dielectric photon detection system for the Vacuum Ultra Violet (VUV) scintillation light produced in LAr when charged particles pass through the medium. The time resolution of those detectors is of $\mathcal{O}(1\,\mathrm{ns})$, which enables an improved event reconstruction. A third novelty developed in the ArgonCube R&D program is a low-profile and highly resistive *field shell*, a new approach to produce and shape the electric field within a LArTPC. Compared to traditional field cages,

the resistive field shell reduces the amount of inactive material between ArgonCube modules and reduces the number count of components, leading to a reduced number of possible failures within the LArTPC. Furthermore, the highly resistive field shell would slow down the energy released in the case of an electric breakdown. The ArgonCube concept and technologies are discussed in detail in Chapter 4.

In the context of this work, I was extensively involved in the ArgonCube R&D program. My work consisted of designing and assembling several prototype detectors to test and characterise the technologies mentioned earlier. In addition, I designed and built several devices for monitoring the detectors during their operation, including liquid argon level-meters and cryocameras. Chapter 5 presents some ArgonCube prototypes and their monitoring system and summarises results from their tests.

The ArgonCube concept found application in the international DUNE experiment, which is currently under construction in the United States of America. Chapter 6 describes the application of the ArgonCube concept in DUNE.

The framework of this thesis allowed for international collaborations with many institutes and research facilities around the world. Apart from the detector hardware development, I was working with the Machine-Learning (ML) group at the Stanford Linear Accelerator Center (SLAC) in California to develop software for the ML-based reconstruction of showers, and neutral pion decays in a modular LArTPC environment. Studies I performed with simulated particle interactions within a modularised LAr volume drove modifications to the neural networks and their training in order to improve the reconstruction accuracy. Chapter 7 describes the ML-based reconstruction in LArTPCs. The developed reconstruction software will be an integral part of future detectors such as the ProtoDUNE-ND and the LAr component of the DUNE ND.

Chapter 8 summarises the thesis and provides an outlook.

Contents

List of Figures

Photos in Figures 4.2, 4.9, 4.10, 5.1, 5.2, 5.4, 5.5, 5.6, 5.9, 5.10, 5.11, 5.12, 5.14, 5.15, 5.18, 5.19, 5.26, 5.27, 5.28, 5.29, 5.30, and Figure 5 in the Appendix: Liquid Argon Neutrino Group, Laboratory for High Energy Physics, University of Bern.

List of Tables

Acronyms

1D 1-dimensional

1p1h 1 particle and 1 hole

2D 2-dimensional

2p2h 2 particles and 2 holes

3D 3-dimensional

ADC Analog-to-Digital Converter

ALEPH Apparatus for LEP Physics

ArCLight ArgonCube Light Readout System

ArgoNeut Argon Neutrino Teststand

ASIC Application-Specific Integrated Circuit

BNL Brookhaven National Laboratory

BSM Beyond Standard Model

CC Charged-Current

CCD Charge-Coupled Device

CERN Conseil Européen pour la Recherche Nucléaire

CKM Cabibbo-Kobazashi-Maskawa

CMF Centre of Mass Frame

CNN Convolutional Neural Network

COH Coherent Scattering

CP Charge-Parity

CPA Closest Point of Approach

CPT Charge-Parity-Time

CPU Central Processing Unit

CSA Charge-Sensitive Amplifier

DAQ Data AcQuisition

DBSCAN Density-Based Spatial Clustering of Applications with Noise

DIS Deep Inelastic Scattering

DONUT Direct Observation of Nu-Tau

DUNE Deep Underground Neutrino Experiment

ECAL Electromagnetic Calorimeter

EDEP Energy Deposition

EM Electromagnetic

FD Far-Detector

FHC Forward Horn Current

FNAL Fermi National Accelerator Laboratory

FPGA Field Programmable Gate Array

FWHM Full Width at Half Maximum

GALLEX Gallium Experiment

GAr Gaseous Argon

GNN Graph Neural Network

GUTs Grand Unified Theories

HIP Highly Ionizing Particle

HV High Voltage

Hyper-K Hyper-Kamiokande

I/O Input/Output

ICARUS Imaging Cosmic And Rare Underground Signals

IMB Irvine-Michigan-Brookhaven

JINR Joint Institute for Nuclear Research

KamiokaNDE Kamioka Nucleon Decay Experiment

KATRIN Karlsruhe Tritium Neutrino Experiment

LAr Liquid Argon

LArTPC Liquid Argon Time Projection Chamber

LBNF Long Baseline Neutrino Facility

LBNL Lawrence Berkeley National Laboratory

LCM Light Collection Module

LEP Large Electron-Positron Collider

LEScat Low Energy Scatter

LF Laboratory Frame

LHC Large Hadron Collider

LHEP Laboratory for High Energy Physics

LN_2 Liquid Nitrogen

LXe Liquid Xenon

MCS Multiple Coulomb Scattering

MEC Meson Exchange Current

MicroBooNE Micro Booster Neutrino Experiment

MINERνA Main Injector Experiment for ν-A

MINOS Main Injector Neutrino Oscillation Search

MIP Minimum Ionising Particles

MISO Master Input, Slave Output

ML Machine-Learning

MOSI Master Output, Slave Input

MPR Multi-Particle-Rain generator

MPV Multi-Particle-Vertex generator

MSC Multiple Coulomb Scattering

MWPC Multi-Wire Proportional Chamber

NC Neutral-Current

ND Near-Detector

ND-GAr Near-Detector Gaseous Argon Component

ND-LAr Near-Detector Liquid Argon Component

NuMI Neutrinos at the Main Injector

PAI Polyamide-imide

PCA Principal Component Analysis

PCB Printed Circuit Board

PDE Photon Detection Efficiency

PDF Probability Density Function

PEEK Polyether Ether Ketone

PEP Positron-Electron-Proton

PFA Perfluoroalkoxy Alkane

PID Particle Identification

PLC Programmable Logic Unit

PMNS Pontecorvo-Maki-Nakagawa-Sakata

PMT Photomultiplier Tube

POT Protons On Target

ppb Part Per Billion

ppm Part Per Million

PPN Point Proposal Network

PSD Pulse-Shape Discrimination

PTFE Polytetrafluorethylene

PVC Polyvinyl Chroride

QE Quasi Elastic

R&D Research and Development

RES Resonant

RHC Reverse Horn Current

RMS Root Mean Square

RS-TPC Resistive Shell Time Projection Chamber

SAGE Soviet–American Gallium Experiment

SAND System for on-Axis Neutrino Detection

SCE Space Charge Effects

SiPM Silocon Photomultiplier

SLAC Stanford Linear Accelerator Center

SM Standard Model of Particle Physics

SN Signal to Noise

SNO Sudbury Neutrino Observatory

SSM Standard Solar Model

SURF Sanford Underground Research Facility

T2K Tokai to Kamioka

TPB 1,1,4,4-Tetra-Phenyl-1,3-Butadiene

TPC Time Projection Chamber

UART Universal Asynchronous Receiver-Transmitter

V1PER Version 1 Pixel Equipped Readout

VUV Vacuum Ultra Violet

WLS Wavelength Shifter

Part I

Preliminaries

Chapter 1

Introduction

The SM has been one of the most successful theories in the history of science as it describes particle interactions on a fundamental level and also made precise predictions of particles before they were found. The Higgs boson, discovered in 2012 at the Large Hadron Collider (LHC) at Conseil Européen pour la Recherche Nucléaire (CERN) [1] [2], is only one of several particles predicted by the SM. However, the discovery of neutrino oscillations in 2002 by the Sudbury Neutrino Observatory (SNO) collaboration [3] showed that not all neutrinos are massless, as they are assumed to be by the SM. Furthermore, the SM cannot explain the observed baryonic matter-antimatter asymmetry in the Universe. To address this problem, Sakharov proposed a possible explanation in 1962, [4] which, requires a breaking of the Charge-Parity (CP) symmetry in the early Universe. Even though CP-violating processes have been found in the quark sector, additional physics beyond the SM is required to explain the size of the observed asymmetry. The answer could be found in neutrino oscillations since this phenomenon allows for a possible CP violation in the lepton sector. The idea of DUNE was born about a decade ago to investigate this. The experiment is currently under construction, with the first data taking planned for the year 2026. DUNE aims to precisely measure neutrino oscillations to answer the question about a possible CP violation in the lepton sector. Furthermore, the experiment is designed to measure how the neutrino masses are ordered, which is still not answered today. For this purpose, massive neutrino detectors capable of accurately measuring neutrino interactions within a high interaction-rate environment are required. Furthermore, those detectors need to reconstruct kinematic variables of particles across a broad range of event topologies.

The LArTPC is one of the detectors of choice for neutrino physics as they provide precise 3D particle tracking information, calorimetry and Particle Identification (PID), and thus are well suited for the neutrino physics experiments as mentioned before. The LAr serves as active detector material and additionally functions as a relatively dense target material as well. However, to build a monolithic LArTPC with masses of the order of $\mathcal{O}(100\,\mathrm{kt})$ or larger, electron drift fields of meter-scale and with local electric field intensities as large as a few hundred $\mathrm{V\,cm^{-1}}$ are needed. That makes it difficult to operate such detectors safely.

The ArgonCube concept is a novel LArTPC design based on detector modularisation. The basic idea is to segment the detector into smaller detector modules, leading to shorter drift distances with considerably smaller electric potential differences across the TPC drift field. The module walls are made of a material that is opaque to the LAr scintillation light signals and thus contains these. As a consequence, the event

reconstruction in the LArTPC is simplified, and a more precise energy reconstruction is enabled, particularly in high-multiplicity environments. The ArgonCube collaboration investigated the development of a photon detection system with a large area-coverage and $\mathcal{O}(1\,\text{ns})$ time resolution, a pixelated charge readout system, and new technology to produce and shape the electric field in a LArTPC using significantly less material than conventional technologies. In the scope of this thesis, I was involved in designing, prototyping, producing, constructing, testing and analysing the performance of those technologies. The concept proposed by the ArgonCube collaboration will be employed in the DUNE ND.

This thesis discusses many aspects and challenges for the successful construction of a LArTPC for future precision neutrino experiments facing high event rates. New technologies, including the photon detection system mentioned above, the pixelated charge readout and the new approach for the electric field shaping in a TPC are presented.

The thesis is structured as follows: Chapter 2 gives an overview of neutrino physics. In particular, a brief history of the neutrino is given, followed by a theory section that discusses the phenomenon of neutrino oscillations, how neutrinos interact with matter and how they can be detected. In addition, a few open questions in neutrino physics are presented. The chapter closes with a brief description of two next-generation neutrino experiments, namely Hyper-Kamiokande (Hyper-K) and DUNE. Chapter 3 discusses relevant concepts of the LArTPC detector. A short history section provides an overview of the TPC development from the first idea towards modern TPCs. Further, the working principle of a LArTPC is described, and the effects limiting the resolution of the detector are discussed. Also, the ArgonCube concepts are introduced. Chapter 4 treats the ArgonCube concepts in detail, beginning with the advantages of a modular design. Furthermore, the chapter discussed the new technologies developed by the ArgonCube collaboration, namely the novel approach to electric field production and shaping, a pixelated charge readout system, and photon detectors with excellent time resolution. Some prototypes built to test and benchmark the ArgonCube technologies are presented in Chapter 5. This chapter furthermore briefly describes a slow-control system developed to monitor the hardware used to perform these tests. Chapter 6 focuses on the application of ArgonCube in the DUNE experiment, beginning with the requirements and motivation for an ArgonCube-like ND. Further, the DUNE ND design is presented, and what a prototype, the ProtoDUNE-ND detector, will look like. This chapter closes with a discussion about the potential application of ArgonCube in the DUNE FD. Chapter 7 treats topics relevant for a machine-learning-based event reconstructions in LArTPCs. In particular, topics related to shower reconstruction and the photon-electron separation in LArTPCs are discussed. Furthermore, the chapter treats the reconstruction of neutral pion decays, which can be used to calibrate the detector. Chapter 8 summarises the thesis and concludes.

Chapter 2

Neutrino Physics

Since the neutrino was first detected in 1956, neutrino physics has seen outstanding progress in neutrino theory, experimental neutrino physics and neutrino detector development. This chapter gives a general overview of neutrino physics, starting with Section 2.1, which briefly summarises the neutrino history relevant to the thesis' scope, with the main focus on experimental results. Section 2.2 discusses neutrino theory, in particular, the properties of neutrinos and neutrino flavour oscillations, how neutrinos interact with matter, and how neutrinos can be detected. Two open questions in neutrino physics, namely how the neutrino masses are ordered and how much, if at all, neutrinos violate the CP-conserving phase, are described in Section 2.2.4. The chapter closes with Section 2.3, which focuses on two next-generation neutrino experiments, Hyper-K and DUNE, which are designed to answer those questions.

2.1 Neutrino History

In 1914, Chadwick discovered that the energy spectrum of electrons from beta emitters show a continuous range [5]. Since only two particles were visible in the decay, Chadwick's observation gave rise to speculations that the energy would not be conserved in beta decays or would only be conserved in the mean. Pauli refused to accept this and postulated in 1930 – in an open letter [6] to the "Gruppe der Radioaktiven" – the existence of a new neutral particle with a small mass. The proposed "unseen" particle originated in a beta decay would take away energy and therefore could explain the observed continuous electron energy spectrum. However, Pauli wagered a case of fine champagne that no one would ever be able to detect this particle. Perrin analysed the shape of the beta spectrum and estimated that the mass of the invisible particle must be at least small compared to the mass of the electron [7]. Fermi proposed to name the unseen particle the *neutrino*. In his 1934 published theory of β radiation [8], Fermi described the energy spectrum of the electrons under the assumption that a neutrino, ν, exists. The calculated spectrum, as proposed by Fermi, showed good agreement with the experimentally found energy distribution. Bethe and Peierls calculated the neutrino interaction cross-section on protons within the same year, concluding that it must be extremely small [9]. The result turned out to correspond to a penetration power of $\mathcal{O}\left(10^{16}\,\mathrm{km}\right)$ in solid matter, larger than the diameter of the earth by a few orders of magnitude. Bethe and Peierls concluded that "there is no practically possible way of observing the neutrino".

It took more than two decades until Reines and Cowan reported the first detection

of the neutrino[1] in 1956 [10]. The discovery happened when the scientists exposed their detector close to the Savannah River nuclear reactor, where the antineutrino flux would be immense. The detector consisted of two tanks of water with dissolved cadmium, sandwiched in between three liquid scintillator tanks with Photomultiplier Tube (PMT)s on the sidewalls. Some of the antineutrinos would interact with the protons in the water, via the inverse beta decay, to produce a neutron and a positron following the interaction

$$\bar{\nu_e} + p \to n + e^+ \qquad \text{(inverse beta decay)}. \tag{2.1}$$

The positron quickly annihilates with a closeby electron, producing a pair of photons, each with an energy of about 511 keV. The produced neutron would be captured by the dissolved cadmium a few µs later and would produce more photons. This delayed coincidence, measured with the scintillator detectors, allowed Cowan and Reines to discriminate antineutrino interactions from background events. About a quarter of a century after the claim that nobody would be able to detect the postulated particle, Pauli bought Cowan and Reines the promised case of champagne.

In 1956, Lee and Yang proposed [11] that the parity could not be conserved in weak interactions, which was confirmed by Wu et al. soon after in 1957 [12]. To incorporate parity violation in the theory of weak interactions, Lee and Yang et al. put forward that the neutrino exists in a left-handed state where the spin is anti-parallel to its 3-momentum vector (negative helicity). In contrast, the antineutrino is right-handed, with the spin parallel to the 3-momentum vector (positive helicity) [13]. In early 1958, Goldhaber et al. reported that they indeed observed only left-handed neutrinos [14].

In 1962, Lederman et al. [15] discovered the muon-(anti)neutrino at Brookhaven National Laboratory (BNL). For the first time, Lederman and his team produced neutrinos using high energy protons from an accelerator. They guided the protons onto a beryllium target where pions (π^+ and π^-) were produced which in turn decayed to (anti)muons and muon-(anti)neutrinos,

$$\begin{aligned} \pi^- &\to \mu^- + \bar{\nu_\mu} \qquad (\pi^- \text{ decay}) \\ \pi^+ &\to \mu^+ + \nu_\mu \qquad (\pi^+ \text{ decay}). \end{aligned} \tag{2.2}$$

Lederman's team discovered that the produced (anti)neutrinos are "very likely different from the neutrinos involved in β decay", where electron-(anti)neutrinos are involved. In other words, the scientists discovered a difference between ν_e and ν_μ and hence demonstrated that the leptons have a doublet structure.

Davis et al. reported the first measurements of the solar neutrino flux in 1968 [16]. Davis' neutrino detector was located about 1500 m underground in the Homestake Gold Mine in Lead, South Dakota. It consisted of a vessel filled with 390 000 L of the liquid tetrachloroethylene, C_2Cl_4. The neutrinos from the sun would interact with the chlorine to produce electrons and unstable argon isotopes,

$$\nu_e + {}^{37}\text{Cl} \to e^- + {}^{37}\text{Ar}. \tag{2.3}$$

After the tank was exposed to the solar neutrino flux, a sophisticated purification system was used to extract the radioactive ^{37}Ar isotopes to measure the total radioactive activity. The measured activity, together with the known half-life of 35 days,

[1] Today, it is known that they observed the antineutrino, $\bar{\nu}$.

allowed the physicists to calculate the number of neutrino interactions during the time the detector had been exposed. The probable upper limit of neutrino interactions in their experiment was about a factor of 3 smaller than predicted by the Standard Solar Model (SSM) published by Bahcall et al. [17], giving rise to the so-called *solar neutrino problem*.

Perl et al. discovered a third charged lepton, later to be called *tau*, in 1976 [18]. Since leptons are found to occur in doublets, this discovery predicted the existence of a third neutrino type, the tau-neutrino.

The Kamiokande-II collaboration observed neutrinos with the successor of the Kamioka Nucleon Decay Experiment (KamiokaNDE) detector, a 3000 t water Cherenkov device. The detection technique was based on the Cherenkov radiation emitted by particles travelling faster than the speed of light in the medium, which allowed for the direction and energy estimation of the incident neutrinos. The signals obtained with the Kamiokande-II detector allowed for the discrimination of electron-like neutrinos and muon-like neutrinos. In a first analysis, the experiment measured neutrinos produced in the Earth's atmosphere. Atmospheric neutrinos are produced when energetic protons from the cosmos hit the atmosphere and produce charged pions, which decay according to Equation 2.2. The (anti)muons in turn decay to (anti)electrons and two more (anti)neutrinos,

$$\begin{aligned} \mu^- &\rightarrow e^- + \nu_\mu + \bar{\nu}_e \qquad (\mu^- \text{ decay}) \\ \mu^+ &\rightarrow e^+ + \bar{\nu}_\mu + \nu_e \qquad (\mu^+ \text{ decay}). \end{aligned} \tag{2.4}$$

In total, the expected ratio of muon-like to electron-like neutrinos hence is 2 to 1. In 1988, the KamiokaNDE collaboration published a paper where a deficiency of ν_μ and $\bar{\nu}_\mu$ produced in the Earth's atmosphere was observed. Kamiokande-II measured a ratio of electron-like to muon-like neutrinos of about 1 to 1, or more precisely, only $(57 \pm 7)\,\%$ of the expected muon-like neutrinos predicted by simulations [19]. This deficiency became known as the *atmospheric neutrino anomaly*. Furthermore, the collaboration analysed solar neutrinos interacting within their detector. However, due to the relatively large detection threshold of 9.3 MeV, only the relatively high-energy solar neutrinos originating from the ^{8}B reaction in the sun could be measured. In 1989, the detection of not more than about half the neutrinos predicted by the SSM was announced [20]. This result was in agreement with the corresponding value obtained by Davis' chlorine experiment, confirming the solar neutrino problem. Later, the Irvine-Michigan-Brookhaven (IMB) experiment, the Soviet–American Gallium Experiment (SAGE) and the Gallium Experiment (GALLEX) also announced to have observed only about half the expected neutrino fluxes [21], [22], [23], again in good agreement with Davis' experimental results.

In 1989, the Apparatus for LEP Physics (ALEPH) collaboration conducted experiments at the Large Electron-Positron Collider (LEP) at CERN. The collaboration announced that the total number of neutrino species, coupling to the weak interaction and with a mass smaller than half the Z^0 mass, was measured to be consistent with three [24]. Furthermore, the experimental results of ALEPH excluded the possibility of a fourth active neutrino type at 98 % confidence level (C.L.).

The *atmospheric neutrino anomaly* was solved in 1998 when the Super-Kamiokande collaboration first found evidence for a zenith-angle dependent deficit of atmospheric muon-neutrinos [25]. Using their 50 kt successor of the Kamiokande-II detector, the collaboration measured the number-ratio of upward-going to downward-going muon-

neutrinos. The remarkable fact was that the experiment observed a bigger deficit of ν_μ for the neutrinos travelling through the Earth than those coming from overhead. The experimental data suggested a disappearance of upward-going muon-neutrinos and was consistent with neutrinos undergoing oscillations, which indirectly implies that the neutrinos have a non-zero mass.

Using nuclear emulsion targets, the Direct Observation of Nu-Tau (DONUT) experiment at Fermi National Accelerator Laboratory (FNAL) observed tau-neutrino interactions for the first time in 2000 [26]. The experiment produced tau-neutrinos by guiding 800 GeV protons onto a tungsten target to produce D_s mesons, which would decay to τ and $\bar{\nu_\tau}$, and the subsequent decay of the τ to a ν_τ. The discovery of the tau-(anti)neutrino confirmed, once again, that leptons come in lepton-doublets.

The *solar neutrino problem* was solved in 2002 by the SNO collaboration. Using a 1 kt heavy-water (D_2O) Cherenkov detector located about 2000 m underground in the Creighton Mine in Ontario, Canada, the experiment measured the flux of neutrinos in a flavour-independent way via the Neutral-Current (NC) interactions

$$\bar{\nu}_\ell + d \rightarrow \bar{\nu}_\ell + p + n, \tag{2.5}$$

where l denotes the flavour. In addition, the Charged-Current (CC) interactions as described in Section 2.2.2 could be measured as well. The SNO collaboration observed a reduced electron-neutrino flux but no deficit in the total neutrino flux as predicted by the SSM, implying that electron-neutrinos change their flavour to muon-neutrinos and tau-neutrinos [3]. Since flavour changes in matter cannot happen if neutrinos are massless, this result intrinsically confirmed that neutrinos have non-zero masses.

Several experiments have been conducted to determined the parameters describing the oscillation phenomena (see Table 2.1). The Double Chooz collaboration presented the first results of reactor-antineutrino disappearance in 2011, indicating a non-zero θ_{13} [27]. In the same year, the Tokai to Kamioka (T2K) experiment, a long-baseline neutrino-oscillation experiment located in Japan, also published indications on a non-zero θ_{13} [28]. In 2012, the Daya Bay collaboration announced a non-zero mixing angle θ_{13} with a significance of 5.2 standard deviations [29], which makes it possible for future experiments to determine the neutrino mass hierarchy. Furthermore, $\theta_{13} \neq 0$ enables measurements of a potential CP violation in the lepton sector via neutrino oscillations in matter.

In 2013, the Planck collaboration confirmed that there is no evidence for other neutrino-like relativistic particles beyond the three families already known [30]. Their measurements provide an upper limit of 0.23 eV for the sum of neutrino masses, close to the limit found in the Karlsruhe Tritium Neutrino Experiment (KATRIN) [31].

In 2014, the T2K experiment first discovered the electron-neutrino appearance via the oscillation of $\nu_e \rightarrow \nu_\mu$ [32]. This result is interesting since a non-zero value for θ_{13} enables the measurement of the CP-violating phase δ_{CP}, as can be seen from Equation 2.13. T2K guides a beam of predominantly ν_μ or $\bar{\nu_\mu}$ from Tokai, Ibaraki to the SuperKamiokande detector located about 295 km away. The most recent results of T2K exclude the CP conservation in neutrino oscillations at 2 σ C.L. and prefer the normal mass hierarchy with a posteriori probability of 89 % [33].

Today, the concept of neutrino oscillation has been experimentally confirmed by several experiments. However, there are still open questions in neutrino physics, as discussed in Section 2.2.4. Those fundamental questions gave rise to new-generation neutrino experiments, Hyper-K and DUNE, discussed in Section 2.3.

2.2 Neutrino Theory

Neutrinos are electrically neutral particles that can have one of three flavours. In fact, neutrinos are the only particles of the SM defined by their flavour, namely electron-neutrino ν_e, muon-neutrino ν_μ, and tau-neutrino ν_τ. Each flavour is associated with a corresponding antiparticle, $\bar{\nu}_e$, $\bar{\nu}_\mu$, and $\bar{\nu}_\tau$, which are uncharged as well. The SM states that neutrinos only couple via the weak interaction and that they are massless. However, experiments showed that neutrinos can change their flavour during their travel, a phenomenon called neutrino oscillation. This phenomenon requires, as will be derived in Section 2.2.1, that (anti)neutrinos have different masses, which in turn implies that at least two of the neutrino types are not massless. Consequently, neutrinos require physics beyond the SM.

2.2.1 Neutrino Oscillations

The phenomenon of neutrino oscillation can be explained within the SM when extending it to have (at least two) neutrinos having non-zero masses. Within the SM, neutrinos only interact via the flavour eigenstates $|\nu_\alpha\rangle$ where $\alpha \in \{e, \mu, \tau, ...\}$. These eigenstates are distinct from the neutrino mass eigenstates $|\nu_i\rangle$ with corresponding masses m_i where $i = 1, 2, 3, ...$ However, the flavour eigenstates are considered to be quantum-mechanical coherent superpositions of the mass eigenstates, as described by

$$|\nu_\alpha\rangle = \sum_i \mathrm{U}_{\alpha i} |\nu_i\rangle \,, \tag{2.6}$$

and in analogy for the antineutrino flavour eigenstate,

$$|\bar{\nu}_\alpha\rangle = \sum_i \mathrm{U}^\dagger_{\alpha i} |\bar{\nu}_i\rangle \,. \tag{2.7}$$

where U is an unitary[2] transformation matrix, and $\mathrm{U}^\dagger$ denotes its hermitean conjugate (or adjoint) matrix. Inverting Equations 2.6 and 2.7, the mass eigenstates can be represented as superpositions of the flavour eigenstates as

$$|\nu_i\rangle = \sum_\alpha \mathrm{U}^\dagger_{\alpha i} |\nu_\alpha\rangle \,, \tag{2.8}$$

and in analogy for the antineutrino flavour eigenstate,

$$|\bar{\nu}_i\rangle = \sum_\alpha \mathrm{U}_{\alpha i} |\bar{\nu}_\alpha\rangle \,. \tag{2.9}$$

Using matrix notation and assuming that the number of neutrino flavour eigenstates is three, e.g. $\nu_\alpha \in \{\nu_e, \nu_\mu, \nu_\tau\}$, the superposition from Equation 2.6 can be written as

$$\begin{bmatrix} |\nu_e\rangle \\ |\nu_\mu\rangle \\ |\nu_\tau\rangle \end{bmatrix} = \underbrace{\begin{bmatrix} \mathrm{U}_{e1} & \mathrm{U}_{e2} & \mathrm{U}_{e3} \\ \mathrm{U}_{\mu 1} & \mathrm{U}_{\mu 2} & \mathrm{U}_{\mu 3} \\ \mathrm{U}_{\tau 1} & \mathrm{U}_{\tau 2} & \mathrm{U}_{\tau 3} \end{bmatrix}}_{\mathrm{U_{PMNS}}} \begin{bmatrix} |\nu_1\rangle \\ |\nu_2\rangle \\ |\nu_3\rangle \end{bmatrix} , \tag{2.10}$$

[2] The unitarity is assumed based on the conservation of the neutrino number.

where U_{PMNS} denotes the Pontecorvo-Maki-Nakagawa-Sakata (PMNS)[3] matrix which shows the composition of the flavour eigenstates in terms of the mass eigenstates. Non-zero values of at least one of the off-diagonal elements in U_{PMNS} lead to neutrino mixing. Figure 2.1 illustrates the mixing between the neutrino flavour and the neutrino mass eigenstates.

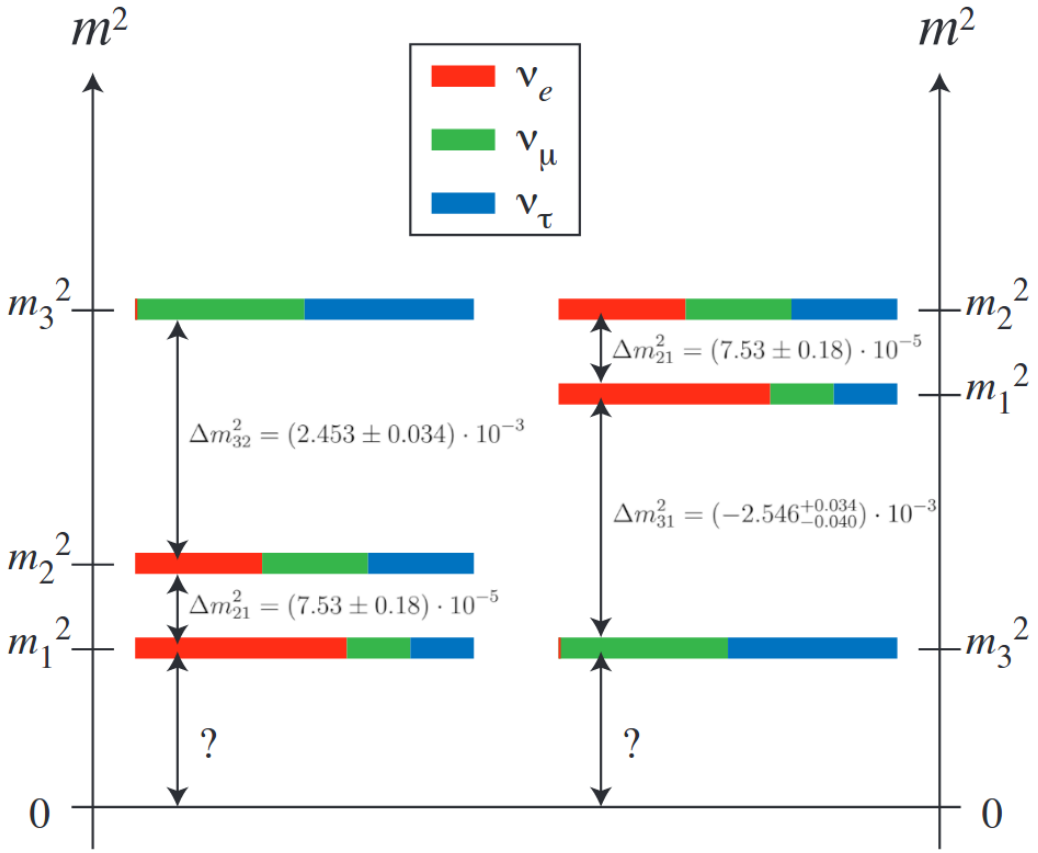

Figure 2.1: Normal (left) and inverted (right) neutrino mass hierarchy. Neutrino-oscillation experiments are only sensitive to the squared mass differences between two mass eigenstates, $m^2_{ij} = m^2_i - m^2_j$, and not on the absolute neutrino mass scale itself. The colour bars show the flavour content of the three neutrino mass eigenstates. The figure has been taken from [34], with modifications made.

In general, a unitary $N \times N$ matrix depends on N^2 independent real parameters which can be separated into mixing angles and phases [35], respectively:

$$\frac{N(N-1)}{2} \qquad \text{(mixing angles)} \tag{2.11}$$

$$\frac{N(N+1)}{2} \qquad \text{(phases)} \tag{2.12}$$

In principle, the neutrino mixing described above is not limited to the number of neutrinos. However, in 1989, the ALEPH collaboration showed that the number of light neutrino states (with masses $\lesssim 45.6\,\text{GeV}$) is consistent with three [24], and

[3] The PMNS matrix is the equivalent of the Cabibbo-Kobazashi-Maskawa (CKM) matrix in the quark sector, which describes the CC interactions of quark mass eigenstates.

that the possibility of the existence of a fourth active neutrino type is excluded at 98 % C.L. Therefore, the assumption of three active neutrino flavours in the following description is valid. In the three-flavour case, the transformation can be expressed in terms of three rotations with mixing angles θ_{12}, θ_{23} and θ_{13} which determine the degree to which the mass and flavour states are mixed. Furthermore, in the three-flavour case, six phase-factors are needed. However, due to correlations, not all phases are physical observables. If neutrinos and antineutrinos are different particles (so-called *Dirac fermions*), all phase factors can be absorbed into one phase δ_{CP}. Because the sign of the lepton number is different for particle and antiparticle, neutrinos would be *Dirac fermions* if the total lepton charge $L = L_e + L_\mu + L_\tau$ is conserved. On the other hand, if the total lepton number is not conserved, neutrinos would be their own antiparticles (so-called *Majorana particles*) and, in addition to the Dirac phase δ_{CP}, three more Majorana phases are needed. However, the experimentally measurable quantities only depend on the differences on the three Majorana phases, and thus a parameterisation with only two physically observable Majorana phases α and β can be done. Accounting for all rotations and possibly observable phases, the U_{PMNS} transformation matrix for the three-neutrino case can be written as

$$
\begin{aligned}
&\mathrm{U}_{\text{PMNS}} \\
&= \begin{bmatrix} \mathrm{U}_{e1} & \mathrm{U}_{e2} & \mathrm{U}_{e3} \\ \mathrm{U}_{\mu1} & \mathrm{U}_{\mu2} & \mathrm{U}_{\mu3} \\ \mathrm{U}_{\tau1} & \mathrm{U}_{\tau2} & \mathrm{U}_{\tau3} \end{bmatrix} \\
&= \underbrace{\begin{bmatrix} 1 & 0 & 0 \\ 0 & c_{23} & s_{23} \\ 0 & -s_{23} & c_{23} \end{bmatrix}}_{\mathrm{U}_{\text{atmospheric}}} \underbrace{\begin{bmatrix} c_{13} & 0 & s_{13}\mathrm{e}^{-i\delta_{CP}} \\ 0 & 1 & 0 \\ -s_{13}\mathrm{e}^{i\delta_{CP}} & 0 & c_{13} \end{bmatrix}}_{\mathrm{U}_{\text{reactor}}} \underbrace{\begin{bmatrix} c_{12} & s_{12} & 0 \\ -s_{12} & c_{12} & 0 \\ 0 & 0 & 1 \end{bmatrix}}_{\mathrm{U}_{\text{solar}}} \underbrace{\begin{bmatrix} 1 & 0 & 0 \\ 0 & \mathrm{e}^{i\alpha} & 0 \\ 0 & 0 & \mathrm{e}^{i\beta} \end{bmatrix}}_{\mathrm{U}_{\text{Majorana}}} \\
&= \begin{bmatrix} c_{12}c_{13} & s_{12}c_{13} & s_{13}\mathrm{e}^{-i\delta_{CP}} \\ -s_{12}c_{23} - c_{12}s_{23}s_{13}\mathrm{e}^{i\delta_{CP}} & c_{12}c_{23} - s_{12}s_{23}s_{13}\mathrm{e}^{i\delta_{CP}} & s_{23}c_{13} \\ s_{12}s_{23} - c_{12}c_{23}s_{13}\mathrm{e}^{i\delta_{CP}} & -c_{12}s_{23} - s_{12}c_{23}s_{13}\mathrm{e}^{i\delta_{CP}} & c_{23}c_{13} \end{bmatrix} \begin{bmatrix} 1 & 0 & 0 \\ 0 & \mathrm{e}^{i\alpha} & 0 \\ 0 & 0 & \mathrm{e}^{i\beta} \end{bmatrix},
\end{aligned}
\tag{2.13}
$$

where $c_{ij} = \cos(\theta_{ij})$ and $s_{ij} = \sin(\theta_{ij})$. The names for the matrices $\mathrm{U}_{\text{atmospheric}}$, $\mathrm{U}_{\text{reactor}}$, and $\mathrm{U}_{\text{solar}}$ are historically due to first measurements of the corresponding mixing angles with atmospheric, reactor, and solar neutrinos, respectively. The fourth matrix, $\mathrm{U}_{\text{Majorana}}$, introduces the two Majorana phases α and β. Even though the Majorana phases α and β would be observable in a neutrino-less double-beta decay, they do not contribute to neutrino oscillations and matter effects and thus will be neglected from here on. If all thre mixing angles are larger than zero, the Dirac phase δ_{CP} would be observable in neutrino-oscillation experiments (see, e.g., Equation 2.17) and would represent a source of CP violations in the lepton sector if $\delta_{CP} \neq 0$ or $\delta_{CP} \neq \pi$. The most recent results of the T2K experiment exclude the CP conservation in neutrino oscillations at 2σ C.L. [33].

The following paragraph derives the three-flavour neutrino oscillation probability in vacuum using the framework of plane waves. The result will only be valid in an approximation because plane waves extend with the same amplitude over the whole space-time, which would require infinite energy and thus cannot be physically correct. However, the linear nature of quantum mechanics allows superimposing plane waves to build wave packets that do show physically correct behaviour. Because neutrinos

are localised in the production process, they can be described by quantum-mechanical wave packets.

Neutrinos are created in weak interactions and therefore exist in weak flavour eigenstates. At the moment of creation, the wave function of the neutrino ν_α at spatial coordinate $x = 0$ and time $t = 0$ takes the form (see Equation 2.6)

$$\begin{aligned} |\nu_\alpha(0,0)\rangle &= \sum_i \mathrm{U}_{\alpha i} \, |\nu_i\rangle \\ &= \mathrm{U}_{\alpha 1} \, |\nu_1\rangle + \mathrm{U}_{\alpha 2} \, |\nu_2\rangle + \mathrm{U}_{\alpha 3} \, |\nu_3\rangle \, . \end{aligned} \tag{2.14}$$

When the neutrino travels a distance of L through space, in the framework of the plane-wave approximation, the wave function at any later time t can be written as

$$\begin{aligned} |\nu_\alpha(L,t)\rangle &= \sum_i \mathrm{U}_{\alpha i} \, |\nu_i\rangle \, \mathrm{e}^{-i(E_i t - |\vec{p}_i| L)} \\ &= \quad \mathrm{U}_{\alpha 1} \, |\nu_1\rangle \, \mathrm{e}^{-i(E_1 t - |\vec{p}_1| L)} \\ &\quad + \mathrm{U}_{\alpha 2} \, |\nu_2\rangle \, \mathrm{e}^{-i(E_2 t - |\vec{p}_2| L)} \\ &\quad + \mathrm{U}_{\alpha 3} \, |\nu_3\rangle \, \mathrm{e}^{-i(E_3 t - |\vec{p}_3| L)}, \end{aligned} \tag{2.15}$$

where E_i and $\vec{p}_i$ $(i = 1, 2, 3)$ denote energy and momentum of the neutrino, respectively. Since the eigenstates represent different masses, and energy and momentum both are functions of the particle's mass, each mass eigenstate evolves differently when the neutrino travels through space. In conclusion, the proportion of each flavour in the wave function changes during the neutrino propagation, which can be observed as the neutrino oscillation. The discovery of neutrino oscillation thus provides direct evidence for non-vanishing neutrino masses and lepton mixing. The non-zero neutrino mass is considered one of the most important discoveries in fundamental particle physics.

To estimate the probability $P_{\nu_\alpha \to \nu_\beta}$ of a neutrino of type ν_α to oscillate into a neutrino of flavour ν_β after having travelled a distance L, the absolute squared oscillation amplitude (corresponding to the projection of the wave function $|\nu_\alpha(L,t)\rangle$ onto the final state $\langle\nu_\beta|$) has to be calculated:

$$P_{\nu_\alpha \to \nu_\beta}(L,t) = |\langle \nu_\beta | \nu_\alpha(L,t) \rangle|^2 \tag{2.16}$$

Calculating explicit oscillation probabilities is mostly a technical procedure. The results can be found in [36]. The oscillation probability of interest for the scope of this thesis is $P_{\nu_\mu \to \nu_\mathrm{e}}$ since the DUNE experiment will measure electron-(anti)neutrino appearance from a muon-(anti)neutrino beam. However, since the muon-(anti)neutrinos from the DUNE beam travel through the Earth's crust, the neutrino oscillation probability needs to be corrected for matter effects. The origin of such matter effects are found in the weak field of matter, mostly from the electrons, which affect the neutrino's dispersion relation. Neutrinos travelling through matter have a different effective mass than neutrinos travelling through vacuum, and therefore the Hamiltonian in the time evolution (see Equation 2.15) slightly changes [37]. Since the matter effects are sensitive to the neutrino mass, they can be used to study the neutrino mass hierarchy depicted in Figure 2.1. The full $P_{\nu_\mu \to \nu_\mathrm{e}}$ oscillation probability, taking into account

matter effects, reads as [38]

$$
\begin{aligned}
P_{\nu_\mu \to \nu_e} \approx & \sin^2(\theta_{23}) \sin^2(2\theta_{13}) \frac{\sin^2(\Delta_{31} - aL)}{(\Delta_{31} - aL)^2} \Delta_{31}^2 \\
& + \sin(2\theta_{23}) \sin(2\theta_{13}) \sin(2\theta_{12}) \frac{\sin(\Delta_{31} - aL)}{(\Delta_{31} - aL)} \Delta_{31} \frac{\sin(aL)}{aL} \Delta_{21} \cos(\Delta_{31} + \delta_{CP}) \\
& + \cos^2(\theta_{23}) \sin^2(2\theta_{12}) \frac{\sin^2(aL)}{(aL)^2} \Delta_{21}^2,
\end{aligned}
\tag{2.17}
$$

where the following substitutions have been used:

$$
\Delta_{ij} = \frac{(m_i^2 - m_j^2)L}{4E_\nu} = \frac{\Delta m_{ij}^2 L}{4E_\nu} \tag{2.18}
$$

$$
a = \frac{G_F N_e}{\sqrt{2}} \tag{2.19}
$$

with G_F denoting the Fermi constant, N_e the number density of electrons (or positrons in the antineutrino case) in the Earth, L the oscillation baseline in km, and E_ν the neutrino energy in GeV. Interestingly, both δ_{CP} and a can change the sign of some terms in Equation 2.17, i.e., a neutrino-antineutrino asymmetry can be introduced by $\delta_{CP} \neq 0$ or $\delta_{CP} \neq \pi$, and by a through matter effects. Consequently, $P_{\nu_\alpha} \to P_{\nu_\beta} \neq P_{\bar{\nu}_\alpha} \to P_{\bar{\nu}_\beta}$ if δ_{CP} is not 0 or π. Therefore, by switching the beam from ν_μ to $\bar{\nu}_\mu$, oscillation experiments can measure the value of δ_{CP}. Furthermore, as the product of a and L is present in Equation 2.17, the neutrino energy and the length of the baseline L determine an experiment's sensitivity for resolving the *neutrino mass ordering problem*. Accelerator-based neutrino-oscillation experiments can tune the baseline L and the neutrino energy E to obtain optimal parameters maximising the sensitivity for δ_{CP} measurements and to resolve the *neutrino mass hierarchy problem*.

Despite the simplicity of the neutrino mixing model, it does not predict the parameters describing the nature of neutrino oscillations. Those parameters have to be determined experimentally. In the case of three active flavours, the set of parameters consist of three mixing angles θ, two squared mass differences Δm^2, and one CP-violating phase. Table 2.1 summarises the neutrino-oscillation parameters obtained from a global parameter fit based on the three-neutrino mixing scheme. It appears that the uncertainty on δ_{CP} is still rather large. Furthermore, due to the large uncertainty on $\langle \Delta m_{32}^2 - \Delta \overline{m}_{32}^2 \rangle$, the sign of Δm_{32}^2 is not yet known and thus it is not yet clear whether the neutrino masses are ordered normally ($m_3 > m_2 > m_1$) or inverted ($m_2 > m_1 > m_3$), as illustrated in Figure 2.1. To determine those parameters with higher accuracy, large neutrino samples collected with neutrino-oscillation experiments sensitive to those parameters are needed. Therefore, future oscillation experiments will have to enhance their sensitivities to those parameters through tuning the energy spectrum of the neutrinos, E, and the length of the oscillation baseline, L, according to Equation 2.17. Recent development in neutrino beam production techniques allowed for much higher neutrino beam intensities, enabling collecting neutrino data with higher statistics in a shorter time.

Parameter	Mass Ordering	Value	Unit
$\sin^2(\theta_{12})$	both	0.307 ± 0.013	-
$\sin^2(\theta_{13})$	both	$(2.18 \pm 0.07) \cdot 10^{-2}$	-
$\sin^2(\theta_{23})$	normal	0.545 ± 0.021	-
$\sin^2(\theta_{23})$	inverted	0.547 ± 0.021	-
Δm^2_{21}	both	$(7.53 \pm 0.18) \cdot 10^{-5}$	eV^2
Δm^2_{32}	normal	$(2.453 \pm 0.034) \cdot 10^{-3}$	eV^2
Δm^2_{31}	inverted	$(-2.546^{+0.034}_{-0.040}) \cdot 10^{-3}$	eV^2
δ	both	$(1.36 \pm 0.17) \cdot 10^{-2}\pi$	rad
$\langle \Delta m^2_{21} - \Delta \overline{m}^2_{21} \rangle$	both	$< 1.1 \cdot 10^{-4}$ (99.7 % C.L.)	eV^2
$\langle \Delta m^2_{32} - \Delta \overline{m}^2_{32} \rangle$	both	$(-0.12 \pm 0.25) \cdot 10^{-3}$	eV^2

Table 2.1: Neutrino oscillation parameters obtained from a global parameter fit based on the three-neutrino mixing scheme. The uncertainties correspond to 1σ, if not stated otherwise. [36]

2.2.2 Neutrino Interactions and Cross Sections

Since neutrinos are electrically neutral and un-coloured particles, the only SM interactions available to neutrinos are those of the weak force. As a result, neutrinos can only be detected indirectly via secondary particles, either scattered or produced, when neutrinos interact with matter. Furthermore, weak interactions (as the name suggests) typically have small interaction cross-sections, especially when the involved particles have low energies. Those facts make the study of neutrino interactions challenging. However, a good understanding of neutrino interactions with matter is essential for precise neutrino-oscillation measurements since those require knowledge about the neutrino type, energy and momentum. From long-baseline neutrino-oscillation experiments, it is known that neutrino interactions are the dominant source for systematic uncertainties.

Weak interactions can be divided into two types, the NC interaction where an electrically neutral Z^0 gauge boson is exchanged between the interacting particles, and the CC interaction where a charged $W^\pm$ gauge boson acts as the mediator between the interacting particles. Figure 2.2 shows NC and CC interactions of electrons with ν_μ and $\bar{\nu}_\mu$. Unlike the force mediators for the electromagnetic and strong interactions (the photon and the gluon, respectively), the weak vector bosons are massive with masses of $\mathcal{O}(100\,\mathrm{GeV})$. Thus, at low energies of a few GeV, the weak interaction vertices appear point-like and cannot be resolved experimentally. Consequently, only the initial and final states of a neutrino interaction within a detector can be determined. Although the total neutrino interaction cross-section is a function of its energy, the momentum transfer of the neutrino to the target particle determines how well the target can be resolved and what final state particles are available for the interaction. However, the momentum transfer strongly depends on the neutrino energy. The following paragraph discusses the most commonly used neutrino interaction types.

In an elastic scattering process, the (anti)neutrino exchanges a Z^0 gauge boson (NC interaction) with a target particle T, e.g. a nucleon or an electron. Elastic scattering causes the target particle to recoil but leaves no other experimental signatures in the detector. Both initial and final states show the same particle types, but with

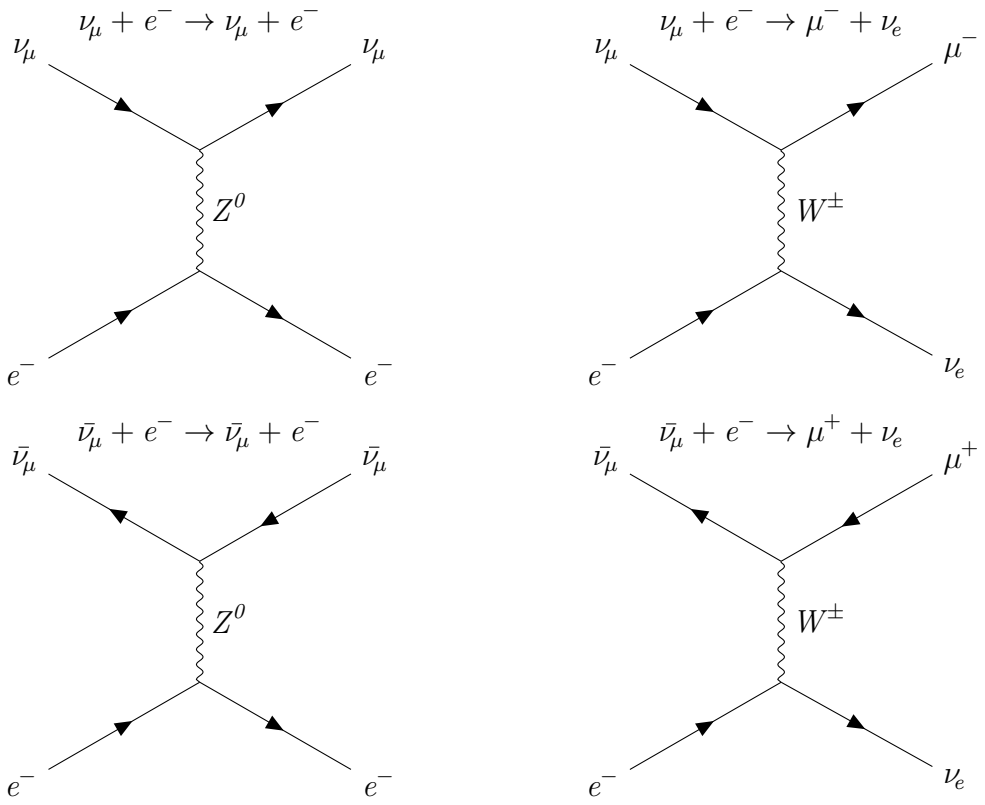

Figure 2.2: Feynman diagrams of ν_μ and $\bar{\nu}_\mu$ NC (left) and CC (right) interactions with electrons. In NC interactions, the involved particles only exchange energy and momentum, and all incident particles appear in the final state. In CC interactions, the $W^\pm$ boson exchanges energy and momentum, and changes each particle to its doublet partner particle (e.g. $\nu_e \leftrightarrow e^-$, $\bar{\nu}_e \leftrightarrow e^+$).

different energies and momenta. Elastic interactions dominate at small momentum transfers and thus are dominant for low-energy (anti)neutrinos. The scattering process can be described as follows:

$$\begin{aligned} \nu_\ell + T &\to \nu_\ell + T \qquad \text{(elastic scattering)} \\ \bar{\nu}_\ell + T &\to \bar{\nu}_\ell + T. \end{aligned} \tag{2.20}$$

The Quasi Elastic (QE) (anti)neutrino scattering process is the CC-equivalent to the elastic NC scattering. A $W^\pm$ gauge boson is exchanged between the target particle (e.g. a proton, neutron or an electron) and the (anti)neutrino, which thus turns into the corresponding (anti)lepton. The target particle recoils but is kept intact. QE interactions can be described by the following interactions:

$$\begin{aligned} \nu_\ell + p &\to \ell + n \qquad \text{(QE scattering)} \\ \bar{\nu}_\ell + n &\to \bar{\ell} + p \\ \nu_\ell + e^- &\to \ell + \nu_e \\ \bar{\nu}_\ell + e^- &\to \bar{\ell} + \nu_e. \end{aligned} \tag{2.21}$$

The available momentum transfer of neutrinos is enhanced at higher energies, and the particles can undergo inelastic scattering. The region of low momentum transfer in inelastic scattering processes is dominated by the class of Resonant (RES) interactions. A RES neutrino interaction excites the nucleus N to a baryonic resonance (for example Δ, Δ^{++}, N^*, ...) before it decays. Usually, the produced resonant state is too short-living to be directly observed. The resonance subsequently decays to a nucleon accompanied in most of the cases by a single pion, which can be detected in the final state. Depending on the resonance, different final states can result in multiple particles like pions, kaons, photons, etc. Two examples of RES scattering interactions are

$$\begin{aligned} \nu_\ell + N &\to \nu_\ell + \Delta \to \nu_\ell + N + \pi^0 \qquad \text{(RES scattering)} \\ \nu_\ell + p &\to \ell + \Delta^{++} \to \ell + p + \pi^+. \end{aligned} \tag{2.22}$$

At high momentum transfers, the inelastic scattering is dominated by the Deep Inelastic Scattering (DIS) where the neutrino scatters directly off a constituent quark from a nucleon, including the sea quarks. The nucleus thus fragments and the scattered-off quark produces jets of hadrons. Typical DIS interactions can be written as (NC and CC interactions, respectively)

$$\begin{aligned} \nu_\ell + N &\to \nu_\ell + X \qquad \text{(DIS scattering)} \\ \nu_\ell + N &\to \ell + X, \end{aligned} \tag{2.23}$$

where X denotes a group of hadrons.

In between the RES and DIS regions, at intermediate momentum transfer, the inelastic scattering sometimes is called *shallow inelastic scattering* where the nucleus neither forms recognisable resonances nor is entirely fragmented. To date, no model capable of describing this scattering region with sufficient accuracy is available.

In addition to elastic, quasi-elastic and inelastic scattering, there is another class, the Coherent Scattering (COH), where the neutrino interacts with a target nucleus N as a whole. The nucleus recoils as a whole and stays intact (un-fragmented) in

the same state as before the interaction. This can only be the case if the momentum transferred to the nucleus is small. COH neutrino scattering processes often produce ρ or K mesons or (neutral) pions, as shown in the following interaction:

$$\nu_\ell + N \rightarrow \nu_\ell + N + \pi^0 \qquad \text{(COH scattering)} \tag{2.24}$$

Although the COH scattering cross-section is small, the COH π^0 production is an important channel to be studied in neutrino-oscillation experiments searching for ν_e appearance, such as the DUNE experiment. The π^0 decays in most of the cases to a pair of photons which can mimic the electron signal from a ν_e CC interaction. That is true for all channels producing neutral pions, e.g. the RES π^0 production described in the first interaction of Equation 2.22.

Another class of interactions is described by xpyh interactions, where x and y are integer numbers describing how many particles and how many holes, respectively, are produced. For example, the QE scattering described in Equation 2.21 corresponds to 1 particle and 1 hole (1p1h) interaction since the (anti)neutrino scatters off one bound nucleus only. Similarly, in a 2 particles and 2 holes (2p2h) interaction, the probe interacts with two bound nucleons and creates two particles and two holes. Since in this interaction, a virtual meson is exchanged inside of the target nucleon, 2p2h interactions sometimes are referred to as Meson Exchange Current (MEC). MEC interactions are important since they can mimic QE interactions and thus can affect the detector response of QE interactions. Table 2.2 summarises the expected rates for the different interaction types in the DUNE ND for both, ν and $\bar{\nu}$ enhanced beams, corresponding to Forward Horn Current (FHC) and Reverse Horn Current (RHC) beam modes, respectively, and with a fiducial mass of 50 t LAr.

Interaction Type	FHC Yearly Rate
ν_μ CC	$8.2 \cdot 10^7$
$\bar{\nu}_\mu$ CC	$3.6 \cdot 10^6$
NC total	$2.8 \cdot 10^7$
ν_μ CC 0π	$2.9 \cdot 10^7$
ν_μ CC $1\pi^\pm$	$2.0 \cdot 10^7$
ν_μ CC $1\pi^0$	$8.0 \cdot 10^6$
ν_μ CC 3π	$4.6 \cdot 10^6$
ν_μ CC other	$9.2 \cdot 10^6$
$\nu_e + \bar{\nu}_e$ CC	$1.4 \cdot 10^6$
$\nu + e^-$ elastic	$8.4 \cdot 10^3$

Interaction Type	RHC Yearly Rate
$\bar{\nu}_\mu$ CC	$2.6 \cdot 10^7$
ν_μ CC	$1.4 \cdot 10^7$
NC total	$1.5 \cdot 10^7$
$\bar{\nu}_\mu$ CC 0π	$1.2 \cdot 10^7$
$\bar{\nu}_\mu$ CC $1\pi^\pm$	$7.6 \cdot 10^6$
$\bar{\nu}_\mu$ CC $1\pi^0$	$2.4 \cdot 10^6$
$\bar{\nu}_\mu$ CC 3π	$8.3 \cdot 10^5$
$\bar{\nu}_\mu$ CC other	$1.2 \cdot 10^6$
$\nu_e + \bar{\nu}_e$ CC	$9.3 \cdot 10^5$
$\nu + e^-$ elastic	$6.4 \cdot 10^3$

Table 2.2: Expected interaction rates in the DUNE Near-Detector Liquid Argon Component (ND-LAr) for ν_μ enhanced (FHC) and $\bar{\nu}_\mu$ enhanced (RHC) beam mode. [39]

The following paragraph briefly introduces the concepts of interaction cross-sections. An interaction cross-section σ has the dimension of an area, typically given in barn ($1\,\text{b} = 10^{-24}\,\text{m}^2$). The smaller the cross section is, the fewer interactions are expected if all other parameters are kept constant. The number of interactions N_i can be written as

$$N_i = \sigma \cdot N_t \cdot \Phi, \tag{2.25}$$

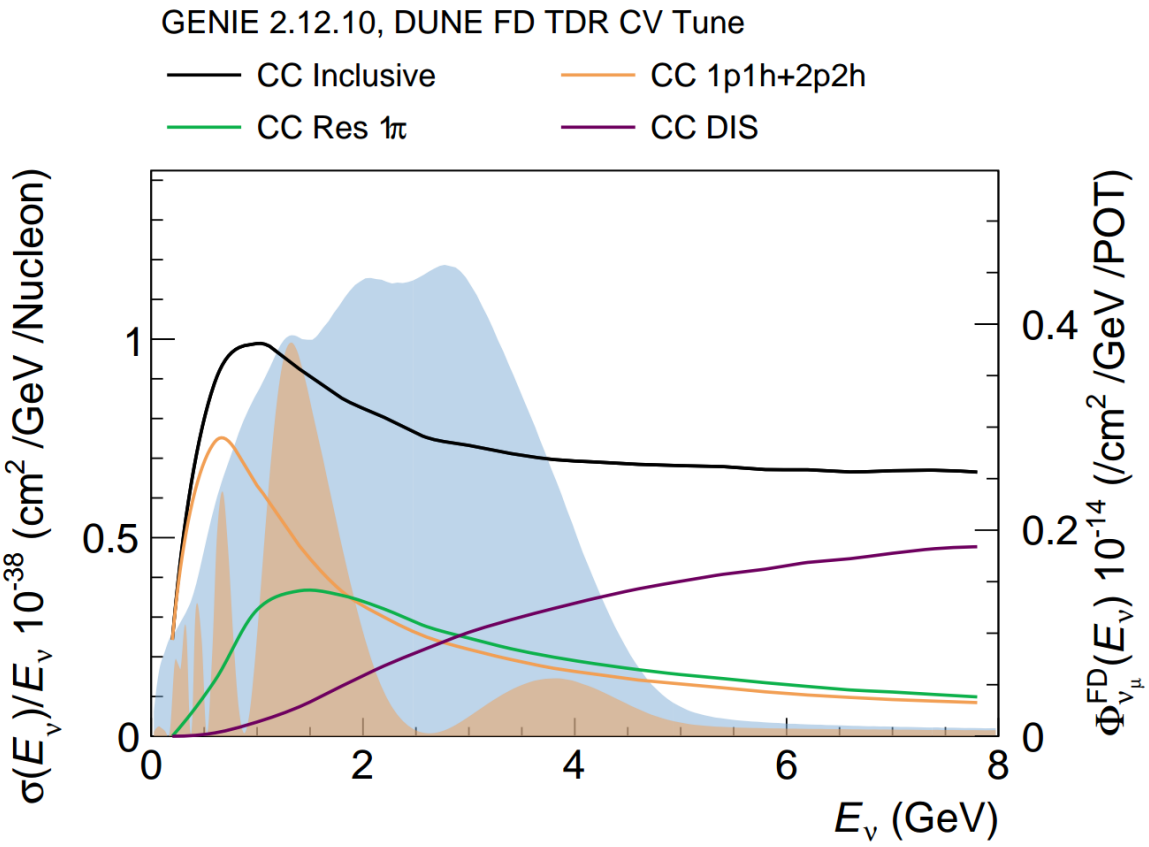

Figure 2.3: Total neutrino-per-nucleon CC cross section (black line) divided by neutrino energy and plotted as a function of the true neutrino energy in the DUNE interaction model. Also shown are the various contributions from CC RES 1π (green line), CC 1p1h + 2p2h (orange line), and CC DIS (purple line). The blue and orange filled regions represent, respectively, the unoscillated and oscillated ν_μ flux at the DUNE FD site. [40]

where N_t is the number of target particles and Φ measures the incident particle flux (number of particles per unit time and per unit area). Since the neutrino interaction cross-section is tiny, a reasonable number of interactions within a detector can only be achieved by a large neutrino flux and many target particles. The cross section in general depends on the particle's energy E,

$$\sigma(E) = \frac{N_i}{N_t \cdot \Phi}. \tag{2.26}$$

Figure 2.3 shows the DUNE flux at the FD position with overlaid interaction cross-sections for different interaction types.

2.2.3 Neutrino Final State Detection

As discussed in Section 2.2.2, the direct observation of neutrinos is not possible. A detector can only record the interactions of the final state particles produced in neutrino interactions. The detection of those final state particles requires understanding the underlying processes happening when particles traverse material. This section describes the basic mechanisms happening when (charged and neutral) particles pass through the active material of a particle detector. Depending on the energy and type of the particle, the detector response might be different. That eventually enables calorimetry, PID, and higher-level reconstruction variables such as the particle-momentum, the event topology, or even the neutrino energy. The focus of this section is on the interactions and particle energies relevant for the scope of this thesis, in particular for the LArTPC technology in the future neutrino-oscillation experiment DUNE (see Section 2.3.1).

Charged particles passing through matter can lose energy via several mechanisms, namely (elastic and inelastic) scattering, ionisation, Bremsstrahlung, Cherenkov radiation, and transition radiation. The last two mechanisms are not very interesting in the context of LArTPCs and are therefore not discussed here. At low momentum transfer between the incident particle and the target, elastic and quasi-elastic scattering occurs, as described in Section 2.2.2. Small angular deflections of the projectile are expected after every scattering process. Most of the interactions happen due to the Coulomb scattering from nuclei, however, for hadronic particles, the strong interaction also contributes to the scattering process. If the incident particle is scattered multiple times, the *central limit theorem* can be used to describe the Multiple Coulomb Scattering (MCS) where the net scattering and displacement are distributed gaussian. The Root Mean Square (RMS) of the scattering angle distribution can be described by the *Highland formula* as

$$\theta_{\text{RMS}} = \frac{13.6\,\text{MeV}}{\beta cp} z \sqrt{\frac{2x}{X_0}} \cdot \left(1 + 0.038 \ln \frac{x}{X_0}\right), \tag{2.27}$$

where p denotes the momentum of the projectile with velocity βc and a charge of z [36]. Furthermore, x/X_0 defines the thickness of the material in units of radiation lengths, which is described with Equation 2.32. The relation given in the *Highland formula* often is used to reconstruct incident particle's momenta utilising their measured distributions of scattering-angles.

At higher momentum transfer, charged particles mainly lose energy due to collision with atomic electrons. That leads to ionisation, atomic excitation, or collective

excitation of the material through which the particle passage happens. The mean rate of energy loss $\langle -dE/dx \rangle_{\text{ion}}$ (or mass stopping power) of moderately relativistic ($0.1 \lesssim \beta\gamma \lesssim 1000$) heavy[4] charged particles due to ionisation only is well described by the *Bethe Bloch relation* [36],

$$\left\langle -\frac{dE}{dx} \right\rangle_{\text{ion}} = Kz^2 \frac{Z}{A} \frac{1}{\beta^2} \left[\frac{1}{2} \ln \left(\frac{2m_e c^2 \beta^2 \gamma^2 W_{max}}{I^2} \right) - \beta^2 - \frac{\delta(\beta\gamma)}{2} \right], \tag{2.28}$$

with the symbol definitions summarised in Table 2.3. Note that this equation is not valid for electrons and positrons as their mass is equal to the mass of the electrons present in the absorber material. Furthermore, in the case of an incident electron, the scattered particle could not be distinguished from the collision partner. In contrast, in the case of incident positrons, the two colliding particles would annihilate. The equivalent of the *Bethe Bloch relation* (Equation 2.28) for electrons and positrons is called the *Bhabha equation*, which can be found in [36]. The mean rate of energy loss defined as in Equation 2.28 has the advantage of being about the same for most materials, only decreasing slightly with a Z/A dependency. The linear stopping power of a heavy charged particle is given by $-\rho \cdot \langle dE/dx \rangle$ where ρ denotes the mass density of the stopping material.

	Symbol	Value, Unit
$4\pi N_A r_e^2 m_e c^2$	K	$0.307\,075\,\text{MeV}\,\text{mol}^{-1}\,\text{cm}^2$
Avogadro's number	N_A	$6.022\,141 \times 10^{23}\,\text{mol}$
Classical electron radius	r_e	$2.817\,940\,\text{fm}$
Speed of light in vacuum	c	$299\,792\,458\,\text{m}\,\text{s}^{-1}$
Charge number of incident particle	z	-
Atomic number of absorber	Z	-
Atomic mass of absorber	A	$\text{g}\,\text{mol}^{-1}$
Relativistic factor (v/c)	β	-
Electron mass	m_e	$0.510\,999\,\text{MeV}$
Relativistic Lorentz factor	γ	-
Max. energy transfer to an electron	W_{max}	MeV
Mean excitation energy	I	eV
Density effect correction (ionisation)	$\delta(\beta\gamma)$	-
Fine-structure constant (in n.u.)	α	0.007 297

Table 2.3: Summary of constants used in this section, particularly for the description of the mean rate of energy loss in Equation 2.28. The mean excitation energy of the absorber material I can be approximated by $I \approx 16Z^{0.9}\text{eV}$. The density effect correction $\delta(\beta\gamma)$ describes the screening of the atomic electrons in the absorber as a function of the incident particle's momentum [36].

Figure 2.4 shows the mass stopping power for positive muons in copper as a function of the muon momentum. The *Bethe Bloch relation* shown in Equation 2.28 precisely describes the behaviour of charged particles others than electrons in the

[4] Heavy refers to particles more massive than electrons.

regime where $0.1 \lesssim \beta\gamma \lesssim 1000$, corresponding to the red curve in Figure 2.4. It appears that there is a broad range of momenta where the particle's mass stopping power is at a minimum. A heavy charged elementary particle, no matter from which type, having a momentum corresponding to this minimum is called Minimum Ionising Particles (MIP). Knowing the mass stopping power of MIPs is important for the development of a particle detector since it provides a measure for the minimum required energy resolution.

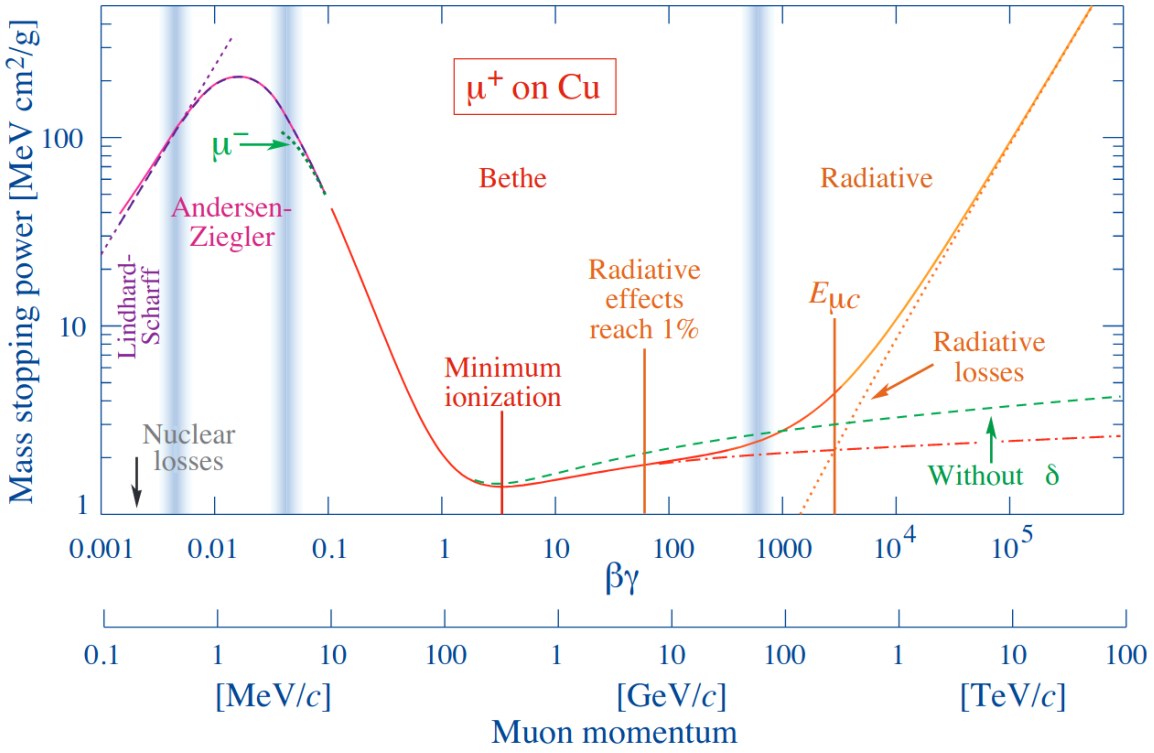

Figure 2.4: Mass stopping power, $\rho \cdot \langle dE/dx \rangle$, for positive muons in copper as a function of the muon momentum. Similar behaviour is found for LAr and other materials. [36]

For LAr, which has a mass density of about $1.4\,\mathrm{g\,cm^{-3}}$, the mass stopping power of a MIP (with single charge) corresponds to

$$\rho \cdot \left\langle \frac{dE}{dx} \right\rangle_{\text{ion, MIP}} \overset{\text{LAr}}{\approx} 2.12\,\mathrm{MeV\,cm^{-1}}. \tag{2.29}$$

For particles with low momenta, $0.1 \lesssim \beta\gamma \lesssim 1$, the mean rate of energy loss drastically increases with a strong $1/\beta^2$ dependency. Such particles deposit more and more energy as they approach their stopping point, which manifests itself as the characteristic *Bragg peak*, a peak in the energy deposition close to the endpoint of a particle's trajectory. In the high-momentum region, $\beta\gamma \gtrsim 1000$, radiative energy losses become dominant. In this momentum regime, the charged particle's energy loss increases with a logarithmic dependency on β, which accounts for the extended transverse electric field of relativistic charged particles travelling through matter. The $\delta(\beta\gamma)$-term in Equation 2.28 corrects for such screening by the atomic shell electrons present in the absorber material. Figure 2.5 shows the mass stopping power of charged particles in the first TPC, Positron-Electron-Proton (PEP)-4/9, containing an argon-methane gas mixture (80 % and 20 %, respectively) pressurized at 8.5 bar [41]. With this TPC,

an outstanding relative dE/dx resolution of 3 % was achieved. From this figure, it appears that the mass stopping power can be used to determine the particle types for traces of energy depositions observed in a TPC, a process called PID. For a precise PID, the quality of the calorimetric information is critical.

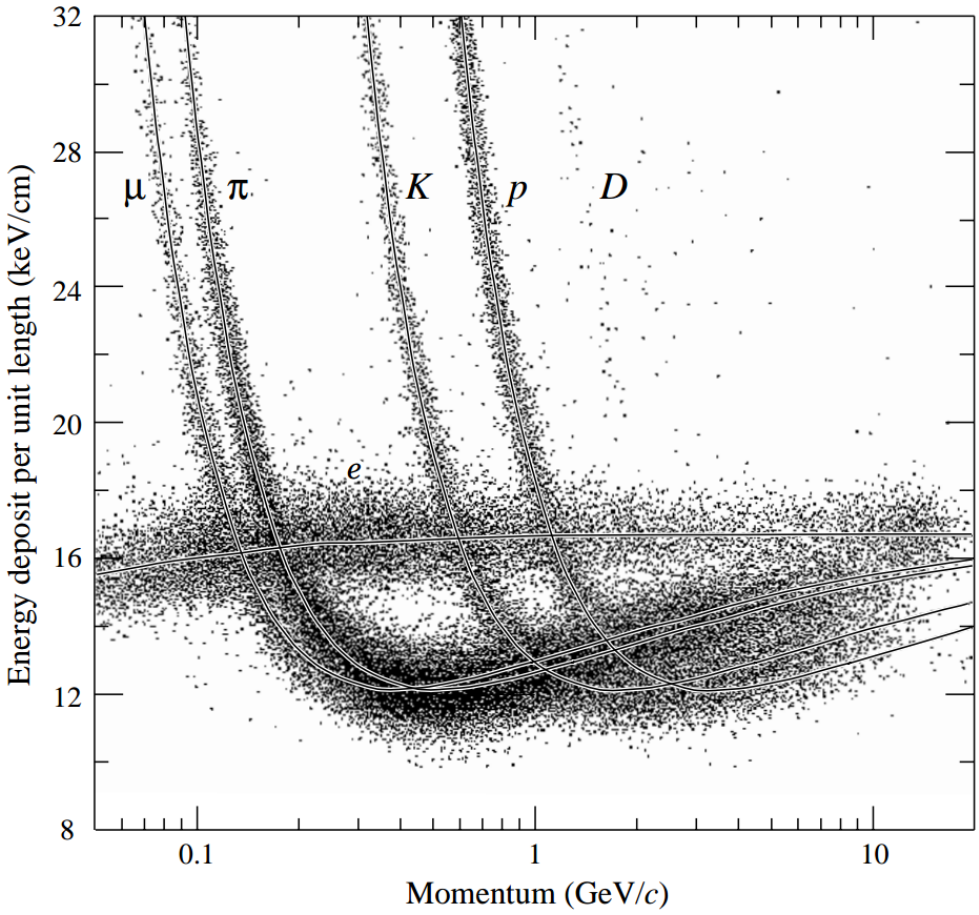

Figure 2.5: Specific energy loss dE/dx in the PEP-4/9-TPC, pressurised to 8.5 bar with an argon-methane gas mixture of 80 % and 20 %, respectively. The relative resolution on dE/dx achieved with this TPC was 3 % [41].

In the high-energy region, where the projectile's energy is much higher than the energy of a MIP, energy loss due to Bremsstrahlung becomes dominant. Bremsstrahlung radiation occurs when electrically charged particles are accelerated in the presence of the Coulomb field from a spectator particle. The amount of Bremsstrahlung photons emitted, σ_{brems}, is related to the projectile's energy E and mass m as follows:

$$\sigma_{brems} \propto \frac{E}{m^2}. \tag{2.30}$$

Due to their small mass, electrons would radiate much more Bremsstrahlung than heavier charged particles with the same energy. The energy loss of a charged particle, including electrons, due to only Bremsstrahlung can be described by

$$\left\langle -\frac{dE}{dx} \right\rangle_{\text{brems}} = \frac{E}{X_0}, \tag{2.31}$$

where E is the projectile's energy and X_0 is the Electromagnetic (EM) radiation length of the absorber. The radiation length defines the characteristic amount of matter

traversed by the incident particle until the related interaction statistically happens. It can be written as

$$X_0 \approx \frac{A}{4\alpha N_A r_e^2 Z \cdot (Z+1) \cdot \ln\left(\frac{183}{Z^{1/3}}\right)}, \tag{2.32}$$

with $\alpha \approx 1/137$ as the fine-structure constant. For electrons, the EM radiation length corresponds to the mean distance over which a high-energy electron loses all but $1/e$ of its energy by Bremsstrahlung. The corresponding value for X_0 for LAr can be found in Table 3.1.

The total mean rate of energy loss for charged particles can be written as

$$\left\langle -\frac{dE}{dx} \right\rangle_{\text{tot}} = \left\langle -\frac{dE}{dx} \right\rangle_{\text{ion}} + \left\langle -\frac{dE}{dx} \right\rangle_{\text{brems}}. \tag{2.33}$$

Further, the critical energy E_{crit} can be defined as the energy where a particle's energy loss due to ionisation equals the particle's energy loss due to Bremsstrahlung,

$$\left\langle -\frac{dE}{dx}\left(E_{crit}\right) \right\rangle_{\text{ion}} = \left\langle -\frac{dE}{dx}\left(E_{crit}\right) \right\rangle_{\text{brems}}. \tag{2.34}$$

Since the critical energy is proportional to the squared mass of the incident particle, $E_{crit} \propto m^2$, it is small for light particles ($\mathcal{O}\,(10\,\text{MeV})$ for electrons) but becomes large for heavier projectiles ($\mathcal{O}\,(1000\,\text{GeV})$ for muons).

While charged particles produced in interactions can be directly detected, neutral particles such as photons first need to be converted to electric charge before it is possible to detect them. One possibility is photoelectric absorption, where a photon transfers all of its energy to an atomic electron that is ejected from the atom with an energy equal to that of the incoming photon minus its binding energy to the atom. The photoelectric absorption in LAr, however, is important only for photons with energies $\lesssim 100\,\text{keV}$. There are two processes of interest for the photon-to-charge conversion for γ with energies $\gtrsim 1\,\text{MeV}$, namely Compton scattering and particle-antiparticle pair production. Both processes attenuate the photon intensity according to the *Lambert-Beer law*,

$$I = I_0 \cdot \exp\left(-\mu x\right), \tag{2.35}$$

where I_0 and I denote the photon intensity before and after, respectively, having passed through the absorber of thickness x. Further, μ is the mass attenuation coefficient, which depends on the absorber material and its properties. Compton scattering, sometimes referred to as incoherent scattering, is the process called when a photon is scattered off an electron from the shell of an atom in the absorber material. The photon transfers some energy to the electron, and thus the photon's frequency is changed. In the particle-antiparticle pair production process, a photon usually produces an electron-positron pair. Since the momentum must be a conserved quantity, this process requires the presence of a so-called spectator particle, e.g. the nuclei of the absorber material or its shell electrons. However, pair production in the electron field is, compared to the pair production in the nuclear field, strongly suppressed, as shown in Figure 2.6. For photon energies below the threshold energy of $2m_{e^-} \approx 1\,\text{MeV}$, no electron-positron pair production can happen. Up to about 11 MeV of photon energy, the Compton scattering cross section is larger than the particle-antiparticle pair production cross section. High-energy photons predominantly lose energy in

matter by the production of electron-positron pairs. The mean free path of a photon to undergo pair production, λ_{pp}, is closely related to the EM radiation length X_0, as follows from

$$\lambda_{pp} = \frac{9}{7} X_0 \overset{\text{LAr}}{\approx} 18.0\,\text{cm}. \tag{2.36}$$

Figures 2.6 and 2.7 show, respectively, the absolute and relative photon cross section on LAr for different processes for γ with energies in the range of 3 to 1000 MeV. For the reconstruction of neutral pions, elucidated in Section 7.4, where photons with energies in the range of about 10 to a few 100 MeV are produced, the Compton scattering cross-section is important as the process changes the direction of the photon and thus can affect the π^0 reconstruction.

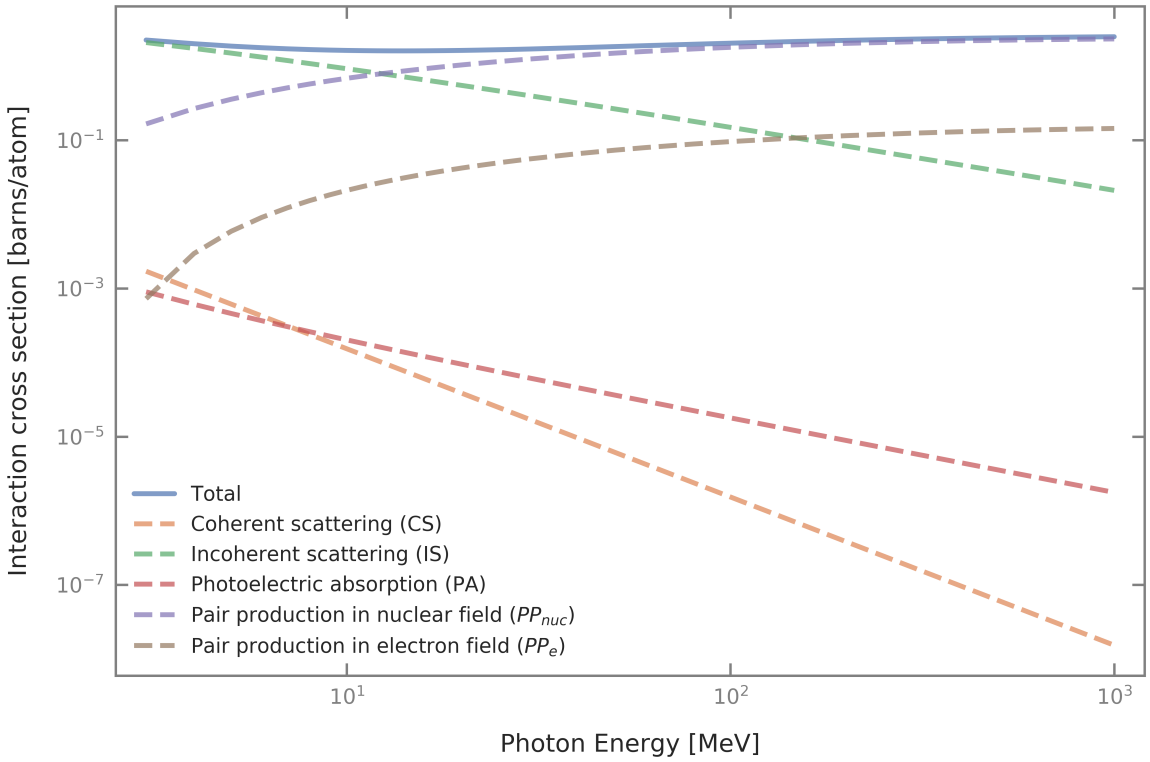

Figure 2.6: Absolute photon cross section on LAr as a function of the photon energy, and broken down to specific interactions. Photons with energies below a few MeV mainly undergo incoherent scattering and pair production. The latter becomes the dominant cross section at energies of about 10 MeV. The data was generated using XCOM[5].

As discussed earlier, the critical energy E_{crit} of electrons and positrons is small, $\mathcal{O}(10\,\text{eV})$, compared to heavier particles. Thus, already relatively low energetic electrons and positrons can radiate Bremsstrahlung photons. The typical distance-scale for this process to happen is given by the EM radiation length X_0, described in Equation 2.32. The produced Bremsstrahlung photons, in turn, can undergo electron-positron pair production at a typical length close to X_0 (see Equation 2.36), corresponding to the mean free path of a photon. Consequently, at energies higher than a few MeV, electrons, positrons, and photons can create each other in an alternating cascade called EM shower. As the length scales for both processes, Bremsstrahlung and pair production, are comparable, the number of particles in the EM shower doubles about every EM radiation length. The process of EM shower formation continues until the particles have too little energy for either radiating Bremsstrahlung

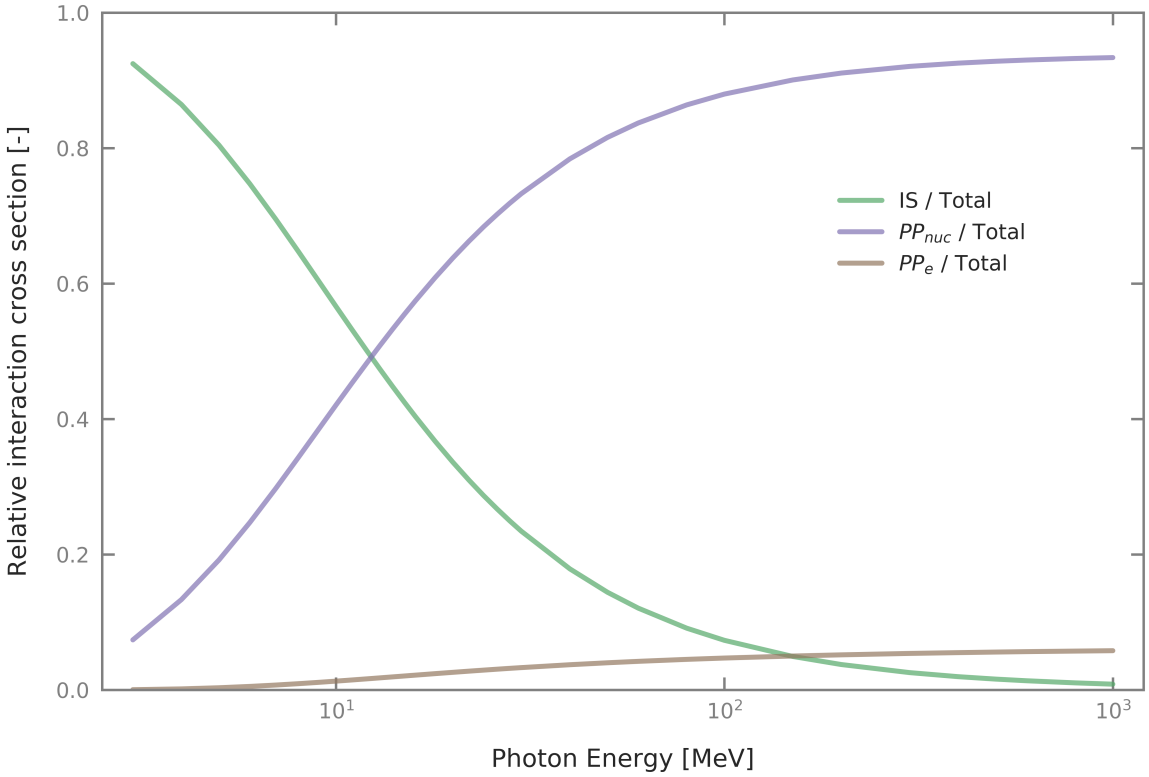

Figure 2.7: Relative photon cross section on LAr as a function of the γ energy. The pair production becomes the dominant process at photon energies larger than a few MeV. Although this is mainly driven by the pair production in the nuclear field (PP_{nuc}), the pair production in the electron field (PP_e) also contributes. The data was generated using XCOM[6].

or producing electron-positron pairs. At this point, the particles mainly lose their energy by Compton scattering (photons) and ionisation (electrons and positrons). Similarly, hadrons can produce hadronic showers. However, as opposed to EM showers where only three types of particles drive the shower development, hadronic showers are, in principle, much more complex because many other particles can be involved.

2.2.4 Open Questions in Neutrino Physics

Even though many experiments conducted during the last few decades have discovered a lot about the nature of the neutrino, some open and fundamental questions about these particles remain unsolved. The following list summarises some of these questions:

- Is CP-symmetry violated in the lepton sector, and if so, how much?
- How are the neutrino masses ordered?
- Is the mixing angle θ_{23} maximal?
- Do sterile neutrinos exist?
- What is the absolute neutrino mass scale?
- Are neutrinos *Dirac fermions* or *Majorana particles*?

The next-generation neutrino-oscillation experiment DUNE, described in Section 2.3.1, is intended to answer the first two questions in particular. These are the most interesting questions in the context of this thesis and will therefore be discussed in more detail here.

According to the standard three-flavour neutrino mixing described with Equation 2.13, there are three sources for a potential CP violation in the lepton sector: One Dirac phase δ_{CP} and two Majorana phases α_1 and α_2. Since the Majorana phases cancel out in the standard three-flavour description of neutrino-oscillations experiments, the only way to probe for CP violation in the lepton sector using such experiments is via the Dirac phase. Knowledge about the CP-violating processes in the lepton sector will promote the understanding of the fundamental process of symmetry breaking and will also play a key role in the mechanism for the baryogenesis in the early Universe.

To date, it is not yet known how the neutrino masses are ordered. There could be two light and one heavy neutrino (the so-called *normal mass hierarchy* where $m_3 \gg m_2 > m_1$) or the neutrinos could be ordered as two heavy and one light mass eigenstate (the so-called *inverted mass hierarchy* where $m_2 > m_1 \gg m_3$), as depicted in Figure 2.1. If the neutrino mass eigenstates were inverted, at least two of the three neutrino masses would be quasi-degenerate, which would be odd in the way as the charged leptons and quarks are ordered normally. However, resolving this mass-hierarchy problem is not only important for fundamental but also practical reasons. For example, the search for the violation of the CP-symmetry in the lepton sector is significantly simplified and can be optimised knowing the neutrino mass ordering. Furthermore, solving the neutrino mass-ordering problem would increase the sensitivity for experiments searching for the absolute value of the neutrino masses and searches of lepton-number violations via neutrino-less double-beta decays. With

an even broader view, solving the mass-hierarchy problem could also constrain Grand Unified Theories (GUTs).

Recently, the T2K experiment excluded a CP conservation at 2 σ C.L. The same analysis prefers the normal mass hierarchy with a posteriori probability of 89 % [33].

2.3 Next-Generation Neutrino Experiments

The next-generation neutrino experiments include Hyper-K and DUNE, two complementary programs designed to resolve some of the open questions in neutrino and astroparticle physics are described in Section 2.2.4. Both experiments consist of massive detectors and use extremely powerful (anti)neutrino beams to collect large enough data samples of (anti)neutrino interactions.

Hyper-K, the successor of Super-Kamiokande, will be a Cherenkov detector filled with 258 kt of ultra-pure water in total [42], [43], serving as a target in the FD. The experiment will use much of the existing infrastructure used by T2K, in particular the ND facility and the beamline that provides (anti)neutrinos with a relatively narrow energy distribution peaking at ≈ 0.6 GeV. The oscillation base-line, defined by the direct distance between the ND and the FD, measures about 295 km. First data taking of Hyper-K is expected in 2027, with an initial beam power of 750 kW which will be increased to about 1300 kW after an upgrade of the beamline.

DUNE consists of a ND complex located at FNAL and a FD at the Sanford Underground Research Facility (SURF) in South Dakota, with an oscillation base-line of 1300 km [38]. The experiment's ND complex is composed of several detectors, including the ArgonCube LArTPC component. Installed deep underground at SURF, the FD consists of four 17 kt LArTPC modules. The DUNE beam line is expected to start operation in 2029 to provide the world's most intense (anti)neutrino beam with a beam power of 1200 kW initially, which will be upgraded to provide up to 2400 kW by 2036.

The complementarity of Hyper-K and DUNE provide important cross-checks on the highly demanding experiments. Since the DUNE experiment plays a key role in the scope of this thesis, the following Sections 2.3.1 and 2.3.2 describe this experiment and its scientific goals, respectively, in more detail.

2.3.1 The DUNE Experiment

DUNE is an accelerator-based long-baseline neutrino-oscillation experiment located in the USA [38], [44], [45], [46]. As shown in Figure 2.8, the experiment consists of a ND facility at FNAL in Illinois, and a FD site at the SURF in South Dakota. The (anti)neutrinos produced at FNAL are sent through the ND and then through the Earth's crust to the FD, an instrumented 70 kt LArTPC located 1.5 km deep underground at SURF 1300 km away. The FD consists of four massive LArTPC modules with a fiducial mass of 40 kt in total. DUNE was designed to precisely measure ν_e ($\bar{\nu}_e$) appearance from an initial ν_μ ($\bar{\nu}_\mu$) beam to measure neutrino oscillation parameters.

A closer view of the beamline and the ND hall is given in Figure 2.9. At FNAL, the *Main Injector* delivers protons in the energy range of 60 GeV to 120 GeV, which are guided onto a graphite target to produce secondary particles, mostly charged pions but also others such as charged kaons. A three-horn beam-focusing system

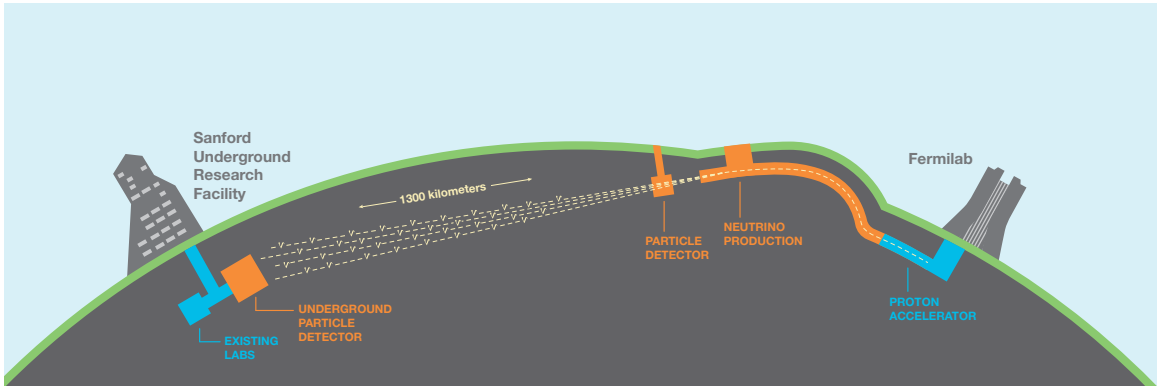

Figure 2.8: Cartoon illustrating the DUNE beam line and the ND complex at FNAL in Illinois and the FD facility at SURF in South Dakota, 1300 km from the neutrino production site. [38]

optimised for DUNE's sensitivity to the CP phase is used to select either positively or negatively charged secondaries. A decay pipe downstream of the focusing horns allows for the decay of the charged pions in flight, which will result in a beam of mostly ν_μ or $\bar{\nu}_\mu$, as described in Equation 2.2, depending on the polarity of the focusing horns. The small amount of K^- or K^+ produced in the proton target mainly produce more muon-(anti)neutrinos, but in some rare cases, with a branching ratio of $(5.07 \pm 0.04)\,\%$ [36], they decay to ν_e or $\bar{\nu}_e$, respectively. Furthermore, some of the muons produced in the charged pion decays may in turn decay to ν_e or $\bar{\nu}_e$ and the wrong type of either $\bar{\nu}_\mu$ or ν_μ, as described in Equation 2.4. Those processes result in the contamination of the beam with unwanted types of (anti)neutrinos. At the end of the decay pipe, an absorber pile removes particles other than neutrinos, mainly hadrons and muons, from the neutrino beam. The beam then passes through the ND hall located 574 m downstream of the proton target and finally is sent to the FD in South Dakota. For precise neutrino oscillation measurements, an estimation of the beam's (anti)neutrino flavour composition at the ND is crucial.

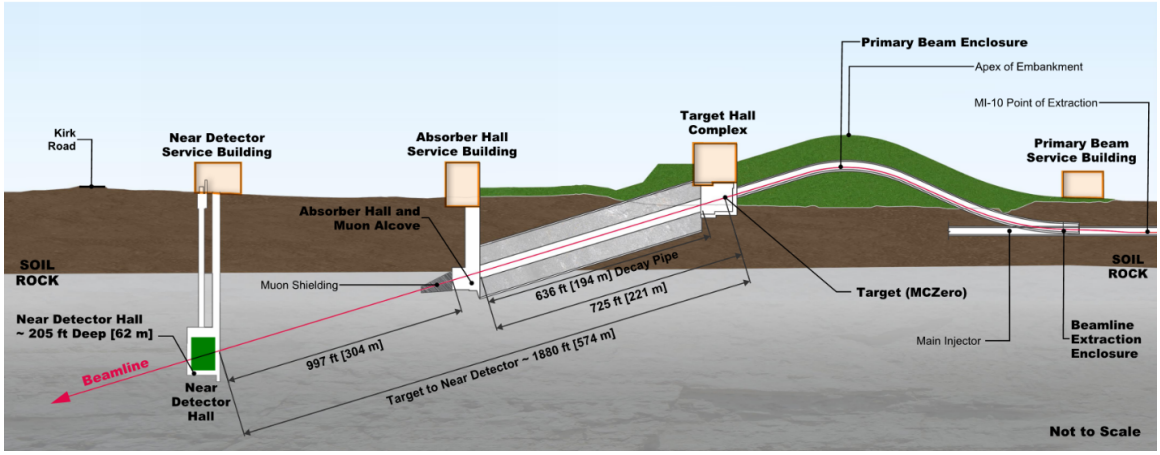

Figure 2.9: Schematic drawing of the DUNE neutrino beam line and the ND hall at FNAL in Illinois. [38]

The produced neutrino beam is pulsed with a spill duration of 10 µs at a cycle time of 0.7 s to 1.2 s, depending on the proton energy [47]. In a first phase, the beam facility will deliver between 1.0 MW and 1.2 MW proton beam power, corresponding

to 7.5×10^{13} Protons On Target (POT) per cycle. After a planned upgrade, the accelerator complex will provide up to 2.4 MW of beam power by 2036, doubling the number of protons per cycle. In a conservative plan, the beam line will operate at 1.2 MW of beam power for the first five years and at 2.4 MW for the following fifteen years.

The DUNE neutrino flux profile at the FD facility is shown in Figure 2.3 as the blue area. The neutrinos cover a broad spectrum of energies, peaking at about 3 GeV and with a width of ≈ 2 GeV. The baseline and energy of the (anti)neutrino beam are tuned according to Equation 2.17 to optimise the sensitivity for the δ_{CP} measurements and for the determination of the mass hierarchy, which are the primary scientific goals of DUNE. These and other physics opportunities are described in more detail in Section 2.3.2.

2.3.2 Physics Opportunities of the DUNE Experiment

The design of the DUNE experiment has been driven by the three-flavour neutrino oscillation paradigm. The experiment will take advantage of the high-intensity Long Baseline Neutrino Facility (LBNF) neutrino beam and a very capable ND, described in Section 6.3, to study many SM and Beyond Standard Model (BSM) physics topics. This section summarises some of these programs.

The primary physics goals of DUNE are the measurement of the δ_{CP} phase and the determination of the mass hierarchy. Figure 2.10 shows the expected significances to the CP violation sensitivity and for the neutrino mass ordering discrimination, both as a function of the experiment's data-taking time. DUNE will be capable of finding evidence ($\geq 3\sigma$) for CP violation for half of the phase space after about 6 years and a discovery ($\geq 5\sigma$) after about 11 years of data taking. One of the key strengths of DUNE is its ability to resolve the neutrino mass ordering for all allowed values of mixing parameters in the three-flavour paradigm, which is achievable after less than about 2.5 years of data-taking.

Apart from those primary scientific goals, DUNE will enable the accurate measurement of Δm^2_{31}, the electroweak mixing angles $\sin^2(2\theta_{13})$, $\sin(\theta_{23})$, and the octant of θ_{23}. The relatively large number of neutrino-nucleus interactions in the DUNE ND will ensure the extraction of those quantities from high statistics data samples. Since the larger part of the neutrinos from the LBNF will be above the τ mass, DUNE will have the possibility to measure the appearance of ν_τ from an initial ν_μ beam via CC interactions in the FD. This will provide an unique opportunity for τ physic studies.

Furthermore, the DUNE ND will be a powerful tool to measure the production of K^+ from beam neutrinos, which is relevant in the scope of the proton decay mode $p \to K^+ + \bar{\nu}$. Since the NC production of K^+ by atmospheric neutrinos is an important background to this process, the powerful LBNF neutrino beam that enables measuring the kaon production in the DUNE ND with high statistics is a key to constrain the proton decay background and to put limits on the proton half-life. Such limits are very valuable for constraining and excluding GUTs theories that predict rates for such processes.

The DUNE ND enables other opportunities to study SM physics, for example to probe the nucleon structure in different targets. Since the ND will employ argon and also hydrogen (bound in hydrocarbon) as target materials, the experiment will offer a rich program for nucleon structure studies. This is in particular important to gain

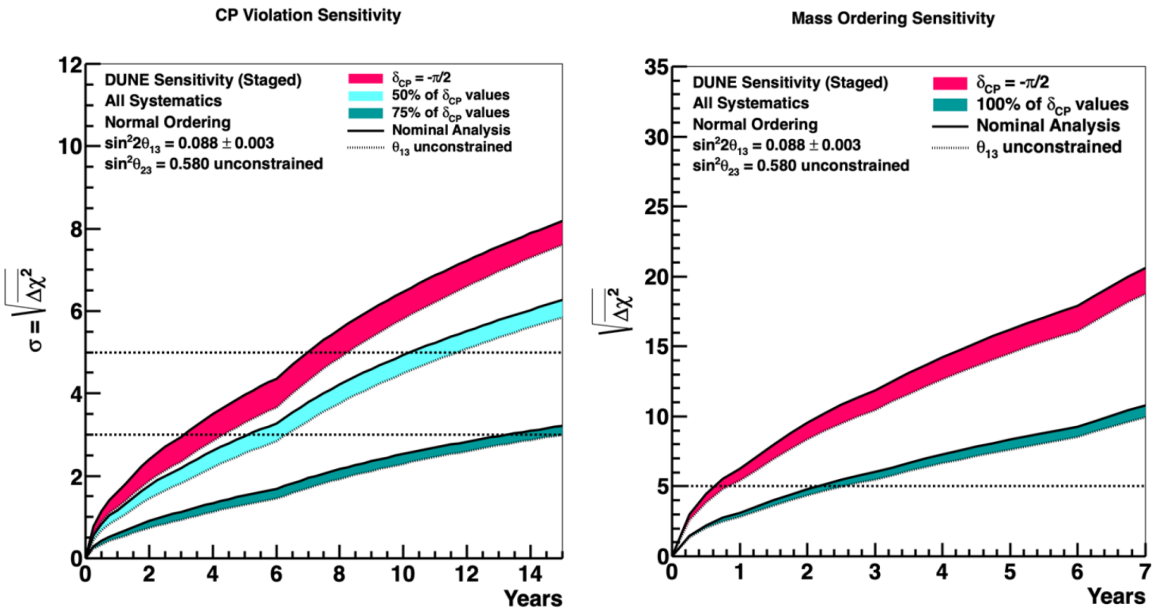

Figure 2.10: DUNE significances for the δ_{CP} phase (left) and the neutrino mass-ordering discrimination (right) as a function of the experiment's accumulated data taking time. For both figures, the normal mass ordering has been assumed. The widths of the bands show the impact of applying an external constraint on $\sin^2(2\theta_{13})$. [38]

knowledge about neutrino-nucleon scattering and to improve and tune the neutrino event generators.

The wide range for BSM physics searches in DUNE includes programs to find new physics in the neutrino trident production where a pair of leptons with opposite charges is produced by a neutrino that scatters off the Coulomb field of a heavy nucleus. The excellent vertex resolution and the magnetic field of the gaseous argon TPC in the DUNE ND provide crucial information to study those rare weak processes and their cross sections. In addition to the neutrino trident production, DUNE will enable searches for heavy neutral leptons, sterile neutrinos, light supersymmetric particles, and light dark matter particles, to name just a few. Also, DUNE will enable searches for non-standard neutrino interactions, Charge-Parity-Time (CPT) and Lorentz violations, as well as baryon number violating interactions. A detailed description about the BSM physics searches in DUNE is given in [48]. The very capable ND together with the world's most intense neutrino beam will provide data samples of yet unprecedented statistics and accuracy to shed light on such processes.

Finally, DUNE will look for neutrinos produced in a core-collapse supernova in the Milky Way to provide insight into such processes. The detection of supernova neutrinos can help to understand the process of neutron star formation and potentially to witness the birth of a black hole.

Chapter 3

The Liquid Argon Time Projection Chamber (LArTPC)

This chapter gives an overview of the LArTPC technology, beginning with a brief history of the LArTPC in Section 3.1. The working principle of a LArTPC is described in Section 3.2, where the advantages of LAr as detector material are discussed, as well as the fundamental mechanisms responsible for the production of the ionisation and scintillation signals within the active detector material. Furthermore, it is described how electric fields in the TPC drift volume are produced and shaped. Section 3.3 summarises the effects limiting the resolution of a LArTPC. In particular, it is discussed how impurities in the LAr and the LAr temperature affect the light and charge signals in the detector. In addition, the diffusion of the free charge carriers in the noble liquid is described, as well as Rayleigh scattering of the scintillation photons and so-called space charge effects. The ArgonCube concepts and ideas for a novel design for LArTPCs are presented in Section 3.4. The chapter closes with Section 3.5, which briefly describes the difficulties of scaling up liquid argon TPCs to large cryogenic systems. Furthermore, the need for a slow-control system to monitor the hardware status and related parameters of the TPC like pressure, temperature, and liquid filling level is motivated.

3.1 Brief History of the Time Projection Chamber

Based on the concept of Charpak's Multi-Wire Proportional Chamber (MWPC) [49], the TPC was invented by Nygren in the 1970s at the Lawrence Berkeley National Laboratory (LBNL) [50]. Nygren first realised in 1974 that the combination of a 2-dimensional (2D) readout plane registering the ionisation charge information (as a function of time) with the knowledge of the time of the event (by some other means), the event would be captured in unambiguous 3D [51]. After Nygren had a concept for his new detector technology, he tried to find a detector material capable of drifting the produced ionisation electrons towards the readout plane. One major problem he faced was the transverse diffusion of the electrons as they move along the drift field lines, as described in Section 3.3.3. The larger the drift distance is, the more significant is the transverse diffusion which directly affects the spatial resolution of the detected charge. However, Nygren found that an argon-methane gas mixture would be good as a detection material since the transverse diffusion of electrons in this mixture could be brought down to the sub-mm scale for a drift length of $\mathcal{O}$(m). Nygren's first TPC prototype was cylindrical with a diameter and length of only a few centimetres, using

an argon-methane gas mixture at atmospheric pressure. A plane of pad electrodes developed by the group of Charpak at CERN [52] was employed for the charge readout. However, with the drift speed of electrons in the argon-methane mixture reaching a few $\mathrm{cm\,\mu s^{-1}}$, a sampling frequency of 10 MHz or higher was required to properly track the electron's arrival times at the charge readout plane. By 1975, no affordable free-running Analog-to-Digital Converter (ADC)-based approach for the digitisation of analogue waveforms existed to instrument a large number of readout channels. Therefore, Nygren made use of the recently developed Charge-Coupled Device (CCD) which allowed for delaying the input signals from the numerous charge readout pads. The idea was to continuously acquire the waveforms from the pads at the desired sampling frequency, about 10 MHz, but digitise only the triggered events at a slower clock rate. The working principle for a large, $\mathcal{O}(100)$, number of readout channels was shown to work in 1978 [53]. Soon after, the group at LBNL realised that their TPC would not only provide particle tracking and momentum reconstruction, it could also be used for the PID through measuring the specific energy loss dE/dx along a particle's trajectory. By changing the pressure[1] of the argon-methane mixture, the ionising particles passing through the chamber would lose more energy by ionising the gas. Hence, this would allow for tuning the capability of the PID according to the expected particle types and their energies, as shown in Figure 2.5.

This led to the idea of the high-pressure gas TPC, which found its first major application in the PEP-4 spectrometer at the PEP colliding-beam system at SLAC [54]. The TPC was pressurised with an 8.5 bar argon-methane gas mixture with a composition of 80 % and 20 %, respectively. The results from the TPC's at PEP proved the concepts of continuous readout and delivered yet unprecedented accuracies for the PID through energy loss at about 3 % resolution on dE/dx [41].

Up to this point in history, TPCs were solely built around accelerator-based beam experiments where the position of the interaction vertex is well known. The active detector material thus only had to provide particle tracking and calorimetry for the charged particles that crossed the detector. While gaseous TPCs are excellent tools for those purposes, their disadvantage is a low active mass resulting in a small interaction rate if being used as a target material for non-accelerator experiments such as dark matter or neutrino experiments. Back in 1974, Willis and Radeka described the use of the much denser LAr as a detector medium in a multiple-plate ion chamber [55]. To make the TPC also applicable to non-accelerator experiments, Rubbia in 1977 proposed to fill a TPC with LAr to realise a multi-hundred-ton neutrino detector [56]. The increased mass of the liquid active material would lead to an increased interaction rate of the processes of interest. In the early 2000s, the Imaging Cosmic And Rare Underground Signals (ICARUS) collaboration commissioned T600, the first large detector containing about 600 t of LAr [57]. T600 was designed for the use in astroparticle, nucleon-decay, and neutrino physics. An interesting feature of the design was its central cathode which split the detector into two separate LArTPCs. This early idea of detector modularisation later was adopted and refined by the ArgonCube collaboration.

[1] Changing the pressure leads to a smaller mean free path of the electrons in the gas mixture and thus affects the charge diffusion in transverse drift direction, as described in Section 3.3.3. Hence, the position resolution at the readout plane is affected by the ambient pressure. Therefore, the optimal value for the gas pressure needs to be studied in light of an experiment's goals and sensitivities.

3.2 Working Principle of a LArTPC

A TPC is a detector technology enabling a 3D track reconstruction of charged particles passing through the active detector material, which, in the case of a LArTPC, is liquefied argon. The liquid is located between a cathode and an anode plane used to apply an electric field across the TPC volume. The basic working principle of a TPC is illustrated in Figure 3.1. Charged particles crossing the LAr interact with argon atoms and excite or ionise them. Those interactions produce scintillation light and ionisation electrons copiously. The applied electric field between the anode and the cathode forces the ionisation electrons to move towards the anode, where they can be detected using a charge readout system. The detection of the scintillation light with a light readout system (not shown in Figure 3.1) provides the time of the interaction. Using the 2D spatial information of the charge readout combined with the time signal of the scintillation light and the knowledge of the electron drift velocity allows for a 3D reconstruction of event vertices and particle tracks.

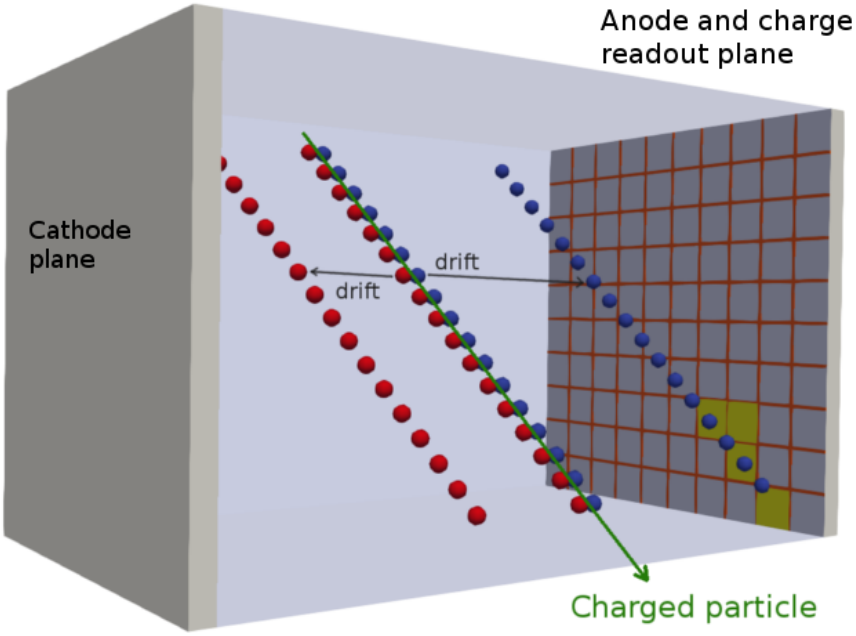

Figure 3.1: Illustration of the working principle of a TPC. Ionisation electrons (blue) and the ionised atoms (red) drift to the anode and the cathode, respectively. At the anode plane, a charge readout system detects the charge. The yellow areas denote charge readout pixels with a charge signal in the first time slice.

Applied to the field of neutrino physics, the LAr not only acts as material for particle tracking but is also being used as a target for the neutrino interactions to happen. Since the interaction cross-section of neutrinos with matter is tiny, it is desirable to have the active detector material as massive as possible. LArTPCs can be scaled up to large active detector masses. Furthermore, their design provides high-accuracy particle tracking and calorimetric information. Those reasons made the LArTPC one of the most commonly used detector types in the field of neutrino physics.

The excellent particle tracking and the calorimetric capability of a LArTPC are only possible due to the high ionisation and scintillation yields of argon, as well as to its very high breakdown electric field, allowing for electric field intensities as high as some

kilovolts per centimetre. This work mainly focuses on so-called single-phase LArTPCs where the charge readout system is located in the liquid phase of the TPC. However, a slightly altered scheme of liquefied noble gas TPCs exists, the dual-phase TPC, where the charge readout is installed in the gas phase above the liquid phase. Dual-phase TPCs are out of the scope of this work and are described in detail elsewhere [58].

3.2.1 Liquid Argon as a Detection Medium

A TPC can only work if several requirements on the active material are fulfilled. First, the material needs to have large enough yields of scintillation light and ionisation charge such that the readout electronics is capable of detecting those signals with a large enough Signal to Noise (SN) ratio. On the one hand, the initially produced electron-ion pairs can recombine to form electrically uncharged argon atoms. Such recombination processes reduce the amount of charge read out at the anode plane, as shown in Equation 3.7. On the other hand, as described in Section 3.2.3, electron-ion recombinations produce more scintillation light and consequently enhance the amount of light arriving at the photon detectors. The electron-ion recombination is affected by the intensity of the applied electric field across the TPC drift volume, as shown in Figure 3.2. It appears that the recombination rate is smaller at higher drift fields than at smaller ones.

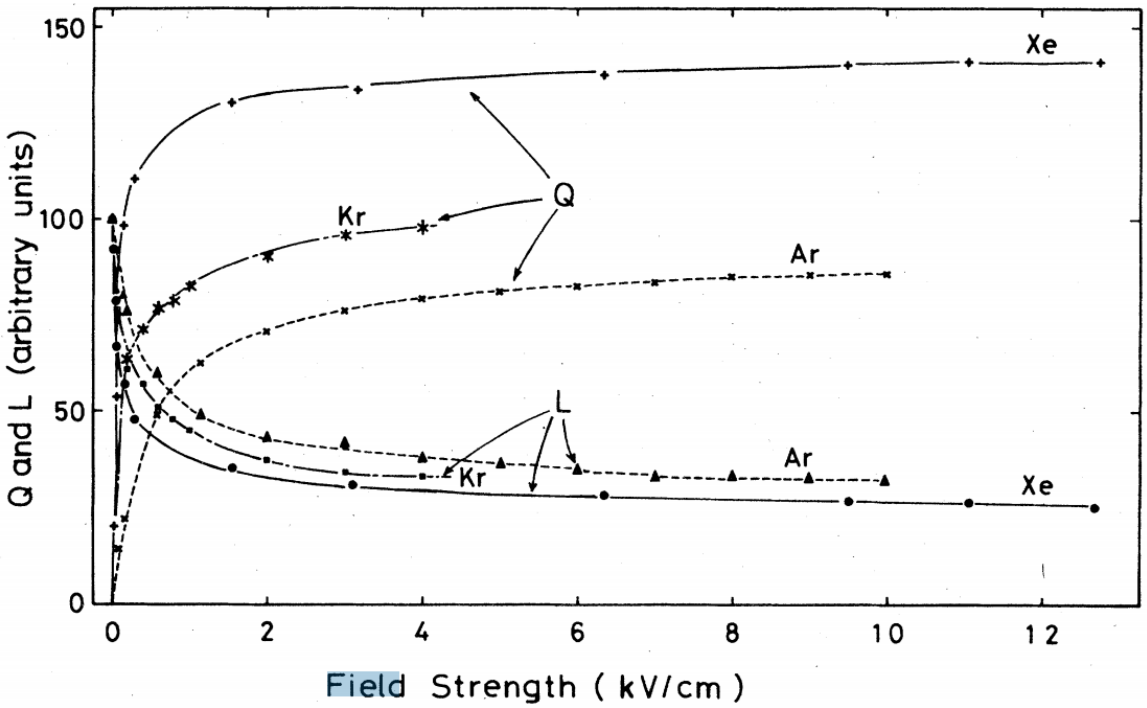

Figure 3.2: Charge (Q) and light (L) yields as a function of the electric field intensity in cryogenic liquids for argon (Ar), krypton (Kr), and xenon (Xe). [59]

The active detector material of the TPC needs to be transparent to its radiation to allow for the detection of the produced scintillation light. Furthermore, the produced ionisation electrons need to be mobile enough to be drifted within short times towards the charge readout plane. Otherwise, charge recombination with possible impurities and diffusion of the electron clouds attenuate (see Sections 3.3.1) and smear (see Sections 3.3.3) the charge signals such that the SN ratio and the spatial resolution are

of too low quality for proper event reconstruction. Due to their low electro-negativity, liquefied noble gases are ideal candidates for drifting free electrons over long distances. A further advantage of using noble liquids as a detection material in TPCs is that they can be purified relatively easy as they are inert to chemical reactions, whereas the impurities are not.

The drift speed v_d of the ionisation electrons in an electric field is related to the electron mobility μ as

$$v_d = \mu \cdot \epsilon, \tag{3.1}$$

where μ itself depends on the electric field intensity ϵ. Figure 3.3 shows the electron drift velocity in LAr as a function of the applied electric field intensity and at different LAr temperatures. A temperature increase of 1 K corresponds to a decrease of the electron drift velocity by almost 2 %.

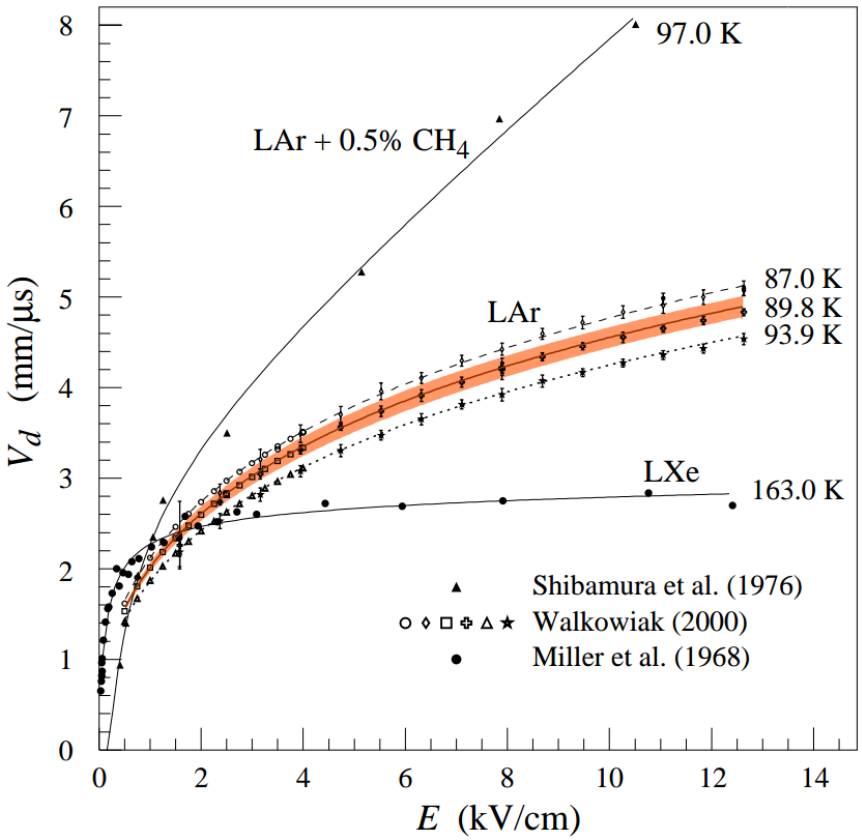

Figure 3.3: Drift velocities of free electrons in LAr and Liquid Xenon (LXe) as a function of the electric field intensity. The drift velocities depend on the LAr temperature and the concentration of impurities such as methane (CH_4) present in the liquid. [36]

Apart from the properties discussed above, the dielectric strength of the active detector material in a TPC must be resilient enough such that large enough drift field intensities can be safely applied on it. Typically, liquefied noble gas TPCs are operated at electric field intensities of the order of several hundreds of V cm^{-1}. Figure 3.4 shows that LAr has a breakdown voltage of a few tens of kV cm^{-1}, which makes it possible to use LAr in high electric field environments. However, the breakdown voltage strongly depends on the presence of electro-negative impurities and the surface structure of the electrodes. If present, impurities in the liquid and on the electrodes lead to higher breakdown voltages.

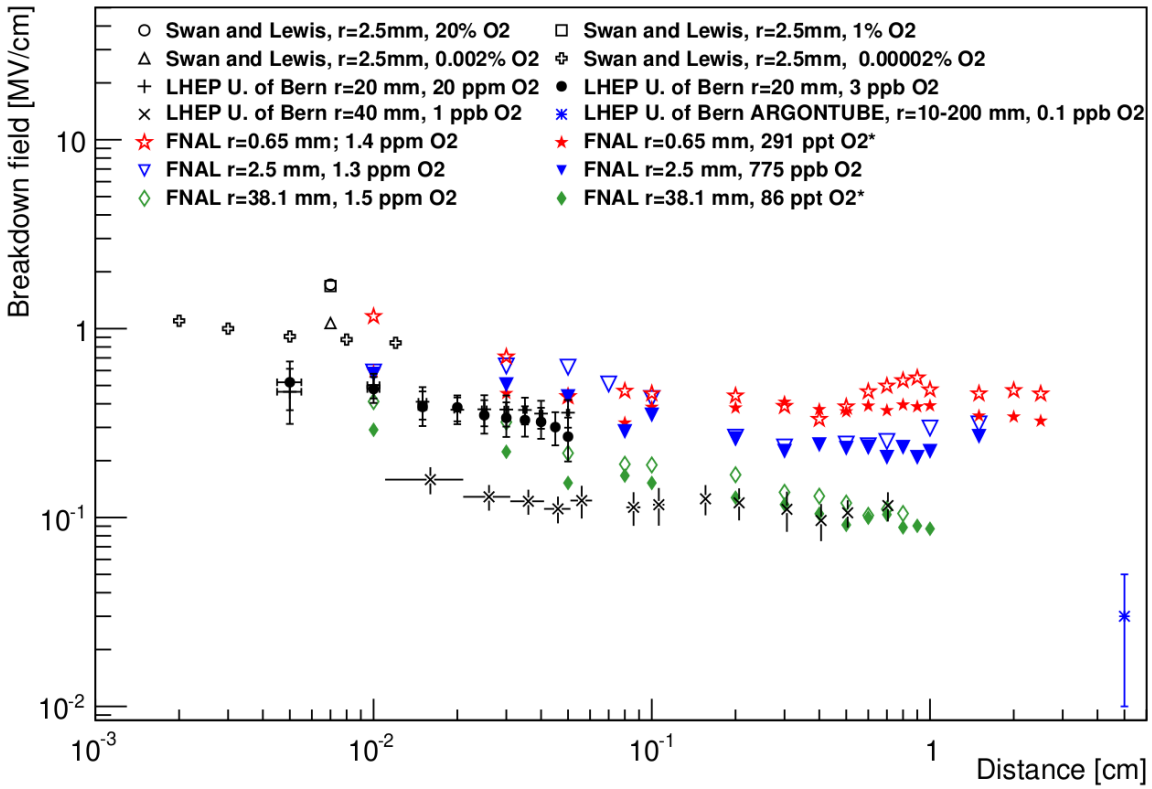

Figure 3.4: Electric field intensities at which electric breakdowns in LAr have been observed. The shape of the electrodes as well as the concentration of LAr impurities present in the noble liquid affect the electric field intensity at which breakdowns occur. [60]

For LAr to be used as a detector material, the hadronic interaction length, λ_{hadr}, and the EM radiation length, X_0, are important quantities as well. They need to be in a particular range to allow for reliable calorimetry. The larger the interaction length is, the less energy per unit length is deposited by a hadron passing through the LAr. Therefore, λ_{hadr} and X_0 directly affect the calorimetric accuracy of the TPC and thus its capability for PID. Furthermore, the interaction lengths put a limit on the minimum LArTPC size required to contain the interactions and events of interest.

LAr is the third most abundant gas in the Earth's atmosphere, about 0.93 % by volume, and comes as a byproduct of the liquid-oxygen production for the steel industry. For this reason, LAr can be commercially bought for an affordable amount of money, $\mathcal{O}\left(1\,\mathrm{CHF\,l^{-1}}\right)$. However, with a LAr boiling point of about 87 K at atmospheric pressure, cryogenic know-how and equipment are required for the operation of LArTPC.

It is worth mentioning that, apart from LAr, there exist several organic liquids which could be used as active material in a TPC as well. However, they show poorer performance compared to noble elements, at least for some of the arguments discussed above. The properties mentioned above make LAr one of the most favourable elements for use in TPCs. Table 3.1 summarises the properties of liquid argon.

	Symbol	Value, Unit	Ref.
Atomic number	Z	18	[58]
Molar mass	μ	39.948 ± 0.001 g mol^{-1}	[61]
Boiling point at 1 atm	T_B	87.303 ± 0.002 K	[61]
Triple point	T_T	83.8058 K	[61]
Liquid density at T_B	ρ	1396 ± 1 kg m^{-3}	[61]
Dielectric constant (liquid) at T_B	ϵ_r	1.504	[62]
Concentration in air (by vol.)	-	9340 ppm	[58]
Mean energy for ionisation	W_i	23.6 ± 0.3 eV/ion	[63]
Mean energy for scintillation	W_{sci}	19.5 ± 1.0 eV/photon	[63]
Scintillation light decay times	$\tau_{sci,fast}$	7 ± 1 ns	[64]
	$\tau_{sci,slow}$	1600 ± 100 ns	[64]
Scintillation light peak wavelength	λ_{sci}	129 ± 10 nm	[63]
Rayleigh scattering length	λ_{scat}	52 ± 1 m	[65]
		66 ± 3 m	[66]
Ratio exciton-ion-pair production	N_{ex}/N_i	0.19 ± 0.02	[67]
EM radiation length	X_0	14.0 cm	[36]
Hadronic interaction length	λ_{hadr}	85.7 cm	[36]
Critical energy for electrons	E_c	32.84 MeV	[36]
Average energy loss for a MIP	$\langle dE/dx \rangle_{\text{MIP}}$	2.12 MeV cm^{-1}	[36]
Fano factor (two different models)	F	0.107, 0.116	[68]

Table 3.1: Properties of LAr relevant in the scope of this thesis.

3.2.2 Ionisation Charge

The mechanism responsible for the production of ionisation charges in LAr can be described by the reaction

$$\mathrm{Ar} \rightarrow \mathrm{Ar}^{+} + e^{-}, \tag{3.2}$$

where an ionisation electron e^{-} is separated from the Argon atom, which turns into a positively charged argon ion Ar^{+}. The energy deposition by radiation in LAr results in the production of many electron-ion pairs, excited atoms, and free electrons with kinetic energy lower than the energy of the first excited energy level (sub-excitation electrons). The total energy deposition ΔE by radiation can be written as

$$\Delta E = N_i E_i + N_{ex} E_{ex} + E_{sub}, \tag{3.3}$$

where N_i is the number of produced electron-ion pairs per average energy deposition ΔE, N_{ex} corresponds the number of produced excited atoms per average energy deposition E_{ex}, and E_{sub} denotes the average kinetic energy of the sub-excitation electrons. The average energy required for the production of an electron-ion pair W_i is defined as

$$W_i \doteq \frac{\Delta E}{N_i} = E_i + \frac{N_{ex}}{N_i} E_{ex} + \frac{E_{sub}}{N_i}. \tag{3.4}$$

Although W_i depends weakly on the energy and type of the incident radiation, it can be assumed to be constant for most of the uses. Therefore, W_i allows for the determination of the deposited energy by measuring the intensity of the ionisation signals. The average energy deposition ΔE can thus be experimentally determined using the relation

$$\Delta E = W_i \cdot N_i \overset{\text{LAr}}{=} 23.6\,\mathrm{eV} \cdot N_i. \tag{3.5}$$

The ultimate energy resolution δ_E of a TPC, expressed as Full Width at Half Maximum (FWHM), can be estimated by the relation

$$\delta_E = 2.35 \cdot \sqrt{F \cdot W_i \cdot \Delta E} \qquad \text{(Fano-limit)}, \tag{3.6}$$

where F corresponds to the Fano factor. F is material dependent (for LAr, see Table 3.1), and needs to be measured experimentally.

In the electric field of a TPC, the ionisation electrons are drifted towards the anode plane where the charge packets can be detected. In an ideal detector where no impurities are present in the noble liquid, the total charge Q at the anode plane only depends on the initially produced ionisation charge Q_0 and a recombination factor R,

$$Q = R \cdot Q_0. \tag{3.7}$$

The primarily produced charge Q_0 is related to the average energy required to form an ion-electron pair W_i. $1 - R$ describes the rate of electron-ion recombinations and depends on the spatial density of the initial ionisation and the electric field intensity in the TPC, as shown in Figure 3.2. The recombination of electrons and argon ions can partially be mitigated by increasing the electric field. However, an increased drift field intensity will decrease the light yield and thus affects the amount and quality of the detected scintillation light.

If electro-negative impurities are present in the LAr, the ionisation electrons eventually can be attached to those impurities, and the total charge Q arriving at the

anode plane in time thus will be reduced. The charge signal attenuation in this case can be written as

$$Q = \exp -t/\tau \cdot R \cdot Q_0, \tag{3.8}$$

where t corresponds to the time needed for the electron to drift to the anode and τ denotes the electron lifetime in LAr. Furthermore, impurities in LAr suppress the detected number of photons since the light is not only absorbed by impurities but also its production is quenched. The suppression of charge and light signals due to impurities in LAr are discussed in Section 3.3.1.

A handful of models were developed during the last few decades to describe the recombination of electron-ion pairs. A good summary of the different models can be found in [69]. Here, the focus is on two widely used models, the *Box model* from [70] and the *modified Birk model* according to the Birk law as described in [71].

The *Box model* assumes zero electron diffusion and zero ion mobility, which is only approximately valid. Furthermore, this model assumes that the ionisation electrons are uniformly produced within a three-dimensional box along the path of the ionising particle. If attenuation effects due to impurities are neglected, the collected charge at the anode plane can be described as

$$Q = Q_0 \cdot \frac{1}{\xi} \cdot \ln\left(1 + \xi\right) \tag{3.9}$$

with

$$\xi = \frac{N_0 K_r}{4a^2 \mu \epsilon} \doteq \frac{\beta}{\epsilon}, \tag{3.10}$$

where a is defined by the linear size of the charge box, N_0 denotes the number of electrons in the box and K_r is the recombination rate constant. In the limit of an infinite electric field intensity, $\epsilon \to \infty$, the collected charge at the anode plane corresponds to the initially produced charge, $Q \to Q_0$.

If attenuation effects due to impurities in LAr are neglected, a *modified Birk model* to describe the collected charge at the anode plane can be defined as

$$Q = Q_0 \cdot \frac{A}{1 + \dfrac{k}{\rho \epsilon} \cdot \dfrac{dE}{dx}} \tag{3.11}$$

where k is a constant fitted to data and $\rho = 1396 \pm 1$ denotes the LAr density. Similar to the *Box model*, the recombination factor goes to unity, $R \to 1$, in the case of infinite electric field intensity, $\epsilon \to \infty$, and thus $Q \to Q_0$. Data acquired with the ArgonCube Module-0 prototype, described in Section 5.1.4, was analysed and the collected charge at the anode plane was fitted with the *modified Birk model*. Figure 5.25 depicts the results.

3.2.3 Scintillation Light

As charged particles travel through LAr, they can excite and ionise the argon atoms:

$$\mathrm{Ar} \to \mathrm{Ar}^* \qquad \text{(excitation)} \tag{3.12}$$

$$\mathrm{Ar} \to \mathrm{Ar}^+ + e^- \qquad \text{(ionisation)} \tag{3.13}$$

For the production of scintillation light, an excited dimer state Ar_2^* needs to be formed. In the presence of ground state argon atoms (Ar), the excited argon atoms (Ar^*) can directly form such excited dimer states via the reaction

$$Ar^* + Ar \rightarrow Ar_2^*. \tag{3.14}$$

This process is often referred to as self-trapped exciton luminescence. Alternatively, the formation of excited argon dimer states can happen through the recombination of thermal free electrons and molecular Ar_2^+ ions, called recombination luminescence, described by

$$\begin{aligned} Ar^+ + e^- + Ar &\rightarrow Ar_2^+ + e^- \\ &\rightarrow Ar_2^{**} \\ &\rightarrow Ar^{**} + Ar \\ &\rightarrow Ar^* + Ar + \text{heat} \quad \text{(non-radiative transition)} \\ &\rightarrow Ar_2^* + \text{heat}. \end{aligned} \tag{3.15}$$

In the processes described with Equations 3.14 and 3.15, the decay of the dimer state results in the emission of a VUV scintillation photon[2], γ, with a narrow wavelength band peaking at (129 ± 10) nm [63],

$$Ar_2^* \rightarrow Ar + Ar + \gamma. \tag{3.16}$$

The argon dimer state can be excited to a singlet ($^1\sum_u^+$) or a triplet ($^3\sum_u^+$) molecular state, both being in a higher energy state than the ground state. Hence, for the process described in Equation 3.16, two different decay times exist. As shown in Figure 3.5, the decay time constants and the pulse shapes both depend on the ionisation density, which reflects the type of particle that initiated the scintillation process. The transition time for the singlet state to the ground state has been measured to be considerably smaller than the decay time of the triplet state, (7 ± 1) ns compared to (1600 ± 100) ns, respectively [64]. The longer decay time for the latter case can be explained by a multiplicity restriction from a spin-orbit coupling in the triplet state. Given the significant difference between the transition times of the two components, effective particle discrimination using a Pulse-Shape Discrimination (PSD) can be performed. The ratio between produced singlet and triplet states is, to the first approximation, not affected by external electric fields.

Assumed that no electrons are escaping, the number of produced scintillation photons N_{sci} at zero electric field intensity can be written as a sum of the number of produced ionisation atoms N_i and the number of produced excited atoms N_{ex},

$$N_{sci} = N_i + N_{ex} = N_i \cdot (1 + N_{ex}/N_i) = \frac{\Delta E}{W_i} \cdot (1 + N_{ex}/N_i)\,. \tag{3.17}$$

Here, ΔE denotes the total energy deposited by the ionising particle and W_i is the average energy required to form an electron-ion pair. The average energy required to produce a scintillation photon by an ionising particle thus can be written as

$$W_{sci} = \frac{\Delta E}{N_{sci}} = \frac{W_i}{1 + N_{ex}/N_i}. \tag{3.18}$$

[2] It is assumed that only one photon per excited dimer state decay is produced.

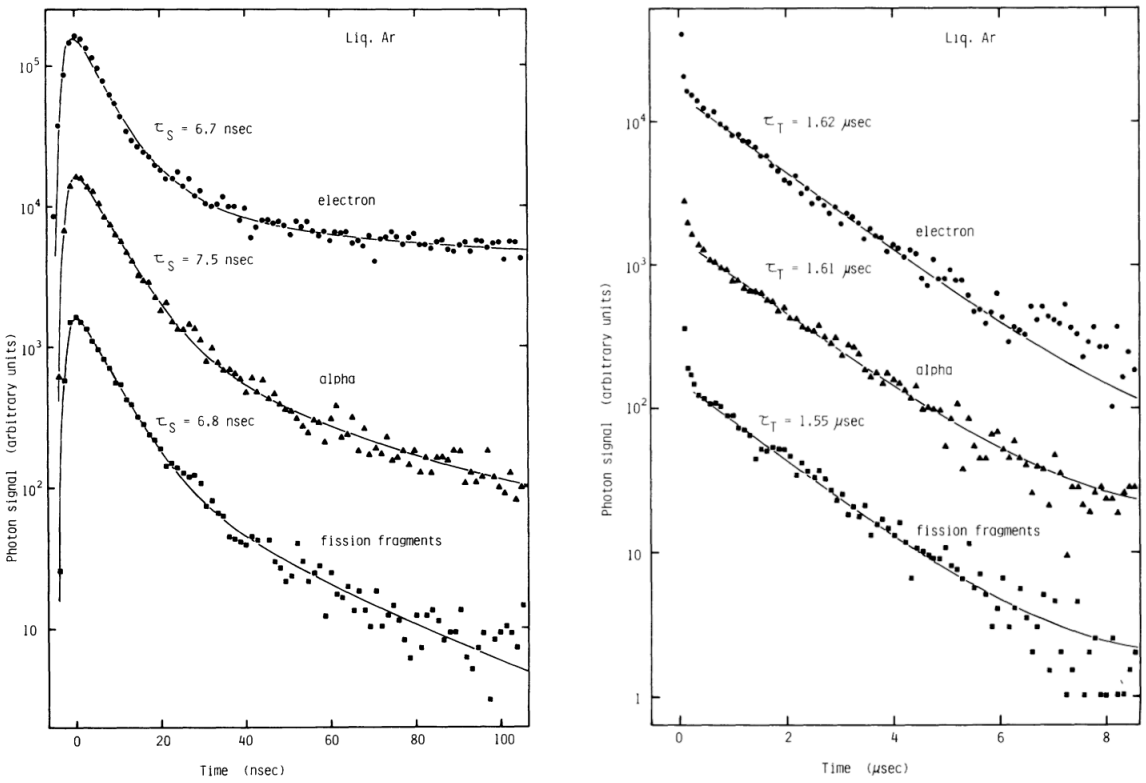

Figure 3.5: LAr scintillation light decay curves for different particle types, roughly following a double-exponential decay. A short transition time of $\mathcal{O}(1\,\text{ns})$ is ascribed to the singlet state (left), whereas a long decay time of $\mathcal{O}(1\,\mu\text{s})$ is explained by the decay of the triplet state (right). The differences in the photon signals between electrons, alpha particles, and fission fragments is explained by the particle-specific density of energy depositions. [64]

The specific numbers for W_i, N_{ex} and N_i are material constants and have to be determined experimentally. Their specific values for LAr can be found in Table 3.1.

If an electric field is applied to the noble liquid, fewer electrons recombine with the argon ions. On the one hand, the smaller electron-ion recombination due to the electric field yields more free electrons and therefore, the charge yield is increased with increasing electric field intensity. On the other hand, an electric field reduces the scintillation light yield since less Ar^+ ions are available to form argon molecules as described with Equation 3.15. Figure 3.2 shows that the scintillation light yield and the ionisation charge yield are complementary to each other and show a dependency on the applied electric field intensity. As presented in [63], an anti-correlation between the charge and light yields as a function of the electric field intensity has been observed.

At non-vanishing electric field intensities, and assumed that no electrons escape, the number of produced scintillation photons is reduced by the number of drift electrons,

$$N_{sci} = N_i + N_{ex} - N_i \cdot R = N_i \cdot \left(1 + \frac{N_{ex}}{N_i} - R\right). \tag{3.19}$$

Section 5.1.4 discusses the light yield and the charge yield measured with the Module-0 detector, one of the ArgonCube LArTPC prototypes. Since the ratio of N_{ex}/N_i was not known a priori, the light yield was parameterised as

$$N_{sci} = W_{sci} \cdot (1 - \alpha \cdot R)\,, \tag{3.20}$$

where α has to be fitted to the data. Figure 5.25 depicts the results obtained with the Module-0 detector.

Not only does the presence of electric fields affect the amount of produced scintillation light, but a quenching effect can also reduce the scintillation light yield. Such quenching mainly happens to non-relativistic protons, alpha particles, and fission fragments [63]. The basic mechanism responsible for the quenching is explained with the reaction

$$\mathrm{Ar}^* + \mathrm{Ar}^* \rightarrow \mathrm{Ar} + \mathrm{Ar}^+ + e^-, \tag{3.21}$$

where the excited argon atoms may diffuse and eventually undergo (bi-excitonic) quenching, resulting in ionising one of the excited atoms. Some of the excitation energy needed for the production of scintillation photons is taken away by the ionisation electron in the form of kinetic energy.

3.2.4 Electric-Field Intensity and Shaping

For an efficient drift of the produced ionisation electrons towards the charge readout plane in a TPC, an electric field intensity of typically several hundred $\mathrm{V\,cm^{-1}}$ is needed. Increasing the field intensity results in a faster electron drift speed, depicted in Figure 3.3, and thus shortens the time window needed for the acquisition of an entire TPC event. That is in particular important in high-multiplicity environments where the event rate is high. On the one hand, a reduced acquisition time window results in a smaller probability of observing multiple events overlapping in the TPC, so-called event pile-up, simplifying the event reconstruction. On the other hand, a higher field intensity worsens the time resolution of the charge readout since the electron clouds are arriving with less time separation on the charge readout plane. Furthermore, the detected charge signals are enhanced since the recombination of electrons with argon ions is suppressed at higher field intensities. However, on the cost of the number of produced scintillation photons, as shown in Figure 3.2. In addition, a higher electron drift speed reduces the charge attenuation due to impurities, as discussed in Section 3.3.1.

The stored energy within the TPC drift field is proportional to its field intensity. In the case of an electric breakdown, a larger amount of energy stored in the electric field imposes more considerable risks for damage to the readout electronics and other hardware components. The High Voltage (HV) feedthrough must be capable of withstanding potential differences corresponding to the full cathode bias voltage. For meter-scale detectors, cathode bias voltages of several tens or even hundreds of kV are usual, demanding a sophisticated HV distribution systems.

The considerations as mentioned above are important factors affecting the performance and accuracy of a TPC, its capability for PID and calorimetry, and the safety aspects during the detector operation. A detailed study considering these aspects needs to be done before the design of any TPC can be validated.

Another important point regarding the TPC drift field is its uniformity. Since the ionisation electrons follow the electric field lines on their drift towards the charge readout system, non-uniformities in the electric field directly affect the reconstructed position of the charge depositions. Therefore, it is of advantage to have an electric field as uniform as possible. The electric field lines usually are shaped employing a field cage, consisting of a series of electrically conducting elements (e.g. metallic rings) and resistors arranged in a way to enclose the active TPC volume between the anode and

the cathode. Within the framework of this thesis, the feasibility to shape the electric field by enclosing the drift volume with a highly resistive sheet instead of a field cage was demonstrated [72]. This continuous resistive field shell has several advantages compared to a traditional field cage, for example, a reduced number count of TPC components and therefore a reduced number of potential points of failure during the detector operation. Furthermore, the amount of dense and inactive material in the detector can be reduced, resulting in an increased ratio between the fiducial mass and the total detector mass.

3.3 Effects Limiting the Resolution of a LArTPC

3.3.1 Charge and Light Signal Attenuation

While the attenuation length for the charge and scintillation light signals are large for pure LAr, electro-negative impurities attenuate these signals and can quench the production of the scintillation light. The process of charge and light signal attenuation can be described by the *Lambert-Beer law* (compare with Equation 2.35),

$$C(x) = C_0 \cdot \exp\left(-\frac{x}{\alpha}\right), \tag{3.22}$$

where $C(x)$ denotes the number of free electrons or photons after having travelled a distance of x if initially C_0 quanta (electrons or photons) were present. Further, α corresponds to the electron mean free path length (in the case of charge signals) or the photon attenuation length (in the case of scintillation signals). Section 5.1.4 discusses the estimation of the electron lifetime in the Module-0 LArTPC prototype. To extract the electron lifetime, an exponential curve fit was applied on the detected charge signals as a function of the drift time.

The most common impurities responsible for the signal attenuation in LArTPCs are water, oxygen, and nitrogen. Water and oxygen in concentrations of $\mathcal{O}(10$ ppm$)$ drastically attenuate the charge signals. There is almost no effect on the charge signal attenuation from nitrogen contaminations up to the percentage level, as can be concluded from Figure 3.6. However, nitrogen in concentrations of $\mathcal{O}(10$ ppm$)$ significantly suppress the scintillation light signal by two processes. Traces of nitrogen absorb the photons as they propagate through the contaminated LAr. Nitrogen also suppresses light production (quenching), which involves an interaction of excimers with impurity molecules, resulting in an excimer dissociation without a photon emission. The quenching predominantly affects the slow component of the scintillation light (see Section 3.2.3) since the longer lifetime of the triplet state is more likely to interact with an impurity molecule before producing a scintillation photon than a singlet state [73].

To ensure reliable TPC operation with a high charge and light SN ratio in meter-scale LArTPCs, the concentration of impurities in LAr has to be smaller or comparable to a Part Per Billion (ppb) level of O_2 equivalent. The longer the distances from the charge or light production point to the point of detection are, the more stringent are the requirements on the LAr purity. Typically, the LAr received from commercial sellers has water, oxygen and hydrogen contaminations of $\mathcal{O}(1$ ppm$)$ and thus would not allow for a reliable LArTPC operation. In addition, impurities present in the air outside of the detector can leak into the cryostat, which would contaminate the LAr.

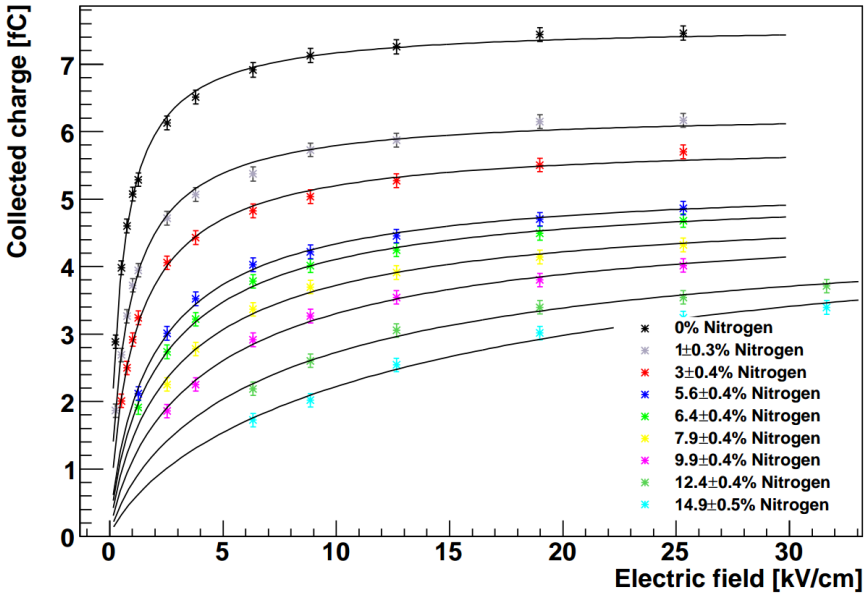

Figure 3.6: Nitrogen contaminations at the percentage level in LAr reduce the collected charge at the readout plane. [74]

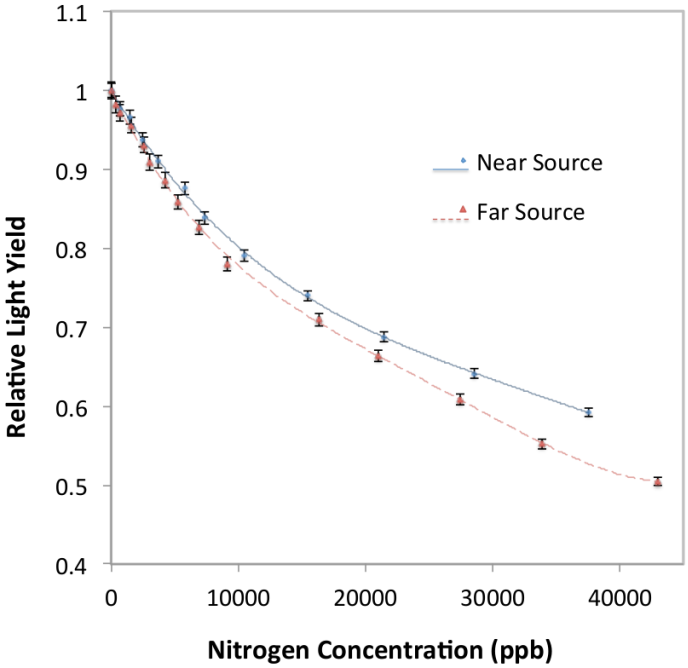

Figure 3.7: Nitrogen contamination at the ppm level significantly suppress the scintillation light yield in LAr. [73]

Furthermore, out-gassing from different detector materials and the liquid containment vessel contributes to the total concentration of electro-negative impurities in the TPC. Hence, a LAr purification system is required, which often has to be continuously operated, even during Data AcQuisition (DAQ) periods. LAr purification usually is done through two different filters, a molecular sieve for the removal of water and traces of nitrogen and oxygen contaminants, and a filter based on activated copper for the removal of oxygen and traces of water. In addition, commercial Zr-based getters can be used for the efficient removal of nitrogen.

3.3.2 Electron Drift Velocity

The 2D position information provided by the charge readout plane combined with the arrival times of the charge packages allow the LArTPC technology to provide 3D particle tracking information. An uncertainty on the electron drift velocity in LAr affects the precision of the reconstructed charge package's coordinate along the drift field of the TPC.

The drift velocities of free electrons in LAr depends on several factors, including the concentration of impurities present in the LArTPC, the LAr temperature, the drift field intensity and possible screening effects caused by space charge effects. As shown in Figure 3.3, the electron drift velocity increases with the presence of LAr impurities such as molecular H_2, N_2, or CH_4 at the percentage level [36]. Furthermore, the electron drift velocity increases with decreasing LAr temperature. A temperature increase of 1 K corresponds to a decreased electron drift velocity of almost 2 %. The average temperature gradient of the free electron drift velocity in LAr can be described by [36]

$$\frac{\Delta v}{v} = (-1.72 \pm 0.08)\,\% \cdot \Delta T. \tag{3.23}$$

The reduced electron drift velocities originating from screening effects due to space charges are discussed in Section 3.3.5.

3.3.3 Diffusion of the Ionisation Charge

The ionisation electrons produced by charged particles interacting in LAr undergo diffusion processes during their drift in the electric field of the TPC. This results in a spreading of the charge cloud, which affects the intrinsic spatial resolution limit of a TPC. The diffusion coefficient D describes the spreading of the charge cloud, which follows the relation

$$D = \frac{\langle E_e \rangle \mu_e}{q}, \tag{3.24}$$

where $\langle E_e \rangle$ denotes the mean electron energy, μ_e is the electron mobility, and q corresponds to the electric charge of the electron [75]. Since μ_e depends on the drift field intensity, the diffusion of electrons in non-vanishing electric fields is, in general, not isotropic. However, the electron diffusion in LAr can be described with a longitudinal (along the electron drift direction) and a transversal (perpendicular to the electron drift direction) component. The longitudinal component affects and broadens the electron cloud's arrival time at the charge readout plane, and the transversal component affects the cloud's spread along the directions defined by the 2D readout plane. In general, the D_L is smaller than D_T, as can be inferred from Figure 3.8. The spreading of the ionisation electron cloud along the drift, σ_L, and across the drift, σ_T, can be written as functions of the electron drift time t,

$$\sigma_{L,T}\,(t) = \sqrt{\frac{2D_{L,T} \cdot L}{v_d}} = \sqrt{2D_{L,T} \cdot t}, \tag{3.25}$$

where D_L and D_T are the longitudinal and transverse diffusion coefficients, L corresponds to the drift length, and v_d is the electron drift velocity. In the absence of a magnetic field and at a moderate drift field intensity of 500 V cm^{-1}, σ_L and σ_T in LAr after a drift distance of $L = 50$ cm are about 0.6 mm and 0.9 mm, respectively.

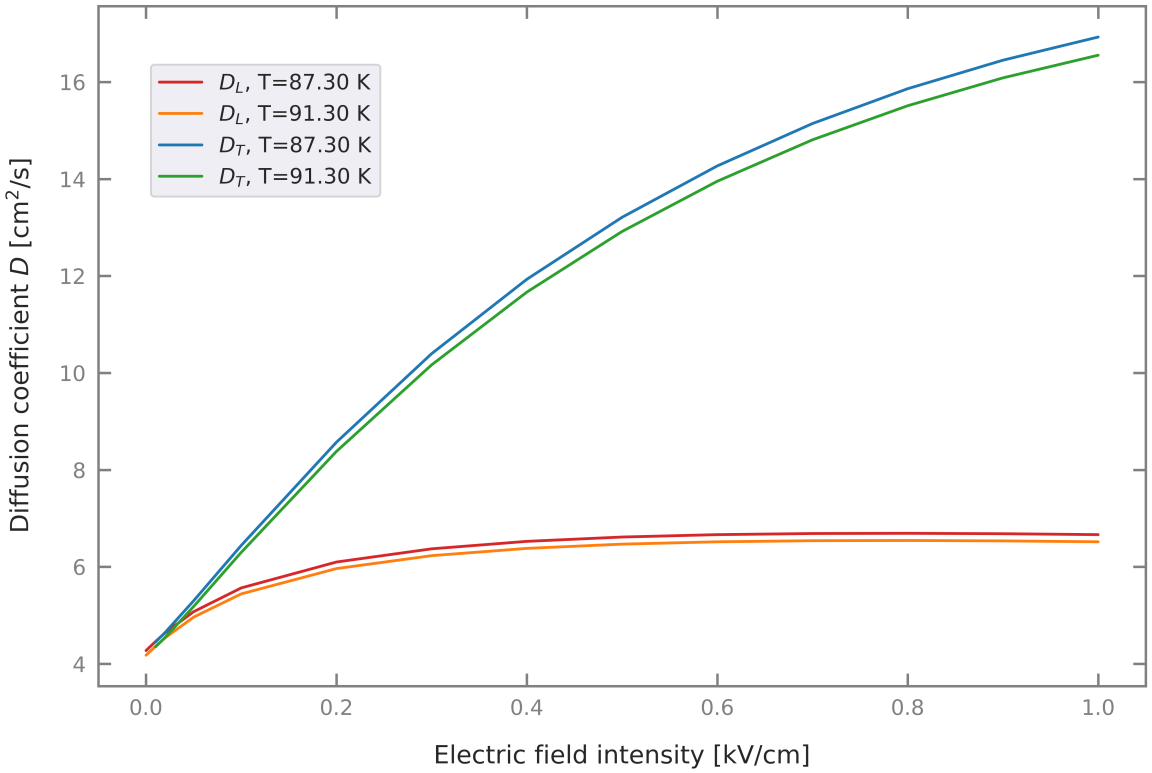

Figure 3.8: Longitudinal and transversal diffusion coefficients of LAr at two different temperatures. The data was produced according to the model described in [75].

3.3.4 Rayleigh Scattering of the Scintillation Light

Rayleigh scattering describes the process of photons scattering off particles smaller than the photon wavelength. The process strongly depends on the photon wavelength and the optical properties of the material the photons pass through.

The intrinsic LAr scintillation light has two time constants, (7 ± 1) ns and (1600 ± 100) ns [64], related to the excimer singlet and triplet states, respectively (see Section 3.2.3). By measuring the scintillation signals in a LArTPC therefore, in principle, allows for a precise, $\mathcal{O}(1\,\text{ns})$, measurement of the time when a particle interaction happened within the detector. However, depending on the intensity of the light signal, Rayleigh scattering can cause a degradation of the time resolution. The reason is the increased path length of the scintillation photons between their production points and their points of detection. A spread in the photon arrival time at the light detection system is the consequence of Rayleigh scattering.

The Rayleigh scattering length λ_{scat} of LAr scintillation photons in LAr has been experimentally measured to be 52.1 cm [65] and (66 ± 3) cm [66]. Theoretical models predict value for the absorption length of 90 cm [76] and (55 ± 5) cm [77], with a disagreement of about 30 %.

Since the LAr VUV scintillation light has a Rayleigh scattering length of some tens of cm, it may place constraints on the design of large LArTPCs with meter-scale drift distances. For this reason, among others, the ArgonCube collaboration followed the approach of building optically segmented LArTPCs with short, $\mathcal{O}(1\,\text{m})$, optical path lengths, as described in Section 4.1.

3.3.5 Space Charge Effects

In a LArTPC, the argon ions have considerably smaller drift velocities than the ionisation electrons. This fact is explained by the small electron mass compared to the ion mass. For example, the electron drift speed in a LArTPC with a drift field intensity of $500\,\mathrm{V\,cm^{-1}}$ is about $1.6\,\mathrm{mm\,\mu s^{-1}}$, which is 2×10^5 times larger than the ion drift speed of about $8.0 \times 10^{-6}\,\mathrm{mm\,\mu s^{-1}}$ [78].

For this reason, the positively charged ions are present in the LArTPC for some seconds or even longer, which might lead to Space Charge Effects (SCE). These manifest themselves by screening the negatively charged cathode, which locally alters the electric field within the TPC. Therefore, the SCE affect the accuracy of reconstructing the position of the detected ionisation charges in a TPC.

Detectors exposed to large cosmic fluxes, e.g. if there is no or only small overburden, or detectors in high-multiplicity environments are more likely to suffer from SCE since the total amount of produced ions is enhanced. However, since the ion drift speed usually is comparable to the speed of the LAr recirculation caused by the LAr purification system, SCE in LArTPCs are challenging to model and predict. One way to infer the drift field distortions in a LArTPC would be the statistical analysis of cosmic muon tracks. This approach was chosen for one of the ArgonCube prototypes, as described in Section 5.1.2. However, this method requires large statistics and thus rather long DAQ time during which the distribution of space-charges in the TPC might have changed already. A much faster way in estimating the electric field uniformity could be the use of VUV laser calibration system as presented in [79]. Unlike cosmic muons, laser beams neither undergo Multiple Coulomb Scattering (MSC) in LAr nor produce delta rays along their trajectories and thus describe straight and clean tracks in the LArTPC. Another benefit is that lasers can be steered to measure the drift field distortions in specific detector regions of interest.

3.4 The ArgonCube Concepts

Monolithic LArTPCs with drift fields of some $100\,\mathrm{V\,cm^{-1}}$ and drift distances of several metres require high cathode bias voltages with a large amount of energy stored in the electric field of the TPC, which pose severe risks for damage in the case of an electric breakdown. That motivated the ArgonCube collaboration to develop a modular design, where several identical LArTPC modules are combined to build a large detector.

Segmenting the large volume into smaller modules naturally reduces the maximum TPC drift distances, leading to smaller cathode bias voltages and a reduced amount of stored electric field energy at the same drift field intensity. The reduced drift time further yields less stringent requirements on the LAr purity during the detector operation since the charge and light signals are attenuated less by effects described in Sections 3.3.1 and 3.3.4. The smaller readout volumes also have a positive effect on the amount and the accuracy of the charge and light signals: As described by Equation 3.25, shorter drift times yield a reduced spread of the ionisation signals due to electron diffusion as discussed in Section 3.3.3. Furthermore, the scintillation light is affected less by the process of Rayleigh scattering, described in Section 3.3.4, if the optical path length in the detector is reduced. Consequently, the modular concept of ArgonCube enhances the amount and the time resolution of the detected scintillation light.

If the module walls are made of a material opaque to the LAr scintillation photons, the VUV light is contained within a single module. Thus, the detected light signal can be matched more reliably to the corresponding charge signal, improving the accuracy of the event reconstruction. That is in particular important for LArTPCs employed in high-multiplicity environments where it can be very challenging to assign specific energy depositions to individual (neutrino) interactions.

To further make the event reconstruction more robust, the ArgonCube collaboration started a R&D program to develop a pixelated charge readout system, presented in Section 4.3, for an unambiguous 3D tracking in liquid noble gas detectors. In parallel, a program for the development of a dielectric light detection system, described in Section 4.4, with a large surface-coverage, a precise time resolution, and a reasonable Photon Detection Efficiency (PDE) for VUV photons has started.

To minimise the amount of inactive material between the ArgonCube modules, a novel approach to produce and shape the drift fields in TPCs was developed and is presented in Section 4.2. The design is based on a thin, $\mathcal{O}(10\,\mu\text{m})$, foil with a high sheet resistance. Compared to traditional field cages, this design reduces the material budget of the TPC. Furthermore, the smaller number count of components in the TPC lead to a more robust detector operation with fewer possible points of failure.

3.5 Scaling LArTPCs to Large Cryogenic Systems

Scaling LArTPCs with active volumes of $\mathcal{O}(1\,\text{m}^3)$ to detectors comparable to the DUNE ND-LAr with a volume of about $100\,\text{m}^3$, or even one of the FD modules with a LAr volume of about $10\,000\,\text{m}^3$, is difficult from an engineering point of view. First of all, the support structures for the cryostat and all detector components need to be strong enough to withstand the forces acting on the relevant detector structures. Apart from gravitational forces, which tend to bend horizontally oriented structures, there are forces originating from pressure differences between the inner cryostat volume and the atmosphere.

The construction of massive LArTPCs is further complicated by the significant temperature differences between cryogenic detector parts and warm components exposed to the cryostat outer surface. As different materials, in general, have different thermal expansion coefficients, the relative sizes and positions of individual parts slightly change with respect to each other, leading to shear and traction forces across different detector structures if not appropriately handled. In the worst case, some of the detector components can break if too much thermal stress is exerted. To reduce those forces during the cool-down or warm-up processes, measuring temperatures, pressures, and LAr filling level must be carefully carried out.

Cryogenic noble liquid detectors usually have some gaseous ullage volume to make the system more rigid to sudden heat input. Monitoring the pressure of the ullage volume can provide indices about unseen processes happening within the cryogenic system. Furthermore, the regulation of the ullage pressure requires some monitoring system to ensure a safe detector operation.

Once the detector was filled with LAr, a slow-control system is required to constantly monitor the parameters mentioned above. Such measurements are needed for the safe operation of the detector, and they facilitate diagnosis and troubleshooting in the case of unexpected behaviour. During my work for this thesis, a slow-control system was developed. This system is briefly described in Section 5.2.

Part II

A Novel Concept of a LArTPC

Chapter 4

The ArgonCube Concept and Technologies

The ArgonCube collaboration found its origin in the ArgonTube [80] collaboration, which investigated the feasibility of LArTPCs with maximum drift distances of 5 metres. ArgonTube found technical difficulties and risks related to the operation of such detectors at cathode bias voltages of many thousand kV, corresponding to electric field intensities of some $\mathrm{kV\,cm^{-1}}$ [81], [82], [83].

The ArgonCube collaboration started a R&D program for the development of a robust LArTPC design with reduced cathode bias voltages. Instead of a monolithic LArTPC, ArgonCube segments the detector into several smaller and identical modules, which reduces the required cathode bias voltages for the same TPC drift field. The modular detector design, in turn, reduces the energy stored in the electric field and thus reduces the risk of damage if an electric breakdown occurs. Using a low-profile module structure keeps the amount of inactive material introduced by a segmented detector design to a low level. Section 4.1 describes the module structure and the advantages of such a design. To further reduce the amount of dense and inactive material in a segmented detector, a new technology for the production and shaping of electric drift fields in LArTPCs was developed, as described in Section 4.2.

In high-multiplicity environments where several neutrino interactions can overlap within the readout window of a LArTPC, the event reconstruction is challenging. The ArgonCube collaboration developed a pixelated charge readout, described in Section 4.4, to address this. This system provides unambiguous 3D imaging of particle interactions with a fine granularity of $\mathcal{O}\left(10\,\mathrm{mm}^3\right)$ and enhances the quality of the event reconstruction. Even though a pixelated charge readout system significantly simplifies the assignment of spatially connected energy depositions to individual neutrino interactions, it remains difficult, if not impossible, to correctly assign detached energy depositions to specific interaction vertices. Precisely measuring the prompt scintillation light with a $\mathcal{O}\left(1\,\mathrm{ns}\right)$ resolution greatly helps to assign detached energy depositions to specific neutrino interaction vertices and thus increases the quality of the event reconstruction. Section 4.4 describes the ArgonCube light detection system developed for this purpose.

Several detector prototypes were built and tested, and their performance analysed to test the novel ArgonCube technologies. The design of some of these prototypes and the results of their tests are described in Section 5.1. The findings from those prototypes often impacted the further development and improvement of the ArgonCube technologies described here.

4.1 A Modular Approach to LArTPCs

The ArgonCube approach to reduce the TPC cathode bias voltages to a few tens of kV is to segment a large detector mass into smaller, identical LArTPC modules. These modules are installed side by side in an array-like configuration immersed in the LAr hosted by a single cryostat. The module structure thereby interfaces between the active detector and the cryostat. Figure 6.2 shows the ArgonCube module concept as it is applied in the DUNE ND, where an array of 5×7 ArgonCube modules each with an active volume of $1\,\mathrm{m} \times 1\,\mathrm{m} \times 3\,\mathrm{m}$ and a maximum drift length of 50 cm is planned.

The key design feature of an ArgonCube module is the central cathode which splits the module into two independent LArTPCs, as shown in Figure 4.1. Each module further incorporates a low-profile field shell, described in Section 4.2, which reduces the amount of inactive material between the modules. A scintillation light detection system with high, $\mathcal{O}(1\,\mathrm{ns})$, time resolution is installed within the field shell, as discussed in Section 4.4, and pixelated charge readout system, covered in Section 4.3, builds the anode plane. The HV is applied on the top of the central cathode, as depicted in Figure 4.1. Running a LArTPC with short maximum drift distances decreases the required HV for biasing the cathode and thus reduces the associated risks of electric breakdowns. In addition, short maximum drift times allow for less stringent LAr purity requirements since the effects of charge and light attenuation due to LAr impurities as described in Section 3.3.1 is reduced. Furthermore, the Rayleigh scattering length corresponds to about the maximum optical path length of the scintillation photons and thus neither significantly reduces the detected light intensity nor smears the time resolution at the light detection system, as discussed in Section 3.3.4. This has been one of the driving factors for the $1\,\mathrm{m}^2$ footprint of a DUNE ND-LAr module. Short drift distances are closely related to little electron diffusion in LAr, as discussed in Section 3.3.3. The smearing of the charge signals due to such diffusion processes in LAr at 87 K and with an ambient field intensity of $0.5\,\mathrm{kV\,cm^{-1}}$ is expected to be $< 1\,\mathrm{mm}$ along and transverse to the drift direction. Thus, with a pixel pitch of $\approx 4\,\mathrm{mm}$ as designed for the DUNE ND-LAr, the diffusion can be neglected.

Several requirements placed on the module structure must be fulfilled to accomplish a reliable and accurate detector operation. First, the module structure needs to be mechanically robust at temperatures ranging from room temperature ($\approx 300\,\mathrm{K}$) down to cryogenic temperatures ($\approx 90\,\mathrm{K}$) during the detector operation. That is challenging to achieve since the different thermal expansion coefficients for various materials used within the detector exert forces on the module structures. Particularly during thermal cycles (cooling down and warming up), enhanced risk for damaging the detector or detector parts, e.g. the ArgonCube Light Readout System (ArCLight) modules, is posed. Furthermore, the module structure must be composed of as little dense material as possible since it increases the probability of particle scattering on such materials. That would alter the 3D images produced by the LArTPC technology and thus could increase the uncertainties in the TPC event reconstruction. Hence, it is desirable to use materials that have hadronic interaction and EM radiation lengths comparable to those of LAr (see Table 3.1) such that the module structure does not significantly distort the particle trajectories and the development of particle showers. Finally, the total inactive volume needs to be as small as possible to avoid more significant dead regions in the detector. The ArgonCube collaboration found several

materials which suit those requirements, including a combination of G-10[1] and FR-4[2] sheets.

Choosing a material that is opaque to the LAr scintillation light, peaking at a wavelength of $\lambda = (129 \pm 10)\,\mathrm{nm}$, has the benefit of contained light within ArgonCube modules. Due to the short optical path lengths, the pulse width of the light signals detected with the scintillation light detectors is kept narrow and thus results in an enhanced time resolution. Since LArTPCs are relatively slow detectors, with charge readout windows of typically $\mathcal{O}(100\,\mu\mathrm{s})$, optical segmentation helps to overcome pile-up related problems if a light readout system with good, $\mathcal{O}(1\,\mathrm{ns})$, time resolution is provided. That is in particular important in high-multiplicity environments where several particle interactions may overlap within the TPC readout window. Hence, an optically segmented detector enables the accurate combination of the TPC charge and light signals and leads to an improved event reconstruction with enhanced accuracy.

A modular detector design, as described above, furthermore enables an easy replacement of individual modules in the case of broken or outdated detector components. Single modules are easier to handle than large monolithic detectors, and thus the transport of the module to a workshop is simplified. Furthermore, a modularised detector can acquire data even though individual modules have been extracted from the detector. Extracting individual modules from the detector is possible without any problems if no cryogenic liquid is inside the cryostat. However, module cold extractions (and re-insertions) from (and to) the cryostat need more sophisticated techniques, as elucidated in Section A.3.

4.2 Electric-field Production and Shaping

The electric field in both LArTPCs hosted by an ArgonCube module is produced with the central cathode plane and the two pixelated charge readout planes located at the two opposing sides of the module. A HV feedthrough penetrating the centre of the module top flange provides the HV cable, which is connected to a socket at the top of the central cathode plane, as indicated in Figure 4.1. The ArgonCube module as planned for the DUNE ND-LAr will consist of a cathode panel covered on both sides with a layer of 25 µm thick Kapton XC, a material used in the protoDUNE-SP cathode [84] which provides a sheet resistance of $\mathcal{O}\left(1\,\mathrm{M\Omega\,sq^{-1}}\right)$ [39]. In the case of an electric HV discharge, the resistive material prevents damage to the sensitive electronics. The conductivity further is large enough to neutralise the positive argon ions at the rate as they are collected by the cathode plane.

The electric field intensity must be as uniform as possible within the entire TPC drift field to drift the ionisation electrons without significant distortions from their point of creation to the pixelated anode plane. That is achieved through the field shell, a highly resistive plane with a sheet resistance of $\mathcal{O}\left(1\,\mathrm{G\Omega\,sq^{-1}}\right)$. A proof of principle was demonstrated with the resistive shell TPC prototype described in Section 5.1.2. Such a field shell continuously decreases the voltage applied between the TPC electrodes. The large bulk resistance of the resistive shell limits the heat load on the shell, which prevents localised boiling of argon. A central copper strip

[1] G-10 is a composite material based on epoxy resin fibreglass laminate.
[2] FR-4 is a flame retardant composite material based on glass-reinforced epoxy laminate.

on all field shell panels is connected to the metallised cathode perimeter and set to the cathode potential to assure a constant voltage at the position where the field shell is connected. High sheet resistance is required to keep the LAr boil-off as low as possible. The local heat input should not exceed about $100\,\mathrm{mW\,cm^{-2}}$, which is the typical heat input density of electronics used in wire-based LArTPCs. Like the cathode plane, the resistive shell has a low profile to minimise the detector's inactive volume. A requirement is that the resistive shell operates reliably under nominal field, which in the case of the DUNE ND-LAr is $500\,\mathrm{V\,cm^{-1}}$. To allow for an adequate flow of purified LAr through the LArTPCs, the top and bottom panels of the field shell are perforated with $\mathcal{O}\,(100)$ holes of 4 mm diameter. The ArgonCube approach to shape the electric field within the LArTPC has several advantages compared to traditional field cages:

- The active volume in an ArgonCube module is increased due to the smaller footprint of the resistive shell.
- The continuous electric field shaping improves the field uniformity, particularly close to the edges of the drift volume.
- Local argon boiling is reduced since the power dissipation is distributed over the entire field shell instead of being localised on the surface of the traditional resistor chain.
- The number of possible failures (e.g., single resistors) is reduced since the resistance is spread over the whole field shell.
- In the case of an electric discharge, the high sheet resistance of the cathode and the field shell would slow down the discharge process and thus would prevent damages on the TPC, including the sensitive electronics.
- The field shell, laminated on rigid planes, provides mechanical support for the TPC structure.

Figure 4.1 shows the exploded view of the ArgonCube module structure as designed for the DUNE ND-LAr described in Section 6.3. It is based on the central cathode plane, four sheets making the resistive field shell, and the two half-detectors instrumented with the light and charge detection systems. The field shell consists of four 6 mm thick FR-4 panels laminated with 100 µm thick duPont Kapton DR8[3] sheets loaded with electro-conductive carbon black [39]. Experiments conducted at SLAC showed that the sheet resistance of the field shell is about $3\,\mathrm{G\Omega\,sq^{-1}}$ at LAr temperature and an applied voltage corresponding to $500\,\mathrm{V\,cm^{-1}}$. With an aspect ratio of $L/W = 0.5\,\mathrm{m}/8.0\,\mathrm{m} = 1/16$ for the shell of one TPC, the bulk resistance for a module is about 94 MΩ. Applying a voltage of 25 kV across both shells of a module results in a total heat load of about 7 W spread over an area of $8\,\mathrm{m^2}$, corresponding to a local heat density of less than $100\,\mathrm{W\,cm^{-2}}$. Module-0, a small scale prototype of an ArgonCube module as designed for the DUNE ND, was successfully tested at the Laboratory for High Energy Physics (LHEP), University of Bern, as discussed in Section 5.1.4.

[3] duPont™, Kapton®, polyimide film, from E. I. duPont de Nemours and Company, www.dupont.com (accessed: 29.06.2021).

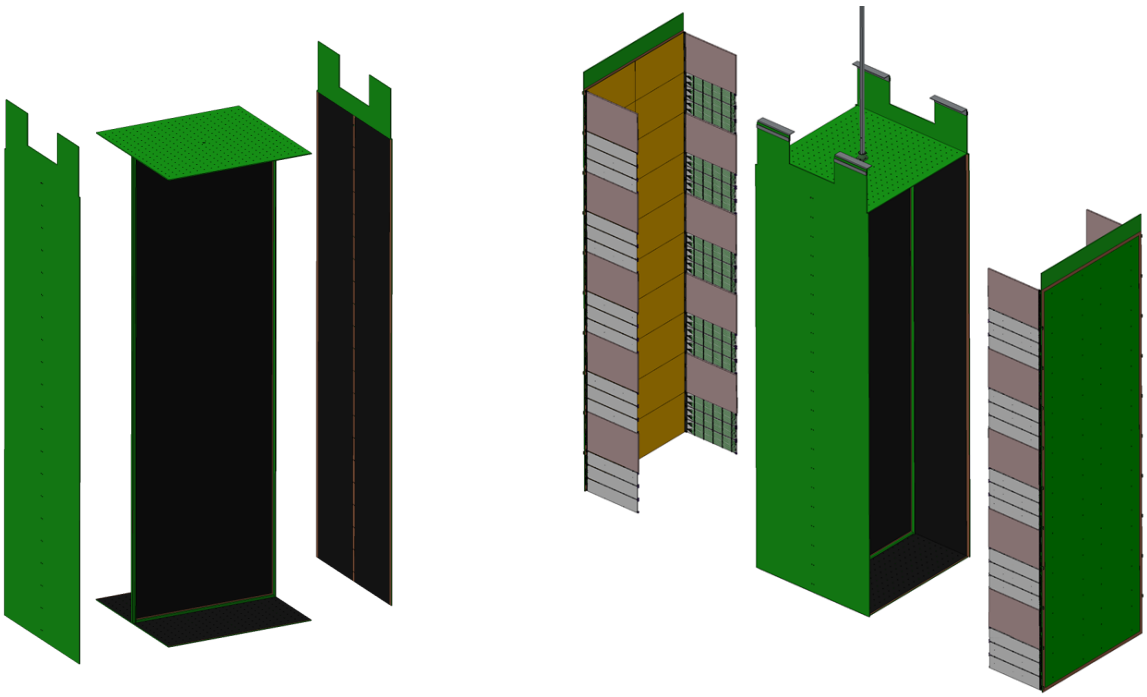

Figure 4.1: Schematic of the module structure as being designed for the DUNE ND-LAr. Left: The central plane is the cathode which splits the module into two independent and optically isolated TPCs. The other four panels build the field shell. ArgonCube collaborators at SLAC developed a technology for laminating the resistive sheets onto the module structure. Right: The charge and light readout systems for both TPCs can be inserted into the module structure as indicated in the second schematic drawing. The pixelated anode planes were developed at LBNL. The light detection system consists of ArCLight and Light Collection Module (LCM) modules developed at LHEP and the Joint Institute for Nuclear Research (JINR), respectively. At the top of the module, the HV cable is connected to the central cathode. [39]

In the context of this section, I mainly contributed to develop and test of a prototype TPC based on the resistive field shell technology as described in Section 5.1.2. Furthermore, I was driving the analysis of the data acquired with this prototype. The findings from the analysis showed the feasibility of a resistive field shell to produce and shape TPC drift fields. Based on those results, ArgonCube collaborators at SLAC studied the properties of different materials suitable for the resistive shell and cathode plane. Furthermore, they investigated a new technology for laminating the resistive sheets onto the ArgonCube module planes. Once a dedicated technology was established, SLAC provided the field shell and cathode planes for the SingleCube and Module-0 detectors described in Sections 5.1.3 and 5.1.4, respectively. I was heavily involved in the assembly of these detectors, including their instrumentation, testing, diagnosis, and commissioning. Furthermore, I contributed to the detector operations and analysed the acquired data.

4.3 Charge readout

Traditional LArTPCs employ two or more projective wire planes for the detection of the ionisation signals. This technology has been demonstrated to work in a number of experiments, e.g. with the ICARUS T600 detector [85], in the Argon Neutrino Teststand (ArgoNeut) [86], and in the Micro Booster Neutrino Experiment (MicroBooNE) [87]. However, the reconstruction of typically complex events in LAr using a limited number of wire planes suffers from ambiguities [88]. In particular, this is problematic for particle trajectories oriented nearly coplanar with the wire readout. These ambiguities are worse in high-multiplicity environments, e.g. as in the DUNE ND, where the signals from several unrelated particle interactions might overlap with each other within a TPC readout window. Compared to projective wire systems, where tracks parallel to wires are reconstructed with much smaller efficiencies, pixelated charge readout systems have a flat response as a function of the angle between the ionisation traces and the pixel orientation, as depicted in Figure 5.13. That allows for a constant reconstruction efficiency regardless of the direction an ionising particle travels through the TPC. Furthermore, wire-based charge readout systems pose challenges regarding mechanical fragility and pose risks of HV discharges in the case of a broken wire.

The ArgonCube collaboration investigated the development of a pixelated charge readout system to address those considerations. As described in Section 3.1, charge readout systems based on charge-sensitive pads were employed already in the first TPCs ever built [53]. However, those detectors were gaseous TPCs, operated at much higher temperatures than the cryogenic noble liquid TPCs. Electronics with preamplifiers operational in LAr, and with relatively small power consumption to avoid excessive heating of the liquid, became available only during the last two decades. Low heat input from the electronics is required to avoid argon bubbles which, if close to the sensitive analogue inputs of the charge readout system, can lead to spurious signals. Furthermore, gas bubbles in a TPC could result in HV breakdowns and thus pose a risk of damage for the electronics.

Cold readout electronics for wire-based LArTPCs has been developed during the last two decades [89]. However, since the number of channels in a pixelated readout system scales quadratically with the linear size whereas the number of channels in a wire-based system scales approximately linearly with the linear size, a pixel

readout would require many more electronic channels than that needed in a projective wire system of the same size and granularity. To resolve this problem, ArgonCube collaborators at LBNL developed an Application-Specific Integrated Circuit (ASIC) called LArPix which enables cold amplification, digitisation and digital multiplexing [90]. Compared to the analogue waveform transmission, digitisation within the cryostat significantly reduces the data transfer bandwidth out of the cryostat. Digital multiplexing allows for operating several ASICs of the readout system as a single daisy chain with all configuration, control and data stream requiring only one data input and one data output line. This approach simplifies the Printed Circuit Board (PCB) design and significantly reduces the cryostat penetrations and thus the risk of heat or impurities leaking into the cryostat.

The pixels are based on gold-plated charge-collection pads printed on one side (front) of a conventional PCB. Based on the findings from an early prototype pixel board used to study different pad sizes and shapes (see Section 5.1.1), and to match the intrinsic energy resolution of the DUNE FD, the pixel pads have a square shape of 4 mm × 4 mm. The charge collected on every pixel is individually amplified and digitised in LAr by the LArPix chip soldered on the other side (back) of the same pixel PCB. Using a conventional PCB design makes the charge readout system mechanically robust and simplifies the scalability of the charge readout system to larger sizes. Figure 4.2 shows a pixel tile with 70×70 pixel pads connected to 10×10 LArPix chips. Such pixel tiles were tested in the prototype detectors SingleCube and Module-0, as described in Sections 5.1.3 and 5.1.4, respectively.

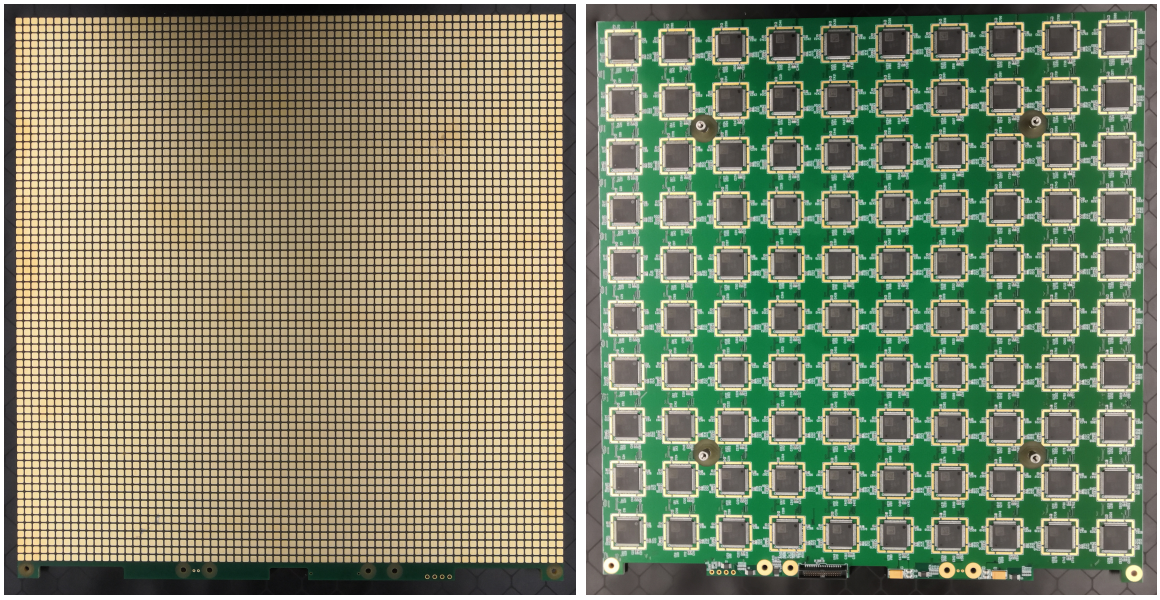

Figure 4.2: Pixelated charge readout PCB as employed in the SingleCube and in the Module-0 detectors. The digitisation and amplification is based on the LArPix-V2 ASIC developed at LBNL. Left: The front side of the 31 cm × 32 cm PCB is populated with 70×70 gold-plated pixels with dimensions of 4 mm × 4 mm at a pitch of 4.434 mm. Right: The back side of the pixel PCB consists of an array of 10×10 LArPix-V2 chips which provide cold amplification and digitisation of the signals collected with the pixel pads.

Even in high-multiplicity environments similar to those in the DUNE ND-LAr, the expected signal rate per pixel is only about 1 Hz per pad. These low rates are

due to the relatively small size of each pixel and enable a design where much of the electronics is in a dormant mode, consuming little power. As soon as a signal occurs, the ASIC wakes up and acquires the data from the corresponding pixel. Each of the 64 channels on a LArPix-V2 chip allows for this self-triggered operation. The digitisation and readout of the charge signals only occur if the collected charge on a pixel pad exceeds its individually programmable threshold. In this way, the power consumption of the chip is further reduced.

The second version of the ASIC, LArPix-V2, has a square footprint of about 1.5 cm × 1.5 cm and contains 64 analogue input channels, 16 along each edge of the ASIC. In addition, the ASIC hosts 4 digital Input/Output (I/O) blocks, labelled Master Input, Slave Output (MISO) and Master Output, Slave Input (MOSI), used for the communication with the ASIC itself, e.g. sending configurations to the chip and obtaining data from the ASIC. A block diagram for one analogue input channel of the LArPix-V2 ASIC is shown in Figure 4.3. The charge collected on a pixel pad is converted by a Charge-Sensitive Amplifier (CSA) to a voltage proportional to the accumulated charge. A buffer downstream of the CSA mirrors its output, which is sent to an 8-bit ADC and a threshold discriminator. If the CSA output voltage is higher than a threshold, which can be individually set for each pixel, a discriminator forces the digital control unit to initiate the ADC conversion of the buffer output voltage. The digital control unit assembles the ADC output to an event, adding a time stamp, the channel number and the chip ID. Also, a reset pulse is sent to the CSA, so it is ready to accumulate the charge from the next charge package. The LArPix chip has a 10 MHz clock rate with a time resolution of 2 µs to ensure approximately the same resolution along the TPC drift axis as given by the pixel pitch.

Several LArPix-V2 chips are daisy-chained to keep the number of physical communication lines small. The previous version of the chip, LArPix-V1, only had one Universal Asynchronous Receiver-Transmitter (UART) per chip with one MISO and one MOSI channel for the communication line. Each LArPix-V1 chip was routed to two of its closest neighbouring chips, with the daisy chain organised in a 1-dimensional (1D) network. A failure of a single UART (or ASIC) consequently would result in the data loss of all chips in the daisy chain located downstream of the defective component. As described in Section 5.1.1, such a failure was observed during tests with a LArPix-V1 instrumented charge readout system. To address this problem, the LArPix-V2 chip incorporates four UARTs, each of which with one MISO and one MOSI channel, enabling the configuration of a more sophisticated network, called *Hydra*. Figure 4.4 schematically compares the architectures of the first two versions of LArPix chips. *Hydra* uses a single LArPix-V2 ASIC functioning as the interface between the network and the control electronics. In the case of a broken ASICs or a failing UART, the defective part can be easily routed around, as illustrated in Figure 4.5.

The control electronics for the charge readout system is located outside of the cryostat. It consists of a commercial Zynq-7000 SoC[4] on a custom made PCB acting as a system with a Central Processing Unit (CPU) and a Field Programmable Gate Array (FPGA). Each control unit enables the communication with $\mathcal{O}\left(10^5\right)$ pixel channels. For the ArgonCube Module-0 prototype described in Section 5.1.4, one control unit was used for each LArTPC.

[4] From XILINX, https://www.xilinx.com (accessed: 29.06.2021).

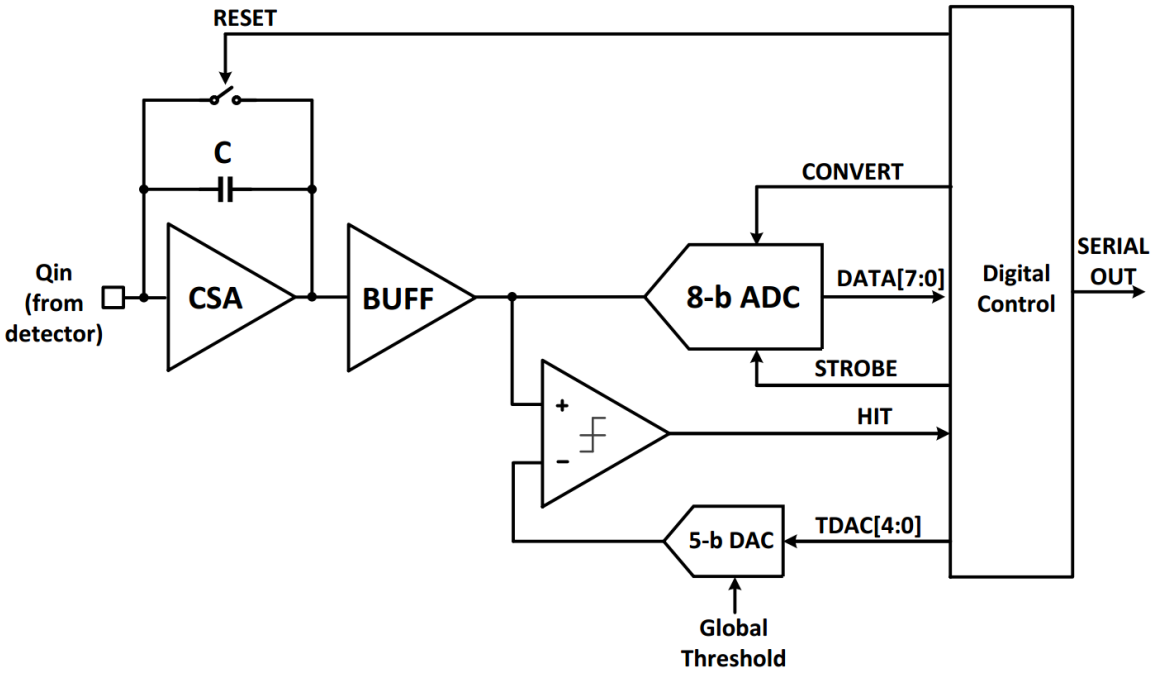

Figure 4.3: Block diagram for an analogue input channel of the LArPix-V2 ASIC. The charge collected on a pixel pad (Q_{in}) is integrated on a feedback capacitance (C) of a CSA. The CSA converts the input charge collected on the pixel pad since the last reset to a voltage proportional to the incident charge. A buffer amplifier (BUFF) following the CSA is used to feed the signal to an 8 bit ADC and a discriminator with a per-channel programmable threshold. As soon as the voltage output from the CSA exceeds the defined pixel threshold voltage, a digital control unit initiates the digitisation of the buffer and resets the CSA to allow for the collection of more charge packages on the pixel. [91]

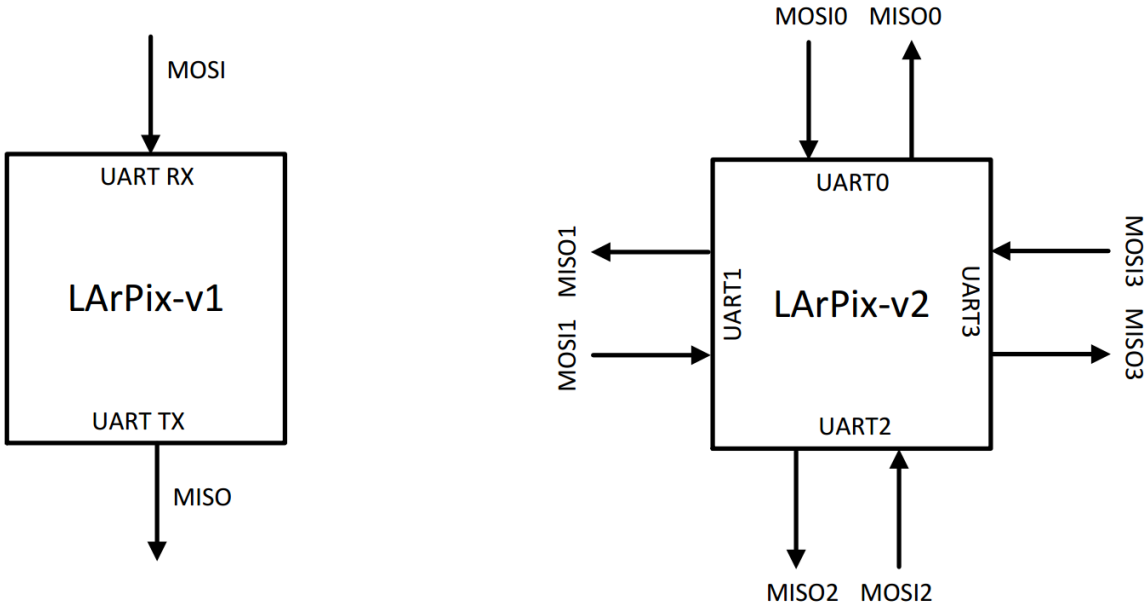

Figure 4.4: Comparison between the communication lines of the LArPix-V1 and the LArPix-V2 ASIC. The former only had two MISO and MOSI channels for the communication line whereas the latter allows for four possible communication line arrangements, making the daisy chain more robust to erroneous UARTs or ASICs. [91]

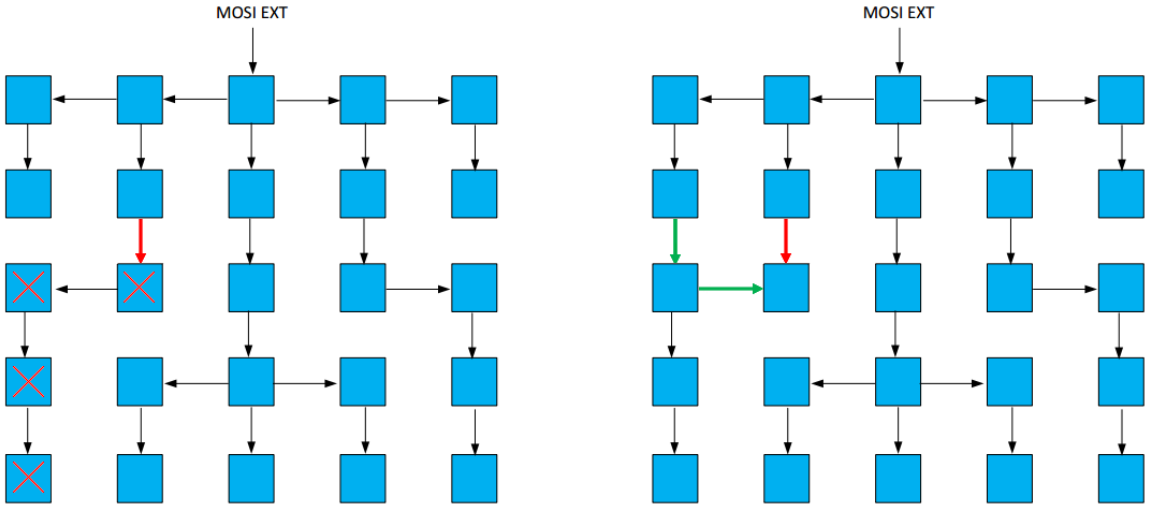

Figure 4.5: Schematic illustration of 5 × 5 LArPix-V2 ASICs organised by the *Hydra* network. Left: In the case of a failing UART, indicated by the red arrow, the four ASICs labelled with a red cross would not be responsive. Right: Routing around the broken UART can be done by reconfiguring the *Hydra* network as indicated with the green arrows. The figure was taken from [91], with modifications made.

Figure 4.6 shows an event display of a cosmic induced shower acquired with the ArgonCube Module-0 detector. Module-0 consists of two independent LArTPCs each instrumented with 8 pixelated anode planes identical to the one shown in Figure 4.2. More details about the Module-0 prototype and more event displays from this detector can be found in Section 5.1.4. These event displays indicate how powerful an unambiguous 3D tracking in pixelated LArTPCs is, especially when dealing with pile-up events.

In connection with the pixelated charge readout, I mainly contributed to the assembly, commissioning, and operation of the LArPix-V1 pixel equipped readout TPC described in Section 5.1.1. I was involved in matching the data obtained by the light and charge readout systems acquired during the experiment. Furthermore, I performed preliminary studies related to the light and charge yields within the aforementioned LArTPC. Once the group at LBNL delivered the LArPix-V2 equipped pixel tiles for the SingleCube and Module-0 experiments, described in Sections 5.1.3 and 5.1.4, respectively, I took the lead in the detector assemblies. In addition, I became the local contact person for the charge readout system since I was responsible for testing all pixel tiles, setting up configurations and the *Hydra* networks, and ensuring a stable operation. I wrote a DAQ software package which simplified the DAQ of the TPC charge signals and performed data quality checks. Furthermore, I was involved in the TPC event reconstruction, worked on the matching of the TPC charge and light signals, and performed data analysis with the matched data.

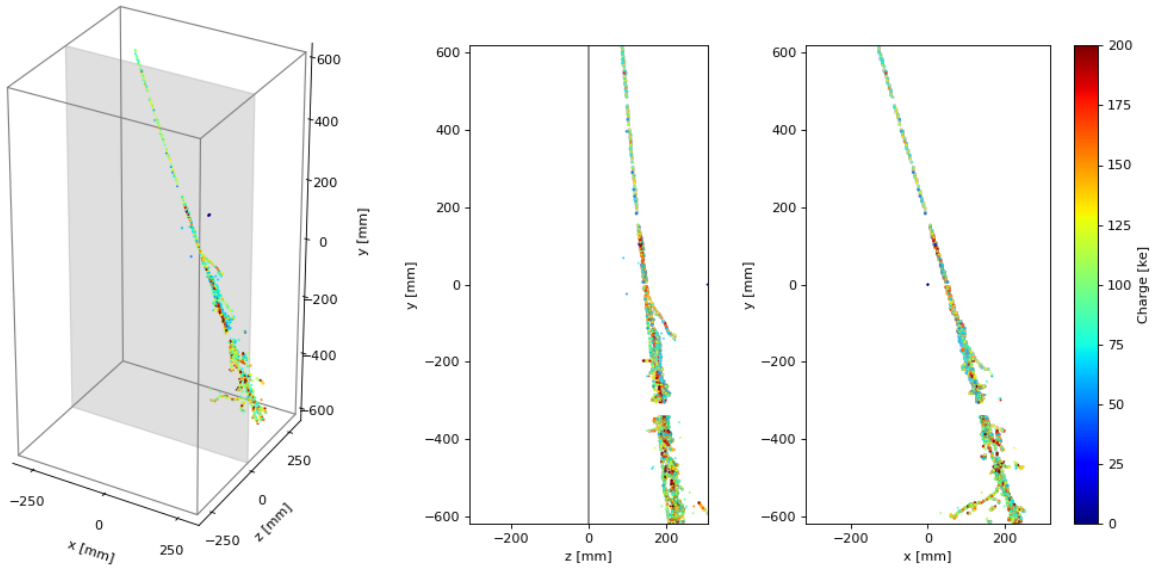

Figure 4.6: Module-0 event display with a candidate of a cosmic induced particle shower in one of the Module-0 TPCs. The grey plane (left) or line (middle) at $z = 0\,\text{mm}$ indicates the cathode plane, which splits the ArgonCube Module-0 into two independent TPCs, each populated with 8 pixel tiles identical to the one shown in Figure 4.2. The ionisation electrons drift along the z coordinate axis. The event display highlights the capability of a pixelated charge readout system for unambiguous 3D tracking with low noise. The regions at $y \approx 480\,\text{mm}$, $y \approx 180\,\text{mm}$, and $y \approx -320\,\text{mm}$ correspond to region with high pixel thresholds or disabled channels. The event display shows raw data with a pixel-wise pedestal correction only. No optimisation or correction was applied to the data.

4.4 Light readout

As charged particles travel through LAr, scintillation light with a wavelength of $\lambda_{sci} = (129 \pm 10)\,\text{nm}$ is produced. At moderate electric field intensities of $\mathcal{O}\left(100\,\text{V}\,\text{cm}^{-1}\right)$, ionising particles produce $\mathcal{O}\left(10^4\right)$ photons per cm track length. However, detecting the scintillation light is challenging since the quantum efficiency of current photon detectors operational in LAr is low for such VUV photons. Therefore, the VUV light usually is shifted by a Wavelength Shifter (WLS) to longer wavelengths where the quantum efficiency of the used detector is enhanced.

In traditional TPCs, the scintillation light signals are mainly used to provide accurate time information of when the particle interactions within the TPC happened. Using this time together with the arrival time of the charge signals and an estimate of the electron drift velocity allows for a 3D TPC event reconstruction, as outlined in Section 3.2. The scintillation light signals, however, can be used for more than this purpose. According to the *Birk law* described in Section 3.2.3, the light yield depends on the energy deposited by the ionising particle(s). Hence, the light signals can be used to improve the calorimetric measurement conducted with the LArTPC. In addition, a segmented light detection system with good, $\mathcal{O}\,(1\,\text{ns})$, time resolution and large enough PDE can help to precisely allocate detached energy depositions to individual particle interaction vertices. That is especially important in high-multiplicity environments where the energy depositions of several particle interactions might overlap within the TPC charge readout window. Contained scintillation light within individual ArgonCube TPCs and short optical path lengths are vital factors enabling an accurate

scintillation light measurement, and thus enable precise matching of charge and light signals.

Contemporary LArTPC-based experiments usually employ PMTs for the detection of the scintillation light. However, PMTs are not suited for use in ArgonCube modules for two main reasons: They cannot be operated within electric fields, and they consume a large amount of space which would significantly reduce the active TPC volume. Based on the ARAPUCA design [92], the ArgonCube collaboration developed two complementary light detection systems using Silocon Photomultiplier (SiPM) optically coupled to dielectric materials which can be employed within electric fields:

- The ArCLight module was to a large extent developed at LHEP in Bern. It is based on a dielectric WLS bulk structure[5]. A self-adhesive dichroic mirror foil[6] coated with a thin layer of 1,1,4,4-Tetra-Phenyl-1,3-Butadiene (TPB) is attached on one side of the bulk structure. The TPB is intended to shift the VUV scintillation light to blue light ($\lambda = 425\,\mathrm{nm}$), for which the dichroic mirror has a large transparency. Once entered the bulk structure, the blue light is shifted by the WLS to green light ($\lambda = 510\,\mathrm{nm}$), for which the dichroic foil has a large reflectance. On all other sides of the dielectric bulk, a specular mirror foil[7] is installed, making the ArCLight module a light trap. Several SiPMs are optically coupled to the WLS bulk, allowing for the efficient detection of the green light. Using the signals from the SiPMs enables a spatial resolution of $\mathcal{O}\,(1\,\mathrm{cm})$. Figure 4.7 shows the working principle of an ArCLight module, and Figure 4.9 shows a photo of a prototype used in the SingleCube and in the Module-0 detectors, described in Sections 5.1.3 and 5.1.4, respectively. Preliminary results obtained with SingleCube showed a PDE of about 0.1 % [93]. More details about the ArCLight technology can be found in [93] and [94].

- The LCM module was mainly developed at the JINR in Dubna. It consists of a bundle of dielectric WLS fibres[8] with a diameter of 1.2 mm arranged on a Polyvinyl Chroride (PVC) plate. Each end of the fibre bundle is optically coupled to a SiPM. The fibres and the PVC plate are coated with a thin layer of TPB which converts the VUV scintillation light to blue light ($\lambda = 425\,\mathrm{nm}$). After entering the fibre, the blue light eventually is shifted to green light ($\lambda = 510\,\mathrm{nm}$), which is trapped and piped within the fibre due to its high efficiency for total internal reflection. Since both ends of the bundle of fibres are connected to a pair of SiPMs, the spatial resolution of the LCM is limited to the panel size. Figure 4.8 shows the working principle of a LCM module and a photo of prototype LCMs installed in the Module-0 detector, discussed in Section 5.1.4. Preliminary results obtained with Module-0 showed a PDE of about 1 % and a time resolution of about 2.3 ns. More details about the LCM technology can be found in [95].

An entire readout chain applicable for both light detection systems was developed at JINR. It consists of the front-end electronics, a power supply unit, and the DAQ software. A detailed description of the readout system can be found in [95].

[5] EJ-280, from https://eljentechnology.com (accessed: 26.05.2021).
[6] DF-PA Chill, 3M Inc., St. Paul, MN, USA.
[7] VM2000, former name for Vikuiti ESR, 3M Inc., St. Paul, MN, USA.
[8] Kuraray Y-11, from https://www.kuraray.com (accessed: 26.05.2021).

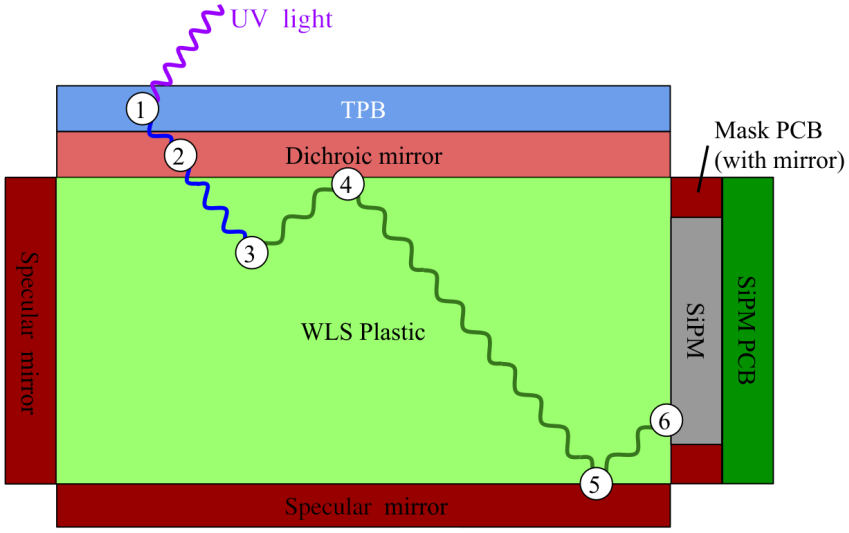

Figure 4.7: Schematic drawing illustrating the working principle of an ArCLight module: (1) The incident VUV photon is shifted by TPB to blue light. (2) The dichroic mirror has a large transparency for blue light. (3) The blue light eventually gets shifted to green light by the WLS in the bulk structure. (4) Green light is efficiently reflected by the dichroic mirror. (5) The light is also reflected by the specular mirror, thus the photons are trapped within the bulk. (6) A SiPM might detect the trapped light. The figure was taken from [93], with modifications made.

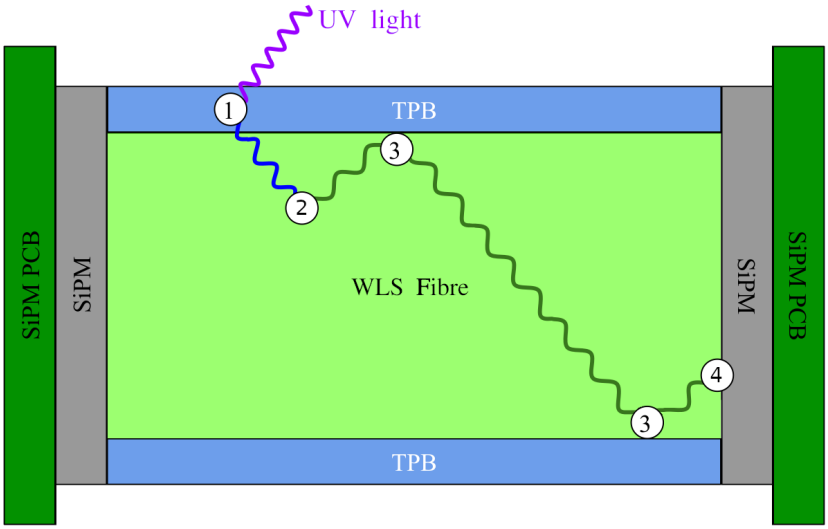

Figure 4.8: Schematic drawing illustrating the working principle of a LCM module, with only one fibre for simplification: (1) The incident VUV photon is shifted by TPB to blue light and enters the WLS fibre with some probability. (2) The blue light eventually gets shifted by the WLS in the fibre to green light. (3) Green light undergoes efficient total internal reflection at the cladding of the fibre. (4) A SiPM might detect the trapped light. The figure was taken from [93], with modifications made.

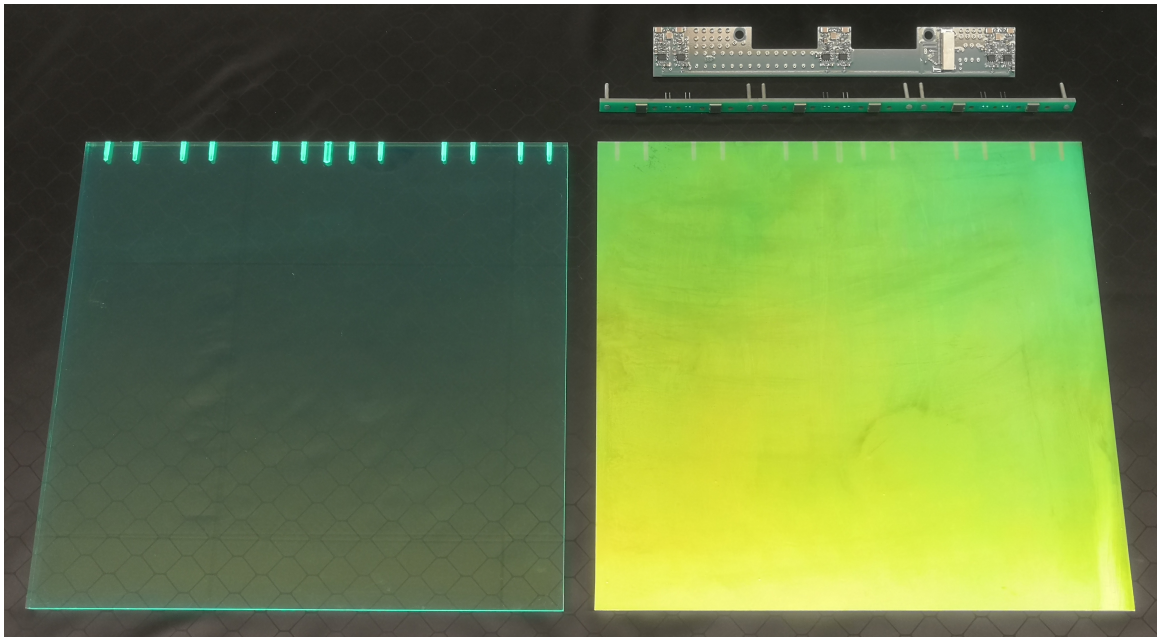

Figure 4.9: An ArCLight module, similar to those used for the instrumentation of the SingleCube and Module-0 detectors described in Sections 5.1.3 and 5.1.4, respectively. The bulk structure (left) has dimensions of 30 cm × 28 cm × 1 cm. A dichroic mirror, coated with a TPB layer, is laminated on the bulk structure (right). Three PCBs, each hosting two SiPMs, are bolted at one edge of the module. An E-shaped board distributes power for the light detectors and provides amplification for the SiPM signals.

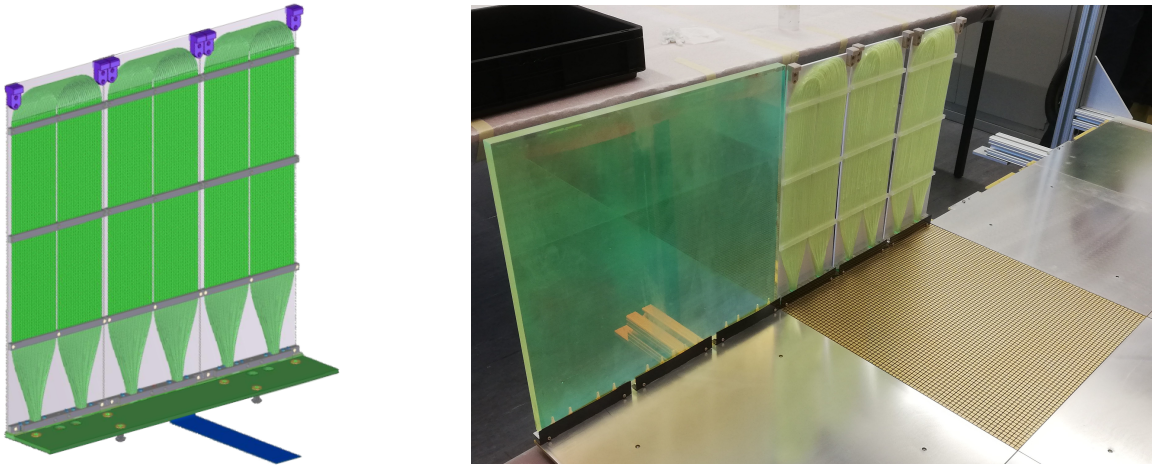

Figure 4.10: Left: Technical drawing of three LCM modules as designed for the Module-0 prototype described in Section 5.1.4. Each LCM has dimensions of about 10 cm × 28 cm × 1 cm. Right: Picture showing an ArCLight module, three LCM modules, and one pixelated anode plane in the partially instrumented Module-0 TPC.

As part of my work done related to this section, I mainly contributed to the development and production of the ArCLight modules. In the beginning, I tested different options for mounting the specular mirror foil on the bulk structure. Since the thermal expansion coefficients of the involved materials differ slightly, attaching the mirrors so that they remain attached during thermal cycles turned out to be challenging. Various methods were tested, including different forms of sliding mirrors held in place using shrink wraps or glueing the mirrors to the bulk structure with adhesive. Problems related to the enhanced absorption of the light by the shrink wraps or the glue were identified and taken into account for future designs. Furthermore, I tested different TPB solutions, based on toluene, ethanol, polystyrene, and TPB, to be air-brushed on the ArCLight surface. It was shown that reproducing similar TPB surface-coverage on different ArCLight panels is difficult. This lead to the idea of coating the panels using a TPB evaporation chamber. Together with a Master's student, the evaporation chamber was designed and several coating procedures tested. Figure 4.11 qualitatively shows the differences between the air-brushed and the evaporated TPB coatings. More results are discussed in [93]. As pointed out in [96], different conditions during the evaporation process, e.g. temperature and pressure variations, can affect the TPB morphology and thus might exhibit different responses to VUV light. Systematic studies covering a broad range of such conditions during the evaporation process might result in a mechanically more stable TPB layer on the detector surface, with an enhanced PDE.

There may be beneficial developments in single-photon detectors in the future. Even though it is risky to speculate, I would like to make some projections. As the SiPM-based technology becomes more and more sensitive to VUV and blue light, future light detector designs for LArTPCs might be affected significantly. The SiPM technology might be sensitive enough such that these detectors could directly be exposed to the LAr scintillation light to efficiently detect single photons. That would render TPB and other WLSs unnecessary, with the benefit of an enhanced time resolution since no wavelength shifting processes would be involved. In addition, problems related to the TPB degradation as discussed in [96] and [97] would be eliminated, as well as the possibly problematic long term stability of the TPB layer on the detector surface, as described in [98] and [99]. The exposure of a bare SiPM array in LArTPCs would also improve its spatial resolution, and, compared to the ArCLight and LCM modules, would consume less volume in the TPC and thus would increase the TPCs total active volume.

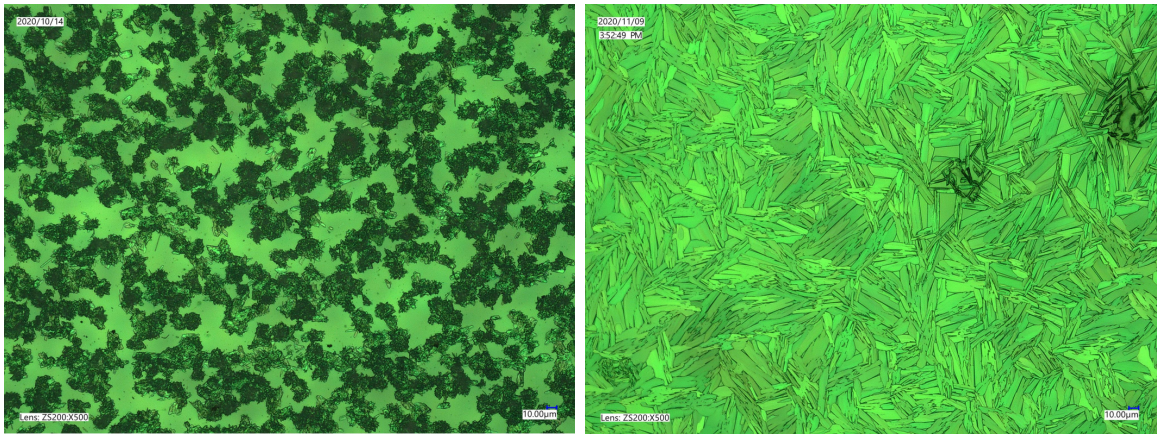

Figure 4.11: Microscopic comparison of the TPB layer on an ArCLight panel using two different coating techniques. Left: The TPB was coated with an air-brush. The dark spots have been identified as polystyrene, which was used for the TPB fixation. Some few TPB crystals with a length of about 10 µm can be identified. Right: Using an evaporation chamber results in much larger crystals with a length of some tens of µm. [93]

Chapter 5

The ArgonCube Prototypes and Results

The scope of this thesis allowed for much work on detector prototypes and associated hardware such as sensors and electronic components. Section 5.1 summaries the most relevant prototypes developed at LHEP and within the ArgonCube collaboration. These prototypes were designed to demonstrate the feasibility of different ArgonCube technologies. To safely operate those detectors, a slow-control system was developed to constantly monitor the status of the hardware, including temperatures and pressures at different positions and the filling level of the cryogenic liquid in a given cryostat. A brief overview of the slow-control system is given in Section 5.2.

5.1 ArgonCube Prototypes

In the framework of this thesis, four major prototypes were built to demonstrate the feasibility of the different ArgonCube technologies:

- Version 1 Pixel Equipped Readout (V1PER) TPC (Section 5.1.1):
  This prototype detector was a cylindrical 59 cm drift TPC with an inner diameter of 10.1 cm. The major goal of the V1PER TPC was to test the first version of a pixel equipped charge readout system for unambiguous 3D particle tracking in LArTPCs. V1PER was instrumented with 28 LArPix-V1 ASICs mounted on the back of a commercially available PCB with 832 gold-plated copper pixel pads spaced at 3 mm to 5 mm. The setup furthermore included two ArCLight prototype modules, each with a surface area of 10 cm × 30 cm.

- Resistive Shell Time Projection Chamber (RS-TPC) (Section 5.1.2):
  The RS-TPC prototype was a small LArTPC with an active volume of 7 cm × 7 cm × 15 cm. The charge readout system consisted of two planes of conducting strips printed on both sides of a Kapton foil, instrumented with cryogenic amplifiers and triggered with two scintillator tiles. The RS-TPC was designed to demonstrate that the drift field of a LArTPC can be produced and shaped utilising a low-profile foil with a high sheet resistance of $\mathcal{O}\left(1\,\mathrm{G\Omega\,sq^{-1}}\right)$. The RS-TPC was the first LArTPC employing the field shell technology.

- SingleCube (Section 5.1.3):
  The SingleCube detector was a LArTPC of cubical shape with an active volume of about 30 cm × 30 cm × 30.2 cm. It was designed to combine the signals from the ArgonCube light and charge detection systems, and to show that those signals can be matched to properly reconstruct TPC events in 3D. The charge readout system was based on a pixelated anode tile with 10 × 10 LArPix-V2 ASICs routed to 70 × 70 square pixels of size 4 mm × 4 mm. An ArCLight module with an area of 30 cm × 28 cm was employed in SingleCube. The electric field was shaped by gold-plated copper strips printed on commercially available PCBs.

- Module-0 (Section 5.1.4):
  This detector was the first ArgonCube module employing all the technologies developed in the ArgonCube R&D program. A central cathode, splitting the Module-0 into two independent TPCs, was made of 25 µm thick Kapton XC laminated on a FR-4 sheet. The electric field was shaped using a 100 µm thick Kapton DR8 shell laminated on FR-4. Module-0 had an active footprint of about 60 cm × 60 cm and a height of 120 cm, corresponding to an active mass of about 600 kg. In a first experiment in October/November 2020, Module-0 was partially instrumented with the same pixel tile and ArCLight module used in SingleCube, and three LCM modules. This experiment was intended to show that the relatively large module structure and the field shell are robust enough to be employed in an ArgonCube module. Furthermore, it should demonstrate the stability of the HV system and the feasibility of the LAr filtration with the corresponding cryogenic loop. In a follow-up experiment in March 2021, Module-0 was fully instrumented with 16 pixel tiles, 8 ArCLight and 24 LCM modules to test the performance of the first complete ArgonCube module.

The Module-0 experiments showed that a fully instrumented ArgonCube module is capable of precisely measuring cosmic-induced particle interactions. Furthermore, Module-0 demonstrated the feasibility of matching tracks and showers across the two independent LArTPCs within a module. The next step towards the DUNE ND-LAr is a detector combining four of these modules. That will be done with the

- ArgonCube 2x2 Demonstrator (Section 5.1.5):
  This detector consists of four modules identical to the Module-0 detectors, arranged in an array of 2 × 2 modules. The modules share a common cryostat with an inner diameter of about 2.2 m and a height of ≈ 2.8 m.The ArgonCube 2x2 Demonstrator will be shipped to FNAL where it will be installed in the Main Injector Neutrino Oscillation Search (MINOS) ND hall to form the core component of ProtoDUNE-ND, described in more detail in Section 6.4.

5.1.1 Version 1 Pixel Equipped Readout TPC

The V1PER TPC, shown in Figure 5.1, is a cylindrical LArTPC with an inner diameter of 101 mm and a maximum drift length of 590 mm to test the first version of a pixel equipped charge readout system based on the LArPix-V1 ASIC. A 117 mm diameter brass disc served as the cathode. To shape the TPC drift field, a traditional field cage consisting of 38 aluminium rings with an inner diameter of 101 mm, a height of

6 mm, and a ring spacing of 6.25 mm were used. The aluminium rings were supported by full acrylic rings and segments of such rings to allow for adequate circulation of purified LAr through the TPC active volume. A voltage divider based on 100 MΩ Vishay Rox metal oxide resistors[1] is used to sequentially reduce the electric potential on the aluminium rings from the cathode bias voltage to the anode potential. Four Polyamide-imide (PAI) pillars are used to support the TPC structure, to hold cathode, charge readout, and the field cage through Polyether Ether Ketone (PEEK) bolts fixing the acrylic rings to the pillars. Two early 10 cm × 30 cm × 0.4 cm prototype ArCLight modules with mirrors on their back plane were mounted on the PAI pillars. Since the LArPix-V1 ASIC features a self-triggered charge readout, there is no need for a light detection system providing TPC triggers. However, for testing these ArCLight modules, they were installed on the setup as well. The HV feedthrough is the same as in [81].

V1PER was used to test the LArPix-V1 chip in LAr, the successor of an analogue multiplexed pixel readout presented in [100]. To some extent, the previous readout was not completely free from ambiguities for the event reconstruction. LArPix-V1 was designed to enable the full 3D tracking capabilities of LArTPCs without ambiguities at all, achieved by wire bonding each pixel pad to a unique analogue input channel of the LArPix-V1 ASIC, which then are digitally multiplexed through daisy-chaining. The capability of unambiguous 3D tracking makes a TPC with pixelated charge readout a viable option for high-multiplicity environments like those found in the DUNE ND.

Figure 5.2 shows the front and the back of the pixelated anode plane, with 832 pixels of different shapes and sizes on the front and 28 LArPix-V1 chips mounted on the back of the pixel plane. The different sizes and shapes of the pixel pads were designed to test their effect on quantities like SN ratio and particle tracking accuracy. Furthermore, the 416 pixel pads on one half of the anode tile are surrounded by a focussing grid to study its effect on the pads' charge collection efficiencies. On the one hand, a smaller pixel pad size increases the spatial resolution for particle tracking. On the other hand, less charge can be collected per pixel if the pad size is reduced, resulting in a poorer SN ratio. For the application in ArgonCube modules where electron diffusion can be neglected, pixel pad spacings of 3 mm to 5 mm are reasonable choices for good detector granularity and charge signal quality. Hence, pixel pad spacings of 3 mm, 4 mm, and 5 mm were chosen for the pixelated anode plane employed in V1PER, to study their relative performance. The time resolution of the LArPix-V1 chip was chosen to yield a similar spatial resolution in the drift direction. Given an electron drift speed of about 1.6 mm µs^{-1} in LAr, with an ambient electric field intensity of 500 kV cm^{-1}, the time resolution corresponds to about 2 µs. Hence, a 5 MHz digitisation clock for the LArPix-V1 ASIC was implemented.

The V1PER system design is based on standard PCB manufacturing techniques to enable scalable and affordable production of pixelated anode planes using commercial facilities. The block diagram of the LArPix-V1 design is very similar to that shown in Figure 4.3, except that for the LArPix-V1 chip, there is no buffer (BUFF). A detailed description of the working principle of the LArPix-V1 ASICs can be found in [90]. One important feature of the V1PER readout system is its capability for digital multiplexing, where several LArPix-V1 ASICs are connected to a daisy chain to keep the number of signal lines small. In this way, only one data input and one

[1] ROX100100MFKEL from VISHAY, https://www.Vishay.com (accessed: 11.06.2021).

Figure 5.1: The prototype V1PER TPC at LHEP, University of Bern. Left: V1PER and two 10 cm × 30 cm × 0.4 cm ArCLight modules with mirrors on their back plane, mounted vertically on top of the TPC. The blue resistor chain connects the cathode and the anode via the aluminium field cage rings. The HV feedthrough with its white ceramic insulator is visible next to the TPC. Right: A close-up picture of the top of V1PER shows parts of the golden pixel plane mounted at the end of the TPC drift volume. A dummy PCB directly above the pixel PCB is intended to protect the wire bonded ASICs of V1PER. Also visible is a part of one ArCLight module, facing with its TPB coated side towards the active TPC volume.

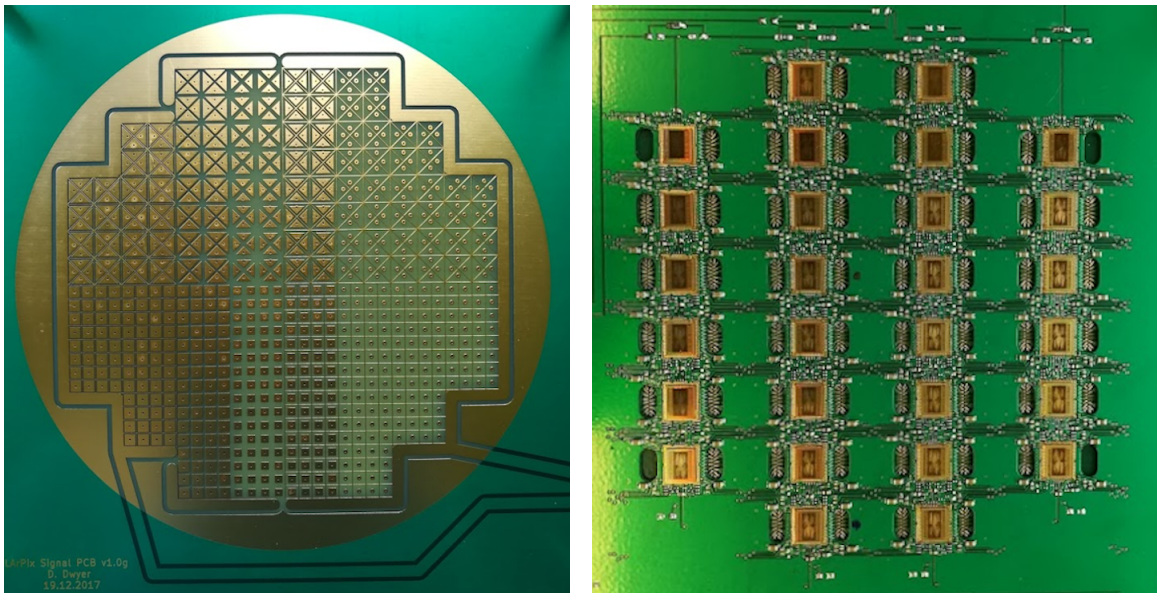

Figure 5.2: LArPix-V1 pixel PCB as employed in the V1PER TPC. Left: 832 gold-plated copper pads with ten different pad configurations are included on the analogue side of the two-layer PCB. Right: The digital side of the charge readout system consists of 28 LArPix-V1 ASICs. Each pixel pad is wire-bonded to an unique analogue input of a LArPix-V1 ASIC.

data output line per daisy chain are required to configure and control the ASICs. The drawback of such a design is that all the ASICs located downstream of a dead chip are not responsive. The failure of a single chip, therefore, could lead to multiple non-responsive ASICs.

The power consumption of the LArPix-V1 ASIC needs to be as low as possible since too much heat input might produce argon bubbles in the LArTPC. Argon gas bubbles near the sensitive analogue inputs of the charge readout electronics can produce spurious signals and thus would affect the event reconstruction. Furthermore, gas bubbles could result in HV breakdowns within the TPC drift field, posing severe risks of damage for the electronics. An upper limit of $10\,\mathrm{W\,m^{-2}}$ of pixelated readout was defined[2] in advance, corresponding to an average dissipation power of $90\,\mu\mathrm{W}$ per channel in the case of $3\,\mathrm{mm} \times 3\,\mathrm{mm}$ pixel sizes.

The V1PER TPC with the configuration shown in Figure 5.1 was stably operated for 7 days at electric field intensities up to $1.0\,\mathrm{kV\,cm^{-1}}$. Occasional recirculation of the LAr through purification filters was performed to maintain a good LAr purity.

Due to a failure in two of the daisy chains, the outermost two rows of ASICs showed no response and thus could not be read out. Consequently, only the 4×4 central ASICs connected to 512 pixel pads in total were active during the experiment. This problem was resolved in the second generation of ASIC, LArPix-V2, where the daisy chains can be re-routed around broken chips or broken UARTs. The so-called *Hydra* network described in Section 4.3 is used to define the daisy chain topology for the anode plane.

Figure 5.3 shows the raw pixel data of a cosmic-induced shower acquired with the LArTPC, from three different perspectives. Each coloured point represents the hit

[2] $10\,\mathrm{W\,m^{-2}}$ corresponds to the estimated heat input through the walls of the cryostat.

record of one pixel, with the colour indicating the detected amount of charge covering an approximate range of 10 k to 20 k electrons per hit.

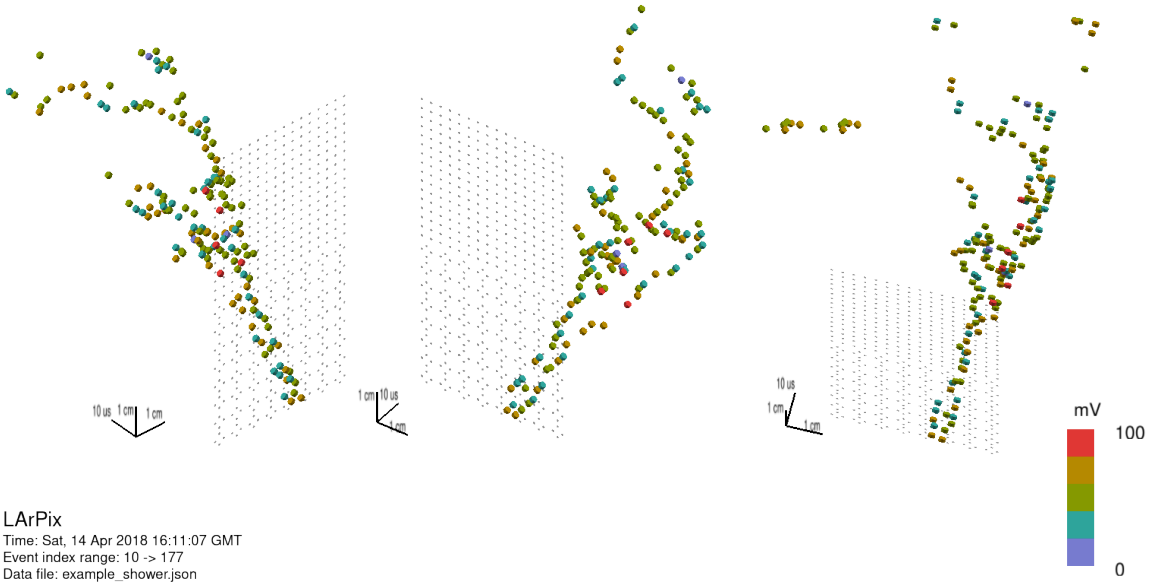

Figure 5.3: V1PER event display showing the same cosmic induced shower from three different angles. No filtering or signal enhancement was applied to the shown data. The ADC values were converted to mV. The grey points represent the position of all responsive pixel pads. Each coloured point represents the hit record of one pixel, with the colour indicating the detected amount of charge covering an approximate range of 10 ke to 20 ke. The two outermost rows of ASICs were not responsive due to a failure in the daisy chain. The same shower from three different angles

The V1PER LArTPC was used in a few other experiments, e.g. during the module cold extraction and re-insertion tests discussed in Section A.3. In those tests, the V1PER LArTPC was used to estimate the electron lifetime in LAr to infer the LAr purity.

5.1.2 Resistive Shell Time Projection Chamber

The RS-TPC prototype is shown in Figure 5.4. It was built at LHEP, University of Bern, with a 7 cm × 7 cm TPC footprint and a maximum drift length of 15 cm. The resistive shell and the cathode plane are made from a single sheet of about 50 µm thick carbon-loaded Kapton[3] foil. The resistive field shell was perforated to ensure adequate circulation of purified LAr into the TPC drift volume.

The structure of the RS-TPC is provided by a frame consisting of two steel squares and four pillars of PAI, as shown in Figure 5.5. The steel squares are positioned at the anode and the cathode plane, while the PAI pillars run through the length of the TPC. The resistive shell is attached to the top and the bottom steel squares using permanent magnets (Halbach arrays), which provide the electrical connection of the field shell to the electrodes. Incorporating the conducting steel squares reduces the actual length of the resistive shell to 13.5 cm. Dividing this length by the shell's 28 cm

[3] duPont™, Kapton®, polyimide film, from E. I. duPont de Nemours and Company, www.dupont.com (accessed: 11.06.2021).

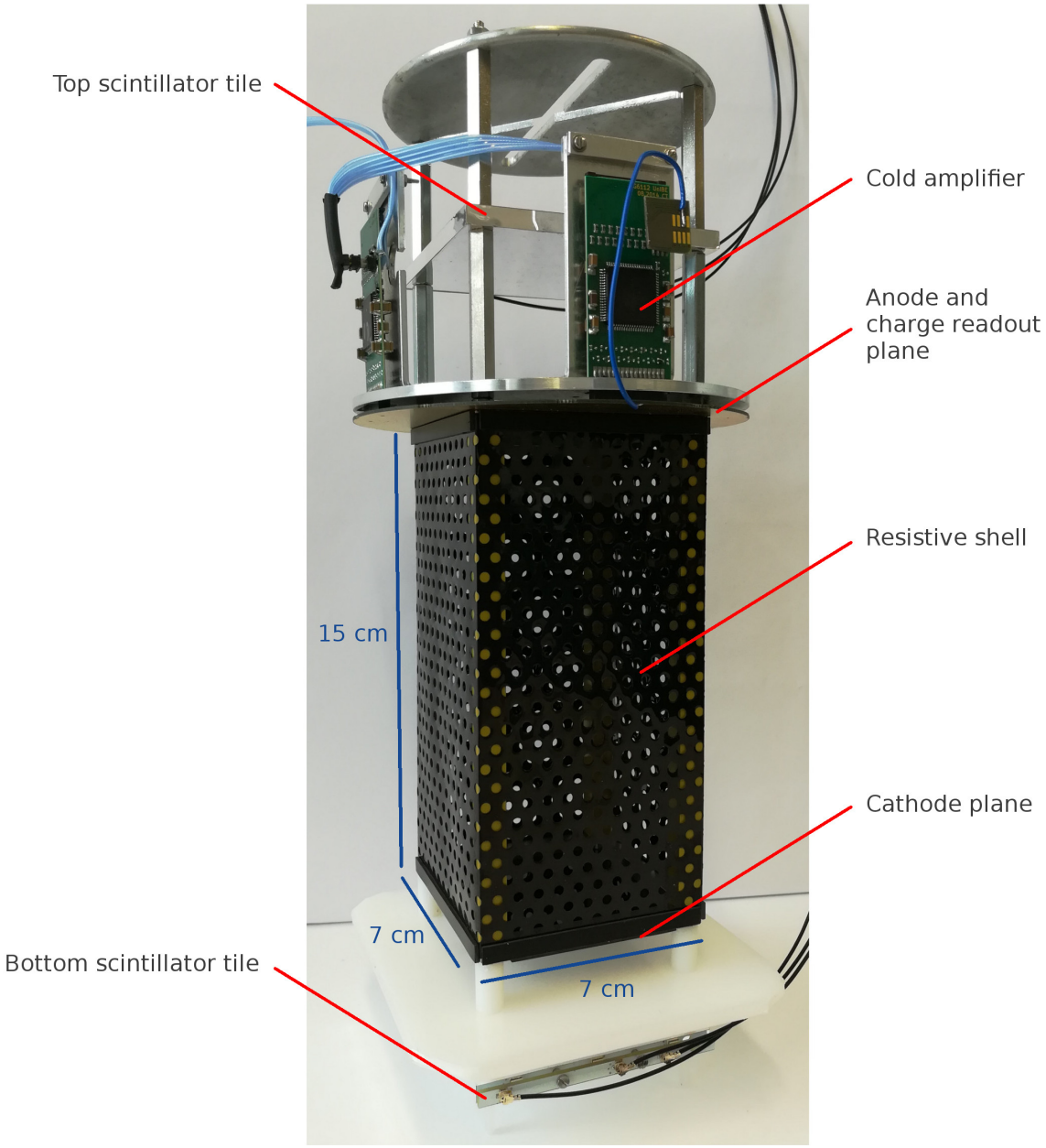

Figure 5.4: Prototype of the RS-TPC used to demonstrate the feasibility of using a resistive foil to produce and shape electric fields in an LArTPC. The resistive shell was perforated to assure an adequate flow of purified LAr from outside into the TPC drift volume.

periphery results in 0.482 sq. A simulation of the electric field in the RS-TPC was done and is presented in Appendix A.1.

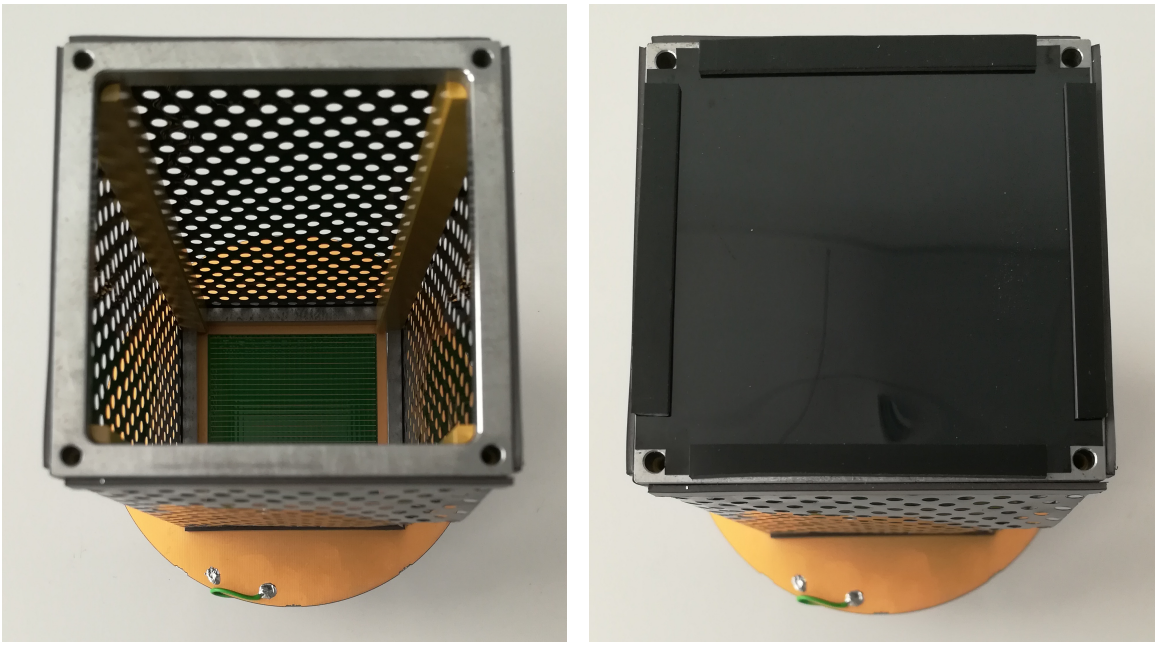

Figure 5.5: RS-TPC mockup without (left) and with (right) the cathode plane attached. Left: Parts of the charge readout system, the green plane with the golden strips, are visible. The field shell was perforated to allow for an adequate LAr flow through the TPC drift volume. Right: The resistive foils of the cathode and the field shell are mounted with Halbach magnets to the iron frames.

Figure 5.6 shows the RS-TPC charge readout system, which consists of two planes of conducting strips printed as parallel lines on either side of a 50 µm thick Kapton foil. The two planes are oriented at 90° with respect to each other and count 2×32 strips at a pitch of 1.7 mm. Four cryogenic preamplifiers, one LARASIC4* [89] and three LARASIC7, are coupled to the two planes. Each preamplifier provides the amplification for 16 channels.

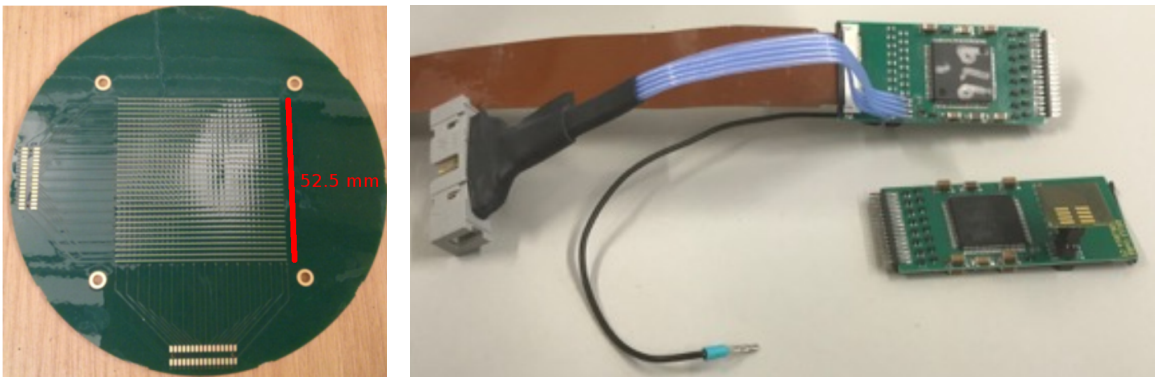

Figure 5.6: The RS-TPC charge readout system consists of 32 conducting strips printed on either side of a 50 µm thick Kapton foil (left), and four LARASICs mounted on two PCBs (left) for the cold amplification and acquisition of the charge signals.

Two scintillator tiles with dimensions of 7 cm × 7 cm × 0.4 cm were mounted above and below the RS-TPC as depicted in Figure 5.4. Each tile is wrapped with a dielectric specular reflecting foil[4] with a reflectance of about 98 % for visible light [101]. Three SiPMs[5] at one edge of the tile are used to detect the scintillation light produced by cosmic particles crossing the tiles. A two-fold coincidence signal from both scintillator tiles provided the trigger for the charge readout system.

The RS-TPC was continuously operated for 80 h at electric field intensities up to 1.6 kV cm^{-1}. Visual inspections during the operation showed no local LAr boiling due to power dissipation across the resistive shell. Particle tracks similar to those shown in Figure 5.7 were observed using a range of electric field intensities.

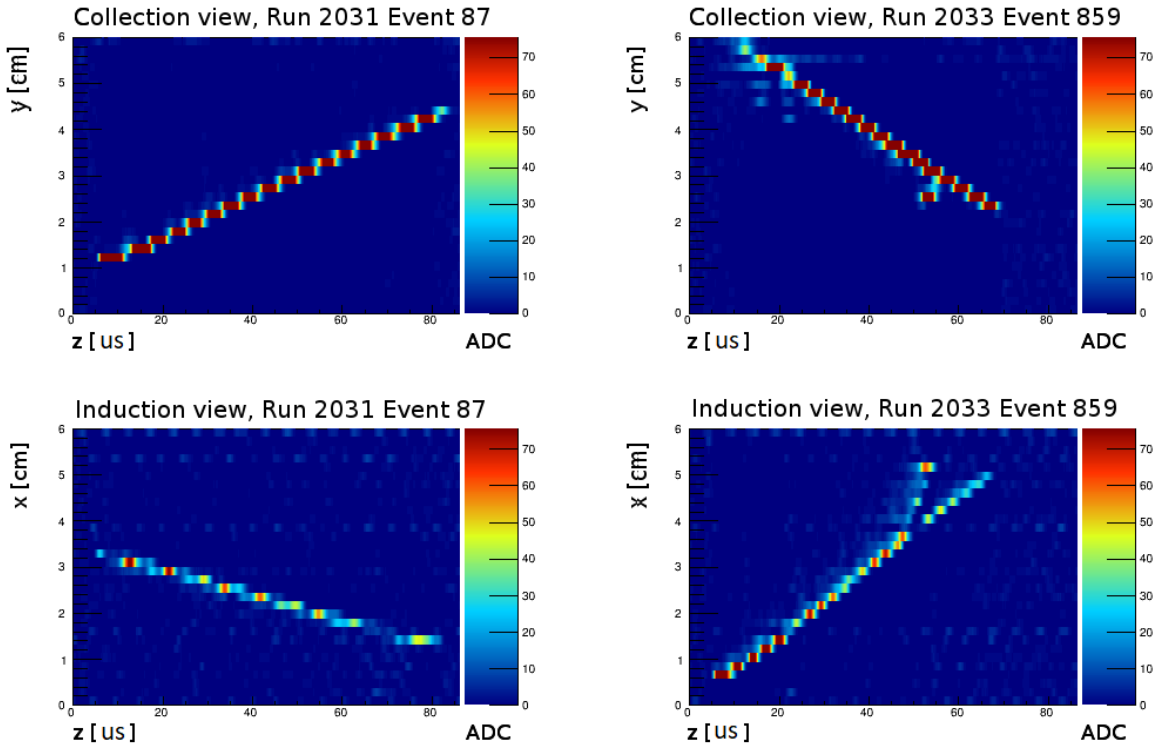

Figure 5.7: Event displays acquired with the RS-TPC showing through-going muon candidate tracks without (left) and with a delta ray candidate (right). The electric drift field intensities for those two events were 0.9 kV cm^{-1} (Run 2031) and 1.6 kV cm^{-1} (Run 2033). x and y correspond to spatial coordinates, and z denotes the drift time in µs.

The electrical properties of the resistive shell were determined by monitoring the current draw as a function of the cathode bias voltage. Figure 5.8 shows the measured currents as well as the derived values for the shell's dissipated power and its sheet resistance as functions of the potential difference between the electrodes. The dissipated power across the whole shell is considerably smaller than 1 W for all electric field intensities up to 1.6 kV cm^{-1}, and the shell's sheet resistance is of $\mathcal{O}\left(1\,\mathrm{G\Omega\,sq^{-1}}\right)$. Measurements conducted at room temperature and in Liquid Nitrogen (LN_2), orange and green data point in Figure 5.8, respectively, indicate a temperature dependence of the sheet resistance. Due to the limited current resolution of 0.5 µA from the HV

[4] VM2000, former name for Vikuiti ESR, 3M Inc.
[5] S13360-3050VE from Hamamatsu, https://www.hamamatsu.com (accessed: 11.07.2021).

power supply[6], the determined sheet resistance has relatively large uncertainties for low cathode bias voltages where the measured current was small.

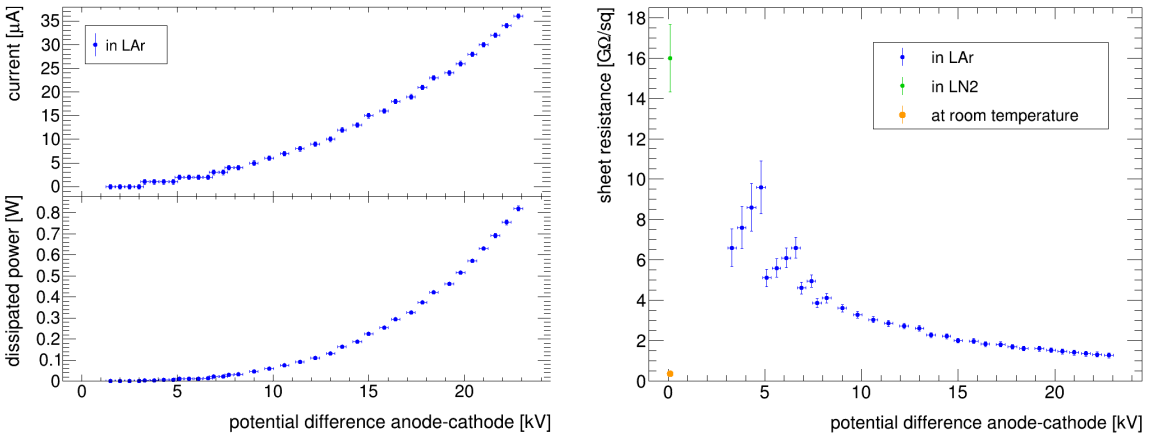

Figure 5.8: Electrical properties of the RS-TPC. Left: The current draw and the dissipated power of the shell as a function of the applied cathode bias voltage. Right: The shell's sheet resistance as a function of the cathode bias voltage. A temperature dependence of the sheet resistance is apparent. Due to the limited resolution of the used HV power supply, the uncertainties for low cathode bias voltages are relatively large.

Since cosmic muons on average produce straight ionisation tracks in a LArTPC, their charge signals can be used to characterise the uniformity of the electric field within a TPC on a statistical basis. For this reason, a selection of cosmic muon candidate tracks were analysed. The results are summarised here, but more details are provided in Appendix A.2, or [72]. In particular, a sample of 280 muon candidate tracks without delta rays or other particle candidates were selected, and a Principal Component Analysis (PCA) applied on those hits. The residual distance from every hit position to the principal component was determined as a function of the hit position in the RS-TPC. The results showed small residual distances of $\mathcal{O}(0.1\,\mathrm{mm})$, which are largest close to the resistive shell and close to the anode or cathode. Those residuals are most likely due to the slightly bent electric field lines originating from the steel frames providing the RS-TPC structure (see Appendix A.1). The analysis indicates that the resistive shell shapes the electric drift field as desired.

In conclusion, the small number of components in the design of the RS-TPC field shell reduce the potential number of failure points during operating the TPC at high bias voltages. Measurements investigating the electrical properties of the resistive shell showed that the technology is suitable for applications requiring low power dissipation. Compared to a conventional field cage with a resistor chain, the resistive shell with its larger surface area minimises the heat load per unit area. It thus reduces the local boiling of the noble liquid.

[6] SL130PN150 from Spellman, https://www.spellmanhv.com (accessed: 11.07.2021).

5.1.3 SingleCube

The SingleCube LArTPC was the first ArgonCube prototype which combined a pixelated charge readout and an ArCLight module within a relatively large LArTPC. The TPC support structure is based on G-10, and the cathode plane and the field cage consist of 3.5 mm thick, commercially available, PCBs with gold-plated copper circuitry. The field cage is made of 60 strips, each with a height of 3.5 mm at a spacing of 1.5 mm. Neighbouring strips are electrically connected via four parallel 100 MΩ SMD resistors, one row of resistors soldered at each edge of the field cage. The first and the last strips are connected to the anode and the cathode, respectively, using resistors equivalent to 13.5 MΩ and 9 MΩ. Thus, the total electric resistance between the anode and the cathode corresponds to ≈ 1.5 GΩ. The field cage encloses a volume with a footprint of approximately 33 cm × 33 cm. Figure 5.9 shows the SingleCube cathode plane with the four PCBs of the field cage during the TPC assembly. Furthermore, a pixelated anode plane and an ArCLight module for the charge and light readout, respectively, are shown.

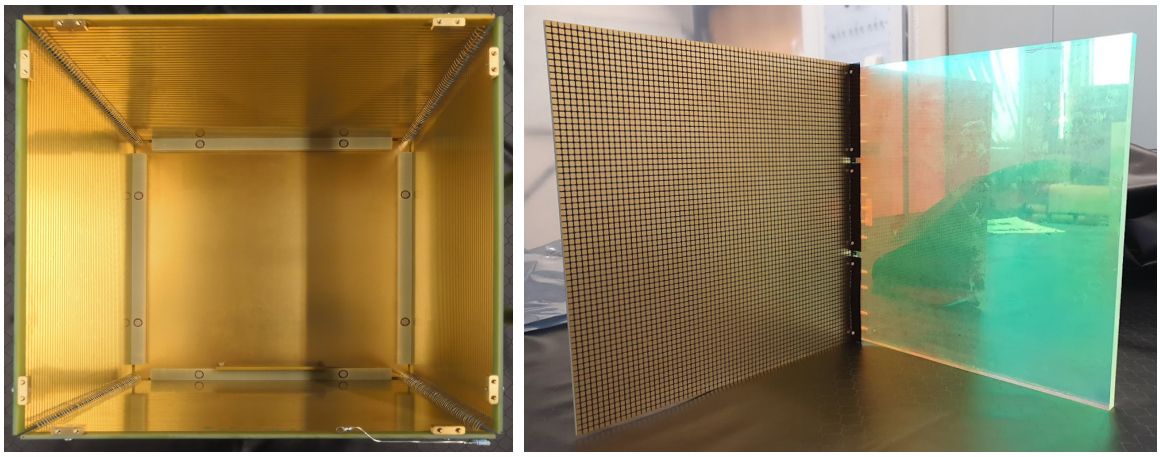

Figure 5.9: Mockup of the SingleCube LArTPC. Left: The TPC field cage consists of four plates, each with 60 gold-plated copper strips printed on 3.5 mm thick PCBs. The cathode is made of a single PCB with a printed layer of gold-plated copper. Right: The SingleCube TPC was instrumented with a pixelated anode plane designed for the Module-0 detector described in Section 5.1.4. For the light detection system, a Module-0 ArCLight panel was used. The SingleCube design would allow for employing three Module-0 LCM panels instead of one ArCLight panel.

The dimensions of the SingleCube field cage and cathode plane were chosen such that the same charge and light detection systems as designed for the Module-0 detector, described in Section 5.1.4, can be used. The pixelated anode plane is instrumented with 10 × 10 LArPix-V2 ASICs, described in Section 4.3, hosting 70 × 70 pixels in total, each with a size of 4 mm × 4 mm at a pitch of 4.434 mm. The active area of the pixel plane is 30 cm × 30 cm, and the maximum TPC drift distance is 30.2 cm, corresponding to an active mass of about 40 kg. For the detection of the LAr scintillation light, an ArCLight panel as described in Section 4.4 but with a dichroic instead of a specular mirror on the back was employed. Six SiPMs[7] are optically

[7] MPPC S13360-6050PE from Hamamatsu, https://hep.hamamatsu.com (accessed: 07.06.2021).

coupled to the 30 cm × 28 cm × 1 cm large ArCLight bulk structure. The ArCLight module could be easily replaced by three LCM modules as designed for the Module-0 prototype. The signals from the SiPMs were fed to the external trigger input of the charge detection system , allowing for triggering the LArTPC on the LAr scintillation light produced by particles crossing the TPC. The whole electronics chain was tested, and the SingleCube TPC was assembled in October 2020 at the University of Bern. Figure 5.10 shows how the ArCLight module is inserted into the SingleCube field cage, and Figure 5.11 depicts how the SingleCube LArTPC is mounted on the top flange of the ≈ 300 l cryostat used to perform the experiment.

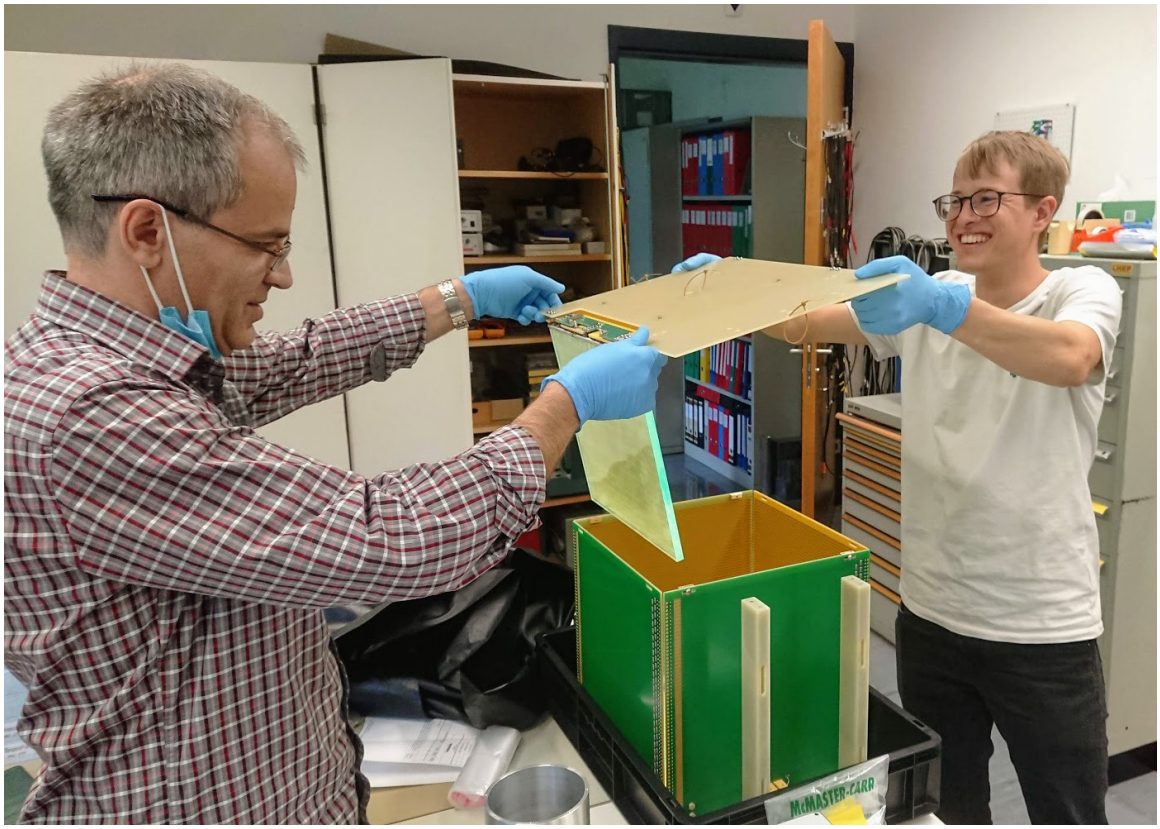

Figure 5.10: Installation of the charge and light readout system in the SingleCube TPC. The dielectric bulk of the ArCLight module is employed within the TPC electric field applied between the cathode and the pixelated anode plane.

As described in Sections 3.3.1 and 3.3.2, a stable and reliable TPC operation requires a high LAr purity. To purify the LAr, a Barber-Nichols[8] pump installed below the SingleCube TPC was used. The pump enables the circulation of the LAr from the bottom of the cryostat through vacuum insulated stainless steel hoses to an external filter and back into the cryostat where the LAr is released above the TPC. The external filter was designed for the ArgonCube 2x2 Demonstrator, described in Section 5.1.5. It contains two filter materials, a molecular sieve[9] and a copper

[8] A BNLNG-01B-000 for the SingleCube and the Module-0 experiments, which was replaced with a HEP-36-000 for the ArgonCube 2x2 demonstrator. Both pumps from Barber-Nichols, https://www.barber-nichols.com (accessed: 08.06.2021).

[9] RCI-DRI 4A Mol-Sieve from Research Catalysts, https://www.catalyst-central.com (accessed: 08.06.2021).

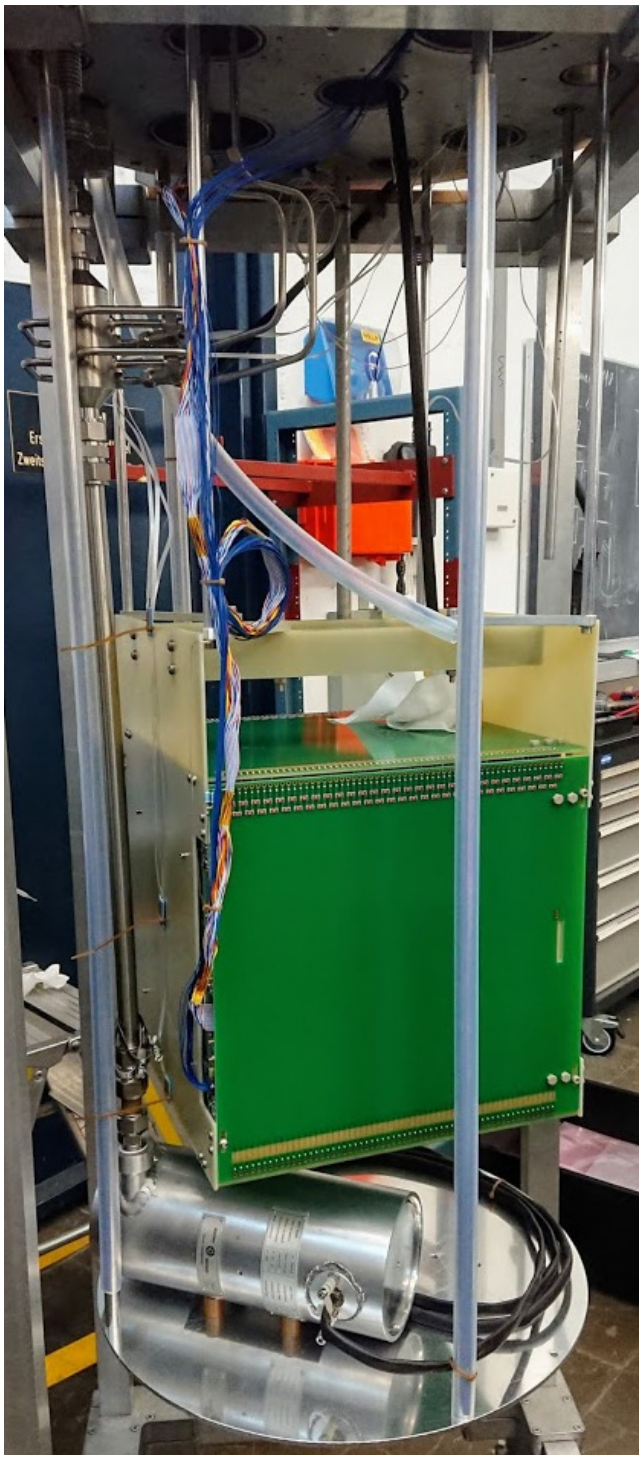

Figure 5.11: Installation of the SingleCube TPC on the top flange of the LAr cryostat. The LArTPC is mounted such that the drift field is oriented horizontally, with the vertical pixel plane located to the left side of the cube. One of the field cage's resistor chains is visible on the top edge of the SingleCube TPC. A Barber-Nichols pump installed below the SingleCube TPC is used for the circulation of the LAr from the cryostat through an external purification system and back into the cryostat.

catalyst[10], both with a volume of 10 l. The filter design is based on the system used in MicroBooNE [102], [103]. At the filter outlet, a 5 µm cartridge from GKN[11] is used as a particulate filter. To provide not only LAr purification but also cooling, the filter was immersed in a cryostat filled with LN_2 and pressurised[12] to about 2.4 bar. Figure 5.12 shows the LAr filtration system used in the experiments.

The main goal of the SingleCube experiment was to demonstrate the feasibility of combining signals from the light and the charge readout system for a reliable TPC operation and event reconstruction. In particular, the experiment was used to show how well the scintillation light signals can trigger the charge readout system. Furthermore, the SingleCube experiment was intended to test the new design of the external LAr filtration system as mentioned above.

In October 2020, the SingleCube LArTPC was operated for 5 days, with drift field intensities ranging from 0.1 kV cm^{-1} to 1.0 kV cm^{-1}. The external LAr filter was used for purification and cooling of the LAr. The cooling power of the filter was enough to completely seal the LAr cryostat at a resulting overpressure of $\approx$ 380 mbar with respect to atmospheric pressure. During the DAQ, many cosmic induced particle interactions within the TPC were detected.

The SingleCube experiment demonstrated the successful combination of light and charge signals using the systems developed by the ArgonCube collaboration. 95 % of the charge readout channels were operational, and the embedding of light triggers in the charge data showed to be feasible. If operated in self-triggered mode, the pixelated charge readout showed about 90 % overall trigger efficiency for MIP like signals. An analysis of cathode-anode-crossing tracks was performed to estimate the electron lifetime in LAr, which turned out to be close to 1 ms. A pixel-wise pedestal and electron lifetime correction was applied on the charge data, and the pixel responses was calibrated using cosmic muon candidate tracks. Figure 5.13 shows the pixelated charge readout system's flat response as a function of the track orientation. The variation of this response is < 3 % across the full 4π coverage of the LArTPC [104].

[10] Q-5 Copper Catalyst from Research Catalysts, https://www.catalyst-central.com (accessed: 08.06.2021).

[11] SIKA-R 5 from GKN Powder Metallurgy, https://www.gknpm.com (accessed: 09.06.2021).

[12] LN_2 at atmospheric pressure has a boiling temperature which is below the freezing point of LAr. Pressurising LN_2 to 2.4 bar increases its boiling point such that the LAr in the filter does not freeze.

Figure 5.12: LAr filtration system as designed for the ArgonCube 2x2 Demonstrator and used in the SingleCube and Module-0 experiments. The LAr filter is immersed in a pressurised ($\approx 2.4\,\mathrm{bar}$) LN_2 cryostat to provide not only purification but also LAr cooling. Left: A schematic view of the filter shows the two filter materials, a molecular sieve (blue) and a copper catalyst (green). A $5\,\mu\mathrm{m}$ GKN cartridge (black) at the filter outlet is used as a particulate filter. Right: A picture showing the green vacuum insulated LN_2 cryostat hosting the LAr filter inside. A custom made liquid level-meter, as well as pressure and temperature sensors, are used to drive two PID (proportional–integral–derivative) controlled LN_2 pneumatic valves (blue) to maintain a constant LN_2 level at the requested temperature.

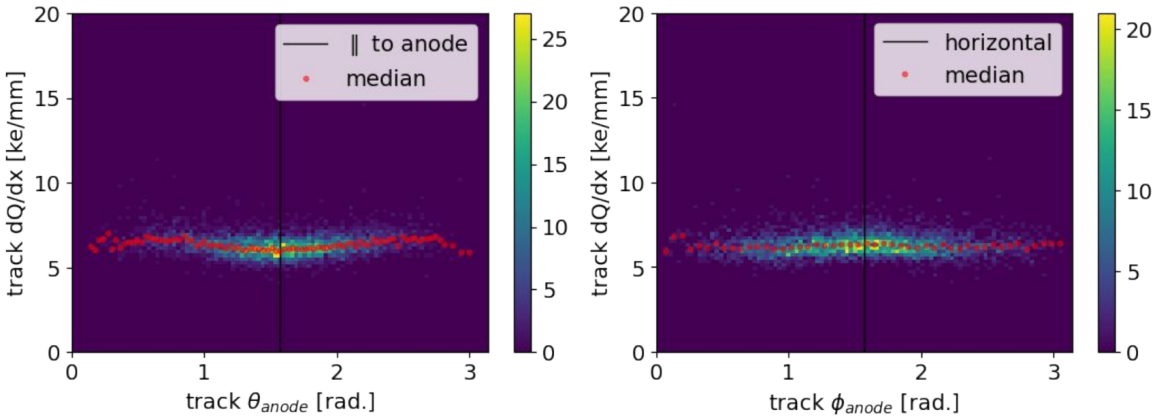

Figure 5.13: The pixelated charge readout system as employed in the SinglCube LArTPC enables a flat response as a function of the track angle. θ_{anode} denotes the absolute value of the azimuthal angle and ϕ_{anode} is the absolute value of the zenith angle with respect to the pixelated anode plane. [104]

5.1.4 Module-0

The Module-0 prototype is a small-scale version of the ArgonCube module as designed for the DUNE ND-LAr detector. With an active LAr volume of 30.2 cm×60 cm×120 cm per TPC, the total active mass of Module-0 corresponds to about 600 kg. As described in Section 4.2, an FR-4 sheet covered on both sides with a layer of 25 µm thick Kapton XC serves as the cathode plane. The field shell consists of four 6 mm thick FR-4 panels laminated with 100 µm thick duPont Kapton DR8 sheets loaded with electro-conductive carbon black. The maximum drift length in Module-0 is 30.2 cm. Figure 5.14 depicts the resistive field shell and the cathode plane of the Module-0 prototype.

In Module-0, the ArgonCube light and charge readout systems are employed for the first time within a resistive field shell. Furthermore, Module-0 is the first detector that makes use of the resistive shell technology to shape a large volume of about 0.43 m^3. Figure 5.15 shows the components needed to instrument one out of the two LArTPCs of the Module-0 prototype. Fully instrumented, the Module-0 detector hosts

- 16 charge readout tiles, each with an active dimension of 30 cm × 30 cm and 10 × 10 LArPix-V2 ASICs hosting 70 × 70 pixels with a size of 4 mm × 4 mm at a pixel pitch of 4.434 mm, 78 400 pixels in total.
- 8 ArCLight modules, each with 6 SiPMs (Hamamatsu S13360-6050PE) optically coupled to the bulk with dimensions of 30 cm × 28 cm × 1 cm.
- 24 LCM tiles as described in Section 4.4, each with 2 SiPMs (Hamamatsu S13360-6050PE) optically coupled to the bunch of fibres and with dimensions of 10 cm × 28 cm × 1 cm.

An engineering drawing of the Module-0 detector is shown in Figure 5.16, with the LAr operation filling level indicated with a blue surface. The detector is inserted into a cylindrical cryostat with an inner diameter of 98.8 cm and 208 cm height, corresponding to a volume of about 1.6 m^3. The LAr purification system is the same as described in Section 5.1.3 and consists of 10 l molecular sieve and 10 l copper catalyst in a filter

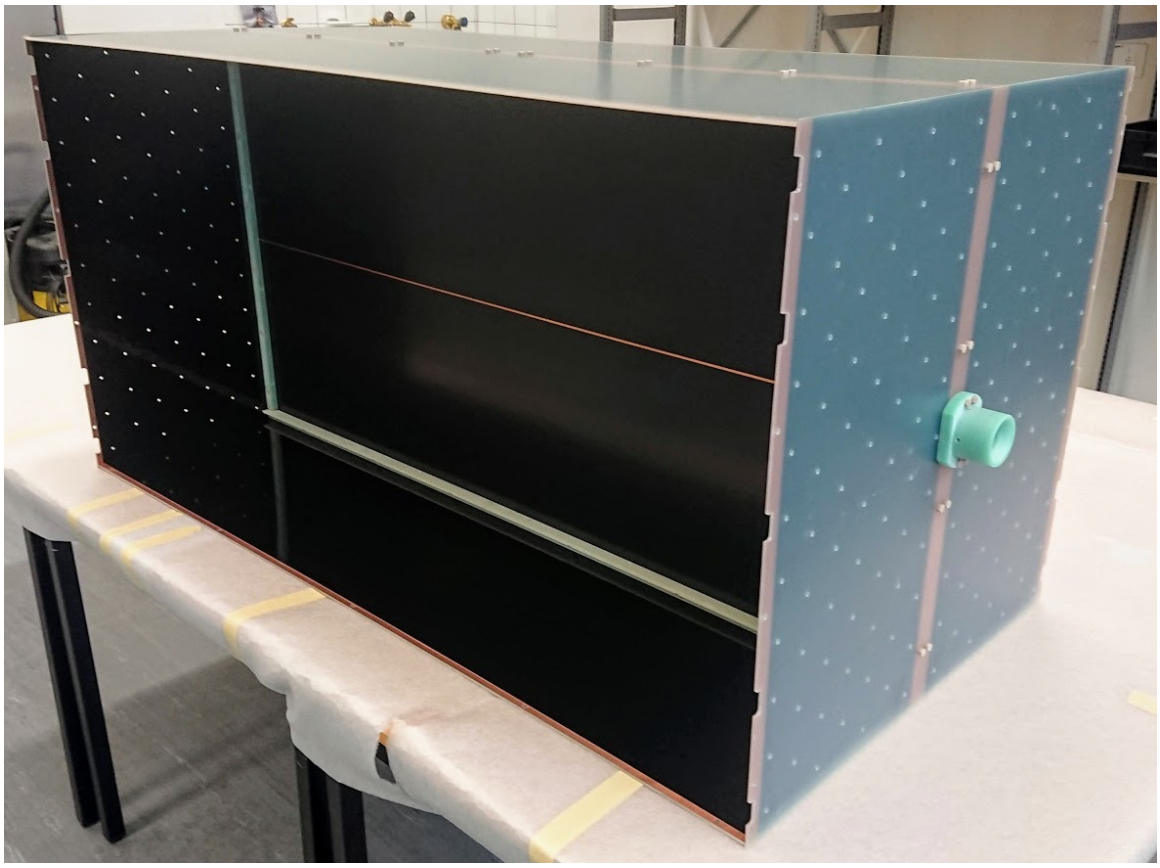

Figure 5.14: Picture of the resistive field shell and the central cathode plane of the Module-0 prototype. The HV cable is connected to the green socket on top of the module (on the right side of the picture). To allow for an adequate flow of LAr through the active TPC volume, the top and bottom plates are perforated with 148 holes with a diameter of 4 mm. The pixelated anode planes (not visible in this picture) will be installed on the open side(s) of the Module-0 detector. With an active volume of about 60 cm × 60 cm and a height of 120 cm, the active mass of one TPC corresponds to about 300 kg LAr.

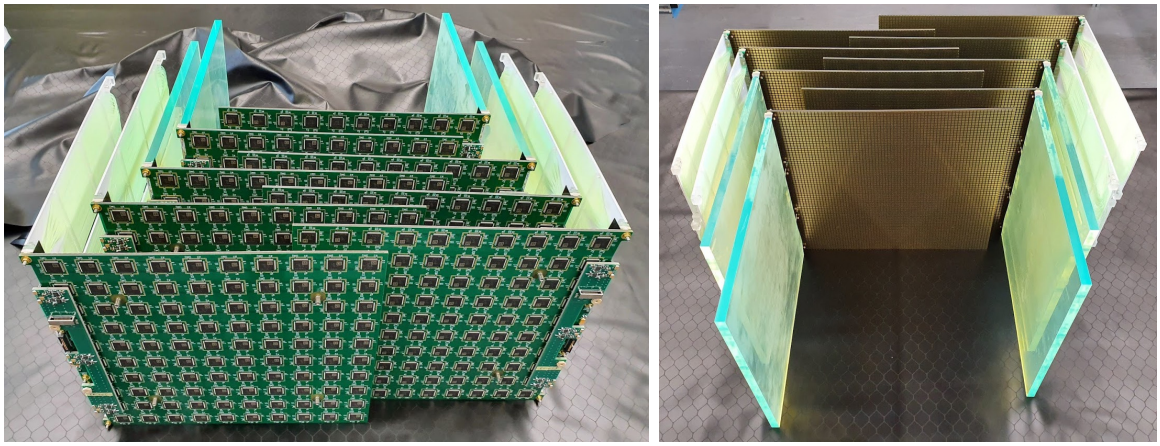

Figure 5.15: The charge and light detection systems used for the instrumentation of one of the two TPC in Module-0: 8 pixelated anode planes, 4 ArCLight modules, and 12 LCM modules.

cartridge immersed in a pressurised ($\approx 2.4\,\mathrm{bar}$) LN_2 cryostat. A dedicated grounding scheme was developed together with specialists from FNAL to ensure running the detector DAQ while the recirculation pump is in operation. A Barber-Nichols pump is used to extract LAr at the bottom of the Module-0 cryostat and to push it through the externally located filter. The purified and cooled argon is injected via a diffuser above each Module-0 TPC. The Module-0 prototype is designed to fit into a G-10 sleeve, shown in Figure 5.19, to enhance the flow of purified LAr through the module.

For a first experiment, Module-0 was partially instrumented with only one pixelated and 15 blank anode tiles, one ArCLight and three LCM modules. This experiment was intended for several tests. First, the experiment should show if the module structure is capable of holding the stress it is exposed to due to the significant temperature differences in LAr and at room temperature. Secondly, the experiment was designed to demonstrate if a sufficient LAr purity can be reached with the designed filtration system. The large surface of the Module-0 structure and the numerous cables in the setup posed the risk of spoiling the LAr purity such that the TPC charge and light signals become too weak for meaningful studies. Furthermore, the experiment was intended to test if the flow across the module through the perforated field shell is sufficient to reach the required LAr purity and to provide enough cooling to the electronics. Thirdly, the partially instrumented Module-0 experiment should demonstrate the functionality and stability of the HV system, the large resistive field shell, and the cathode plane at a nominal electric field intensity of $500\,\mathrm{V\,cm^{-1}}$. Finally, the experiment served as a platform to tune and optimise detector operation parameters such as the PID-controlled LN_2 cryostat hosting the LAr filter, the slow-control system, and the DAQ interfaces.

After the LAr cryostat was evacuated for three days, the residual pressure read $8.6 \times 10^{-5}\,\mathrm{mbar}$. The cryostat then was purged for four days in total, first with warm and then with cold Gaseous Argon (GAr) to cool down all the detector components at a low rate. During the LAr filling process, the temperature gradient across the Module-0 structure was kept small, less than $40\,\mathrm{K\,m^{-1}}$. With a mean cooling rate of about $15\,\mathrm{K\,h^{-1}}$, peaking at about $20\,\mathrm{K\,h^{-1}}$, the module structure and components shown to be stable with no observed damage. After the cryostat was filled with LAr, the partially instrumented Module-0 was continuously operated for 5 days in November and December 2020, with TPC drift field intensities ranging from $0.1\,\mathrm{kV\,cm^{-1}}$ to $1.0\,\mathrm{kV\,cm^{-1}}$.

The Module-0 cryostat was sealed to atmosphere and operated with about 400 mbar overpressure. The LAr recirculation ran continuously at a rate of about $100\,\mathrm{l\,h^{-1}}$, which was close to the maximum limit of the recirculation pump. Since the cryostat of the ArgonCube 2x2 Demonstrator will be larger and populated with four Module-0 detectors, higher heat input is expected. Thus the pump will be replaced with one providing a larger throughput[13]. At the nominal TPC drift field intensity of $0.5\,\mathrm{kV\,cm^{-1}}$, the HV system and the resistive field shell performed as desired. Increasing the electric field intensity to $1.0\,\mathrm{kV\,cm^{-1}}$ revealed some instabilities observed at the HV power supply unit. The applied cathode bias voltage sometimes dropped a few hundred volts but recovered a few minutes later. The electrical properties of the field shell were determined during the experiment, at a LAr temperature of about 91.5 K. With an applied cathode bias voltage of 15.1 kV, corresponding to $0.5\,\mathrm{kV\,cm^{-1}}$ drift

[13] A Barber-Nichols HEP-36-000, from https://www.barber-nichols.com (accessed: 08.06.2021).

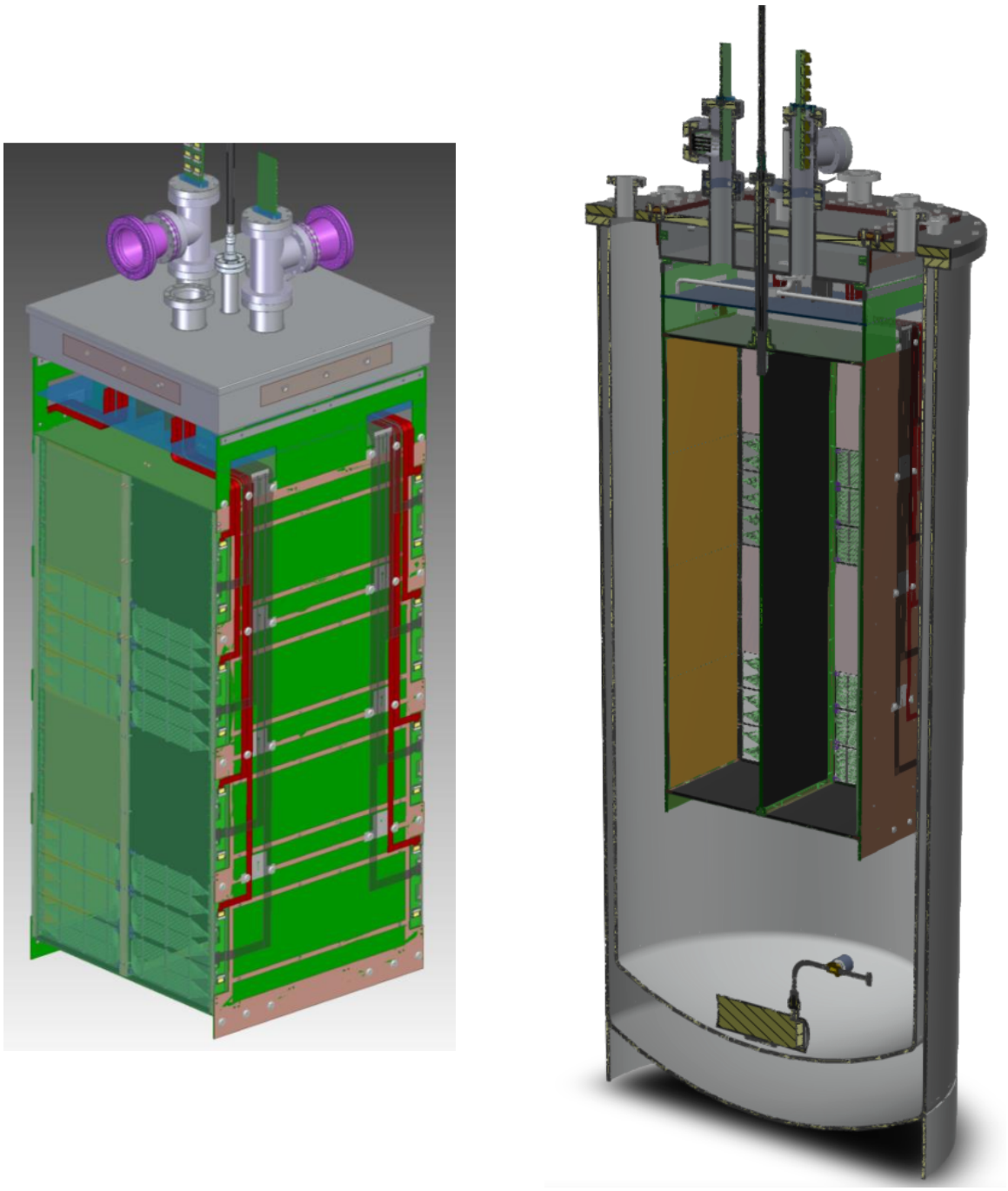

Figure 5.16: Engineering drawings of the Module-0 prototype. Left: Four ArCLight modules and twelve LCM modules are partially visible in the plane facing to the left side. Since this plane is drawn with some transparency, the central cathode plane splitting the Module-0 into two independent LArTPCs and parts of the pixelated anode plane are visible. Red lines correspond to the cables related to the light and charge detection systems. The grey top flange is vacuum insulated to reduce heat leaking into the cryostat. The blue surface indicates the LAr filling level during the detector operation. Right: The Module-0 as being installed in the cryostat. A Barber-Nichols pump, located at the bottom of the cryostat, is used to recirculate the LAr through an external filter (not visible in this figure). The purified and cooled LAr is injected through two diffusers on top of each LArTPC. For an improved LAr purification, a G-10 sleeve (not visible in this figure) can be installed around the Module-0 prototype. Courtesy of K. Skarpaas (SLAC).

field intensity, the current draw through the resistive field shell was determined to be 212 µA. Consequently, the total bulk resistance of the Module-0 field shell at nominal field intensity corresponds to about 71.2 MΩ, or for a single TPC about 142.5 MΩ. With a TPC aspect ratio of $L/W = 0.302\,\mathrm{m}/(2 \cdot (0.660 + 1.200))\mathrm{m} = 0.081$, or 0.041 for the entire Module-0, the sheet resistance of the field shell was estimated to be $1.75\,\mathrm{G\Omega\,sq^{-1}}$.

Cosmic induced particle interactions within the LArTPC were detected. Figure 5.17 shows the charge detected at the pixelated anode plane as a function of the reconstructed z coordinate, corresponding to the drift direction. An exponential fit through the data points was used to estimate the electron lifetime according to Equation 3.22. The result indicated a lifetime of $\mathcal{O}(1\,\mathrm{ms})$, which fulfilled the requirements defined before the start of the experiment.

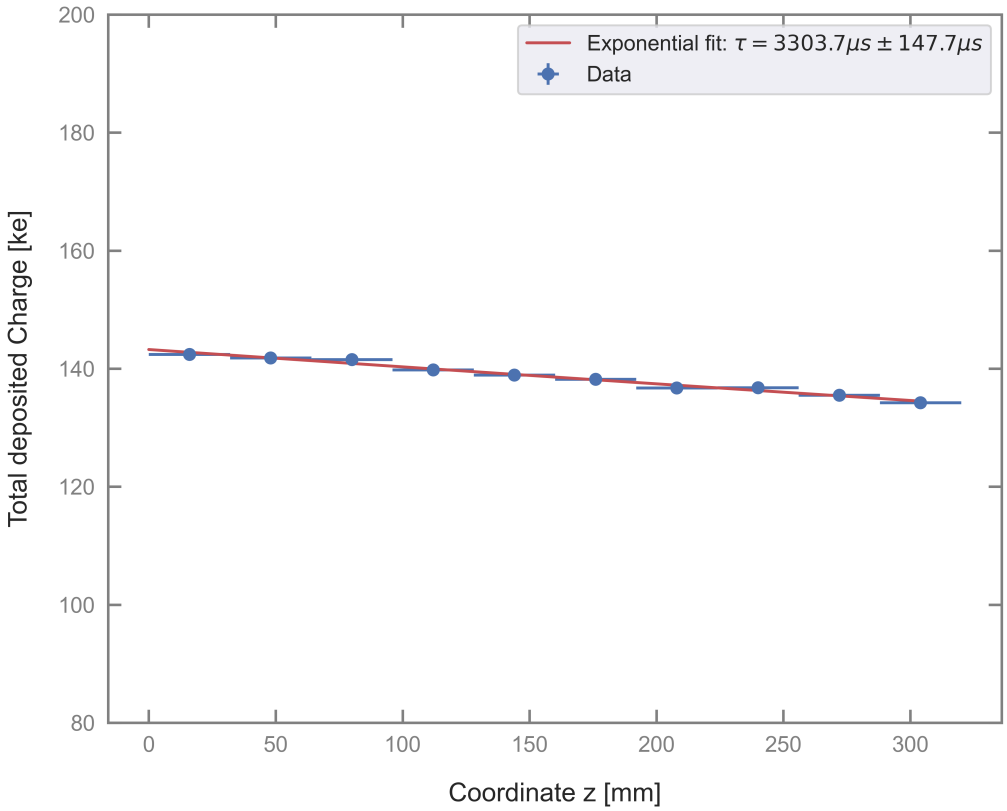

Figure 5.17: Estimated electron lifetime in the partially instrumented Module-0 detector using a single data run with a duration of 20 min. The electric field intensity during this data run was set to $0.4\,\mathrm{kV\,cm^{-1}}$. The plot shows the mean detected charge at the pixelated anode plane as a function of the reconstructed z position in the TPC, corresponding to the drift time.

After the partially equipped Module-0 showed the desired performance, it was fully instrumented with 16 pixelated anode tiles, 8 ArCLight modules, and 24 LCMs. Figure 5.18 shows the assembly of the fully instrumented Module-0, which happened in March 2021. Figure 5.19 depicts the fully instrumented Module-0 without and with the G-10 sleeve, designed to allow for an improved LAr flow across the module.

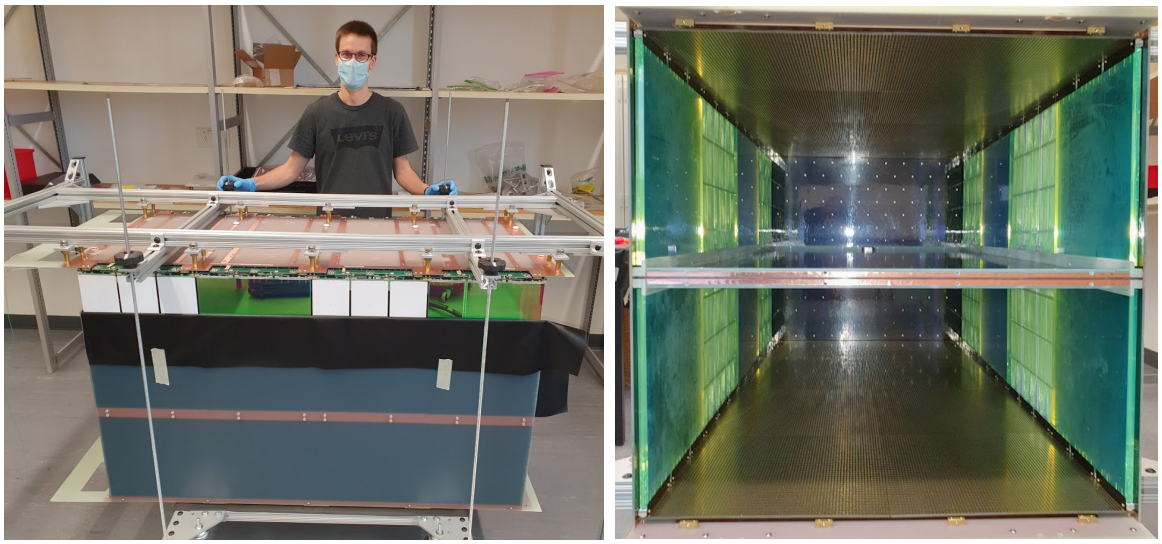

Figure 5.18: Module-0 during the assembly process. Left: A Module-0 half-detector, consisting of 8 pixelated anode planes, 4 ArCLight modules, and 12 LCMs, is carefully inserted into the resistive field shell. The black foil is used to prevent scratching the resistive field shell or the back of the photon detectors. Right: After the insertion of both half-detectors, the picture was taken from the bottom of the module with the bottom plane of the resistive field shell removed.

In March 2021, the fully instrumented Module-0 was operated in LAr for 10 days. Similar to the previous experiment, the cryostat was evacuated for two days until a pressure of 4×10^{-5} mbar was obtained. Afterwards, the vessel was flushed with GAr. A gas chromatograph, described in Section 5.2.4, measured an O_2 content of about 10 ppm in the gaseous argon. This relatively high level of oxygen contamination has been attributed to the permeability of the Perfluoroalkoxy Alkane (PFA) tubes connected to the gas chromatograph. The cooling process of the detector took less than one day, with an average cooling rate of about $15\,\mathrm{K\,h^{-1}}$, peaking at $25\,\mathrm{K\,h^{-1}}$, and the filling with LAr took another day. With the LAr recirculation running, the cryostat was sealed at an overpressure of about 100 mbar with respect to atmospheric pressure. Following three days of detector calibration, the DAQ run for seven days. Afterwards, the cryostat was emptied using the recirculation pump connected to a LAr exhaust line. The detector warm-up took two more days, using electric heaters and a warm GAr supply line.

The experiment demonstrated that the cooling power provided by the LAr filtration system is sufficient to take the total heat input originating from the electronics and the cryostat walls. In addition, the stability of the fully instrumented Module-0 structure, the resistive field shell, and the HV system were demonstrated to be feasible. 6×10^7 of cosmic induced LArTPC events were detected, at 19 different electric field intensities ranging from $0.05\,\mathrm{kV\,cm^{-1}}$ to $1.00\,\mathrm{kV\,cm^{-1}}$. Figures 5.20, 5.21, and 5.22 show Module-0 event displays of cosmic induced particle interactions within the

Figure 5.19: Fully assembled Module-0 and insertion into the LAr cryostat. Left: The Module-0 is bolted on the vacuum insulated stainless steel pillow of the top flange, supported by an aluminium frame. Right: The Module-0 detector, inserted into the G-10 sleeve to enable an improved LAr recirculation, is ready to be placed in the LAr cryostat.

detector. These event displays show, respectively, candidates for a muon producing delta rays, a muon decaying to a Michel electron, and an event with multiple particles originating from an interaction vertex. The data shown correspond to the raw pixel data where only a pixel-wise pedestal correction was applied. Further calibration to perform more sophisticated calorimetry and PID are in progress. The event displays demonstrate that the signals acquired with the pixelated anode tiles can be used to reconstruct ambiguity-free 3D LArTPC events at a low noise level and across two independent LArTPCs. Apart from the muon decay candidate, the tracks qualitatively describe straight lines indicating that the electric field is shaped rather well across the volume containing more than 400 l of LAr. A quantitative analysis of the electric field uniformity using cosmic muon candidate tracks is in progress.

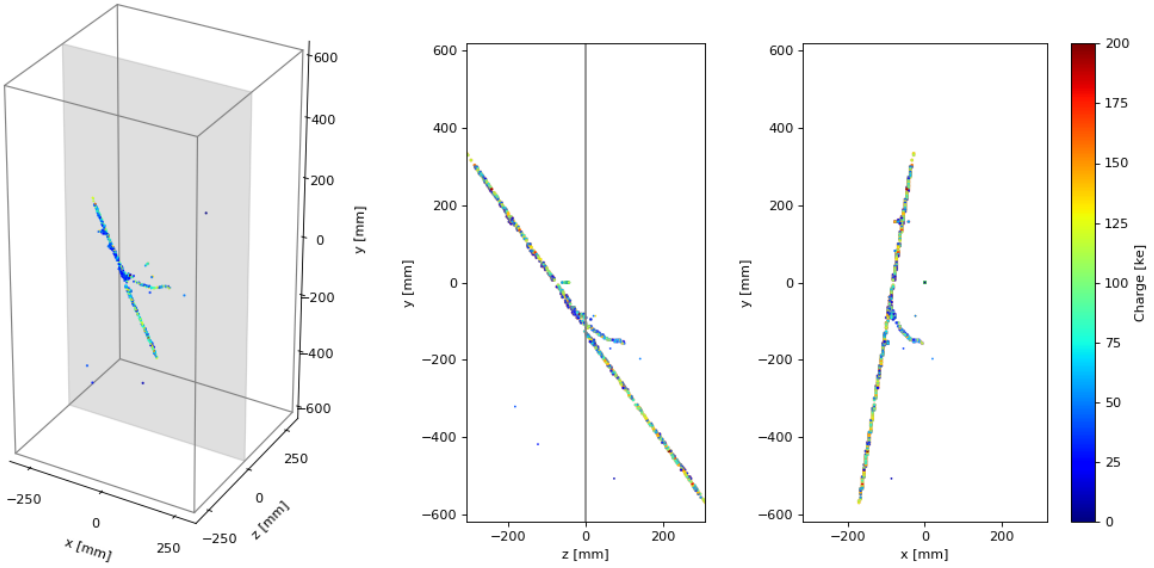

Figure 5.20: Module-0 event display with a candidate of a cosmic muon with two or three delta ray candidates. The grey plane or line at $z = 0\,\text{mm}$ indicates the cathode plane. The ionisation electrons drift along the z coordinate axis. The event display shows raw data with a pixel-wise pedestal correction only. No optimisation or correction were applied to the data.

The electron lifetimes in LAr were estimated for individual data runs, using anode-cathode crossing muon candidate tracks. As shown in Figure 5.23, the electron lifetime is roughly stable at about 2.5 ms. There was a tendency for it to increase during the run period which is ascribed to the LAr purification system which was continuously operated during the experiment.

The time resolution of the LCMs was estimated using the signals from the SiPMs of two neighbouring LCM modules, one from each Module-0 LArTPC. Figure 5.24 shows the standard deviations of the time difference distribution between these signals for five different intervals of light intensities, namely $0 - 50$ photo-electrons (p.e.), $50 - 100$ p.e., $100 - 150$ p.e., $150 - 200$ p.e., and $200 - 250$ p.e. The error bars denote the error of the corresponding standard deviations. Apparently, the LCM time resolution is a few ns, with better resolution at higher light signal intensities.

As described in Sections 3.2.2 and 3.2.3, the charge and light signals produced in a LArTPC depend on the applied electric field intensity and follow an anti-correlated behaviour. Figure 5.25 shows the detected amount of charge and light as a function of the applied electric field intensity in the fully instrumented Module-0.

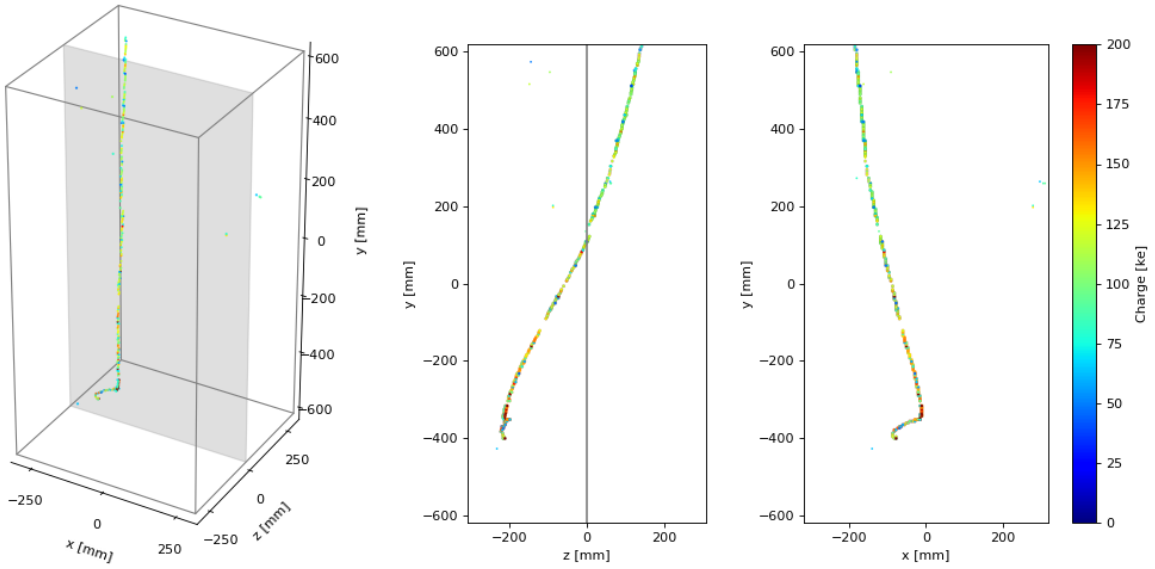

Figure 5.21: Module-0 event display with a candidate of a cosmic muon decaying to a Michel electron. This event display shows a candidate for a muon decaying to an electron and an invisible electron-neutrino. Close to the decay vertex, the muon candidate deposits more energy per unit length, which is visible as the *Bragg peak*. The grey plane or line at $z = 0\,\text{mm}$ indicates the cathode plane. The ionisation electrons drift along the z coordinate axis. The region at $y \approx -100\,\text{mm}$ corresponds to a region with high pixel thresholds or disabled channels. The event display shows raw data with a pixel-wise pedestal correction only. No optimisation or correction were applied to the data.

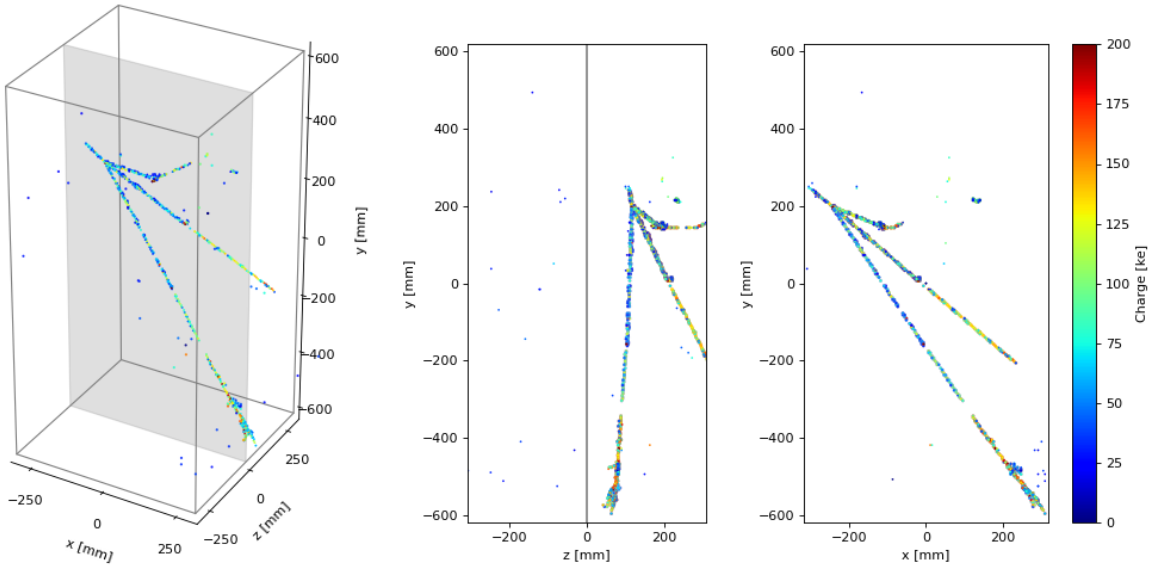

Figure 5.22: Module-0 event display with several cosmic induced particle trajectories. The grey plane or line at $z = 0\,\text{mm}$ indicates the cathode plane. The ionisation electrons drift along the z coordinate axis. The region at $y \approx -320\,\text{mm}$ corresponds to a region with high pixel thresholds or disabled channels. The event display shows raw data with a pixel-wise pedestal correction only. No optimisation or correction were applied to the data.

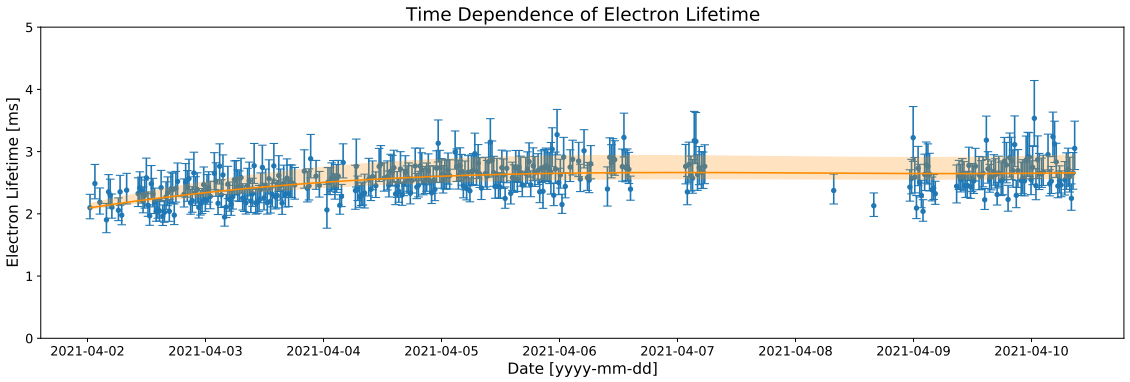

Figure 5.23: Estimated electron lifetime in the fully instrumented Module-0 detector using many data runs. To estimate the electron lifetime, anode-cathode crossing cosmic muon candidate tracks were used. The electron lifetimes are shown to be stable at about 2.5 ms, with a tendency to increase during the run period, which is ascribed to the continuous LAr recirculation. [105]

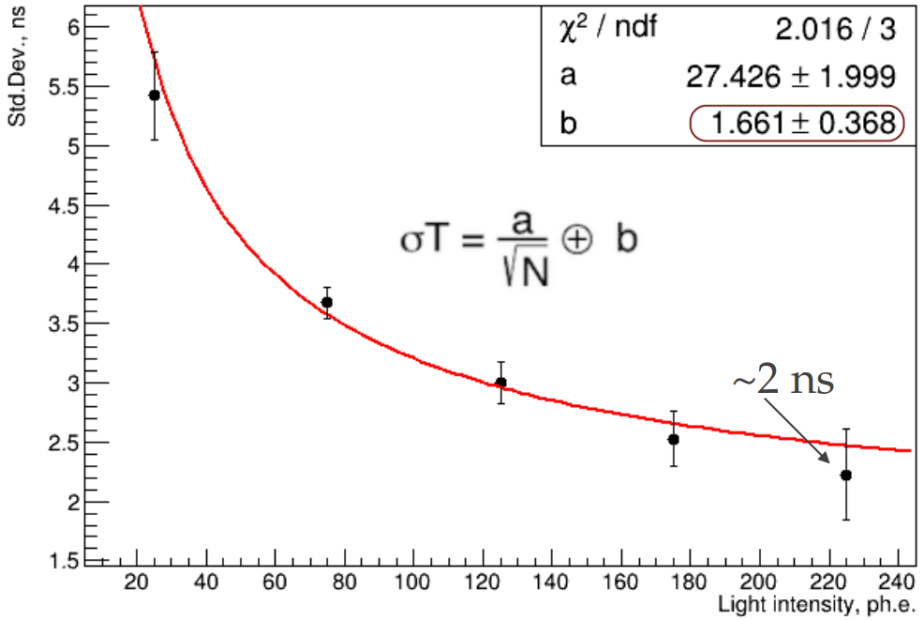

Figure 5.24: Time resolution of the LCM modules tested in the fully instrumented Module-0 experiment. This figure was produced using the time differences between two neighbouring LCM panels, one from each Module-0 TPC operated at an electric field intensity of 0.5 kV cm^{-1}. The data points show the standard deviations of time difference distribution between signals from two LCMs for five different intervals of light intensities, and the error bars denote the error of the corresponding standard deviation. The time resolution is a few ns, with better resolutions achieved for larger detected light signals. [105]

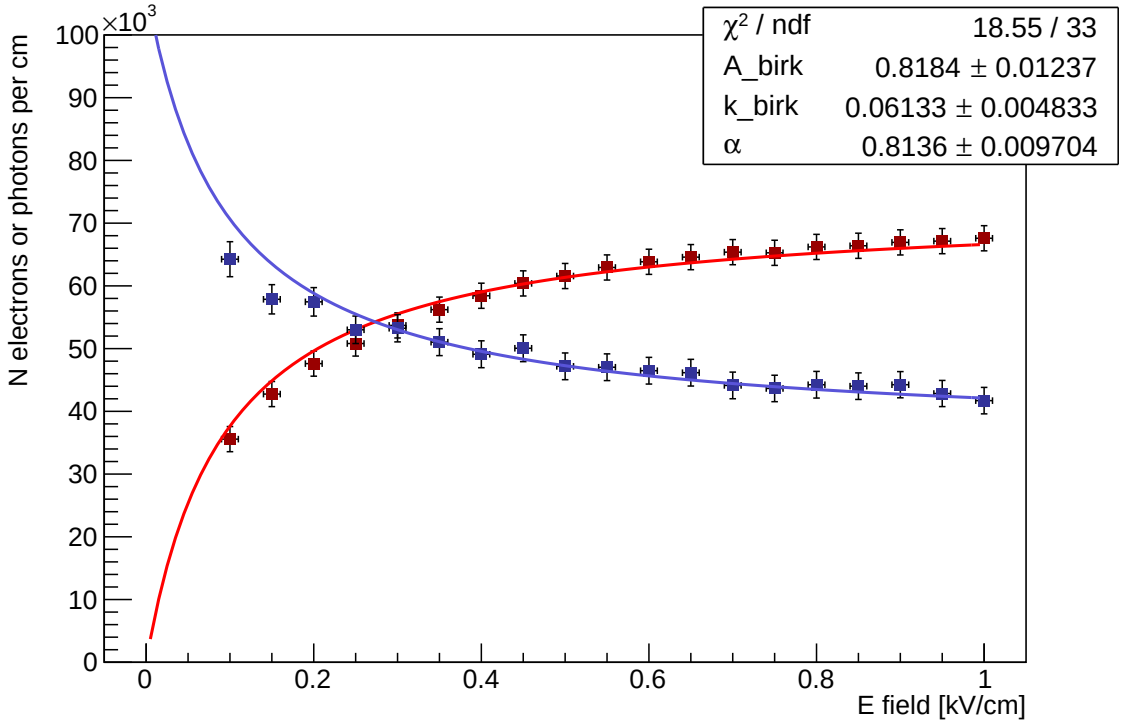

Figure 5.25: Module-0 light yield (blue dots) and charge yield (red dots) as determined at different electric field intensities. The blue and red lines correspond to the combined *modified Birk model* fits presented in Sections 3.2.2 and 3.2.3. The Module-0 data shows similar behavior as shown in Figure 3.2. [105]

The successful operation of the fully instrumented Module-0 allows to proceed with the instrumentation of the ArgonCube 2x2 Demonstrator described in the next Section 5.1.5.

5.1.5 ArgonCube 2x2 Demonstrator

The ArgonCube 2x2 Demonstrator will consist of a cryostat capable of hosting 4 Module-0 detectors arranged in a 2×2 array. This prototype represents the first detector that integrates multiple ArgonCube modules, combining all technologies developed during the ArgonCube R&D program, namely detector modularisation, a pixelated charge readout, the ArgonCube light detection systems, and the resistive field shell.

Each module has active dimensions of about $0.6\,\mathrm{m} \times 0.6\,\mathrm{m} \times 1.2\,\mathrm{m}$. Thus, the total active mass of the ArgonCube 2x2 Demonstrator corresponds to $\approx 2.4\,\mathrm{t}$.

The cryostat of the ArgonCube 2x2 Demonstrator is a vacuum insulated vessel with an existing LN_2 cooling system. It is cylindrical with an inner diameter of about 2.2 m and a height of $\approx 2.8\,\mathrm{m}$, corresponding to a volume of $\approx 10.7\,\mathrm{m}^3$. For the LAr purification, a custom made filter based on the MicroBooNE filter design was produced. The filter is located in a LN_2 cryostat, pressurised to $\approx 2.4\,\mathrm{bar}$, to provide LAr purification and cooling. More details about the filter design can be found in Section 5.1.3. Figure 5.26 shows an engineering drawing and a picture of the ArgonCube 2x2 demonstrator.

The ArgonCube 2x2 Demonstrator serves as a platform to evaluate the relative performance of multiple ArgonCube modules operating within a common LAr bath. In addition, the prototype detector is used to study the impact of inactive volumes on the event reconstruction. Inactive volumes, for example, are originating from the module walls and the electronics. In particular, the detector can be used to study the performance of calorimetry and PID in a modular environment, with particles crossing multiple LArTPCs and modules.

As depicted in Figure 5.27, the ArgonCube 2x2 Demonstrator was shipped in June 2021 to FNAL for the installation and operation in the Neutrinos at the Main Injector (NuMI) neutrino beam, where it will form the core component of the ProtoDUNE-ND, described in Section 6.4. Among others, ProtoDUNE-ND can be used to test the event reconstruction of neutrino interactions across multiple modules and multiple detector types.

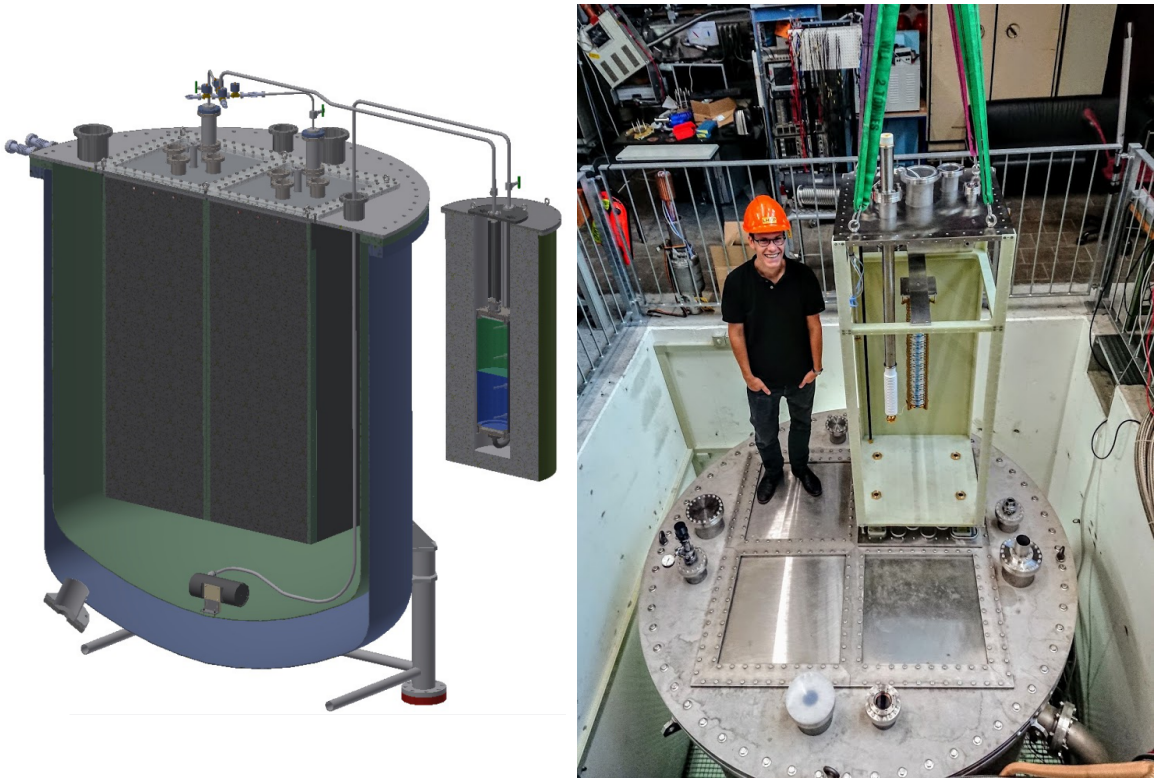

Figure 5.26: The ArgonCube 2x2 Demonstrator consists of a vacuum insulated cryostat capable of hosting four ArgonCube modules similar to the Module-0 prototype. The four modules share a common LAr bath. Left: Engineering drawing of the ArgonCube 2x2 Demonstrator. A Barber-Nichols pump, located at the bottom of the cryostat, is used to push the LAr through (vacuum jacketed) lines to an external filter. The filter, immersed in a LN_2 filled cryostat pressurised at about 2.4 bar, provides not only purification but also cooling of the LAr. The LAr then is injected on top of each LArTPC where it will supply purified and cooled argon needed for the TPCs to operate reliably. Right: Picture showing a physicist standing on top of the ArgonCube 2x2 Demonstrator. An early prototype of an ArgonCube module, instrumented with the V1PER TPC described in Section 5.1.1, is shown as well.

Figure 5.27: In June 2021, the ArgonCube 2x2 Demonstrator was prepared for shipping to FNAL. The picture shows the cryostat being loaded onto a truck in front of the LHEP, University of Bern.

5.2 Slow-Control

For a safe and reliable operation of the ArgonCube prototypes described in the previous Section 5.1, the framework of this thesis allowed for the development of a slow-control system to measure various hardware parameters like the temperatures at various locations in an experiment (see Section 5.2.1), the cryostat ullage pressures (see Section 5.2.2), and the LAr or LN_2 filling level in the cryostat (see Section 5.2.3). Furthermore, the knowledge about the concentrations and types of impurities present in the argon showed to be helpful, especially during piston-purging the cryostat and during the detector operations. For this purpose, a gas chromatograph was installed to analyse the amount and type of several traces of impurities in the GAr (see Section 5.2.4). A cryocamera was developed to acquire video information from the LAr (see Section 5.2.5). This camera was used to identify leaks in the G-10 module structure in an early ArgonCube module prototype.

The data collected with various sensors and devices was pushed to an InfluxDB[14] database set up on a local server. Several Grafana[15] dashboards, customised for every experiment or even sub-system, were set up to visualise the time series or current values of different parameters and to send alerts in the case of unexpected behaviour (see Section 5.2.6).

5.2.1 Temperature

To measure the temperatures of different detector components during the operation and the thermal cycles (cooling down and warming up), and of the LAr itself, the sensors employed need to reliably deliver measurements for temperatures ranging from about 80 K to 300 K. That was accomplished with standard resistance thermometers with an appropriate temperature range, such as platinum sensors[16].

The sensors were connected to an RTD sensor amplifier[17] using the 4-wire sensing method. To prevent out-gassing in the LAr, and especially in the GAr phase of the cryostat, cables based on Polytetrafluorethylene (PTFE) or a PTFE derivative were used whenever possible.

The communication with the RTD Sensor Amplifier was done using a Raspberry Pi 3[18] with the python scripts from [106]. The scripts running on the Raspberry Pi pushed the data directly to a local InfluxDB database from where it was accessed and visualised by the Grafana server, as shown in Section 5.2.6.

In later experiments, a Programmable Logic Unit (PLC) was used for the control of PID (proportional–integral–derivative) automated valves and safety alarms. For those safety-relevant applications, several thermocouple devices were used, for example, in the external LAr purification filter described in Section 5.1.3.

[14] https://www.influxdata.com (accessed: 11.06.2021).
[15] https://grafana.com (accessed: 11.06.2021).
[16] For example the PT100 Sensor P0K1.102.4W.B.010 from https://www.ist-ag.com (accessed: 11.06.2021).
[17] For example the PT100 RTD Sensor Amplifier from Adafruit, https://www.adafruit.com (accessed: 11.06.2021).
[18] A Model 3 B+, from https://www.raspberrypi.org (accessed: 11.06.2021).

5.2.2 Pressure

For measuring the pressures of the cryostat ullage volume, the ambient atmospheric pressure at the cryostat outer surface, or of the cryostat insulation vacuum, standard pressure gauges[19] were used in combination with the corresponding controller units[20]. To make the pressure measurements available for later use and for the visualisation with the Grafana interface (see Section 5.2.6), the controller units were connected to a Raspberry Pi that enabled remote communication with the controller units and pushed the acquired data to an InfluxDB database hosted on a local server. The python scripts used for the communication with the controller units can be found in [107], [108], and [109].

For the control of PID (proportional–integral–derivative) automated valves and safety alarms, a PLC was used to read the pressure values from the corresponding sensing devices.

5.2.3 Cryogenic Liquid Level

For measuring the cryogenic liquid filling level, capacitive cylindrical level-meters were designed based on the idea described in [110]. All materials were chosen to consist of either stainless steel or PAI to prevent out-gassing and ensure a high level of robustness over a large temperature range. Figure 5.28 depicts a $\approx 50\,\text{cm}$ long level-meter. For an improved accuracy over the whole range of the level-meter, the distance between the electrodes needs to be as uniform as possible. For this purpose, several spacer rings were mounted on the inner electrode. The spacer rings furthermore enabled calibration of the level sensor.

The communication and readout were achieved using a UTI evaluation board[21] connected to a Raspberry Pi. The software package from [111] was used to acquire the data and push it to an InfluxDB database or a PLC for further use.

For the R&D tests performed at LHEP, several level-meters of different lengths up to 2 m were employed in LAr or LN_2. The level-meters provided important information about the cryogenic liquid levels with a precision better than 5 mm.

5.2.4 Measuring Contaminations in Argon

To find possible sources of contamination or leaks in the systems used to test the LArTPC prototypes, a gas chromatograph[22] was set up to directly trace impurities such as H_2, O_2, N_2, CH_4, CO, and H_2O in GAr. The gas chromatograph was specified to be sensitive in the range from 50 ppm to 10 ppm for traces of impurities as mentioned earlier, with a relative accuracy of $\pm 1\,\%$.

To operate the gas chromatograph with various sample gas inputs, the gas flow

[19] For example the TPG 362 pressure sensor from Pfeiffer Vacuum, https://www.pfeiffer-vacuum.com (accessed: 11.06.2021).
[20] For example the TPG 362 controller unit from Pfeiffer Vacuum, https://www.pfeiffer-vacuum.com (accessed: 11.06.2021).
[21] The Universal Transducer Interface (UTI) Evaluation Board from Smartec, https://www.smartec-sensors.com (accessed: 12.06.2021).
[22] MultiDetek2 from LDetek, http://www.ldetek.com (accessed: 12.06.2021).

Figure 5.28: Capacitive level-meter with a length of about 50 cm designed for use in cryogenic liquids such as LAr and LN_2. The level-meter consists of two cylindrical electrodes made of stainless steel. Left: Partially assembled level-meter with outer electrode and top lid removed. Middle: The socket, the adjustable spacer rings, and the top lid are made of PAI. Cut outs in socket, spacer rings and top lid allow for cabling and a flow of the cryogenic liquid through the volume between the electrodes. Right: Fully assembled level-meter.

panel shown in Figure 5.29 was designed. A bottle with high-purity[23] argon gas provided the carrier gas for the chromatography. To improve the robustness of the obtained results, the gas panel provided purification of the carrier gas using a getter[24]. To detect the O_2 traces in gaseous argon, a designated chromatography column was installed. This column is required to be flushed every few measurement cycles with an O_2 doped argon carrier gas to maintain a high O_2 saturation level. Therefore, an additional line was added to the gas flow panel depicted in Figure 5.29.

The gas chromatograph allowed for continuous operation, with a duration of about 10 min per measurement cycle. The acquired data was pushed to a local InfluxDB database to be monitored graphically with a Grafana interface, as described in Section 5.2.6. Measuring the impurities in gaseous argon was particularly useful to monitor the cryostat piston-purge processes. Furthermore, it provided helpful information about the argon purity during the LArTPC operations allowing us to identify possible leaks in the cryostat sealings or elsewhere.

5.2.5 Cryocamera

A cryocamera was developed for the acquisition of video material when immersed in LAr. The used camera, a small cylindrical endoscope with an outer diameter of 8 mm and a length of approximately 4 cm, showed reliable operation only for temperatures between approximately −20 °C and 60 °C. To enable the camera operation in LAr, which has a temperature of about −190 °C, the camera chip was instrumented with a temperature sensor (see Section 5.2.1) and a thermistor directly mounted on the camera PCB. Instead of the standard camera housing, several layers of super-insulation were used to wrap the camera PCB into it. An infrared camera showed to be beneficial in finding heat leaks in order to optimise thermal insulation.

The insulated endoscope was inserted into a ≈ 7 cm long stainless steel hose with an outer diameter of 1.8 cm with standard CF-16 flanges welded at the end caps. All cables from the camera, from the temperature sensor, and from the thermistor were soldered to a standard CF-16 10-pin feedthrough[25] which sealed the end cap of the camera housing. The front of the camera was connected to a flexible CF-16 hose from a vacuum pump to remove the air present in the enclosure. After having evacuated the housing for several hours, the flexible CF-16 hose was removed under a nitrogen atmosphere to flush the volume with nitrogen which would not condense at the expected LAr temperature. In addition, several grains of silica gel were inserted into the camera enclosure to absorb residual humidity. A CF-16 flange with a borosilicate window[26] sealed the camera front. Figure 5.30 shows pictures of the developed cryocamera.

A python script [112] running on a Raspberry Pi enabled controlling the camera and acquiring videos. Furthermore, the script was used to read and control the temperature on the camera chip, using a transistor to control the current draw of the thermistor to keep the temperature within a defined range. An example Grafana dashboard used in the Module-0 experiment is depicted in Figure 5.31. Such dashboards

[23] Ultra High Purity (UHP) argon of grade 5.0 or higher.
[24] LDP-1000 from LDetek, http://www.ldetek.com (accessed: 12.06.2021).
[25] CF16-VB-1B-10 from Vacom, https://www.vacom.de (accessed: 12.06.2021).
[26] VPCF16B-K-1ALU from Vacom, https://www.vacom.de (accessed: 12.06.2021).

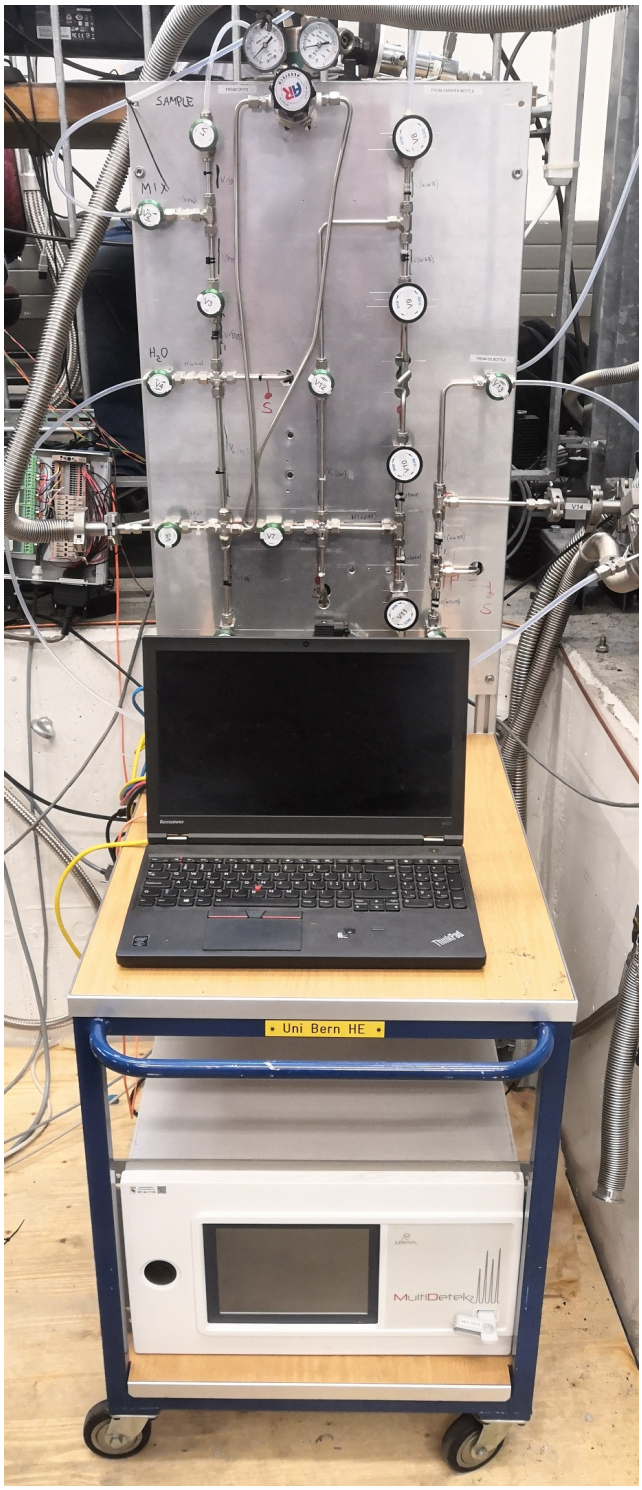

Figure 5.29: Movable gas chromatograph stem with the MultiDetek2 detector for the chromatography on the lower shelf, and a computer enabling control of the system. The gas flow panel at the back is used to sample from different argon sources, including the GAr phase of the Module-0 cryostat and a calibration bottle with known amounts of impurities in argon.

Figure 5.30: Cryocamera designed for use in LAr. Top: The camera is housed in a stainless steel tube with a length of ≈ 7 cm with standard CF-16 flanges welded at the end caps. Bottom left: Front view of the cryocamera, with a CF-16 borosilicate window. Bottom right: Rear view of the cryocamera, showing the CF-16 10-pin feedthrough.

were used to monitor the camera chip's temperature and stream the video material acquired with the cryocamera. Using two of these cryocameras in several experiments helped to find weak points in the experiments, e.g. leaks in the G-10 module structure or GAr bubble production due to boiling in LAr.

5.2.6 Grafana Interface

Grafana is a powerful web application to interactively visualise the data collected with the various sensors described above. It allows easy access to data stored in a database, e.g. InfluxDB, and to apply basic calculations or operations on the data, such as taking the derivative, integrate, or aggregate time series. Furthermore, Grafana enables streaming from a web camera. To safely operate the prototype detectors described in Section 5.1, several alerts and warnings were implemented in Grafana to be sent to mobile phones or other communication platforms.

Figure 5.31 shows an example of a dashboard used in an experiment to test the performance of the Module-0 prototype described in Section 5.1.4. The data shown in the dashboard time series (middle column) corresponds to the entire experiment's duration, covering about 21 days.

Figure 5.31: Example of a Grafana dashboard for monitoring various hardware and related parameters during the Module-0 experiment. The Grafana interface allows for visualising data in numerous ways, including basic operations and aggregations on the input data sets. For example, derived quantities such as change rates, integrated values, mean values, and many more can be displayed. Furthermore, streaming pictures from web cameras and sending alert messages to mobile phones is possible.

Chapter 6

ArgonCube Application in the DUNE Experiment

This chapter focuses on the application of the ArgonCube concepts in DUNE, a next-generation long-baseline neutrino-oscillation experiment currently under construction in the USA. An overview of DUNE and its scientific goals is given in Section 2.3.1. A ND with the capability to precisely measure neutrino interactions within the high-multiplicity environment close to the neutrino source is required to fulfil those goals. Section 6.1 summarises the demands on the DUNE ND, and Section 6.2 elucidates why ArgonCube would fit very well an application in the ND. The requirements on the ND strongly guided its design, which is presented in Section 6.3. In the framework of this thesis, I was involved in the design of a medium-scale ArgonCube prototype, called ProtoDUNE-ND, which will be employed in a neutrino test beam to show the feasibility of the ArgonCube concepts. Details about ProtoDUNE-ND can be found in Section 6.4. This chapter closes with Section 6.5 describing the potential application of the ArgonCube concept in the fourth DUNE FD module.

6.1 Requirements on the DUNE Near-Detector

The primary purpose of the DUNE ND is the measurement of the initially unoscillated ν_μ and ν_e energy spectra, and that of the corresponding antineutrinos. Furthermore, the ND needs to measure the neutrino-argon interaction cross section to predict the observations at the FD. Typical quantities to be predicted are the number of neutrino interactions and the interaction type as a function of the neutrino energy. It is desirable to employ – at least partially – the identical target material, LAr, and similar detection techniques in the ND and the FD to reduce systematic uncertainties on those predictions. That will improve the sensitivity to nuclear effects and detector-driven systematic uncertainties when extracting the oscillation signal at the FD. Therefore, the use of a LArTPC in the ND is strongly motivated.

For neutrino-nucleus cross-section measurements with the ND, it is vital to acquire data with enough statistics covering the entire phase space of neutrino energy and interaction type. Therefore, an ND-LAr component must have reconstruction capabilities comparable or exceeding those of the FD. The spatial resolution of the LArTPCs thus must be equal or better than the spatial resolution of the FD, which will be $\leq 4.7\,\mathrm{mm}$. To reduce systematic uncertainties, the electric field intensity in the ND-LAr component should match the drift field in the FD, which will be $\geq 250\,\mathrm{V\,cm^{-1}}$, with the goal of $500\,\mathrm{V\,cm^{-1}}$.

The LAr-component of the ND needs to completely contain the relevant event

topologies across the whole neutrino phase space, e.g. where hadrons originate from the interaction vertex. Also, its active size must be large enough to provide high statistics of $\geq 10^8$ ν_μ CC interactions per year on-axis, and its active volume must be large enough to provide good hadron containment. Muons with momentum higher than about 0.7 GeV likely will not be contained in the LAr volume. For the reconstruction of the incoming neutrino, the muon momentum is a substantial quantity, and thus a muon range stack or a muon spectrometer is needed downstream of the ND-LAr component. The spectrometer must be capable of measuring the charge and the momentum of the muons, thus it is desirable to have it magnetised.

Since the ND will be operated close to the very intense (anti)neutrino source it will be facing a high-rate environment with an expected rate of roughly 10 interactions per 100 t of LAr and per 10 µs beam spill. Since the beam spill duration is considerably smaller than the readout window of LArTPCs, typically of $\mathcal{O}(100\,\mu s)$, all interactions from the spill will effectively occur instantaneously. The charge readout system of the ND-LAr component thus must be capable of delivering high-accuracy 3D images within the high-rate environment to mitigate overlapping ionisation traces from separate neutrino interactions. Mitigating such pile-up events is important as the association of particles to the wrong interaction vertex results in a bias in the reconstructed neutrino energy and can yield an incorrect classification of the neutrino interaction type. Correctly associating tracks to a neutrino vertex if the tracks are connected in the vertex should not be difficult. However, the association of detached energy depositions to individual neutrino vertices can be very challenging, especially if the chunks of energy depositions are small and suffer from an imprecise direction estimation. Therefore, a high-accuracy charge-light signal association within volumes $\leq 3\,m^3$ needs to be enabled, demanding for a photon detection system with spatial information and a time resolution ≤ 20 ns.

6.2 Motivation for ArgonCube in the DUNE Near-Detector

The requirements on the DUNE near-detector highly motivate the use of a LArTPC in the ND. However, such a ND-LAr component needs to fulfil several challenging demands, e.g. the capability of delivering high-resolution 3D images within the high-multiplicity environment at the ND site as well as the spatially precise association of charge and light signals within the large detector volume.

The ArgonCube concepts presented in Chapter 4 provide a reasonable choice for the fulfilment of those requirements. With the modular detector design, almost any size can be accomplished without losing precision in particle tracking and calorimetry (see Section 3.3 for effects limiting the resolution of a LArTPC). For example, short drift distances that go along with modularisation allow for less stringent requirements on the LAr purity. Also, electron diffusion processes play a sub-dominant role and have almost no effect on the detector's spatial resolution.

Short drift distances furthermore enable a stable and safe TPC operation with drift field intensities up to a few hundred $V\,cm^{-1}$ at relatively low cathode bias voltages. Also, the stored energy within the drift field is reduced, which imposes a lower risk for damage in the case of an electric breakdown. The highly resistive field shell reduces the number count of components in the TPC and therefore reduces the possible points

of failure.

A pixelated charge readout system allows for native 3D particle tracking with unprecedented spatial resolution. The charge-collecting pixels allow for an unambiguous event reconstruction, which is particularly important for high-multiplicity environments as envisaged in the DUNE ND. The pixel's flat response as a function of a track's direction makes the pixelated charge readout an ideal device to be employed in high-rate environments.

The modular design enables contained scintillation light within modules. Hence, an accurate matching between charge and light signals is possible within volumes comparable to the module size. Using triangulation, the large-coverage and highly efficient VUV light detection system developed by the ArgonCube collaboration can be used to associate detached energy depositions to individual neutrino interaction vertices, allowing for a yet improved energy and event reconstruction.

6.3 The DUNE Near-Detector Design

Based on the requirements on the DUNE ND, the design as described in this section was elaborated during the last few years. The DUNE ND complex will include the following three main detector components:

- ND-LAr, a LArTPC based on the ArgonCube design, containing the same target nuclei as being employed in the FD.
- Near-Detector Gaseous Argon Component (ND-GAr), a high-pressure gaseous argon TPC surrounded by an Electromagnetic Calorimeter (ECAL) in a 0.5 T magnetic field.
- System for on-Axis Neutrino Detection (SAND), an on-axis beam monitor based on a lead/scintillating-fibre calorimeter in a 0.6 T magnetic field.

Figure 6.1 shows a schematic of the DUNE ND hall with those detector components. The first two components, the ND-GAr and the ND-LAr, can move up to 30.5 m off-axis[1] relative to the neutrino beam, allowing for a change in the neutrino energy spectrum. As the detectors move off-axis, the incident neutrino-flux spectrum changes and the mean neutrino energy spectrum becomes more narrow and peaks at lower energy. That allows for collecting data samples at different neutrino flux spectra, enabling the deconvolution of flux and cross-section uncertainties and the combination of different fluxes during the data analysis. In the on-axis position and at a beam power of 1 MW, about 15 neutrino interaction per beam spill are expected in the entire ND LAr component. Table 2.2 summarises the expected ND-LAr interaction rates for both, ν enhanced (FHC) and $\bar{\nu}$ enhanced (RHC) beam modes, in an event topology breakdown. In addition to the beam-induced interactions, the expected cosmic ray rate in the ND-LAr component is estimated to about 0.3 interactions per spill at a rock overburden of about 60 m in the ND hall. The ND-LAr component thus will be facing a high-multiplicity environment. SAND will be at a fixed position on-axis and is used to measure the neutrino energy spectrum as well as the neutrino flux.

[1] Corresponding to ≈ 50 mrad.

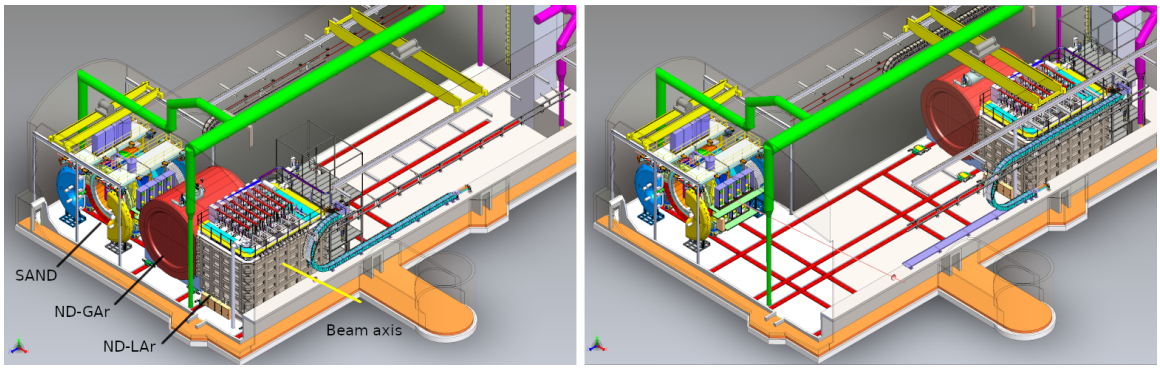

Figure 6.1: Schematic of the DUNE ND hall with its detector components all in the on-axis configuration (left) and with the ND-LAr and ND-GAr in an off-axis configuration (right). The SAND detector is installed in a fixed on-axis position. The yellow line indicates the beam axis. Courtesy of A. Bross (FNAL).

The following few sections will mainly focus on the ND-LAr component since this is the most relevant in the scope of this thesis. A full description of the DUNE ND can be found in [39].

The ND-LAr component was chosen to consist of an array of 5 (in beam direction) times 7 (transverse to the beam) ArgonCube modules, as indicated in Figure 6.2. This configuration is optimised to contain the complex hadron showers that can originate from a neutrino interaction in the liquid argon. Furthermore, this configuration allows for contained high-angle (side-ways going) muons and thus is fulfilling the requirements on the ND-LAr component (see Section 6.1). All modules share a common purified bath of LAr placed in a single membrane cryostat. The cryostat itself is installed on a movable platform which allows for moving the detector off-axis with respect to the (anti)neutrino beam, as depicted in Figure 6.1.

Figure 6.2 (left) shows a technical drawing of the ArgonCube module structure. Each module is based on a low-density cathode and a resistive field shell as described in Section 4.2, which reduce the amount of inactive material of and between the modules. The module structure is based on FR-4, which is opaque to VUV photons. Thus the scintillation light is contained in each module. That is particularly important in high-multiplicity environments since optical segmentation allows for an independent identification of (anti)neutrino-argon interactions employing the fast scintillation light detection system. The active dimension of each module is 1 m × 1 m (footprint) and a height of 3 m. Thus, the ND-LAr detector has an instrumented volume of 105 m^3, corresponding to an active mass of 147 t. An external HV system provides the cathode bias voltage for every single module. Furthermore, the power supplies and associated electronics for the charge and light readout systems are connected externally to the module top flanges. The two TPCs of a module are instrumented with a pixelated charge readout system with associated low-power electronics and a light detection system with a large area coverage and a very precise time resolution of about 2.3 ns, as described in Sections 4.3 and 4.4, respectively. The charge readout consists of 20 pixelated tiles per TPC, each of which with 80 × 128 square pixels with a size of 4 mm × 4 mm at a pitch of 4.434 mm. A signal-time bin-width of 2.5 µs corresponds to 4 mm in drift direction, assumed the electric field intensity is 0.5 kV cm^{-1}. Each TPC is instrumented with 10 ArCLight and 30 LCM modules. The two functionally identical, SiPM-based systems are ideal for the efficient detection of the VUV scintillation

photons over a large surface area. The LCM modules with their large PDE provide useful information for the energy reconstruction, and the ArCLight detectors deliver enhanced spatial resolution. Combining both systems not only provides accurate information about the time of particle interactions within the TPC but also helps to assign chunks of charge signals to individual neutrino interactions to overcome the pile-up in the high-rate environment. Their dielectric bulk structure enables the installation within the field-shaping structure without distorting the drift field. More details on specific detector components can be found in Chapter 4 or in [39].

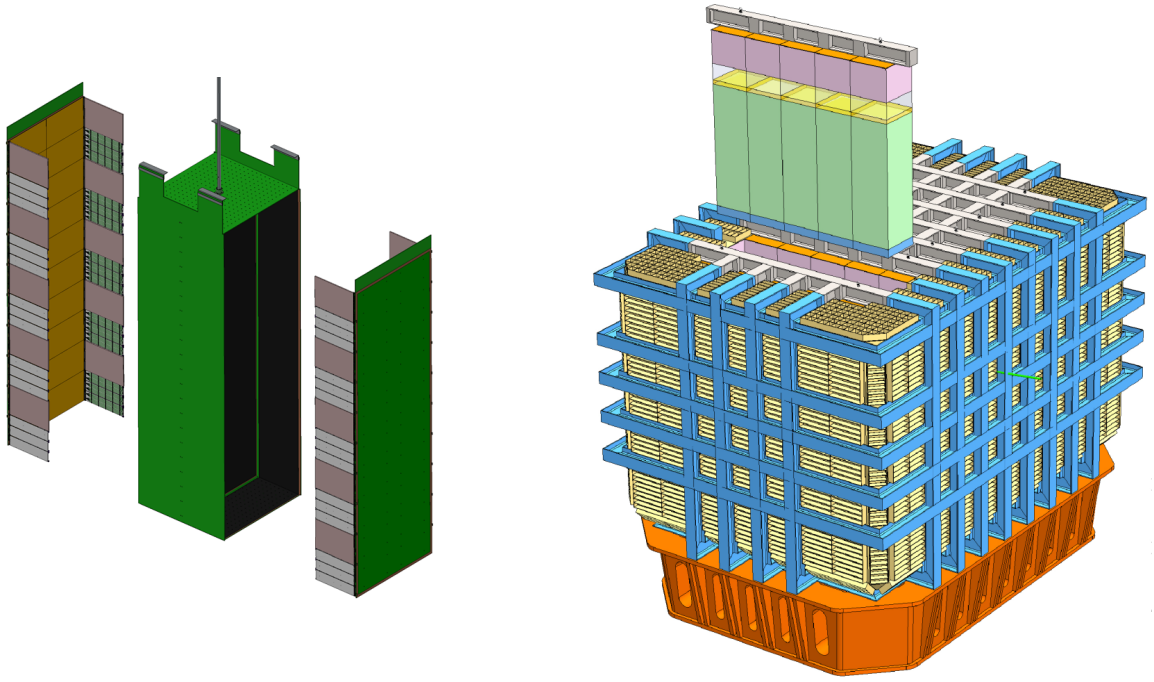

Figure 6.2: Components for the DUNE ND-LAr. Left: The technical drawing of an ArgonCube module shows the module structure and the components for both TPCs. Yellow areas correspond to the pixelated anode planes. Dark and light purple areas denote the ArCLight and LCM light detection systems. Right: The ND-LAr cryostat is designed to host 7 rows of 5 modules, each with active dimensions of 1 m × 1 m × 3 m. Courtesy of K. Skarpaas (SLAC).

6.4 ProtoDUNE-ND

As described in Section 5.1.5, the medium-scale prototype called ArgonCube 2x2 Demonstrator (here referred to as 2x2) was designed and constructed at LHEP, University of Bern. The 2x2 serves as a platform to test the scalability of all detector technologies developed within the ArgonCube collaboration. In particular, the detector will be used to demonstrate the feasibility and performance of ArgonCube concepts like modularisation, the pixelated charge readout, the large area-coverage light readout systems, and the resistive field shell for electric field shaping. Furthermore, the 2x2 detector will show how well signals from individual TPCs and modules can be matched to produce high-quality data for reliable event reconstruction.

In June 2021, the 2x2 was shipped to FNAL where it will be placed in the MINOS

ND hall to be exposed to the intense NuMI [113] (anti)neutrino beam. In combination with some modules from the Main Injector Experiment for ν-A (MINERνA) detector [114], the 2x2 will form the core of ProtoDUNE-ND [115]. Figure 6.3 shows the deployment of the 2x2 in the MINOS ND hall, with MINERνA panels up- and downstream of the 2x2. Scintillator planes from the MINERνA detector will be installed upstream of the 2x2 to enable tracking of beam-related particles produced outside of the 2x2. On the downstream side, the MINERνA EM calorimeter and several hadronic calorimeter planes will be placed to contain some of the EM and hadronic showers exiting the 2x2 detector.

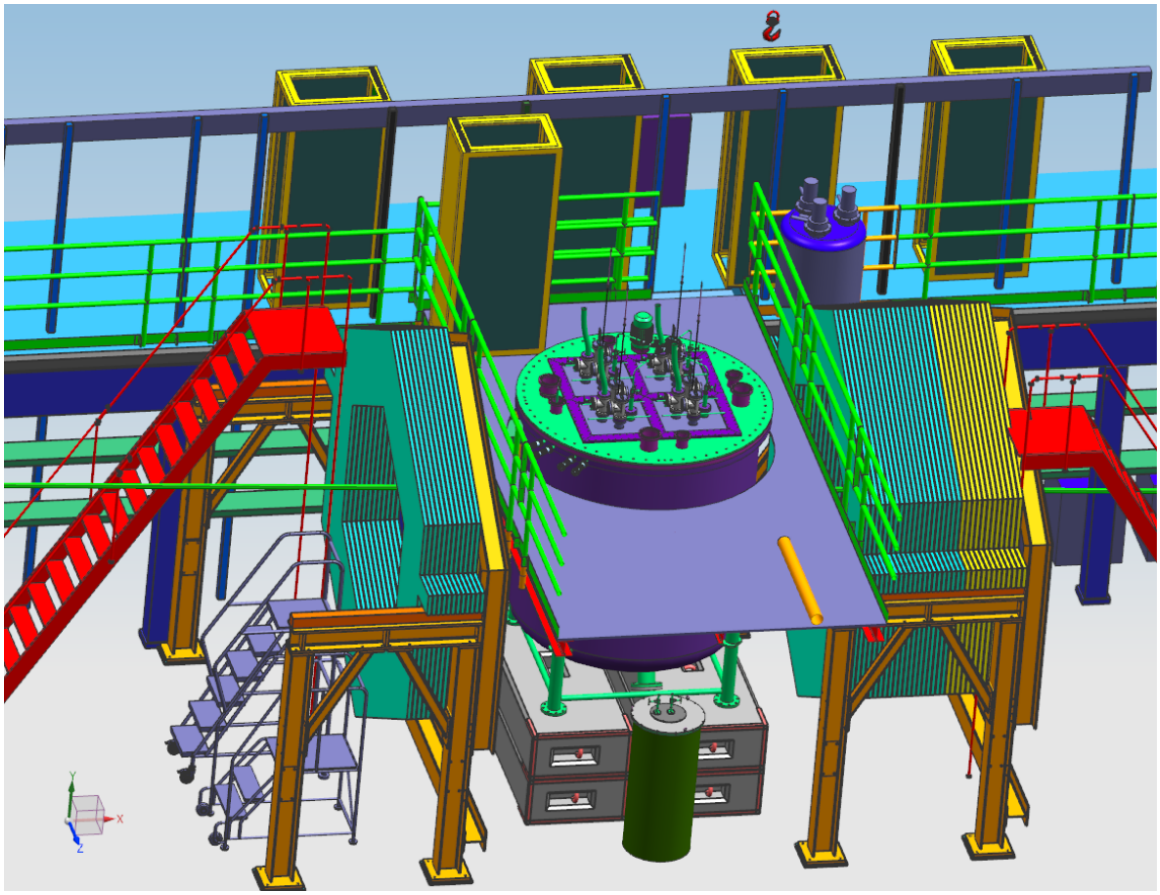

Figure 6.3: The ProtoDUNE-ND in the MINOS ND hall. The intense neutrino beam from NuMI is incident from the left. Parts from the MINERνA ND are located up- and downstream of the ArgonCube 2x2 Demonstrator. Courtesy of T. Miao (FNAL).

The goal of ProtoDUNE-ND is to study the ArgonCube module performance in response to the intense NuMI beam. Those studies are important in the view of the final design for the DUNE ND-LAr component as the modular approach of ArgonCube has never been tested on such a large scale. ProtoDUNE-ND will show how stable the ArgonCube components and cryogenics performs in the long term. Furthermore, ProtoDUNE-ND enables developing, testing and benchmarking event reconstruction techniques with LArTPC signals across several modules. The reconstruction of events in a modular environment is more complicated than in a monolithic TPC since the inactive module materials, e.g. from the module walls, the cathode, and the readout systems, correspond to gaps in the active detector volume. Consequently, the traces of ionising particles can be segmented, which might affect the accuracy of the PID.

Matching the ionisation traces across modules might be relatively simple for long tracks. However, for EM or hadronic showers, it can be very challenging. In addition to those studies, ProtoDUNE-ND can be used to test pile-up mitigation techniques in a high-multiplicity environment. In particular, ProtoDUNE-ND can show how well the ArgonCube components perform in a high-multiplicity environment and how well the charge and light signals can be combined under such conditions. As described in Section 6.1, the association of traces of energy depositions to an individual neutrino vertex is a crucial part for the DUNE ND-LAr component for pile-up mitigation. Furthermore, the experiment can be used to test track-merging from the LArTPC and the external MINERνA detector components, a task which will be very valuable in the view of merging ND-LAr and ND-GAr signals in DUNE.

The NuMI beam predominantly consists of (anti)neutrinos produced in the decays of secondary particles originating when the 120 GeV protons from the FNAL *Main Injector* hit a graphite target. Figure 6.4 shows the expected fluxes (left) and event rates (right) as a function of true (anti)neutrino energy for both locations, the DUNE ND hall and the MINOS ND hall. The NuMI beam peaks at about 6 GeV (anti)neutrino energy where the LBNF flux has its maximum at a lower value of about 3 GeV. As shown in Figure 6.4, the LBNF flux in the DUNE ND hall will be much more intense than the flux of NuMI in the MINOS ND hall. However, due to the increased (anti)neutrino interaction cross section at higher energies, the interaction rates in ProtoDUNE-ND are comparable to those expected in the DUNE ND-LAr. Figure 6.5 shows the expected number of MIP and Highly Ionizing Particle (HIP) particles originating from single (anti)neutrino vertices as simulated with Genie v2.12.10 [116]. Consequently, the scale of the reconstruction problem is similar for both detector types, and thus ProtoDUNE-ND is a reasonable choice for testing and benchmarking the event reconstruction currently in development for DUNE.

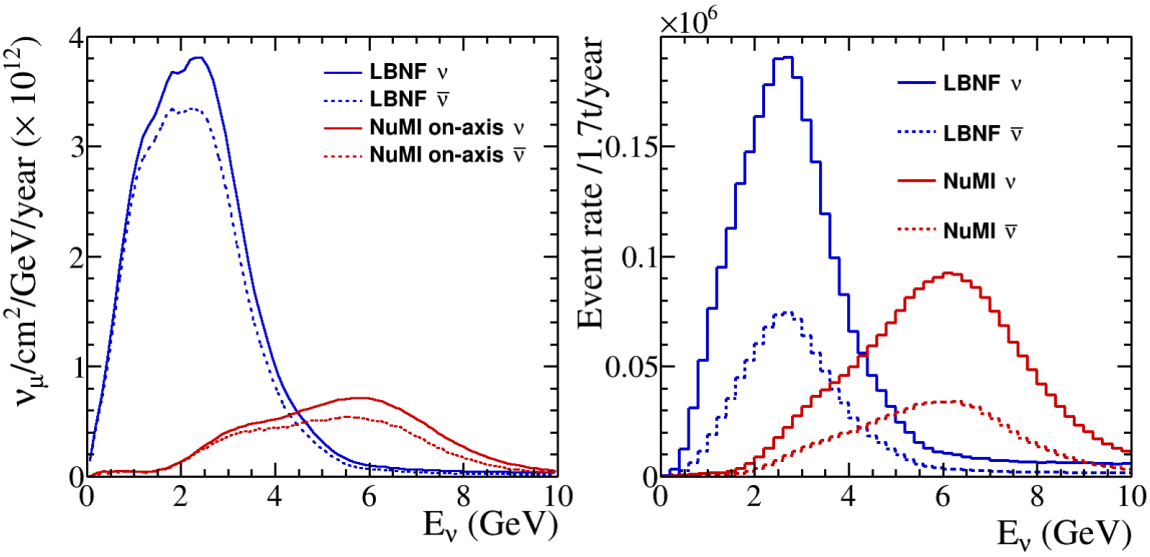

Figure 6.4: Expected (anti)neutrino fluxes and interaction rates as a function of the true (anti)neutrino energy for the LBNF and the NuMI beam lines. The expected interaction rates were normalised to a mass of the 1.7 t active LAr mass of the 2x2. [39]

In particular, ProtoDUNE-ND will be very useful to test and benchmark the neutral pion reconstruction developed in the framework of this thesis and discussed in Section 7.4. Figure 6.6 shows the primary π^0 multiplicity and the neutral pion

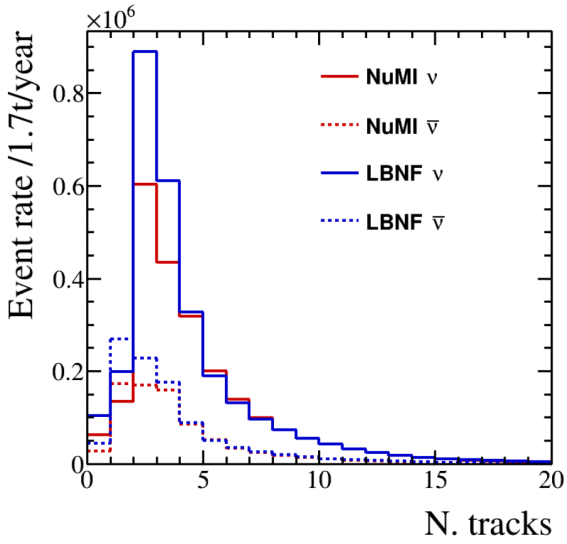

Figure 6.5: Expected number of events per year and per 1.7 t LAr for the LBNF and the NuMI beam lines. Here, the multiplicity is defined as the number of MIP and HIP particles originated from the true simulated (anti)neutrino vertex. [39]

momentum distribution for a LAr mass of 1.7 t exposed for one year to the LBNF and the NuMI beamlines. Several million neutral pions will be produced within ProtoDUNE-ND in a single year of exposure to the NuMI beam. Although it is expected that the vast majority of the neutral pion induced showers are not fully contained within ProtoDUNE-ND, the samples from the experiment will provide an opportunity for testing, tuning and benchmarking the π^0 reconstruction.

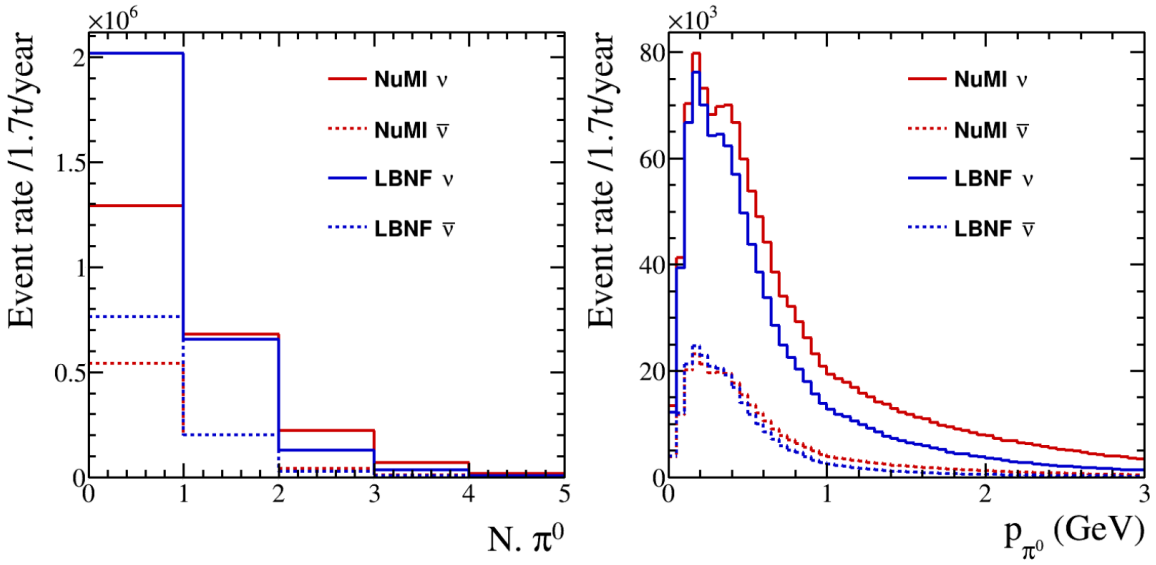

Figure 6.6: Expected neutral pion production rate (left) and the π^0 momentum distribution (right) per 1.7 t LAr exposed for one year to the LBNF and NuMI beam. [39]

6.5 Potential Application of ArgonCube in the DUNE Far-Detector

From the four proposed DUNE FD modules, three were assigned to single-phase or dual-phase LArTPCs, but the design of the fourth module has not yet been decided. In 2019, we proposed to apply the ArgonCube concepts on the fourth DUNE FD [117].

The application of ArgonCube concepts in the DUNE FD module would, first of all, reduce the risks and technical issues related to the very high cathode bias voltages required for the operation of LArTPCs with long drift distances and moderate electric field intensities of $\mathcal{O}(\mathrm{kV\,cm^{-1}})$. A segmented detector would significantly reduce the cathode bias voltage and, in turn, would decrease the amount of stored energy in the TPC.

In the aforementioned proposal, splitting the DUNE FD into 10 individual TPCs across the width of the detector was suggested. This would reduce the maximum drift length per TPC to 1.4 m, assuming the same overall detector dimensions as the proposed single-phase FD [46]. In this case, only 70 kV cathode bias voltage is required to maintain a drift field of $0.5\,\mathrm{kV\,cm^{-1}}$. To further minimise the risk of damage in the case of an electric breakdown, the stored energy within the TPC can be further reduced if the cathode planes are segmented in smaller pieces, with each cathode section electrically insulated from its neighbours. If the 58 m long cathode planes are segmented into twenty 2.9 m sections, the total stored energy (approximating the TPC as a parallel-plate capacitor) in the whole FD module would correspond to about 2 J, considerably less than the 100 J stored energy in the single-phase FD [117].

Using an array of ArgonCube modules requires a module structure with hadronic and EM interaction lengths comparable to LAr with as little as possible material budget for a maximised active detector volume. In ArgonCube, this has been achieved by using compound materials and a resistive field shell, described in Sections 4.1 and 4.2, respectively. The module walls would provide a robust dielectric layer around each module, protecting the inner TPCs in the case of an electric breakdown in a neighbouring TPC. In addition, the dielectric module walls would eliminate the need for a clearance volume around the LArTPC, improving the ratio of active to inactive detector volume.

The reduced maximum drift length in a modular FD design would reduce the requirements on the LAr purity as emphasised in Section 3.3. In addition, it would have a positive effect on the detection of the scintillation light since the module walls would contain these signals within modules, increasing the light readout system's sensitivity to the VUV photons. An enhanced sensitivity could be used for calorimetry and thus could increase the accuracy of the event reconstruction. Since the ArgonCube charge readout is based on a conventional PCB construction, the anode plane can be built with mechanically robust tiles. Compared to the wire-based charge readout systems commonly used in traditional LArTPCs, the pixelated PCBs would mitigate risk accompanied to a broken wire. Also, a pixelated charge readout would provide unambiguous 3D particle tracking, which is independent of the directions of the charged particles. Given the physics goals of DUNE described in Section 2.3.1, the pixel's flat response as a function of a track's direction would improve the quality of the collected data. For example, the (anti)neutrino energy reconstruction would be improved since the particle detection efficiency and calorimetry would be the same in all directions. In addition, pixels would improve the background detection efficiency,

which is crucial for the high-precision oscillation studies DUNE aims to perform. In the view of DUNE's program for solar neutrino searches where angular dependent effects are important, a pixelated charge readout would exceed the acceptance compared to traditional wire-based systems. Furthermore, pixels are ideal for use where the particle trajectories do not have a preferred direction, such as in supernova neutrino or proton decay searches.

Tests with the pixelated charge readout system showed that the power consumption is less than 100 µW per pixel. Assuming a pixel size of 4 mm × 4 mm, a power consumption of less than about 6.25 $\mathrm{W\,m^{-2}}$ can be achieved. Considering the large surface area over which the power is dissipated, this seems to be a tolerable value if sufficient cooling from a LAr recirculation system is provided.

Compared to projective wire readout covering the same area, a pixelated charge readout does not increase the bandwidth of the DAQ. The daisy-chain based data transmission from the cold electronics to the outside of the cryostat allows for as few as $\mathcal{O}(10)$ I/O lines at the feedthrough per $\mathrm{m^{-2}}$ readout plane. The digital DAQ data rate in the DUNE FD environment is expected to be only $\mathcal{O}(0.1\,\mathrm{MB\,s^{-1}\,m^{-2}})$, for which commercially available FPGA boards are more than sufficient.

The production cost for a pixelated charge readout is estimated to be $\approx 2000\,\$\,\mathrm{m^{-2}}$ for fully commercial ASIC, PCB production, and assembly. Assuming an instrumented area of about $\mathcal{O}(1000\,\mathrm{m^2})$, the charge readout system would cost about 2 million $.

Chapter 7

Event Reconstruction in LArTPCs

Even though a proper LArTPC event reconstruction is essential to extract particle physics results, I started to work on the event reconstruction for a different reason: Detector calibration. To be more specific, I intended to use the laws of particle physics to test and calibrate the energy reconstruction scale of LArTPCs. These sorts of calibrations are needed for precise calorimetric measurements, which affect the PID and thus the accuracy of the event reconstruction in LArTPCs.

Neutral pion decays are ideal candidates for the energy scale calibration since their reconstructed particle mass can be used as a standard candle. To reconstruct the mass of neutral pions (π^0) in a LArTPC, I used several ML techniques, described in Section 7.1. Especially for accelerator-based neutrino experiments which exploit high event rates, the development of a fast and automated event reconstruction of high quality is essential. For an accurate π^0 reconstruction, a good handle on particle showers is required. The shower reconstruction is briefly described in Section 7.2. The ability to separate electrons from photons is crucial, since electron-induced showers are a background for the neutral pion reconstruction. Section 7.3 describes a method for the electron-photon discrimination in LArTPCs. Finally, Section 7.4 is dedicated to neutral pions, including a description of the entire π^0 reconstruction chain and its performance. Section 7.5 draws possible next steps for the ML-based event reconstruction of LArTPC data.

7.1 Machine-Learning based Reconstruction Techniques

LArTPCs have excellent particle tracking and calorimetric capabilities, detector properties which result in high-resolution 3D images with a lot of information encoded in it. Those pieces of information can be used to perform a PID as described in Section 2.2.3. High-level variables like the reconstructed particle type, momentum, and energy, in turn, allow for a complete event reconstruction with interaction types, topology, and neutrino energy. This section describes how the ML-based event reconstruction in LArTPCs can be done using the full reconstruction chain presented in [118]. This reconstruction relies on the lartpc_mlreco3d repository maintained by the DeepLearnPhysics[1] collaboration and is available in [119]. The data samples

[1] https://github.com/DeepLearnPhysics (accessed: 15.07.2021).

used for the training and validation of the ML-based reconstruction are described in Section 7.1.1.

Instead of applying one (convolutional) neural network on the input image provided by the LArTPC, a chain of neural networks with different purposes is applied to reconstruct the event. Instead of using a single-step convolutional neural network to extract the neutrino type and energy from a LArTPC image (as done in [120]), a chain of neural networks with different purposes is applied to reconstruct the event.

Such a hierarchical reconstruction was chosen since the topologies of neutrino interactions in LAr are too complex and varied to be reduced to simple variables in one step. Furthermore, a hierarchical structure allows for a better understanding of possible points of failure at each reconstruction stage. If one of the networks, for whichever reason, makes a mistake, it is much easier to trace back where the failure happened in a hierarchical network than in a single-staged neural network. In a hierarchical reconstruction chain, every ML module can be trained separately and optimised together, which generally yields more robust results since the downstream networks can take account of the mistakes done in upstream elements. Furthermore, a single-staged neural network would cause severe problems when trying to directly predict the interaction type or the topology in a high-multiplicity environment as in the DUNE ND. There, piled-up neutrino interactions would dramatically affect the accuracy of a single-staged event reconstruction. Using a reconstruction chain based on multiple stages enables the division of the input image into individual neutrino interactions and thus is expected to perform significantly better.

For those reasons, the reconstruction was designed as a chain of several neural networks with the following structure: In the first step, a Convolutional Neural Network (CNN) is used for feature extraction on the pixel level [121], so-called semantic segmentation. The CNN in this stage returns a class score (e.g. shower-like, track-like, etc.) for every single Energy Deposition (EDEP) in the input image. A Density-Based Spatial Clustering of Applications with Noise (DBSCAN) [122] algorithm applied on all semantic classes yields clusters of spatially connected EDEPs. Using a Point Proposal Network (PPN) [123] then is used to predict points of interest in the event, such as the start and endpoints of tracks, shower start points, and interaction vertices. In this way, individual tracks originating from the same interaction vertex can be broken into particle instances. However, the clustering on EM particle instances, e.g. showers initiated by electrons or photons, is complex since the fragments of energy depositions often are spatially detached objects. For this purpose, a Graph Neural Network (GNN) [124] was developed, which clusters those detached EDEPs to shower instances. Combining the particle instances with the reconstructed start and endpoints is used to infer the specific energy loss of each particle instance, which in turn enables the PID (described in Section 2.2.3), and an estimation of the particle momentum. Finally, a high-level particle-flow interaction and topology reconstruction can be done based on the output of the previous steps. Figure 7.1 outlines the hierarchical reconstruction procedure described above.

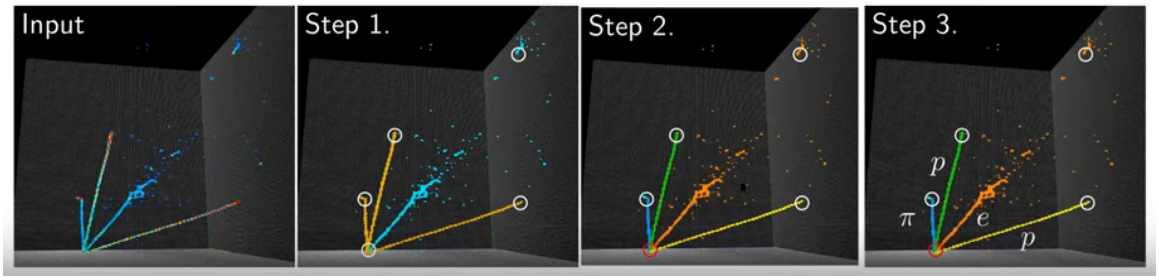

Figure 7.1: ML-based reconstruction chain. The chain consists of several neural networks organised in a hierarchical structure. In the first step, a CNN is used for the prediction of class scores (semantic segmentation) for every single EDEP. Furthermore, a PPN makes predictions of points of interest, e.g. shower start points and track start and endpoints. In a second step, particle clustering and interaction-vertex finding are done. Finally, a high-level PID is performed in a third step, enabling the reconstruction of the event topology. Courtesy of F. Drielsma (SLAC).

7.1.1 Data Samples

This section summarises the data samples used for the studies presented in this chapter.Here, only a brief overview with the most important characteristics is given. A detailed description of the data sets and how they were produced can be found in [125].

The data samples were created using the event generator from [126], followed by a GEANT4[2] [127] particle tracking simulation, applied to a LAr volume. To mimic the finite resolution of a LArTPC, the produced EDEPs along the particle trajectories were spatially smeared using a Normal distribution with a spread of 3 mm. Other smearing, e.g. from the detector's readout electronics, electric field non-uniformities, or the recombination and attenuation of the ionisation electrons, have not yet been implemented. After the smearing was applied, the simulated EDEPs were voxelised. The voxels, each with a size of 3 mm × 3 mm × 3 mm were uniformly distributed within a cube volume of 768^3 voxels. Please note the slightly smaller voxels compared to the pixelated charge readout employed in the SingleCube and Module-0 prototypes (described in Sections 5.1.3 and 5.1.4). The reason for these discrepancies is found in the fact that the simulation was done before the prototype design was finalised.

The events from all used data samples were simulated independently from each other. Each event was populated with particles from two sources, from a Multi-Particle-Vertex generator (MPV) and a Multi-Particle-Rain generator (MPR). The MPV represents a particle bomb where all produced species originate from a single vertex. It has simulated N particles of type e^-, γ, $\mu^\mp$, $\pi^\mp$, p, and π^0 originating from a unique vertex, where N is a uniformly distributed integer between 1 and 6. The maximum allowed particle multiplicities and kinetic energies per type and event for the MPV are described in Table 7.1. The MPR was used to overlay the MPV particles with apparently independent and detached stand-alone trajectories. It has generated particles of the types e^-, $\mu^\mp$, and p. The probability for each MPR particle category to be produced was set to 20 %, 60 %, and 20 % for electron, (anti-)muon, and proton, respectively. A maximum multiplicity of 5 particles per category and

[2] GEANT4 version v4.10.1.P03 with physics list QGSP_BIC.

event was defined. Table 7.2 summarises the MPR particle properties, including their kinetic energies ranges.

Particle Species	Max. Multiplicity per Event	Kinetic Energy Range [MeV]
e^-	1	50 to 1000
γ	3	50 to 1000
$\mu^\mp$	1	50 to 1000
$\pi^\mp$	2	50 to 1000
p	2	50 to 400
π^0	1	50 to 400

Table 7.1: Configuration parameters for the MPV including the maximum particle multiplicity and the kinetic energy range of the individual particle species. Within this range, the kinetic energies have been uniformly distributed. [125]

Particle Species	Max. Multiplicity per Event	Kinetic Energy Range [MeV]
e^-	5	50 to 1000
$\mu^\mp$	5	50 to 1000
p	5	50 to 400

Table 7.2: Configuration parameters for the MPR including the maximum particle multiplicity and the kinetic energy range of the individual particle species. Within this range, the kinetic energies have been uniformly distributed. [125]

Table 7.3 summarises the properties of the specific data samples. For the first two samples (number 1 and 2), the kinetic energies of all MPV and MPR samples have been distributed according to Tables 7.1 and 7.2, respectively. However, for the π^0 samples (number 3 and 4), the minimum kinetic energies was lowered to 0 MeV for all MPV and MPR particles. The π^0 produced with the MPV sample have been uniformly distributed in the range of 0 MeV to 400 MeV, with a maximum multiplicity of $1\pi^0$ per event.

7.1.2 Semantic Segmentation for Energy Deposition Classification

Semantic segmentation in the context of this chapter is referred to the task of predicting a class of particle type at the voxel level. In LArTPCs, each voxel contains information about the amount of deposited energy, which spans a broad range of values depending on the kinetic energy and the type of the ionising particle. Taking into account the correlations of each voxel's EDEP with its neighbouring voxel values allows for the prediction of every voxel's class score. For the task of semantic segmentation, five classes have been defined. Those classes are

Sample Number	File name	Type	N events	Minimum E_{kin}	Generators
1	train.root	training sample	125 480	50 MeV	MPV + MPR
2	test.root	validation sample	22 439	50 MeV	MPV + MPR
3	pi0-v1	validation sample	20 000	0 MeV	MPV + MPR
4	pi0-v2	validation sample	20 000	0 MeV	MPV (without e^-) + MPR

Table 7.3: Summary of the data samples used in the ML-based LArTPC event reconstruction. The MPR particles have been overlaid to those produced with the MPV. The number of π^0 per event only counts primary neutral pions produced with the MPV. The minimum E_{kin} corresponds to the lowest possible kinetic energy of the produced particles.

- Shower: This semantic type classifies EDEPs produced by showering particles. Showers typically are initiated by electrons, positrons, and photons.
- Track: Track-like particles usually produce long and relatively straight tracks with just a little energy deposition per voxel. Candidate particles are typically MIP particles, e.g. muons or charged pions, but also protons.
- Michel Electron (Michel): Michel electrons are produced by decaying muons. Since those electrons typically have energies of a few MeV, they produce short tracks. Michel electrons are distinguishable from other electrons by the pronounced Bragg peak of the decaying muon.
- Delta-ray (Delta): Delta rays are produced when charged particles scattering off atomic shell-electrons, which have enough energy to escape the potential of the atomic nucleus. The electrons themselves can ionise the argon atoms, and leave relatively short tracks in the detector. Delta rays typically appear right next to a particle track (somewhat collinear), making their topology easily distinguishable from other electrons.
- Low Energy Scatter (LEScat): This class is used to describe isolated EDEPs, with a fragment size of < 10 EDEPs.

The architecture of the ML network is called UResNet, which is a hybrid between two popular architectures, namely U-Net and ResNet, as described in [121]. The upper half of Figure 7.2 shows a simplified version of UResNet, whereas the lower half explains the structure of the PPN network described in Section 7.1.3. UResNet is made of two parts, an encoder and a decoder. The encoder consists of repeated blocks of convolution and stride convolution layers which down-sample the image resolution while increasing the feature dimension. In the encoder part, the network learns from key features in an image at different spatial scales, yielding a tensor with a low spatial resolution but a large number of channels containing compressed feature information.

In the decoder path, the feature maps of deeper levels are concatenated with the feature maps of higher network layers. In this way, the decoder extracts feature at various scales, i.e. at various network depths. That allows for the restoration of the original resolution of the input image with the additional information of high-level features at the voxel level. While the input image is single-channeled (it contains only information about the deposited energy per voxel), the output image has many channels containing additional information about class scores.

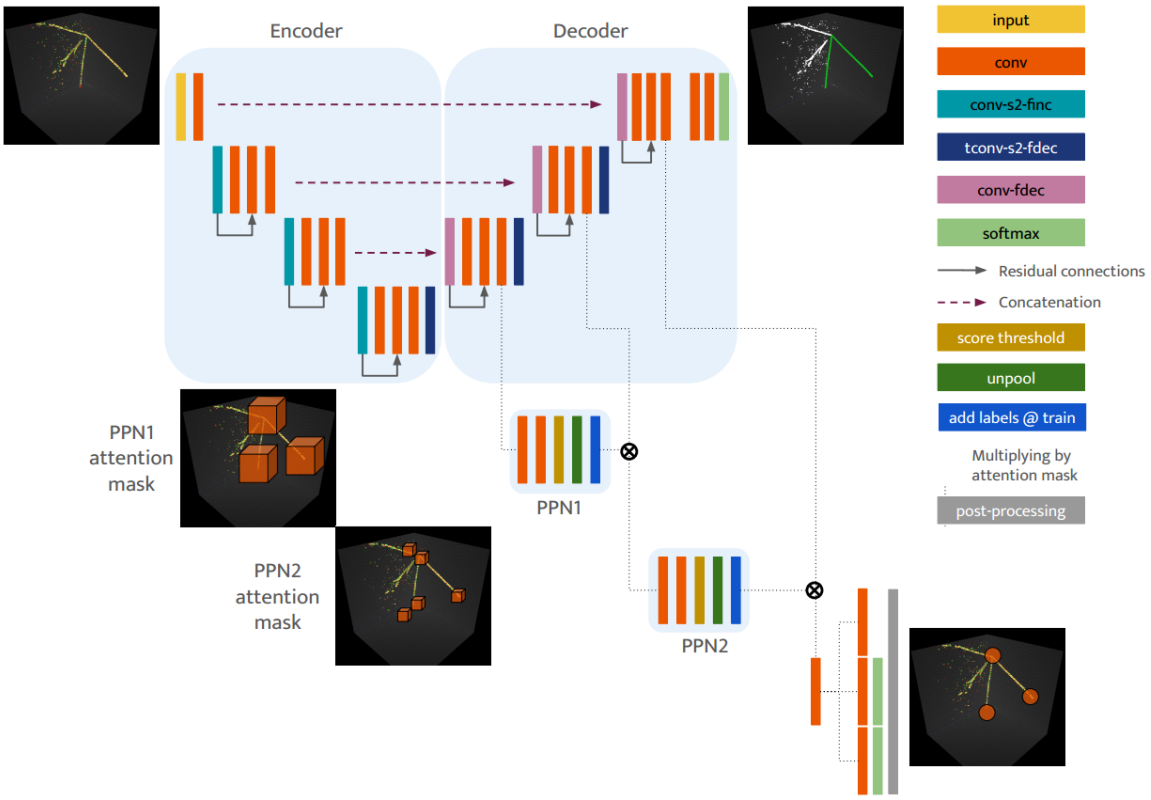

Figure 7.2: Illustration of the UResNet architecture for semantic segmentation (upper half) and point proposal (lower half). This particular network has a depth of three since it consists of three down-sampling operations. Light blue boxes represent convolution layers, and dark blue boxes are transpose convolutions, each with a stride of two. Purple boxes refer to convolutions with a stride of one that decrease the number of filters. Note that the size of feature maps is constant across the horizontal dimension. The dashed arrows represent residual connections (additional connections between different layers) which allow skipping some layers in the network architecture. Those connections enable a faster learning process and, thus, in general, deeper networks. At the deepest level of the network, where the spatial resolution is coarsest, the so-called PPN1 produces a class score of a value between 0 and 1 for each voxel, indicating whether or not the voxel contains a point of interest. The result of PPN1 is then up-sampled to an intermediate spatial resolution of PPN2, which in turn predicts a score for containing a point of interest or not. Finally, the result of PPN2 is again up-sampled to the original image resolution. [123]

Particle interactions within a bare LAr volume were simulated, as described in Section 7.1.1. The EDEPs in each voxel and from each particle were recorded, thus allowing for labelling the data with true information. The network was trained with knowledge about the true labels, using the sample number 1 (see Section 7.1.1). Figure7.3 show the simulated energy depositions produced by particle interactions in

LAr and the semantic segmentation network output from the trained UResNet.

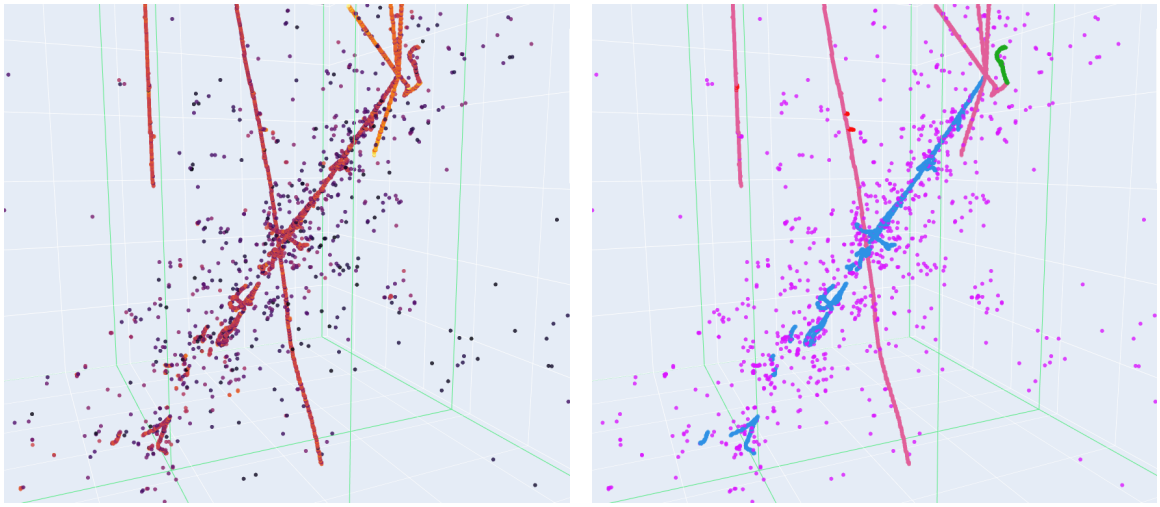

Figure 7.3: Event display showing the application of the semantic segmentation to simulated particle interactions in LAr. Left: The network input image with energy depositions per voxels in a logarithmic colour scale. Right: The networks class predictions are shown. Magenta - LEScat, light red - Track, blue - Shower, dark red - Delta, green - Michel. The light green lines indicate the boundaries of the ArgonCube 2x2 Demonstrator modules (see Section 5.1.5). These plots were generated using event-ID 527 from the data sample number 3 (see Section 7.1.1).

To estimate the performance of the semantic segmentation, sample number 2 (see Section 7.1.1) was used to validate the trained neural network. For this purpose, a confusion matrix as depicted in Figure 7.4 was generated. A confusion matrix shows the true vs predicted class labels to illustrate the accuracy of the semantic segmentation. It appears that the semantic segmentation performs very well, with accuracies of ($> 99\,\%$ for all true shower- and track-like EDEPs. Even though the EDEPs with a true Michel, Delta, or LEScat label are reasonably well reconstructed, about $14.5\,\%$ of all Delta rays are wrongly reconstructed as tracks. That is understandable since there is some spatial overlap between the EDEPs of both classes close to the vertex point. Furthermore, about $4\,\%$ of the Michel electrons and the LEScat are wrongly reconstructed as showers. Confusing shower-like particles with the semantic class LEScat is understandable since low-energy scatters look similar to shower-like EDEPs but only are limited to the fragment size (< 10 EDEPs). However, the $\approx 4\,\%$ of Michel electrons which are wrongly predicted as showers are more complicated to understand. In those cases, the network might confuse the muon's Bragg peak with a vertex and thus predicts the EDEPs of the Michel electron as shower-like.

To test the semantic segmentation on a π^0 sample, similar confusion matrices were produced. Figure 7.5 shows the results for all energy depositions (left) and only those EDEPs closer than 20 pixel pitches to a true π^0 decay vertex (right). From the left plot, it appears that the matrix is close to diagonal, indicating that the semantic segmentation overall performs well. However, in comparison with the confusion matrix from the validation sample shown in Figure 7.4, the accuracy of the shower- and track-like EDEPs dropped by about $2\,\%$. The other classes performed with a similar pattern already observed: About $12.6\,\%$ of the EDEPs with a true Delta ray label are mis-identified by the network as tracks. Further, some ($3.79\,\%$) of the energy

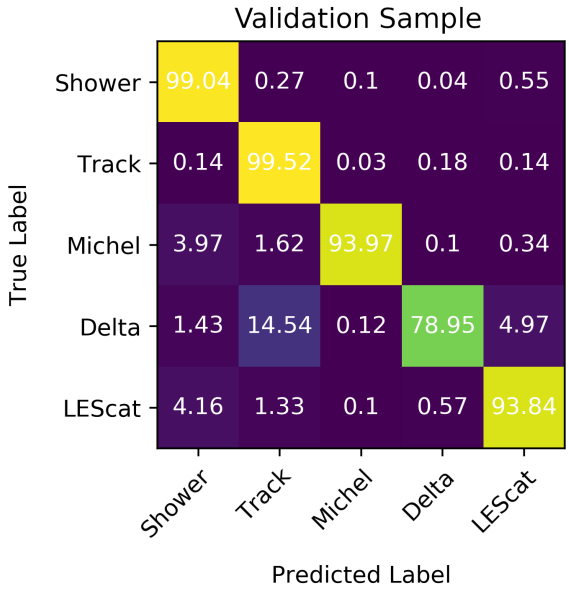

Figure 7.4: Confusion matrix for the semantic segmentation of individual EDEPs applied on a a validation sample. The numbers denote the percentage of all classified EDEPs for every bin. It appears that the semantic segmentation performs very well ($> 99\,\%$ accuracy), for shower- and track-like EDEPs. However, about $14.5\,\%$ of all Delta rays are wrongly reconstructed as tracks, and some of the Michel electrons and LEScat are wrongly reconstructed as showers (each $\approx 4\,\%$). This plot was generated using the first 10 000 events from the data sample number 2 (see Section 7.1.1).

depositions produced by Michel electrons are wrongly reconstructed as shower-like EDEPs. The poorer accuracies are ascribed to the fact that the π^0 sample has no limit on the particle's kinetic energies. In contrast, the particles in the validation sample all have energies larger than 50 MeV (see Section 7.1.1). For those EDEPs close (< 20 pixel pitches) to a true π^0 decay vertex, the predictions of the classifier are less accurate, as shown in the right plot in Figure 7.5. The largest source of confusion originates from Michel electrons mis-identified as showers ($50.5\,\%$). Furthermore, EDEPs with a Delta label are often mis-reconstructed as shower-like ($29.9\,\%$) or track-like ($20.4\,\%$). Investigations to understand and improve the confusions close to interaction vertices mentioned above are ongoing.

The observed larger confusion close to π^0 decay vertices can cause problems for the π^0 reconstruction in a LArTPC. For example, an electron originating from a vertex where a π^0 was produced might lead to significant confusion in the classifier. If the classifier wrongly reconstructs the first few EDEPs of the electron-induced shower, the reconstructed shower's start point would be off by a few pixel pitches from the true shower's start point and thus might look like a photon-induced shower.

The reason for the poorer classifier accuracy close to interaction vertices has not yet been determined. The simplest solution to understand where the problem originated would be to train UResNet with more weight given to energy depositions close to particle interaction vertices. If this would not resolve the problem, it could be that the UResNet did not train deep enough and thus has a lack of spatial resolution for resolving the classification at the deepest level. Further studies should investigate those observations in more detail.

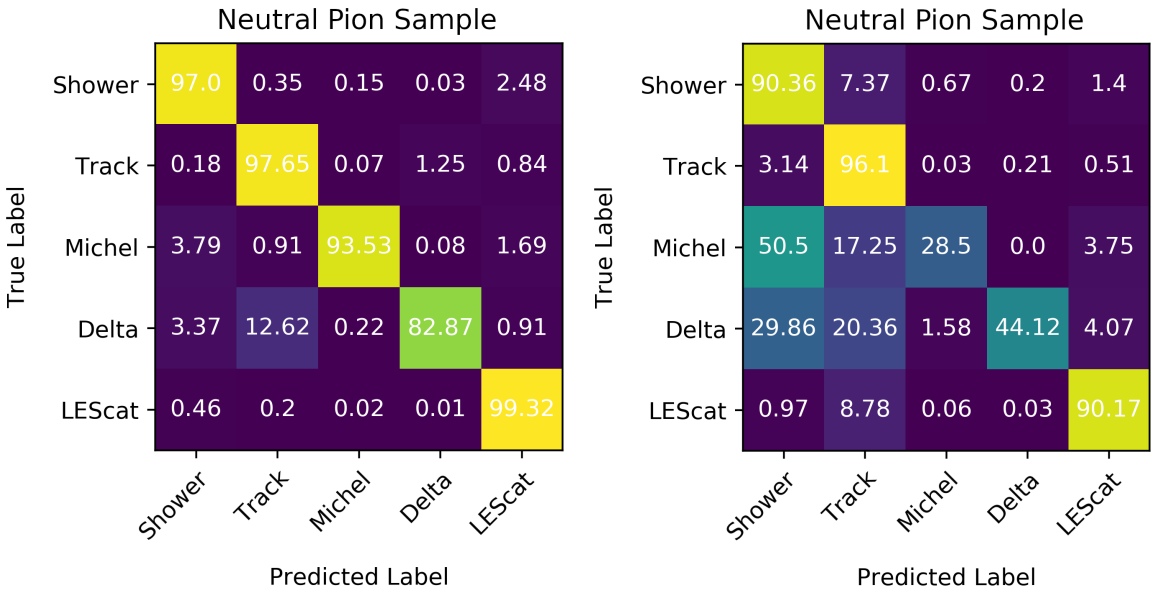

Figure 7.5: Confusion matrix for the semantic segmentation of individual EDEPs applied on a neutral pion sample. Left: Confusion matrix for all EDEPs in the the data set. Right: Confusion matrix for EDEPs only closer than 20 pixel pitches to a true π^0 decay vertex. These plots were generated using the first 10 000 events from the data sample number 3 (see Section 7.1.1).

7.1.3 Point Proposal Network for Finding Points of Interest

The PPN is designed to identify points of interest in particle trajectories, e.g. their start point, endpoint, or kinks. Furthermore, the PPN predicts the semantic type (Shower, Track, Michel, Delta, LEScat) of each proposed point. Applying the PPN at an early stage of the reconstruction chain enables the possibility of clustering EDEPs of particle trajectories, which in turn allows for the reconstruction of kinematic variables and PID. Regarding the task of clustering showers or shower fragments, the initial point can help to define a general direction of these structures, which can consist of hundreds of EM secondaries. In the framework of this thesis, a neutral pion reconstruction algorithm was developed (see Section 7.4), which relies on an accurate shower start-point and direction reconstruction. Apart from that, the knowledge of the start (and end) point of each particle's trajectory naturally includes vertices, e.g. from neutrino interaction or π^0 decays, and thus allows for more robust event reconstruction.

The architecture of the PPN is illustrated in Figure 7.2. In the encoder path, the feature extraction consists of convolution and pooling layers which generate a data tensor with a lower spatial resolution than at the input image. The PPN1 at the coarsest spatial resolution uses this data tensor to generate rectangular shaped boxes of regions that likely contain a point of interest. The output from PPN1 then is up-sampled to an intermediate spatial resolution of PPN2, which in turn produces rectangular shaped boxes with predictions for containing a point of interest or not. In a third step, the result of PPN2 is again up-sampled to the image resolution equal to the input image resolution where PPN3 makes its predictions. A more detailed description of the PPN network architecture can be found in [123].

The PPN was trained using the data sample number 1 described in Section 7.1.1).

The accuracy of the PPN network was estimated with a π^0 sample (number 3, described in Section 7.1.1), which contains electron and photon-induced showers. Figure 7.6 shows the distances of the first step (corresponding to the shower's true start position) to the closest point predicted by PPN for showers initiated by electrons (blue) or photons (red). For the vast majority, the true shower's start point is closer than 2 pixel pitches distant from a point predicted by PPN, indicating that the neural network performs very well.

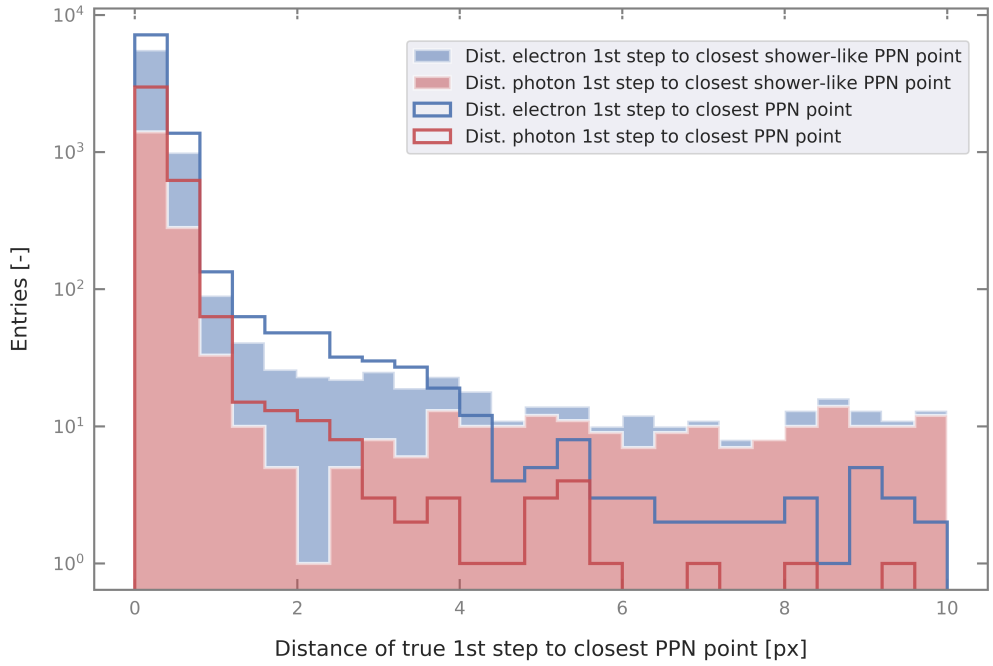

Figure 7.6: Accuracy of the PPN applied on showers. However, the overall shapes between the two distributions seem to be in agreement. It appears that the true shower's start point is closer than 2 pixel pitches distant from a point predicted by PPN, demonstrating that the neural network performs well. This plot was generated using the first 6000 events from the data sample number 3 (see Section 7.1.1).

7.1.4 Graph Neural Network for Particle Instance Clustering

One of this thesis highlights is the reconstruction of neutral pions, where showers play a crucial role. This section mainly focuses on clustering showers. Such showers usually exhibit spatially detached traces of EDEPs with different orientations and morphology, which makes it very challenging to cluster these fragments to shower instances accurately. When I started to work on shower clustering, the first approach to group those fragments was a fragment-wise cone-clustering algorithm. The idea of the cone-clustering was to back-propagate each fragment's directions to merge it with a second fragment if the direction of the former fragment crossed the forward-propagated cone of the second fragment. However, the algorithm showed some weak points related to relatively large uncertainties of the PCA results and possible mistakes happening in the fragment's start point identification.

Earlier studies have shown that GNNs are powerful tools capable of clustering spatially detached objects, e.g. EDEP fragments, into larger structures, e.g. shower instances. This motivated colleagues working at SLAC to add an implementation of a GNN [124] to the reconstruction chain used here.

In comparison to the UResNet (Sections 7.1.2) and PPN (Section 7.1.3), the GNN neither has an encoder nor a decoder path. Instead, the GNN has a set of message-passing steps which iteratively update the node and the edge features by communicating information in a graph. Applied to showers, each node corresponds to a fragment of spatially connected EDEPs, and the edges can be interpreted as the invisible photons connecting the nodes. Node features are used to identify primaries (fragments at the start of showers) whereas edge features are used to group the nodes to clusters. In total, there are 22 node features,

- Normalised covariance matrix (9 features)
- Normalised principal components axis (3 features)
- Centroid (3 features)
- Number of voxels (1 feature)
- Initial point (3 features)
- Normalised initial direction (3 features)

and 19 edge features,

- Closest Point of Approach (CPA) (6 features)
- Displacement between CPAs (3 features)
- Outer product of displacement (9 features)
- Length of displacement (1 feature).

After the features have been extracted, a threshold applied to the edge scores determines which nodes are clustered together. The node score with the maximum value in a cluster is used to reconstruct the primary fragment, which likely corresponds to the initial shower fragment. Figure 7.7 shows the working principle of the GNN used here.

Figure 7.8 illustrates the application of the developed GNN to a typical electromagnetic shower in LAr. The input to the GNN are shower fragments which previously were clustered using a DBSCAN applied to EDEPs with semantic type shower. The output of the GNN are shower instances.

To illustrate the performance of the implemented GNN, Figure 7.9 shows two events, each containing a relatively large amount of shower fragments. The predicted edge and node scores from the GNN were used to predict the shower instances. It appears that these predictions are very accurate. A more quantitative analysis showed that the overall fragment clustering has efficiencies and purities of more than 99 % [124].

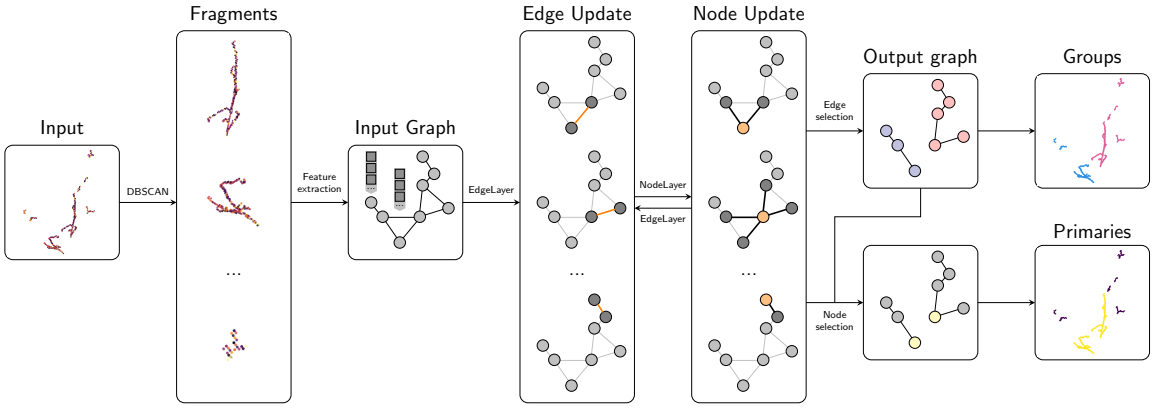

Figure 7.7: Illustration of the GNN architecture used to cluster spatially detached shower fragments and to identify primary fragments. A DBSCAN is applied to the input image to form dense shower fragments. Each fragment is encoded into a set of node features in a graph connected by arbitrary edges with edge features. A series of message passing steps iteratively update the node and the edge features by communicating information in a graph. The updated node features are used to identify primary fragments (fragments at the start of showers), and the edge features are used to constrain the connections in the graph for grouping the nodes into clusters. [124]

7.2 Shower Direction and Energy Estimation

This section discusses the performance for the reconstruction of the direction and total energy of showers. An accurate reconstruction of these quantities is essential for the neutral pion reconstruction discussed in Section 7.4.

Once single shower instances were assembled and their start points found, e.g. by using the GNN and PPN described in Sections 7.1.4 and 7.1.3, the shower's directions can be reconstructed. To reconstruct the direction of individual showers, a PCA on the EDEPs closest to the reconstructed shower start point was performed. However, the accuracy of the direction estimate turned out to depend significantly on the number of EDEPs taken into account for the PCA, and on the overall shape of the shower. For straight showers, a large number of EDEPs generally yields a reasonably good shower direction estimate. However, for bent showers or showers with kinks and forks, the best direction estimate is obtained using only those few EDEPs closest to the shower's start point. This lead to the development of an improved algorithm taking into account a variable number of EDEPs, based on the spread of these energy depositions in space. Figure 7.10 shows the performance of the new shower direction estimator, compared with the previous one. It appears that the new direction estimator (labelled R_n^* in the plot mentioned above) is predicting a shower's direction with an accuracy better than 10° for the vast majority of the showers, with a most probable value peaking at about 2°. The new algorithm for the estimation of showers was implemented in the GNN [124] (see Section 7.1.4). The tail of the blue distribution shown in Figure 7.10 is ascribed to low-energy showers, as can be concluded from Figure 7.11.

A study using showers initiated by electrons and photons was performed to estimate the discrepancy between the true shower energy deposition and the reconstructed shower energy. Figure 7.12 shows that the reconstructed shower energy, in general, is smaller than the total true energy deposited by the shower. A linear fit suggests that the average missed energy per shower corresponds to about 17 % of the true

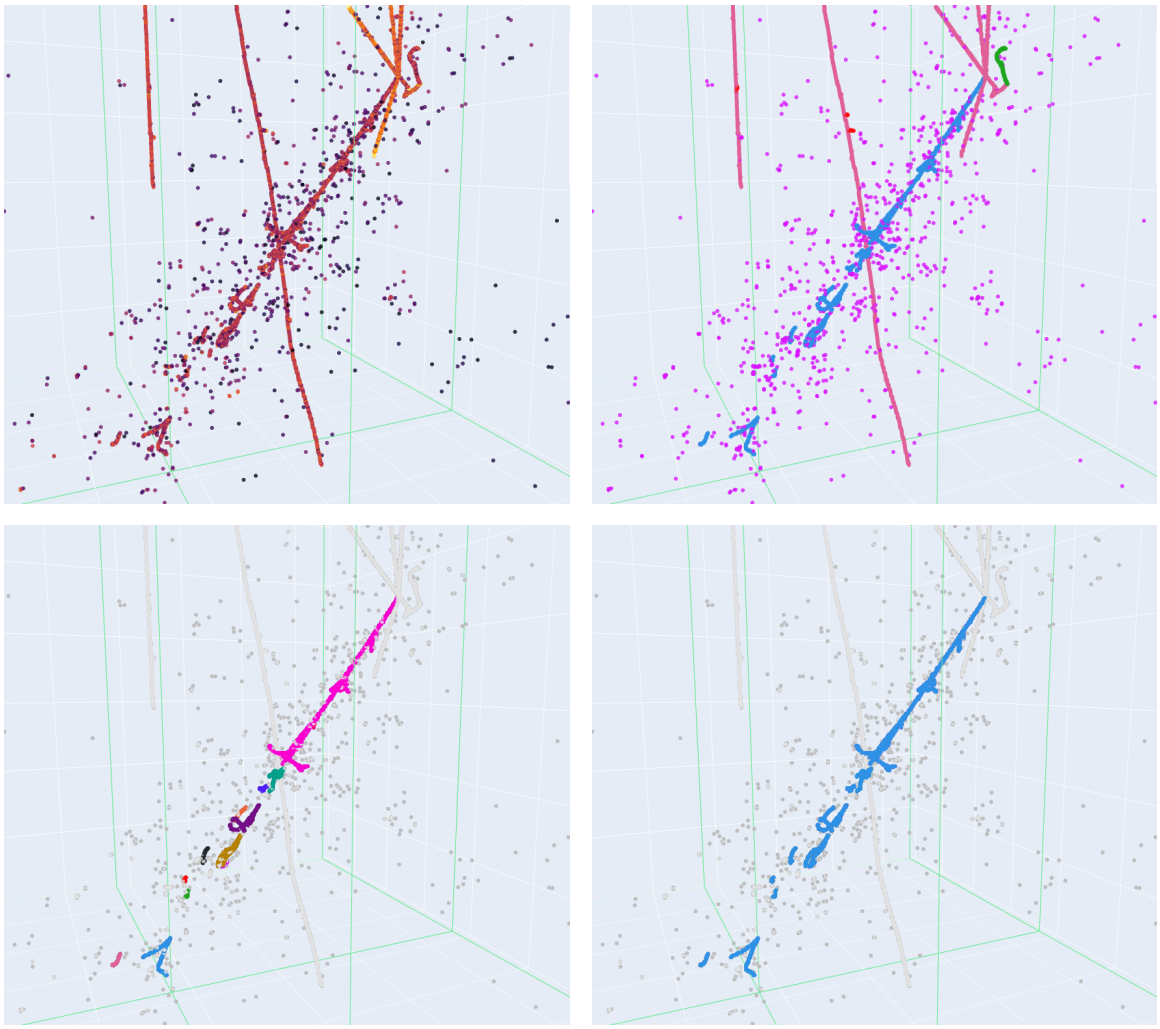

Figure 7.8: GNN-based shower clustering, applied on simulated particle interactions in LAr. A GNN can be used to cluster spatially detached objects like shower fragments to larger structures like shower instances. The light green lines in the figures indicate the boundaries of the ArgonCube 2x2 Demonstrator modules (see Section 5.1.5). Top left: The LArTPC input image with energy depositions per voxels in a logarithmic colour scale. Top right: A semantic segmentation predicts class-scores for every individual EDEP. Magenta - LEScat, light red - Track, blue - Shower, dark red - Delta, green - Michel. Bottom left: A DBSCAN algorithm, only applied to EDEPs with semantic type shower, clusters individual EDEPs to shower fragments. The coloured EDEPs correspond to fragments, with the colour code referring to the fragment number. Bottom right: The GNN is applied on all shower fragments to cluster them to shower instances. These plots were generated using event-ID 527 from the data sample number 3 (see Section 7.1.1).

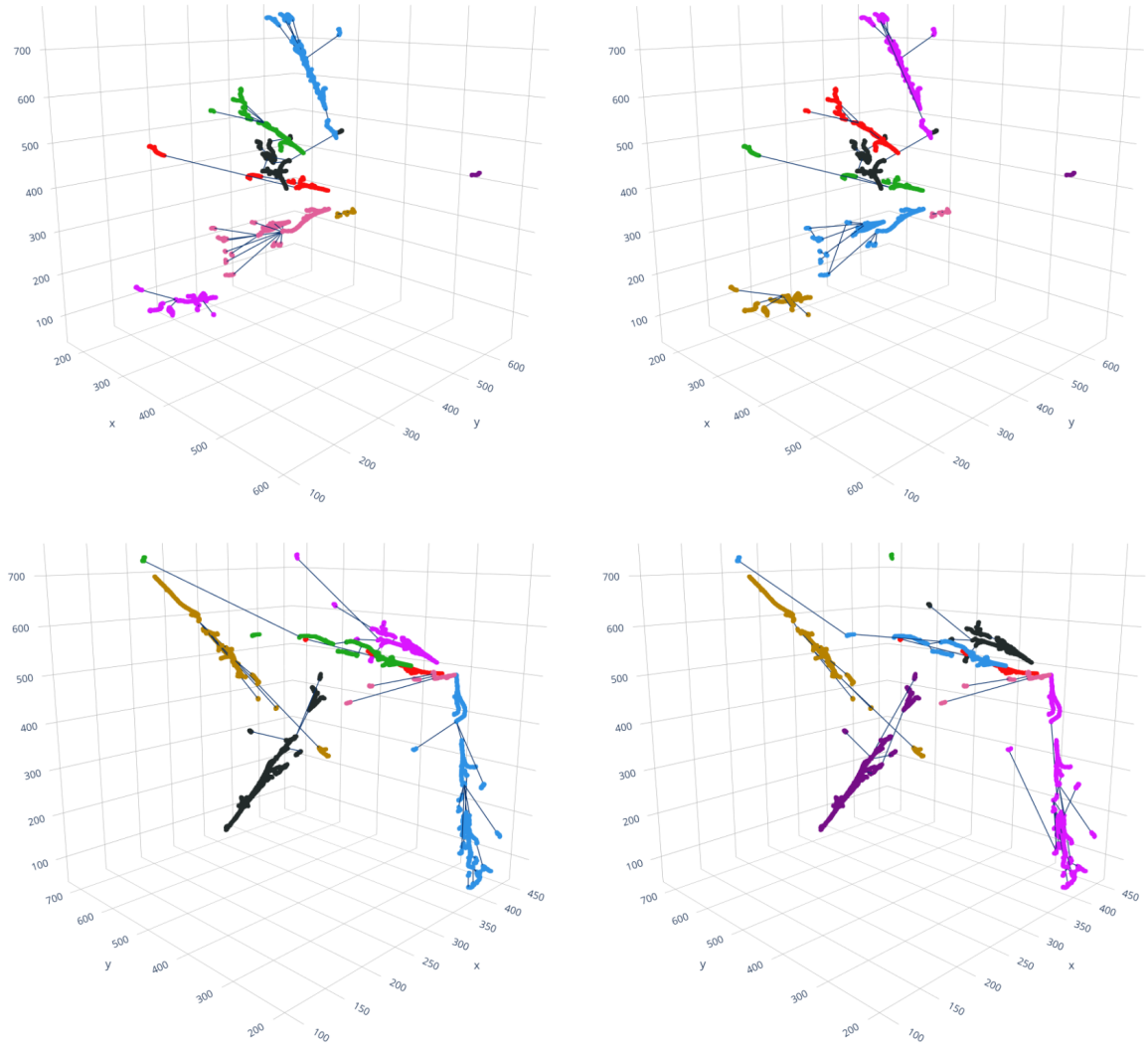

Figure 7.9: GNN-based shower clustering, applied on two events (one in each row) from the data sample number 2. The colours of the fragments correspond to the true cluster number (left) and the predicted cluster number (right). Dark blue lines denote the edge scores (> 0.5 only). The GNN performs very well, even on small fragments with a large separation from the main cluster. Of particular interest is the second event, where a small fragment (green in the prediction) is not connected by an edge with a score > 0.5. Consequently, this fragment is predicted to be a stand-alone cluster. [124]

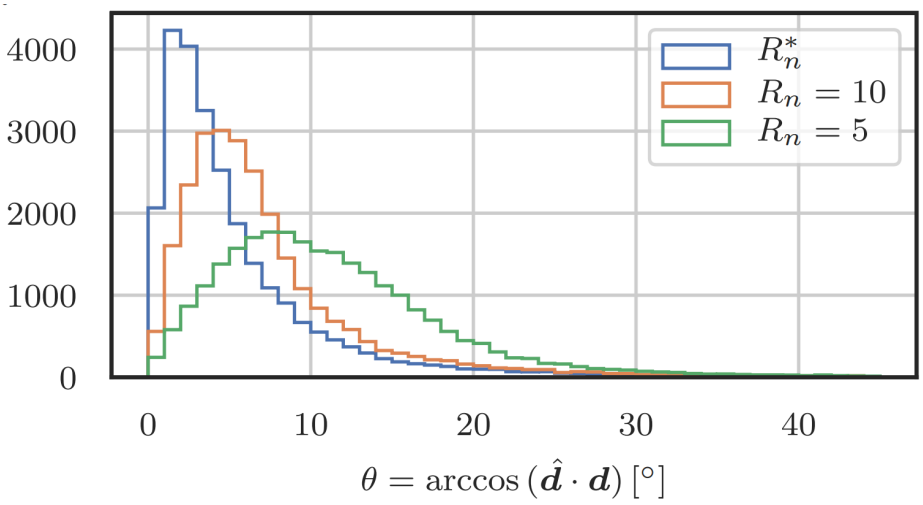

Figure 7.10: Reconstructed shower direction with respect to the true shower direction for a collection of about 30 000 showers. θ denotes the difference between the true shower's direction and the reconstructed direction. The green and orange histograms correspond to the residual distribution obtained with the old direction estimator (taking into account the EDEPs closer than 10 pixel pitches and closer than 5 pixel pitches, respectively, to the reconstructed shower's start point). The blue histogram corresponds to the residual distribution obtained with the new direction estimator. [124]

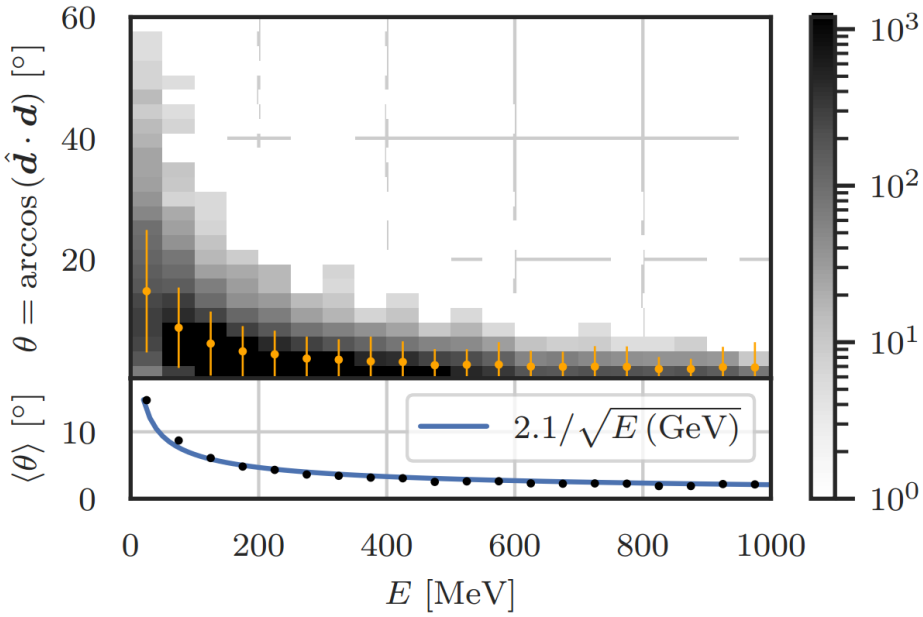

Figure 7.11: Reconstructed shower direction residual distribution as a function of the true shower energy. θ denotes the difference between the true and the reconstructed shower's direction. The orange markers represent the mean values, and the error bars their root mean square (RMS). [124]

shower energy. This missing energy is primarily ascribed to those EDEPs classified as LEScat which were not taken into account during the shower clustering process. However, the missing energy of the reconstructed showers can be taken into account with a so-called Fudge factor, which acts as a correction coefficient to better fit the observations to the expectation. A Fudge factor of $F = 1/0.83 \approx 1.205$ would take into account the 17 % missing shower energy. Figure 7.12 furthermore shows that there are almost no entries above the diagonal (dashed blue) line in the histogram, indicating that contributions from mis-identified EDEPs to the reconstructed shower energy and from wrongly merged shower fragments are small.

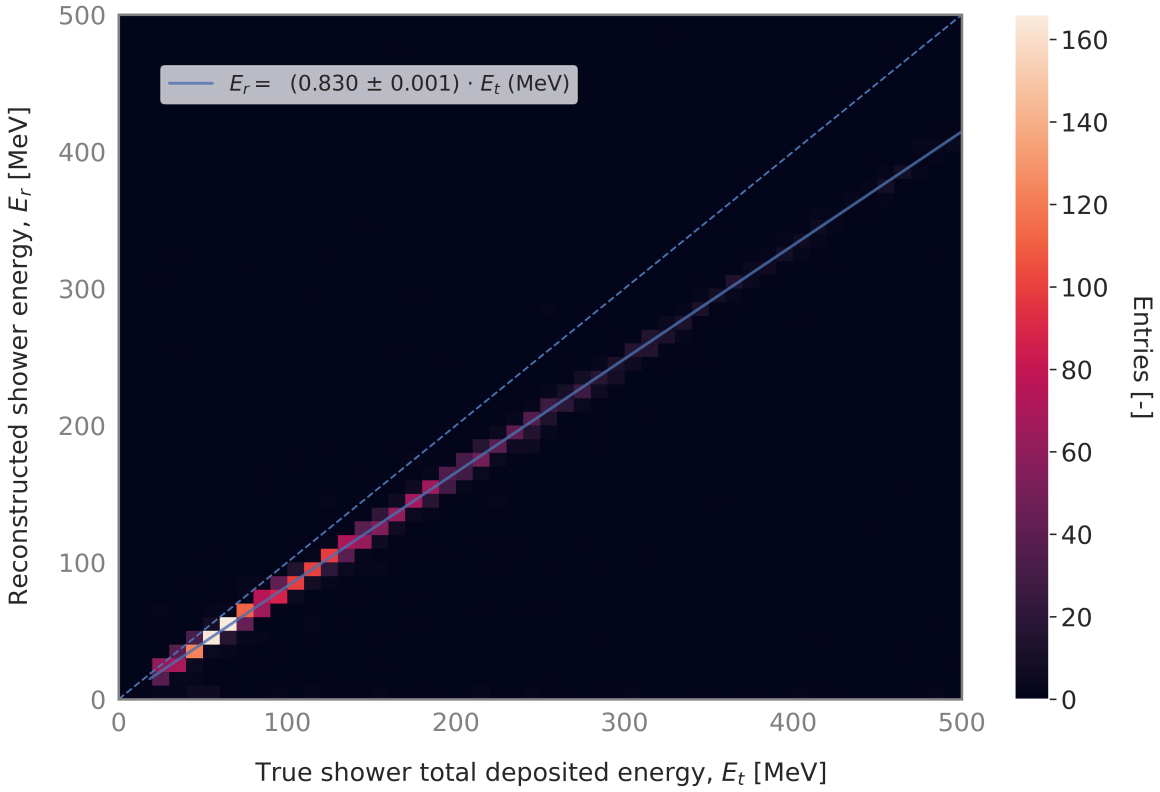

Figure 7.12: Reconstructed vs true energy for showers in LAr. The dashed blue line denotes the diagonal line for which the true shower energy deposition equals the reconstructed shower energy. The solid blue line indicates a linear fit to the reconstructed shower energy. The slope of the fit is determined to 0.83 ± 0.01, indicating that about 17 % of the true shower energy is in average missing. This plot was generated using the first 4000 events from the data sample number 3 (see Section 7.1.1).

The reconstruction of a shower's start point using the PPN showed to be very accurate, as depicted in Figure 7.6. The shower clustering using the GNN described in Section 7.1.4 was validated in [124] with data sample number 2 (see Section 7.1.1), showing shower clustering purities and efficiencies of > 99 %.

7.3 Electron-Photon Separation

In liquid argon time projection chambers, electrons and positrons (from now on just called electrons or e^-) can appear almost identical to photons. However, discriminating e^- from γ is important in the scope of this thesis for at least two reasons. First,

electron-induced showers can be a background for the π^0 reconstruction, which is useful for detector calibration purposes. Secondly, it is important for neutrino-oscillation experiments to not wrongly reconstruct a γ-induced shower as an e^- which might look like a ν_e CC interaction. For those reasons, it is crucial to have a good handle on discriminating electrons from photons.

Discriminating e^- from γ in LArTPCs can be achieved with a sufficiently high spatial and calorimetric resolution to resolve the very first part of a shower. The electron deposits one charge per unit length whereas the photon[3] produces electron-positron pairs and therefore deposits twice the charge per unit length. For photons that do not initially produce an electron-positron pair but, instead, are scattered incoherently on electrons (Compton scattering), the situation becomes more complicated since the energy deposition at the shower's start is mainly driven by the scattered electron. The following Figure 7.13 shows the sum of simulated energy depositions within the shell of a sphere and as a function of the distance of the shell to the shower's start point. This start point is defined as the first EDEP occurring during the shower development. It appears that the photon-induced shower deposits roughly twice the energy per path length than the electron. This observation can be used for electron-photon discrimination.

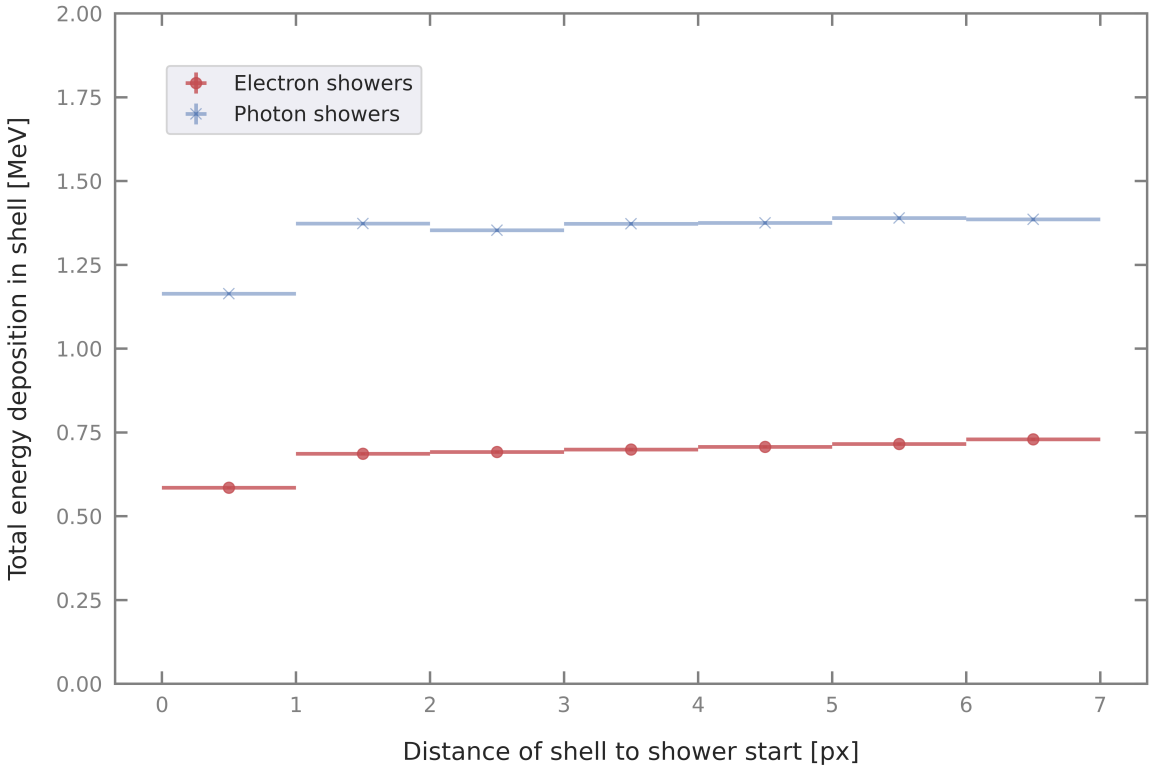

Figure 7.13: Mean summed EDEPs at the start of showers initiated by electrons and photons. Photons with energies of more than a few MeV predominantly undergo pair production when travelling through LAr. Consequently, showers initiated by photons deposit roughly twice the amount of energy compared to electron showers. This enables the discrimination of electrons and photons. This figure was produced with the 20 000 events from the data sample number 3 (see Section 7.1.1). The error bars, which are not visible in the plot, denote the standard error of the mean.

[3] Depending on the photon energy, as shown in Figure 2.6.

Summing up all EDEPs in the very first segment of a shower allows for an estimation of the specific energy loss dE/dx. Figure 7.14 shows the specific energy loss distributions for a collection of showers initiated by photons and electrons. These distributions can be fitted with a Landau distribution [128], or approximated with a Moyal distribution [129], which reads

$$p(x) \approx \frac{1}{\sqrt{2\pi}} \exp\left(-\frac{x + e^{-x}}{2}\right) \qquad \text{(Moyal approximation)}. \tag{7.1}$$

Fitting the Moyal distribution to the measured specific energy losses enables the extraction of (relative) photon and electron likelihood fractions, described later.

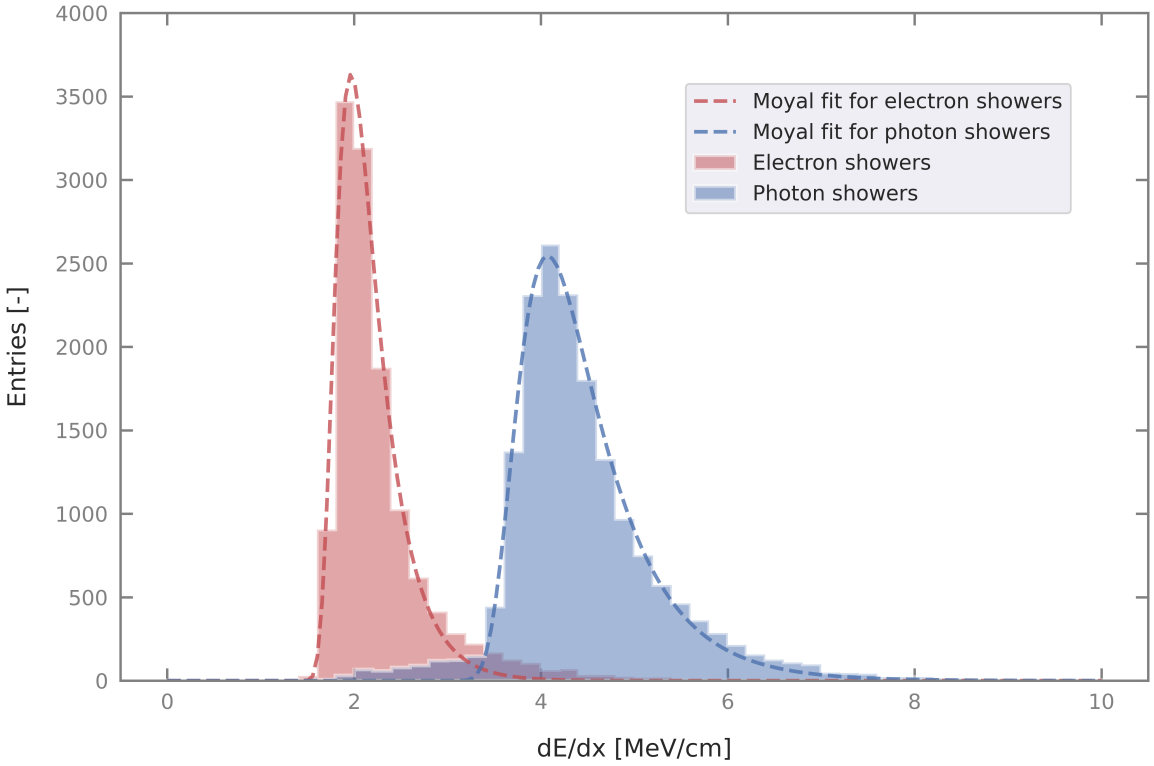

Figure 7.14: Specific energy deposition dE/dx at the start of showers induced by e^- and γ. Due to the process of pair production, the photon-induced showers deposit about twice as much energy per unit length than electron-induced showers. The left tail of the blue distribution is partially ascribed to photons that undergo incoherent (Compton) scattering and thus initially produce only electrons instead of electron-positron pairs. This plot was produced with the 20 000 events from the data sample number 3 (see Section 7.1.1).

The response of a detector to a particle species (here: electron or photon) can be described by a Probability Density Function (PDF). The PDF, written as $\mathcal{P}(x; H)$, describes the probability for the detector to respond to a track produced by a particle species H (here: $H \in \{e^-, e^+, \gamma\}$) with a signature x (e.g. the average energy loss by unit length dE/dx). The vector x may describe a single or several measurements acquired in one or more detector systems. As a normalisation condition, the PDF must fulfil

$$\int \mathcal{P}(x; H)\, dx = 1. \tag{7.2}$$

The likelihood function $\mathcal{L}(H; x)$ provides an estimate for the likelihood that a track with a measurement vector x was produced by a particle of specific species H. It

appears that the functional form of the PDF and the likelihood function are the same,

$$\mathcal{P}\left(x;H\right) \equiv \mathcal{L}\left(H;x\right). \tag{7.3}$$

However, there is a subtle difference between those quantities: On the one hand, the PDF is a function of the measurable quantities, x, for a fixed particle hypothesis, H. On the other hand, the likelihood is a function of particle type H for a measured variable x. Thus, a likelihood can be ascribed to a particle for which its variable x was measured. To distinguish between the photon and the electron hypotheses using the specific energy loss as observable, the photon and electron likelihood fractions can be written as

$$\mathcal{L}_{\gamma} = \frac{\mathcal{L}(\gamma; dE/dx) \cdot P(\gamma)}{\mathcal{L}(\gamma; dE/dx) \cdot P(\gamma) + \mathcal{L}(e^{-}; dE/dx) \cdot P(e^{-})} \tag{7.4}$$

$$\mathcal{L}_{e^{-}} = \frac{\mathcal{L}(e^{-}; dE/dx) \cdot P(e^{-})}{\mathcal{L}(\gamma; dE/dx) \cdot P(\gamma) + \mathcal{L}(e^{-}; dE/dx) \cdot P(e^{-})}, \tag{7.5}$$

where $P(\gamma)$ and $P(e^{-})$ denote weighting factors which, respectively, take into account the relative occurrence of photons or electrons in the analysed sample.

Based on the simulated data presented in Figure 7.14, the likelihood fractions for the electron and the photon hypotheses were calculated. Figure 7.15 depicts these fractions. With a measured specific energy loss of $\lesssim 3\,\mathrm{MeV\,cm^{-1}}$, the shower has an electron likelihood fraction of $\mathcal{L}_{e^{-}} \approx 1$ and a photon likelihood fraction of $\mathcal{L}_{\gamma} \approx 0$. However, at higher measured specific energy losses, the photon likelihood fraction rapidly increases on the cost of the electron likelihood fraction.

7.4 Neutral Pion Reconstruction

The focus of this section is on the reconstruction of neutral pion decays in LArTPCs using the ML techniques presented in Section 7.1. The neutral pion, π^{0}, is an electrically uncharged meson which predominantly decays into two photons, as can be seen from the π^{0} decay modes [36]:

- $\pi^{0} \rightarrow \gamma + \gamma$ (BR[4] ≈ 0.99)
- $\pi^{0} \rightarrow \gamma + e^{+} + e^{-}$ (BR ≈ 0.01)
- other decay modes (BR $\lesssim 10^{-5}$)

The two photons produced in the first decay mode can initiate showers in a LArTPC. Measuring the energies of each photon-induced shower and the angle between the two showers allows for the reconstruction of the π^{0} mass, as described in Section 7.4.2. The mass of the π^{0} is a well known quantity [36],

$$m_{\pi^{0}} = (134.9766 \pm 0.0006)\,\mathrm{MeV}. \tag{7.6}$$

Given the high branching ratio of the first decay mode as well as the fact that this three-body decay allows for the reconstruction of the π^{0} mass make neutral pions a valuable tool for benchmarking the response of a detector.

[4] Branching Ratio.

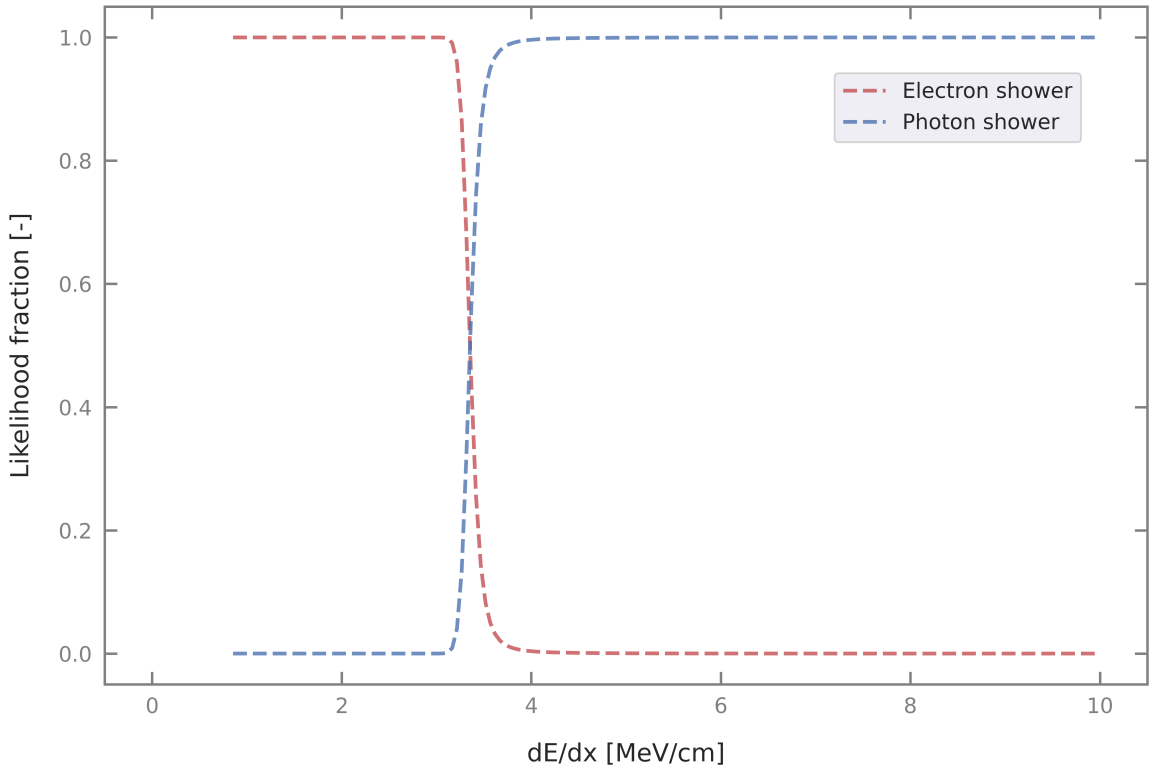

Figure 7.15: Likelihood fractions for electron and photon induced showers. These likelihood fractions allow for an efficient discrimination of showers initiated by electrons from showers that were produced by photons. This plot was produced with the 20 000 events from the data sample number 3 (see Section 7.1.1).

7.4.1 Motivation

As mentioned in the introduction of this chapter, my motivation to reconstruct neutral pion decays with a LArTPC was mainly driven by the idea of calibrating the detector's energy reconstruction scale. That dramatically increases the detector's calorimetric accuracy and thus the event reconstruction. However, in the scope of this thesis, the capability of reconstructing neutral pions has other advantages. First, a proper energy scale calibration of the ND-LAr and the FD in the DUNE experiment would allow for their operations at different electric field intensities. That is of interest in particular since the DUNE ND-LAr will have to face a high-multiplicity environment where an increased drift field intensity – with respect to the field intensity in the FD – can be helpful. Secondly, neutral pions can be a major source of background in neutrino-oscillation experiments searching for ν_e CC interactions with an electron in the final state, e.g. in the DUNE FD as a signal event, or in the DUNE ND to measure the ν_e beam contamination. The photons produced in the π^0 decay can mimic an electron, particularly true if one of the photons is unseen (e.g. if it leaves the detector or has too little energy to be reconstructed as a shower) or undergoes Compton scattering. Thus, a good handle on e^--γ-separation (see Section 7.3) and an efficient and accurate π^0 reconstruction is desirable.

7.4.2 Neutral Pion Decay Kinematics

The focus in this section is on the kinematics of the particles involved in the π^0 decay (the first decay channel described in Section 7.4.1). Figure 7.16 depicts the π^0 decay in both, the Centre of Mass Frame (CMF) and the Laboratory Frame (LF).

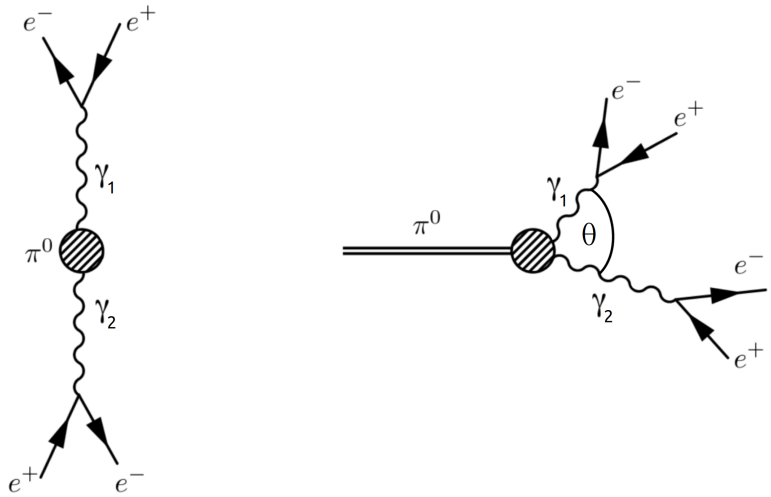

Figure 7.16: The neutral pion decays with a branching ratio of about 99 % to two photons. In the CMF (left), those photons are back-to-back whereas in the LF (right), the photons have an opening angle θ smaller than 180° due to the kinetic energy of the π^0.

In the pion's rest frame (CMF), the two produced photons are emitted back-to-back isotropically. Each photon is carrying the energy corresponding to half of the pion mass, m_{π^0}. This follows directly from the definition of the invariant mass, which

is defined as

$$m = \sqrt{\left(\sum_i E_i\right)^2 - \left(\sum_i \vec{p}_i\right)^2}, \tag{7.7}$$

where E_i corresponds to the total energy of the i$^{\text{th}}$ particle and $\vec{p}_i$ denotes its (three) momentum. The invariant mass is, as its name suggests, invariant and consequently is the same in every reference frame. In the CMF, the total momentum is zero by definition and therefore the momenta of the photons must be

$$\vec{p}_{\gamma_1}^{\,\text{CMF}} = -\vec{p}_{\gamma_2}^{\,\text{CMF}} \tag{7.8}$$

and the invariant mass reduces to

$$m^{\text{CMF}} = \sqrt{\left(\sum_i E_i^{\text{CMF}}\right)^2} = \sum_i E_i^{\text{CMF}}. \tag{7.9}$$

Applied to the neutral pion decay yields

$$m_{\pi^0}^{\text{CMF}} = \sum_i E_i^{\text{CMF}}. \tag{7.10}$$

Applying the momentum conservation law leads to the observation that each photon has to carry the energy equivalent to $1/2 \cdot m_{\pi^0}$.

In the laboratory frame (LF), the situation is slightly more complicated since the total momentum of the final state particles in general does not vanish. In the LF, the photon opening angle θ contains information about the π^0 momentum. In the case where the π^0 decays to two photons, the invariant mass is written as

$$m_{\pi^0} = \sqrt{\left(\sum_{i=1}^{2} E_{\gamma_i}\right)^2 - \left(\sum_{i=1}^{2} \vec{p}_{\gamma_i}\right)^2}, \tag{7.11}$$

and its square

$$\begin{aligned} m_{\pi^0}^2 &= E_{\gamma_1}^2 + E_{\gamma_2}^2 + 2E_{\gamma_1}E_{\gamma_2} - \left(\vec{p}_{\gamma_1}^{\,2} + \vec{p}_{\gamma_2}^{\,2} + 2\vec{p}_{\gamma_1}\vec{p}_{\gamma_2}\right) \\ &= \left(E_{\gamma_1}^2 - \vec{p}_{\gamma_1}^{\,2}\right) + \left(E_{\gamma_2}^2 - \vec{p}_{\gamma_2}^{\,2}\right) + 2E_{\gamma_1}E_{\gamma_2} - 2\vec{p}_{\gamma_1}\vec{p}_{\gamma_2} \\ &= P_{\gamma_1} + P_{\gamma_2} + 2E_{\gamma_1}E_{\gamma_2} - 2\vec{p}_{\gamma_1}\vec{p}_{\gamma_2}. \end{aligned} \tag{7.12}$$

Here, the four momentum of the i$^{\text{th}}$ photon has been defined as $P_{\gamma_i} = \left(E_{\gamma_i}, \vec{p}_{\gamma_i}\right)$. Without loss of generality, it can be assumed γ_1 propagates along the z axis. Therefore, its four momentum vector reads

$$P_{\gamma_1} = \left(E_{\gamma_1}, \vec{p}_{\gamma_1,x}, \vec{p}_{\gamma_1,y}, \vec{p}_{\gamma_1,z}\right) = \left(E_{\gamma_1}, 0, 0, E_{\gamma_1}\right). \tag{7.13}$$

This expression used the fact that a (real) photon has no mass and thus its energy and momentum are the same, $\left(E_\gamma = P_\gamma\right)$. The four momentum vector of the second photon, defined to propagate in the $x-z$ plane, is given by

$$P_{\gamma_2} = \left(E_{\gamma_2}, \vec{p}_{\gamma_2,x}, \vec{p}_{\gamma_2,y}, \vec{p}_{\gamma_2,z}\right) = \left(E_{\gamma_2}, E_{\gamma_1} \cdot \sin\theta, 0, E_{\gamma_1} \cdot \cos\theta\right). \tag{7.14}$$

Using Equations 7.13 and 7.14 in Equation 7.12 yields

$$\begin{aligned} m^2_{\pi^0} &= P_{\gamma_1} + P_{\gamma_2} + 2E_{\gamma_1}E_{\gamma_2} - 2\vec{p}_{\gamma_1}\vec{p}_{\gamma_2} \\ &= ... \\ &= 2E_{\gamma_1}E_{\gamma_2} \cdot (1 - \cos\theta)\,, \end{aligned} \tag{7.15}$$

and consequently,

$$m_{\pi^0} = \sqrt{2E_{\gamma_1}E_{\gamma_2} \cdot (1 - \cos(\theta))}. \tag{7.16}$$

7.4.3 Neutral Pion Reconstruction Chain

Once the LArTPC data set was prepared for the application of the ML techniques, the reconstruction of neutral pions can be performed. In collaboration with a group working at SLAC, a π^0 reconstruction chain was developed and made available in [130]. The chain makes use of the ML techniques presented in Section 7.1. When running the reconstruction chain on a LArTPC data set, an event-by-event loop executes operations according to the following (and simplified) pseudo-code:

- Set the semantics:
  Obtain the class scores for each non-zero voxel as described in Section 7.1.2. Proceed with the next event if there are no EDEPs classified as shower-like.

- Reconstruct shower fragments:
  This step clusters shower-like EDEPs into locally dense fragments using a DBSCAN algorithm. Proceed with the next event if there is no shower fragment in the event.

- Reconstruct shower primaries:
  Identify those shower fragments that initiated a shower as shower primaries. That is done using the GNN described in Section 7.1.4. For each of the identified primary fragments, associate a unique shower object with it. Proceed with the next event if there is no shower fragment in the event.

- Reconstruct the start points of the shower primaries:
  Identify the starting points of each shower primary. using the output from the PPN described in Section 7.1.3.

- Reconstruct the directions of the shower primaries:
  The direction of each shower primary is reconstructed using a PCA with a variable number of EDEPs, as described in Section 7.2.

- Reconstruct shower clusters:
  This step is used to merge shower fragments into shower clusters, using the GNN described in Section 7.1.4.

- Reconstruct the energies of the shower clusters:
  For every shower cluster, sum up the energies of all EDEPs to obtain the cluster' reconstructed energies. If a Fudge factor has been defined in the chain configuration, it will be taken into account.

- Reconstruct the types of the shower clusters:
  Obtain the type (either electron-like or photon-like) for every shower cluster as described in Section 7.3.

- Identify shower clusters which are contained within the fiducial volume:
  The fiducial volume can be defined using the chain's configuration file. Based on this definition, every shower cluster that has > 1 EDEP outside of the fiducial volume is marked with a flag telling that the shower cluster is not fully contained within the volume.

- Identify π^0 decays:
  This step identifies those pairs of shower clusters whose back-propagated direction estimates are in a good angular agreement with a track-labelled PPN point, which likely is the π^0 decay vertex. If no cluster pair was identified as products from a π^0 decay, proceed with the next event.

- Recalculate the shower cluster's directions:
  The reconstructed positions of the π^0 decay vertex and the shower cluster's start point can be used to estimate the cluster's directions. If enabled in the chain's configuration, the directions of both shower instances will be recalculated based on the π^0 decay point and the corresponding cluster's start position.

- Compute the masses of the identified π^0 decays:
  Use Equation 7.16 and the reconstructed shower clusters' properties, directions and energies, to obtain the π^0 mass.

The performance of the π^0 reconstruction chain as described above is summarised in Section 7.4.4.

7.4.4 Neutral Pion Reconstruction Performance

To estimate the performance of the ML-based π^0 reconstruction chain as described in Section 7.4.3, the efficiency and the purity of matching photon-pairs to neutral pions have been defined as follows:

$$\text{Efficiency} = \frac{\text{Number of all correctly matched } \pi^0}{\text{Number of all true } \pi^0} \tag{7.17}$$

$$\text{Purity} = \frac{\text{Number of all correctly matched } \pi^0}{\text{Number of all reconstructed } \pi^0} \tag{7.18}$$

For a pair of showers being classified as *correctly matched*, the reconstructed start points of both involved showers need to be close (≤ 20 pixel pitches) to the start positions of the true showers originated from a π^0 decay. In addition, the reconstructed showers' directions need to agree with the true shower's directions to better than 20°.

The matching efficiencies and purities were estimated with the sample number 3 (see Section 7.1.1), on which the following event selection cuts were applied:

- An event must contain exactly 1 true π^0.

- The energies of both showers originating from the π^0 decay must be $\geq 20\,\text{MeV}$.

- Both showers originating from the π^0 decay must deposit $\geq 95\,\%$ of their energies within the LAr volume.

From the 20 000 events present in the data sample, 8070 passed the selection cuts. Figure 7.17 shows the matching efficiencies and matching purities as a function of the true π^0 kinetic energy. The results look very promising, with an overall efficiency of 80 % and a corresponding purity of 92 %. Apart from the first two bins, both distributions are flat in the true π^0 kinetic energy space. As described in Section 7.1.1, the kinetic energies of the produced primary neutral pions are in a range of 50 MeV to 400 MeV. However, the primary particles were propagated using a GEANT4 simulation, enabling the production of secondary neutral pions with sometimes low kinetic energies. These secondary neutral pions are responsible for the entries in the first two bins in Figure 7.17.

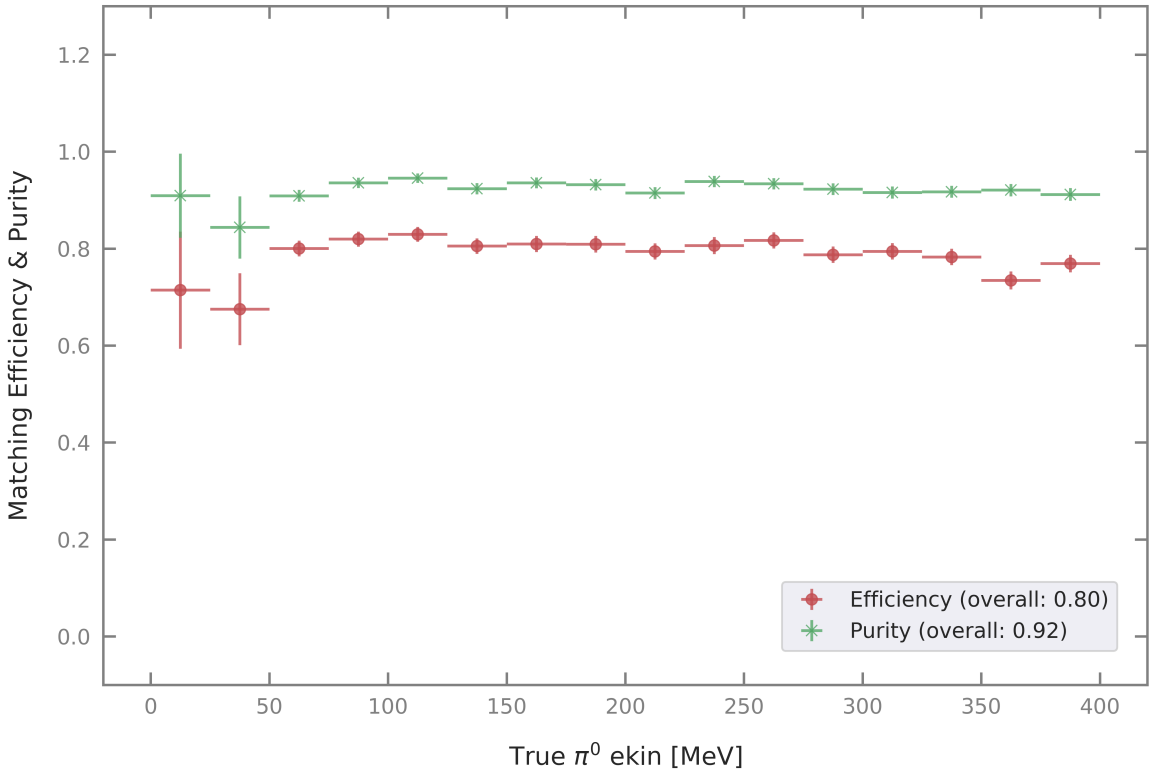

Figure 7.17: Neutral pion matching efficiency and purity as a function of the true π^0 kinetic energy. The uncertainties were calculated using the beta-binomial distribution. This plot was generated using the data sample number 4 (see Section 7.1.1), with the event selection described in the text.

Since the reconstruction accuracy of low-energy showers is expected to be slightly worse than for high energy showers, a breakdown of the γ energies is of interest. Figure 7.18 shows the true energy depositions for photons originated from π^0 decays, divided into two distributions consisting of the photons with leading and the photons with sub-leading energies. Due to the second selection cut, which requires a true γ energy $\geq 20\,\text{MeV}$, neither of the distributions has entries at true γ energies $< 20\,\text{MeV}$. Although both distributions have a relatively broad width, the sub-leading photon distribution peaks at roughly 80 MeV whereas the leading photon distribution peaks at about 200 MeV.

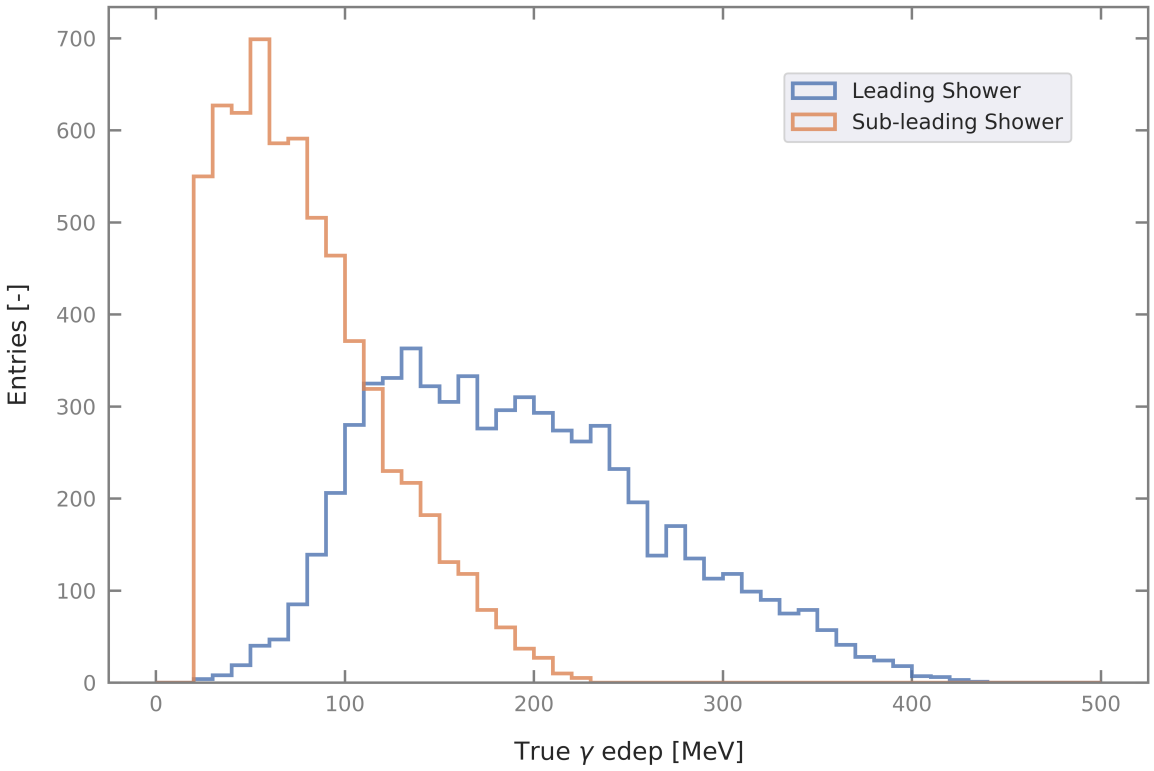

Figure 7.18: True energy depositions of photons produced in π^0 decays, broken down into the leading and the sub-leading γ energy distributions. This plots was generated using the data sample number 4 (see Section 7.1.1), with the event selection described in the text.

Figure 7.19 shows the matching efficiencies and purities as a function of the true sub-leading γ energy. As expected, the matching efficiency is not as flat as before but decreases slightly with decreasing energy of the sub-leading photon at energies $\lesssim 100\,\mathrm{MeV}$. This observation is ascribed to the more difficult reconstruction of showers with lower energy depositions, which, for example, affects the direction estimation and thus the π^0 matching performance.

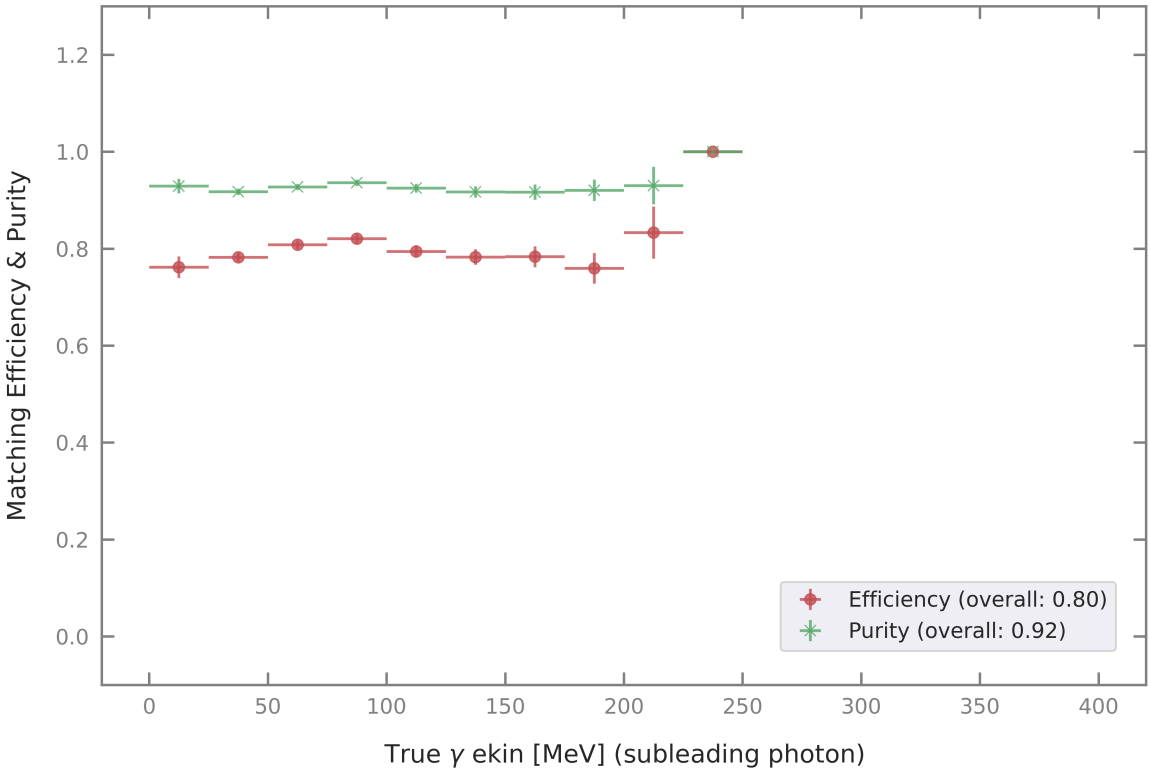

Figure 7.19: Neutral pion matching efficiency and purity as a function of the sub-leading γ true kinetic energy. The uncertainties were calculated using the beta-binomial distribution. This plot was generated using the data sample number 4 (see Section 7.1.1), with the event selection described in the text.

Figure 7.20 depicts the reconstructed π^0 masses, with a breakdown of the wrongly and correctly matched neutral pions. The reconstructed π^0 mass peaks at about 131.0 MeV with a width of approximately 10.3 MeV (Gaussian fit). To obtain this result, a Fudge factor of 1.205 as obtained from Figure 7.12 was applied to the shower energy reconstruction. The reconstructed π^0 mass distribution peaks at an energy which is about 3 % lower than the expected (134.9766 ± 0.0006) MeV. However, the most probable value of the distribution is in agreement with the expectation. It appears that the distribution is slightly asymmetric, with a tail towards lower reconstructed π^0 masses. That is explained by missing energy depositions in individual showers. The absence of such a tail at the high energy part of the histogram indicates that the shower clustering performs well and does not merge too many shower fragments. The reconstructed π^0 mass of wrongly matched showers is approximately distributed uniformly across the phase space shown in Figure 7.20.

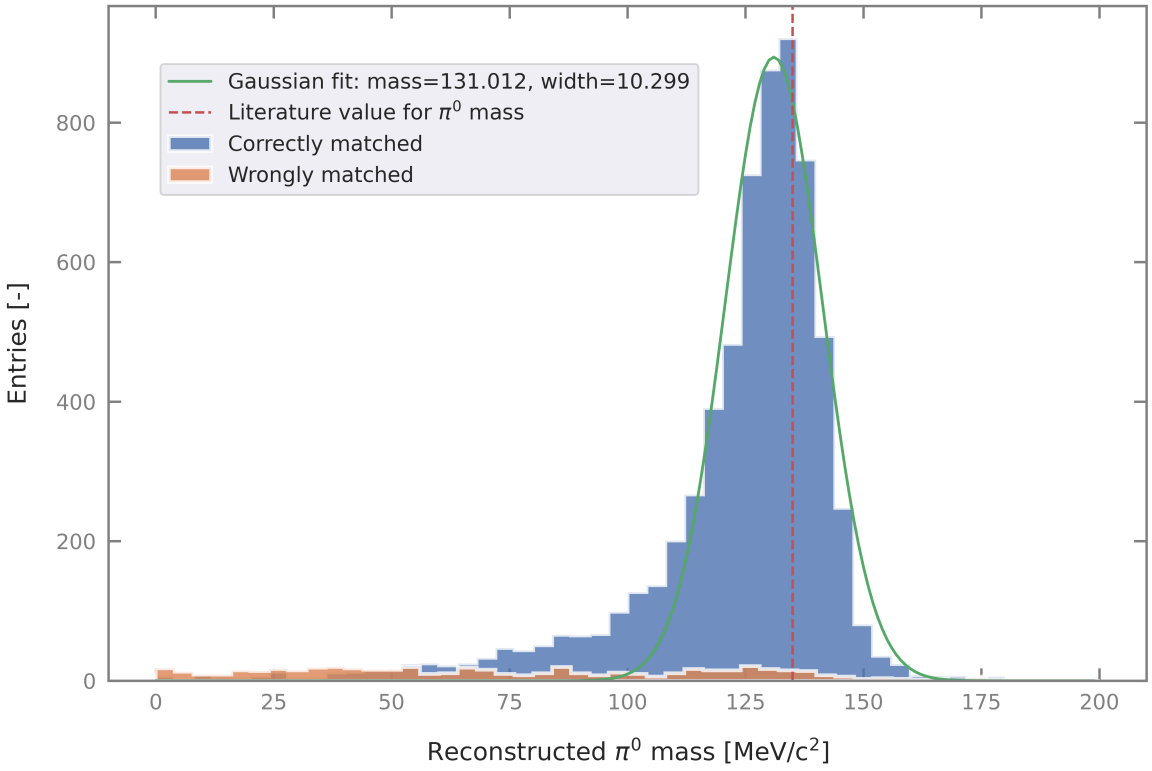

Figure 7.20: Reconstructed π^0 mass peak showing the distributions of photon-pairs classified as correctly matched (blue) and wrongly matched (orange). The green line corresponds to a fitted normal distribution, which peaks at about 131.0 MeV, with a width of about 10.3 MeV. A Fudge factor of 1.205 was applied on each of the reconstructed shower's total energies. The dashed red line indicates the literature value for the π^0 mass. An asymmetry of the distribution can be observed, with a tail towards lower reconstructed π^0 energies. Missing energy depositions in individual showers could explain this observation. This plot was generated using the data sample number 4 (see Section 7.1.1), with the event selection described in the text.

Figure 7.21 shows the event display of a correctly matched π^0. More of them can be found in Section A.4.

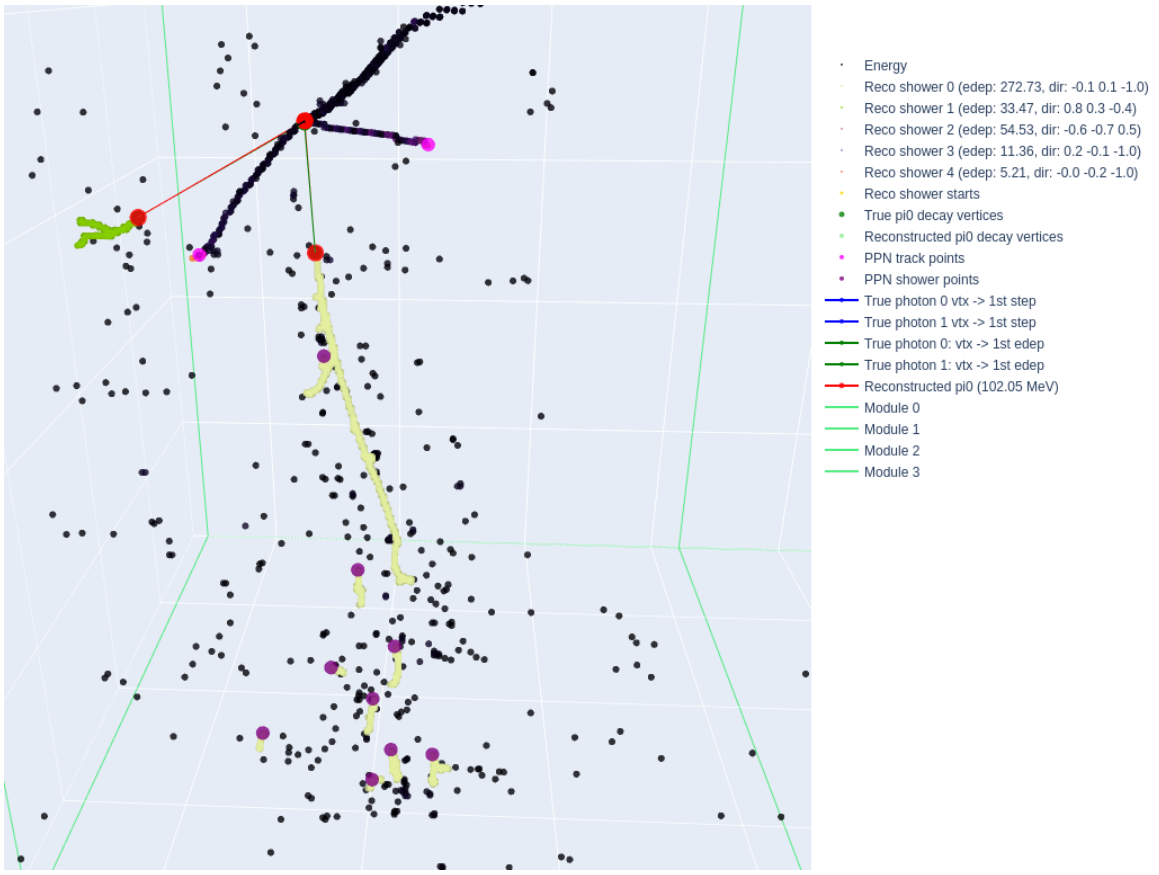

Figure 7.21: Event display of a correctly reconstructed π^0, event ID 32 from data sample number 4 (see Section 7.1.1). Light green lines indicate the module edges from the ArgonCube 2x2 Demonstrator (see Section 5.1.5). Energy depositions with a semantic class other than shower-like are drawn as black points. The coloured EDEPs correspond to the shower clusters, with the colour code representing the cluster number. Light and dark purple points represent track-like and shower-like points from the PPN, respectively. The reconstructed green and yellow showers have been correctly matched (indicated with the red dots and lines) to a π^0 decay, with a reconstructed π^0 mass of 102.05 MeV (no Fudge factor applied).

Several event displays without any or with a wrongly reconstructed π^0 were examined to understand the origin of failures in the π^0 reconstruction. Figures 7.22, 7.23, 7.24, and 7.25 show representative event displays to explain the most important failures happening in the π^0 reconstruction chain, which are:

- Figure 7.22:
  More than 2 photon-like showers are pointing to the same π^0 vertex candidate.
- Figure 7.23:
  No (shower-like) PPN point at the shower start position. Mistakes in the semantic segmentation have been discussed in Section 7.1.2, and confusion matrices are shown in Figures 7.4 and 7.5.
- Figure 7.24:
  Inaccurate shower direction estimation.
- Figure 7.25:
  Mistake in the shower fragment clustering.

Although the performance of the π^0 reconstruction chain is already rather good, these points have to be addressed for an improvement of the π^0 reconstruction accuracy.

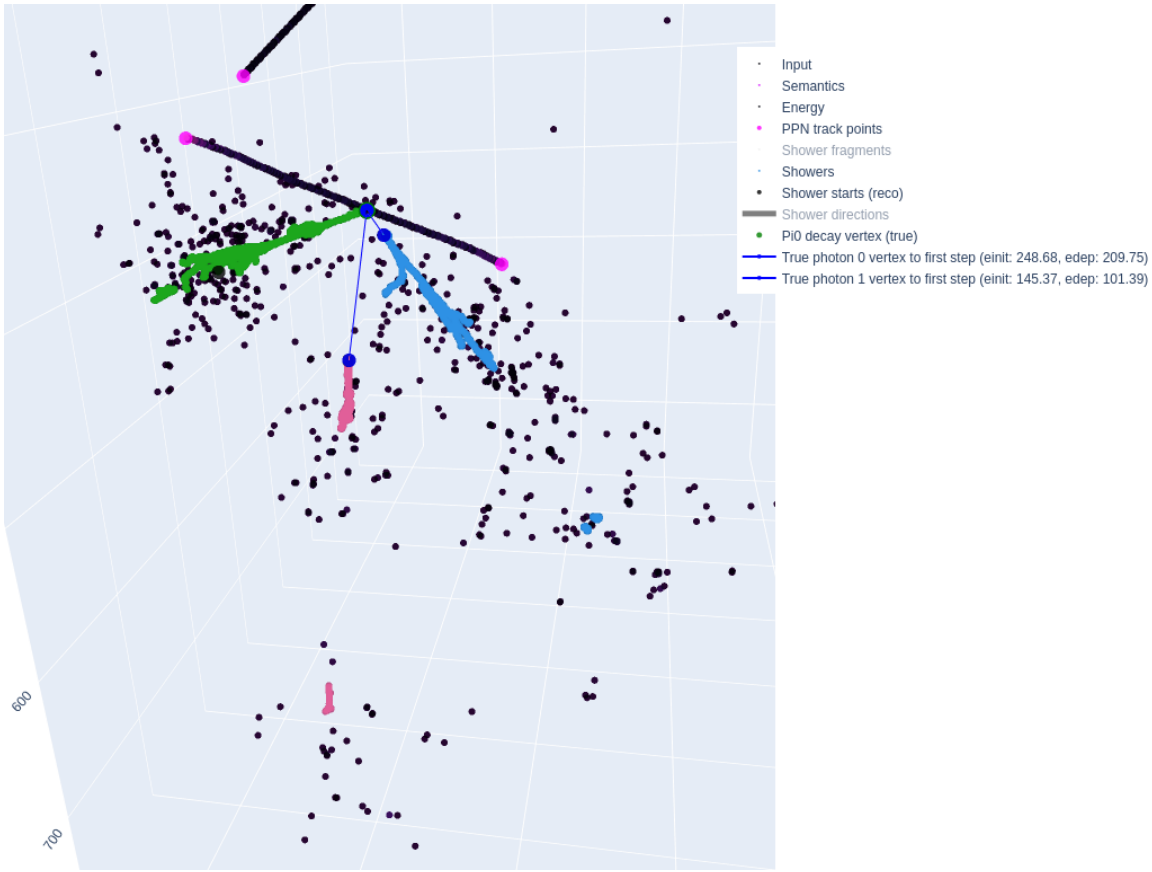

Figure 7.22: Event display with no reconstructed π^0, event ID 21 from data sample number 3 (see Section 7.1.1). Energy depositions with a semantic class other than shower-like are drawn as black points. The coloured EDEPs correspond to the shower clusters, with the colour code representing the cluster number. Light purple points represent track-like points from the PPN. The blue dots indicate the true π^0 decay vertex and the first EDEPs of the originating photons. Since three showers point to the same track-like PPN point (below the topmost blue dot), the matching algorithm does not try to match a pair of showers to a π^0 decay. The correct identification of the shower as being initiated by an electron would resolve this problem. Another possibility would be the rejection of showers starting very close to a π^0 candidate vertex position (proximity method in the reconstruction chain).

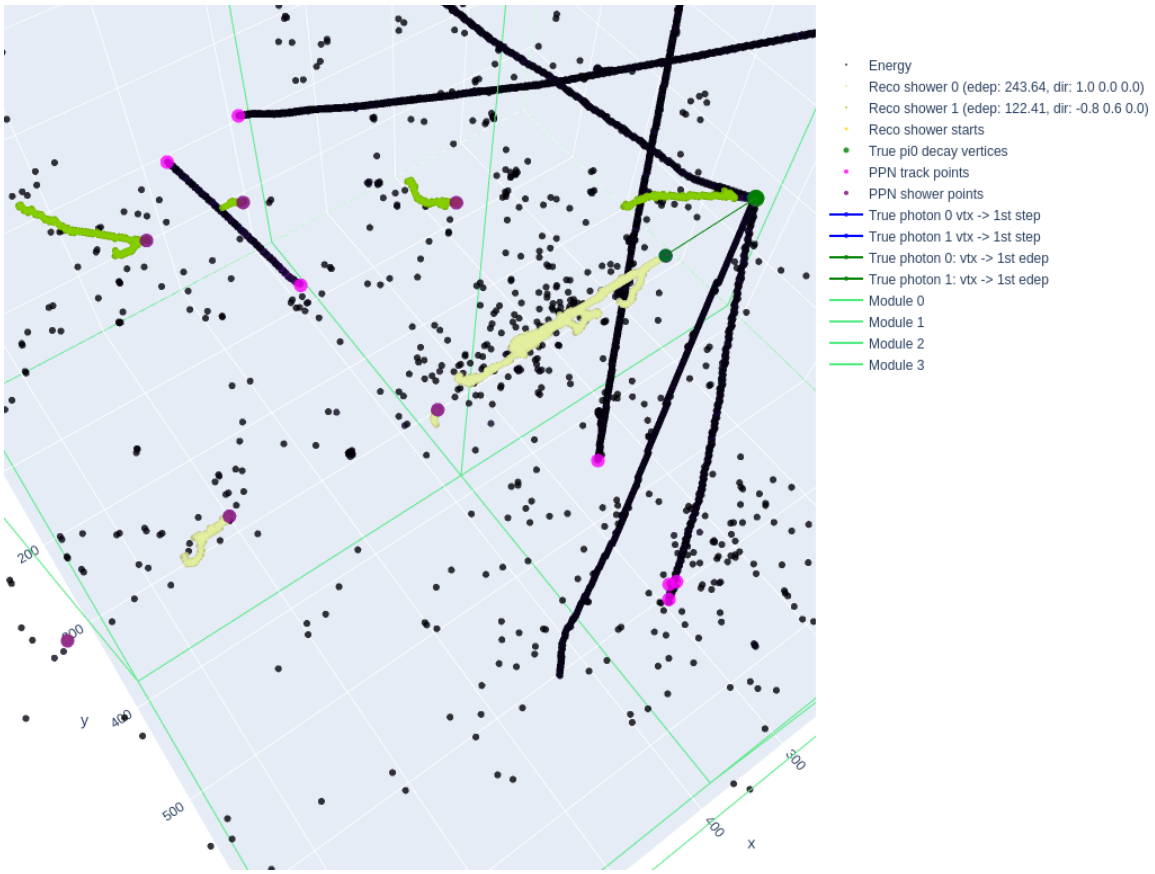

Figure 7.23: Event display with no reconstructed π^0, event ID 97 from data sample number 4 (see Section 7.1.1). Energy depositions with a semantic class other than shower-like are drawn as black points. The coloured EDEPs correspond to the shower clusters, with the colour code representing the cluster number. Light and dark purple points represent track-like and shower-like points from the PPN, respectively. The reconstructed green and yellow showers should have been matched to a π^0 decay (as indicated with the green line and dots). However, a mistake in the semantic segmentation of the EDEPs close to the π^0 decay vertex affected that the green shower has no shower-like PPN point at its start position. The problem of wrongly classified EDEPs around interaction vertices was discussed in Section 7.1.2, in particular with the Figure 7.5.

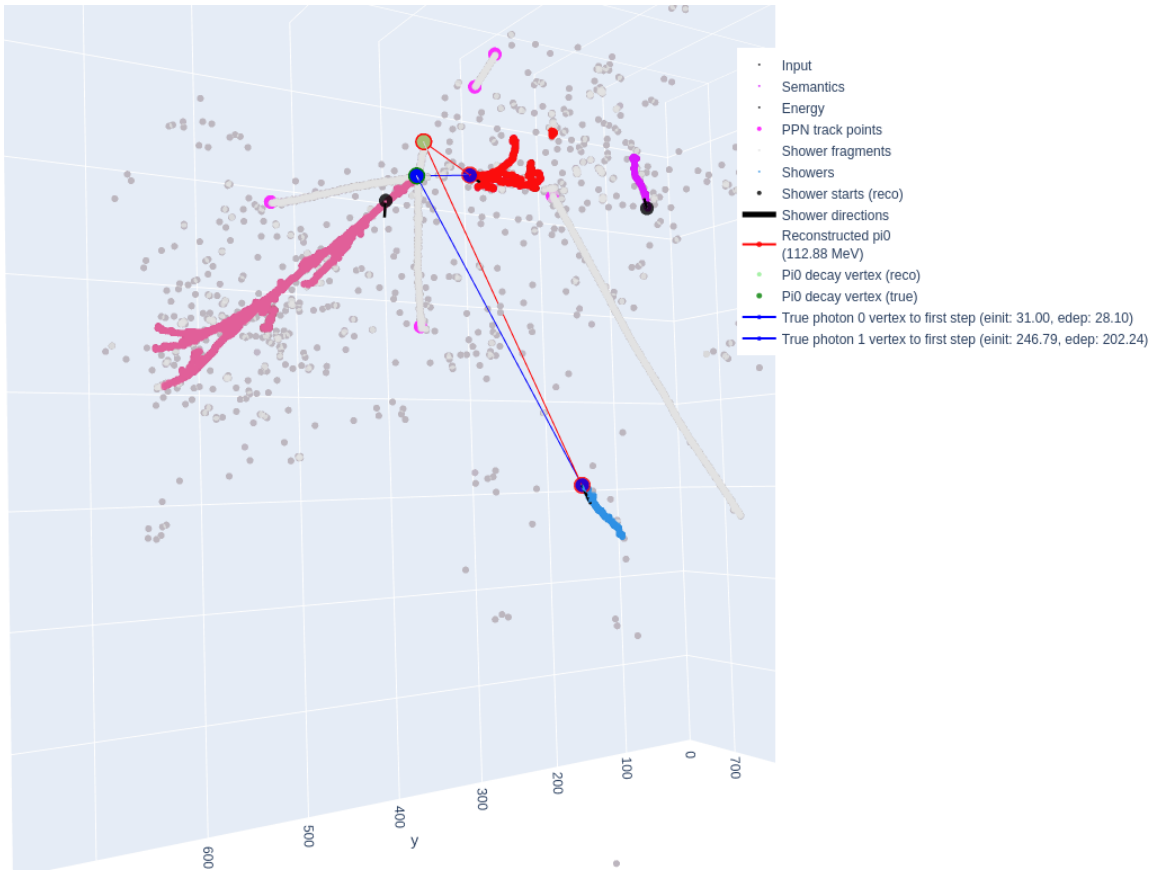

Figure 7.24: Event display with a wrongly reconstructed π^0, event ID 55 from data sample number 3 (see Section 7.1.1). Energy depositions with a semantic class other than shower-like are drawn as grey points. The coloured EDEPs correspond to the shower clusters, with the colour code representing the cluster number. Purple points represent points from the PPN. The blue dots indicate the true π^0 decay vertex and the first EDEPs of the originating photons, and the red dots and lines correspond to the wrongly matched shower start and π^0 decay vertex. The blue and the red shower have been classified as wrongly matched pair since the true π^0 decay vertex was not reconstructed correctly. A better shower direction estimate could have led to a correctly matched π^0.

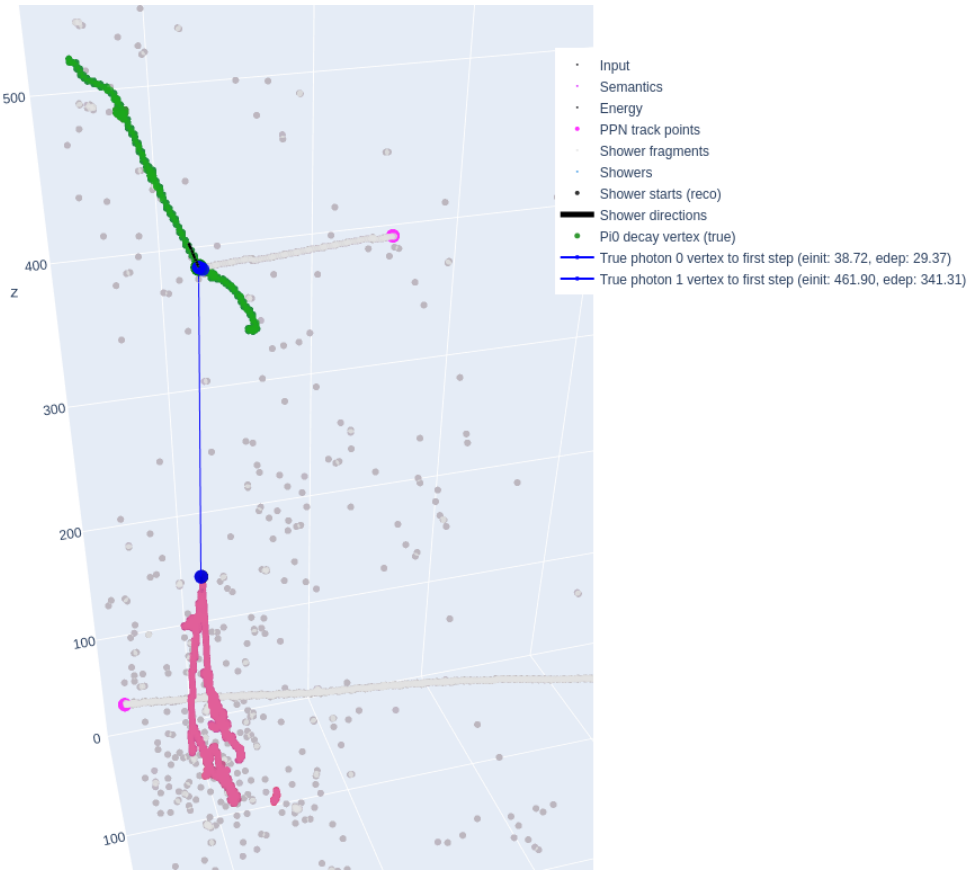

Figure 7.25: Event display with a wrongly reconstructed π^0, event ID 28 from data sample number 3 (see Section 7.1.1). Energy depositions with semantic class other than shower-like are drawn as gray points. The coloured EDEPs correspond to the shower clusters, with the colour code representing the cluster number. Purple points represent points from the PPN. The blue dots indicate the true π^0 decay vertex and the first EDEPs of the originating photons. The red shower and the lower part of the green shower should have been identified as a π^0 decay. However, due to a mistake in the shower clustering, two showers have been merged to the green one.

7.5 Outlook to Further Studies

Up to now, the event reconstruction was trained and tested with particle interactions simulated within a bare LAr volume. The following steps would involve the implementation of specific detector components, e.g. those from the ArgonCube 2x2 Demonstrator (Section 5.1.5), within the simulation. Such components introduce inactive volumes, where no EDEPs can be detected, and thus the particle traces might appear incoherent with gaps. Simulating particle interactions with included detector geometries will yield more realistic data samples, which can be used to train the neural networks used for the ML-based reconstruction. Using such samples for the validation of the reconstruction chain performance will be very interesting and valuable for the further development of the automated event reconstruction in LArTPCs.

In the next step, more realistic models, e.g. for the charge diffusion, should be implemented in the simulation. The reconstruction chain then should be tested and validated with real data acquired with one of the ArgonCube prototypes, preferably with the ArgonCube 2x2 Demonstrator hosting four modules. It is expected that the event reconstruction will not perform very well at this stage just because the different detector responses have not yet been implemented within the simulation. To name a few, energy thresholds, finite detector resolutions, and electronics noise can be reasons for discrepancies. Furthermore, the UResNet used for the semantic segmentation has not yet been trained on digitised data as provided by the ArgonCube charge readout system. Consequently, an iterative data-driven tuning based on the detector response with more realistic models is indispensable.

Finally, the reconstruction can be used to select a sample of neutral pion decays to reconstruct the π^0 rest mass to be compared with the literature value. The reconstructed π^0 mass distribution can provide information about the energy reconstruction scale and possible biases. Of course, the full reconstruction chain could also be used to select other types of events interesting for the detector calibration or physics studies, including neutrino interactions within a modular LArTPC.

Chapter 8

Summary and Outlook

The data collected in neutrino-oscillation experiments make it possible to study the fundamental properties of nature. These experiments showed that the three known neutrinos all have a different mass, which is not predicted by the SM where these particles are massless. How the neutrino mass eigenstates are ordered is one of the open fundamental questions in Particle Physics. Furthermore, it is not yet fully understood how much neutrinos violate CP-symmetry. Solving this problem might shed light on the observed asymmetry between the amount of matter and antimatter in the Universe, as pointed out in Section 2.2.4.

The future neutrino-oscillation experiment DUNE, which is currently under construction, aims to answer those questions (Section 2.3). For this purpose, neutrino detectors with unprecedented mass and extraordinary sensitivity to the produced signals are needed to provide high-precision data samples with enough statistics. Due to their scalability to large detectors and their excellent particle tracking and calorimetric capabilities, DUNE will employ the LArTPC technology in the FD and the ND.

ArgonCube is a novel concept for LArTPCs that segments the total detector volume into several electrically and optically isolated LArTPC modules sharing a common cryostat (Section 4.1). That has the advantages of smaller cathode bias voltages needed for the TPC operation and less energy stored within the electric TPC field, leading to a reduced risk of damage in the case of HV breakdowns. The inactive material originating from the ArgonCube module structure is reduced using new technology for electric field shaping; a sheet of highly resistive material laminated on a fibre-glass reinforced resin (G-10) is used as a low-profile electric field shell (Section 4.2). This technology also slows down the energy released in the case of an electric breakdown and increases the reliability of the TPC operation with a reduced number of components.

The ArgonCube collaboration developed a pixelated charge readout system to provide unambiguous 3D particle tracking with high granularity (Section 4.3). Compared to the traditionally used projective wire readout systems, a pixelated charge readout significantly simplifies the event reconstruction, especially in high-multiplicity environments, and thus enables an improved accuracy for the detected signals. The contained scintillation light produced within ArgonCube modules allows for an enhanced time resolution to detect these light signals. Two novel light detection systems were developed by the ArgonCube collaboration, allowing for measuring the scintillation light signals with a very precise time resolution (Section 4.4). That helps assign detached energy depositions to individual interaction vertices, thus increasing

the accuracy of the event reconstruction in high-multiplicity environments. Due to these novelties in the field, the ArgonCube concepts found application in the DUNE ND. Furthermore, it has been proposed to apply the ArgonCube concepts to the fourth DUNE FD module (Section 6.5).

I was involved in the ArgonCube R&D program, where I contributed to the development of the various ArgonCube technologies. Furthermore, I was taking part in the design and assembly of several prototype detectors used to test these technologies. Those tests often required cryogenic equipment, for which I developed significant parts of the slow-control system to monitor the status of the hardware (Section 5.2). During the experiments, I engaged in the data taking periods, and I often drove the data processing and analysis. Their results provided input for improvements of the detector prototypes or related hardware and software.

In 2018, the V1PER TPC, instrumented with the LArPix-V1 pixel readout, was assembled and tested (Section 5.1.1). That was the first time an ArgonCube pixel readout, using cold electronics, provided unambiguous 3D particle tracking in a LArTPC. However, the first version of the LArPix ASIC was daisy-chained with one MISO and one MOSI only. During the experiment, a faulty chip or connection caused a communication failure of all ASICs located downstream of the malfunction, causing the outermost rows of chips – 12 out of 28 in total – to stop responding. This problem was solved in the LArPix-V2 ASIC by integrating 4 MISO and 4 MOSI lines.

Later in 2018, the RS-TPC prototype was designed, assembled, and operated (Section 5.1.2). We demonstrated the feasibility of a low-profile foil with a high sheet resistance to produce and shape electric fields with this prototype. The RS-TPC was the first LArTPC that employed such a resistive field shell. This experiment gave rise to the development of a larger-scale electric field shell. The result was implemented in the Module-0 prototype, as discussed later.

In 2019, several experiments were conducted to test the cold extraction and re-insertion of an ArgonCube module (Section A.3). These experiments showed the difficulties associated with the mechanical structure and LAr purity requirements for the module extraction and re-insertion. The findings from those experiments influenced the cryogenics scheme and the module structure design of the DUNE ND-LAr detector.

Also, in 2019, designs for the SingleCube and Module-0 prototypes were initiated, and preparations for their installation were conducted.

In 2020, the SingleCube prototype (Section 5.1.3) was assembled and instrumented with one ArCLight module and a LArPix-V2 pixel readout. Based on the findings from the V1PER TPC, the LArPix-V2 was upgraded to serve four MISO and four MOSI lines, allowing for a sophisticated daisy-chaining via the so-called *Hydra* network. The SingleCube experiment showed that signals from the light detection system can trigger the charge readout efficiently. Furthermore, the SingleCube experiment demonstrated the feasibility of matching the charge and the light signals to reconstruct unambiguous 3D LArTPC events.

Later in 2020, the partially instrumented Module-0 (Section 5.1.4) went into operation to test the stability of the enlarged module structure and the field shell, which was laminated on FR-4 panels. In addition, we tested the newly designed LAr purification filter which was located in a LN_2 cryostat pressurised to $\approx 2.4\,\mathrm{bar}$. These tests demonstrated that the purification and cooling performance meet the requirements posed by the Module-0 detector. That was the first time that all

ArgonCube technologies were unified within a single detector.

In 2021, the fully instrumented Module-0 detector went into operation, hosting 8 ArCLight modules, 24 LCMs, and 16 pixelated anode planes with 78400 individual pixels in total. With this first complete ArgonCube module, sixty million cosmic-induced particle interactions were observed. The Module-0 detector instrumented a LAr volume of about $0.43\,\mathrm{m}^3$ with an impressive equivalent of approximately 5.5 million charge-sensitive voxels, and a light readout system with excellent time resolution of $\mathcal{O}(1\,\mathrm{ns})$. That, in my opinion, can be considered without understatement a huge success.

Future work will be to build three more modules identical to Module-0. Four of these modules will populate the ArgonCube 2x2 Demonstrator (Section 5.1.5), which will form the core component of the ProtoDUNE-ND (Section 6.4), that will be exposed to the NuMI beam at FNAL. With its active mass of about 2.4 t of LAr exposed to the high-intensity neutrino beam, ProtoDUNE-ND will acquire millions of neutrino interactions per year of exposure. The collected data samples will serve as a platform to extensively test the ArgonCube concepts.

For the analysis of the ProtoDUNE-ND data, an automated and accurate LArTPC event reconstruction is required. I joined the SLAC group in 2020 to contribute to the ML-based event reconstruction in LArTPCs, with the focus on π^0 reconstruction (Section 7.4). With a production rate of a few million π^0 per year of exposure of ProtoDUNE-ND, there will be plenty of fully contained π^0 decays to test, tune and benchmark the developed π^0 reconstruction. I'm very curious about the performance of the π^0 reconstruction I developed in the framework of this thesis, and I will be incredibly excited to see the first event and π^0 decay in ProtoDUNE-ND.

In parallel to the ProtoDUNE-ND commissioning, a full-scale DUNE ND-LAr module, with an active size of $1\,\mathrm{m} \times 1\,\mathrm{m} \times 3\,\mathrm{m}$ will be built according to the ND design (Section 6.3). Tests of this full-scale module in a 1.5 m diameter and 4 m tall cylindrical cryostat will be conducted to determine the stability of the cryo-mechanical structure, the HV, and the LAr purity. Furthermore, the full-scale module experiment will test if the noise of the pixelated charge readout and the efficiency of the scintillation light detectors fulfil the specifications for the DUNE ND-LAr component. Once these tests showed to be successful, the ArgonCube collaboration will start production of 40 DUNE ND-LAr modules in 2023. If everything goes as planned, the DUNE FD will start taking data in 2026, and the ND in 2029.

Acknowledgements

First and foremost, I would like to thank Prof. Dr. **Igor Kreslo** for supervising this thesis and giving me the opportunity of working on topics of great current interest. I am thankful for all the dedicated support and open-minded discussions during the last few years. His vast knowledge and intuition in many fields have influenced this work, and more importantly, my thinking. Furthermore, I am grateful for the possibility to attend international schools, workshops and conferences.
A big thank you goes to my external referee and examiner, Prof. Dr. **Alan Bross**.
Also, I would like to thank Prof. Dr. **Peter Wurz** for chairing the examination.
In addition, I am very grateful to Prof. Dr. **Michele Weber** for his instructive scientific guidance and valuable advice related to this thesis.
I thank Dr. **Francesco Piastra** for very helpful and constructive discussions about physics, endless night-shifts, and numerous but definitively too short evenings in local pubs. Thanks also to Dr. **James Sinclair** for very helpful and constructive discussions about structuring this thesis, and, almost as important, for many pleasant hours spent together on our mountain bikes and in the mechanical workshop to fix the bikes. I thank Dr. **Callum Wilkinson** for numerous Bladnoch-Stories, and even more serious discussions about physics.
Furthermore, I would like to thank my fellow students Dr. **Yifan Chen**, Dr. **Patrick Koller**, Dr. **Thomas Mettler**, and Dr. **Patrick Stähli**, for inspiring discussions and countless hours of fun, including experiments with frozen tissues and theories about Lord Nelson's life (and death).
Thanks to **Livio Calivers** for a productive time in the lab, including working with the evaporation chamber. Also, your entertainment with «drum swirls» on the blue and white plastic boxes next to the Grosse Schanze is appreciated.
I am grateful to Dr. **Kazuhiro Terao** and Dr. **Francois Drielsma** for the guidance in any machine-learning related problems. Without their ideas and contributions, the neutral pion reconstruction would never show such good results. Thank you for the fun times during the numerous meetings in Bern, Chicago, Geneva, and Colmar.
Special thank goes to our mechanical and electronics workshop, **Jan Christen**, **Roger Hänni**, **Lino Risch**, **Lorenzo Meier**, and **Camilla Tognina**. Their technical support has been invaluable. Thanks for all the devices I asked you to build (just to be repaired and modified after the first test). Also, I would like to thank our IT service, Dr. **Gianfranco Saccia** and **Marco Indermühle** for all kinds of computing support.
Thanks to **Ursula Witschi** and **Marcella Esposito** for all the administrative support and (almost?) endless patience with physicists like me.
Furthermore, I would like to thank all (former) members of the Institute for the friendly working atmosphere and fruitful discussions in the B52 coffee room.
Last but not least, I would like to thank **Bettina** who has supported me in all my endeavours in good but sometimes stressful times.

Appendix

A.1 COMSOL Simulation of the RS-TPC Electric Field

To understand the effect of the steel frames in the RS-TPC design (see Figure 5.5), the electric field has been simulated using COMSOL[1]. The results are shown in Figure 1. At the edge of the TPC drift volume close to the steel frames, the magnitude of the electric field intensity is slightly larger than in the central region. The field lines, therefore, are bent towards the centre of the TPC's active volume. The maximum electric field distortions in the x (similar for the y) direction are about $\mathcal{O}\left(1\,\mathrm{kV\,cm^{-1}}\right)$ at the very top and bottom of the drift volume and close to the anode and cathode, respectively. However, those distortions rapidly decrease with the distance to the steel frame.

Simulations of the RS-TPC without the two steel frames confirmed the expectation that the electric field lines are no longer bent but describe straight lines between the anode and the cathode.

[1] COMSOL Multiphysics Version 5.2, https://www.comsol.com (accessed: 15.07.2021).

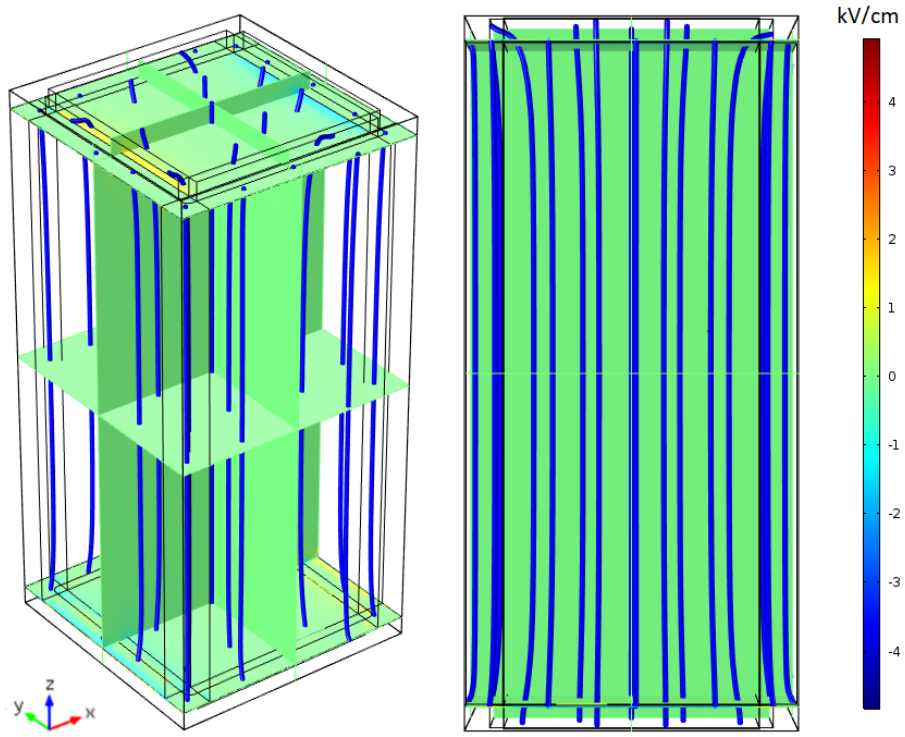

Figure 1: Electric field lines (blue tubes) and the electric field distortions in the x direction simulated with COMSOL Multiphysics. The distortions in the x direction are largest, $\mathcal{O}\left(1\,\mathrm{kV\,cm^{-1}}\right)$, very close to the steel frames but vanish for most of the active volume. The distortions in the y direction (not shown in those figures) are similar to the distortions in the x direction.

A.2 Characterisation of the RS-TPC Electric Field Uniformity

The capability of the resistive shell to shape the electric field has been assessed using cosmic muon candidate tracks producing long and straight ionisation tracks within the RS-TPC. The source code used for this analysis can be found in [131]. During a measurement campaign of about 4 d in July 2018, straight ionisation tracks induced by cosmic particles have been selected. Events with delta electron candidates or more than one track have been rejected for the event selection. The selected data sample consisted of 280 muon candidate tracks with an average of 12.3 hits per track and a most probable track length of 130 mm. Assuming a muon energy of about 4 GeV (see [36]), the expected transverse spread due to MSC described by Equation 2.27 is of $\mathcal{O}(0.1\,\text{mm})$ and thus has been neglected. A PCA has been applied on all hits of a selected event to extract the principal components axis of the muon candidate track. On a statistical basis, electric field non-uniformities would lead to non-zero residual distances from single hits to the principal components axis. Therefore, the hit's deviations from this axis have been studied as a function of the reconstructed position in the RS-TPC. In particular, the active TPC volume has been partitioned in 25 cubic regions (cuboids between the anode and the cathode), as shown in Figure 2.

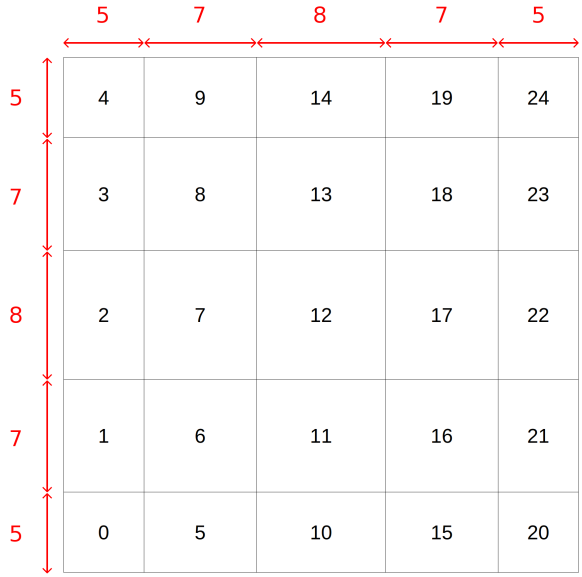

Figure 2: Top view to the active volume of the RS-TPC divided into 25 regions labelled with black numbers between 0 and 24. The red numbers denote the width and the length of each region in units of conducting strips (see Section 5.1.2).

The distributions of the three coordinates of the shortest vector (residual) from the hits to the principal components axis have been obtained for each region as a function of the z-axis, corresponding to the TPC drift direction. Those distributions for 8 interesting regions are shown in Figures 3 and 4 as profile plots showing the mean x and y components of the residuals for all 280 selected events.

The x and y coordinates of the residuals appear to be distributed around zero with almost no dependence on the z coordinate, indicating that the hits are distributed along a pretty straight line. However, the slightly bent profile plots for the residual's x component in the edge regions number 2 and 22 (Figure 3) indicate some electric

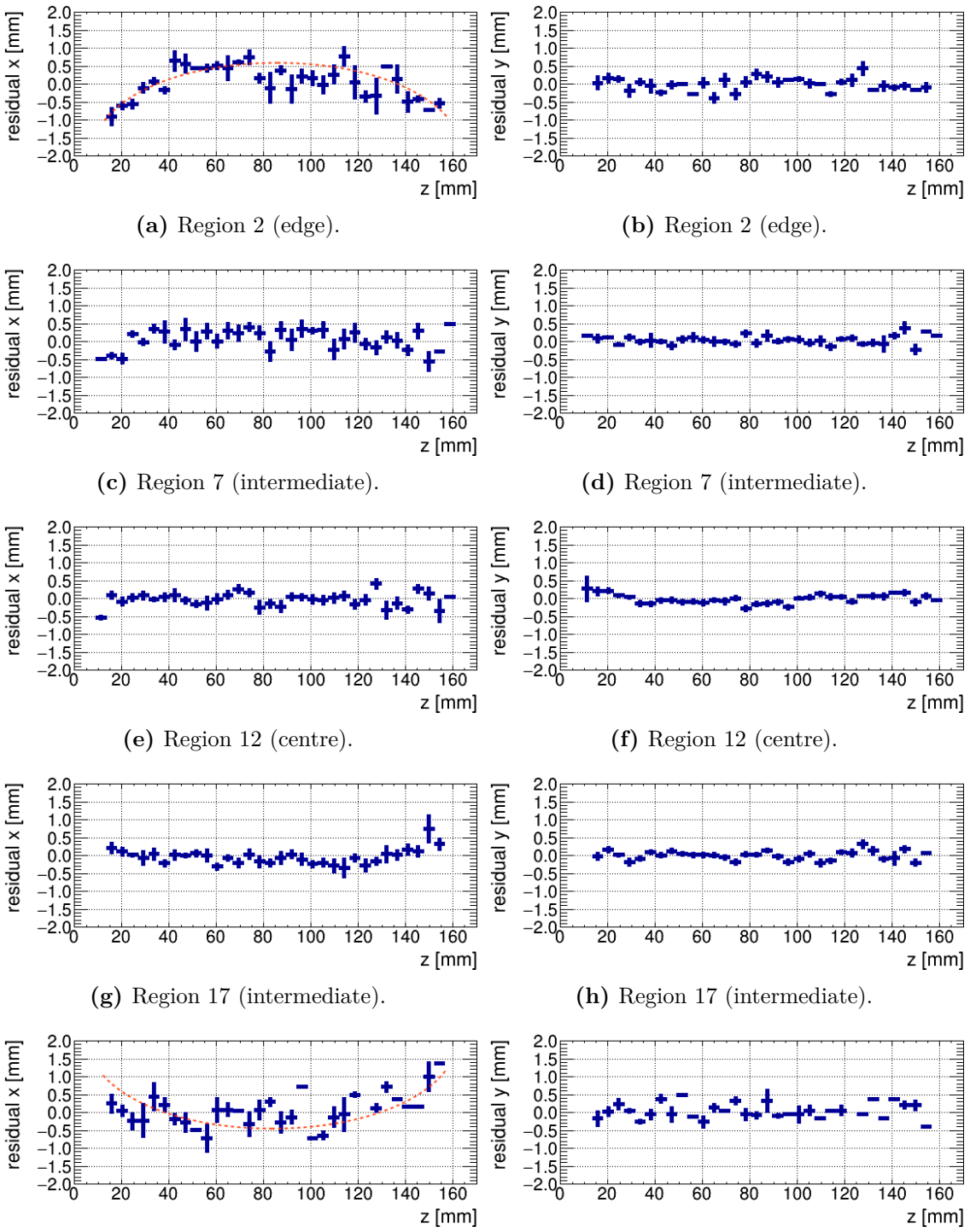

(a) Region 2 (edge). **(b)** Region 2 (edge).

(c) Region 7 (intermediate). **(d)** Region 7 (intermediate).

(e) Region 12 (centre). **(f)** Region 12 (centre).

(g) Region 17 (intermediate). **(h)** Region 17 (intermediate).

(i) Region 22 (edge). **(j)** Region 22 (edge).

Figure 3: The residual's x (left) and y (right) components as a function of the drift distance z for five adjacent regions. Dashed orange lines are used to illustrate the tendency. The statistical uncertainties are shown as errorbars.

field distortions in the x direction near the anode ($z = 0\,\text{mm}$) and the cathode ($z = 150\,\text{mm}$). Despite the limited statistics in those peripheral TPC regions, the x component of the residuals tend to have opposite signs for region numbers 2 and 22. Since the residual y component looks flat for the same two regions as a function of the z coordinate, the distortion of the electric field must be relatively uniform in y direction.

Similar but less pronounced behaviour is observed for regions number 7 and 17 (Figure 4) where the profile plots of the residual y components appear to be slightly bent for hits close to the electrodes. This bending indicates slight electric field distortions in the y direction. Similar to the observations made before, the residual's x component for the regions number 7 and 17 do not deviate significantly from zero, indicating vanishing field distortions in the x direction.

As the ionisation electrons drift along the electric field lines, electrons produced at the edges of the TPC drift volume tend to move outwards and are expected to have more significant deviations from the principal component axis than charges produced at the centre of the TPC drift volume. Furthermore, electrons that start to drift from regions closer to the electrodes will be reconstructed with a smaller x-y deviation than those starting from the centre of the TPC. This is qualitatively consistent with the bent profile plots of the x and y residual components observed in the most peripheral regions number 2, 22, 10 and 14 (Figures 3 and 4). However, for a more quantitative comparison between the predictions obtained by the COMSOL simulation (see Appendix A.1) and the observed deviations, a larger data sample for the periphery regions of the RS-TPC is needed. Since the prototype TPC is relatively small, with a drift-field volume of only $15\,\text{cm} \times 7\,\text{cm} \times 7\,\text{cm}$, the characterisation of the electric field uniformity obtained with the experiment is limited.

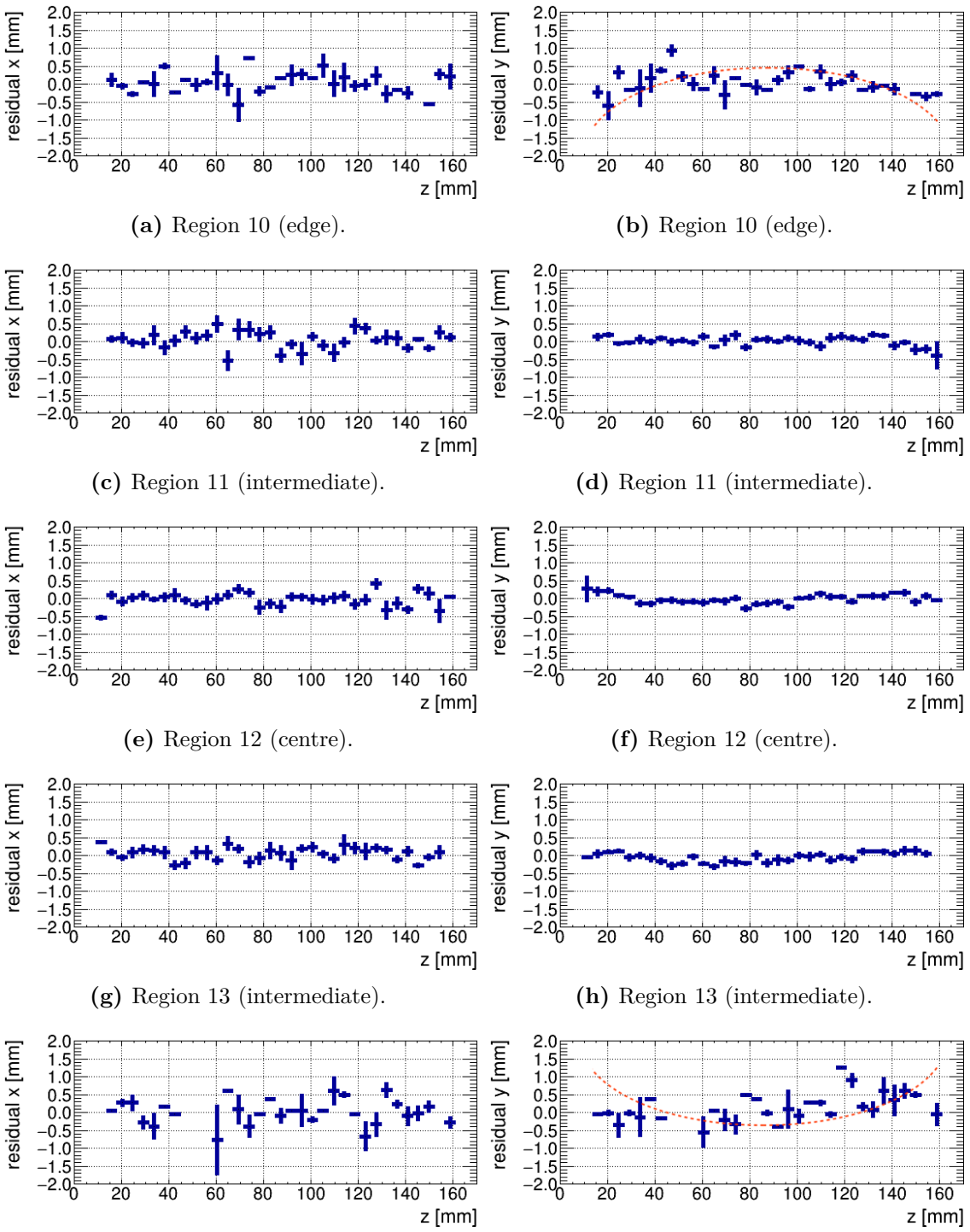

(a) Region 10 (edge). **(b)** Region 10 (edge).

(c) Region 11 (intermediate). **(d)** Region 11 (intermediate).

(e) Region 12 (centre). **(f)** Region 12 (centre).

(g) Region 13 (intermediate). **(h)** Region 13 (intermediate).

(i) Region 14 (edge). **(j)** Region 14 (edge).

Figure 4: The residual's x (left) and y (right) components as a function of the drift distance z for five selected regions. Dashed orange lines are used to illustrate a possible tendency. The statistical uncertainties are shown as errorbars.

A.3 Module Cold Extractions and Re-Insertions

The modular ArgonCube detector design has many advantages, one of which is the ability to extract individual modules from the larger detector to repair or upgrade detector components easily. One of the early ideas of the ArgonCube collaboration has been to extract a module from the cryostat while all other modules in the detector were in operation. In such a way, an individual module could be maintained without losing time in data taking. However, the module cold extraction and re-insertion from and into the LAr filled cryostat needed to be tested for feasibility.

In 2019, several module cold extractions and re-insertions have been conducted for this purpose. An early ArgonCube module and the cryostat of the ArgonCube 2x2 Demonstrator have been utilised for these tests. The aforementioned module, instrumented with the V1PER TPC described in Section 5.1.1, enabled electron lifetime measurements to infer the LAr purity. The right picture from Figure 5.26 shows the employed ArgonCube module with the V1PER TPC on top of the ArgonCube 2x2 Demonstrator. A dummy flange has been mounted at the bottom of the module to seal the cryostat as soon as the module had been extracted from it.

Several difficulties have been identified concerning the module cold extraction. First, the pure LAr in the cryostat must not be contaminated with air. Either the overpressure in the cryostat would need to be high enough to ensure almost no air penetrating the cryostat, or the openings to the cryostat inner volume should be isolated from the atmosphere. Figure 5 depicts two attempts of a module cold extraction. In the left picture, the module has been taken out from the LAr-filled cryostat without having hermetically sealed the inner cryostat volume from the atmosphere, but providing a large flow of GAr out from the cryostat. The right picture in Figure 5 shows the other approach, where a thin plastic enclosure flushed with GAr has been used to prevent air from entering the cryostat. This method had the advantage that no air condensed on the module after having been extracted. However, the plastic enclosure has made it more difficult to access and seal the dummy flange on the cryostat top flange. Secondly, to reduce the time the cryostat would be opened at its top, which posed the risk of LAr contamination, a fast module cold extraction (and re-insertion) would be beneficial. However, the temperature change needed to be slow enough not to damage any of the module components. In particular, the ArCLight bulk structure has been identified to be one of the most critical parts regarding fast and large temperature changes. That certainly was more difficult to ensure during the module insertion process. The third difficulty worth mentioning is the difference between the inner module pressure and its surrounding, e.g. the atmosphere or the inner cryostat volume. Any pressure difference higher than a few mbar would deflect the module walls noticeably. Such deflections would pose the risk of damage to the electronics inside of the ArgonCube module. Hence, either these pressure differences had to be small enough or the module walls thick enough to withstand more considerable pressure differences, at the cost of a larger amount of inactive material between the ArgonCube modules. For these tests, a precise pressure regulator system[2] with a flow rate of $\mathcal{O}$ (100slpm) has been tested. These tests showed the feasibility of maintaining pressure differences of less than 5 mbar between the inner module volume and its surrounding.

[2] Equilibar Series 41, from https://www.equilibar.com (accessed: 01.07.2021).

The tests we performed showed that it would be difficult to extract an ArgonCube module from the cryostat filled with LAr without either spoiling the purity or risking damaged detector parts due to thermal shocks. Apart from those difficulties, the capability to extract individual ArgonCube modules from the cryostat has another disadvantage, namely that every module would need to have its cryogenic system, which would make the total detector very expensive. For those reasons, the DUNE ND-LAr design does not incorporate the possibility of module cold extraction and re-insertion. The ND-LAr component of DUNE is designed to be composed of rows of 5 modules sharing the same support structure, as shown in the right picture of Figure 6.2.

Figure 5: Cold extraction of an early module prototype from the cryostat of the ArgonCube 2x2 Demonstrator filled with LAr. Left: One attempt to extract the module from the cryostat has made use of a large flow of GAr from the inner volume of the cryostat to reduce air entering the vessel. Right: Another attempt made use of a plastic cover flushed with GAr to encapsulate the module and the cryostat opening from the surrounding atmosphere.

A.4 Event Displays of Successfully Reconstructed Neutral Pions

This section shows some properly reconstructed π^0 decays using the ML-based reconstruction chain described in Section 7.4.3.

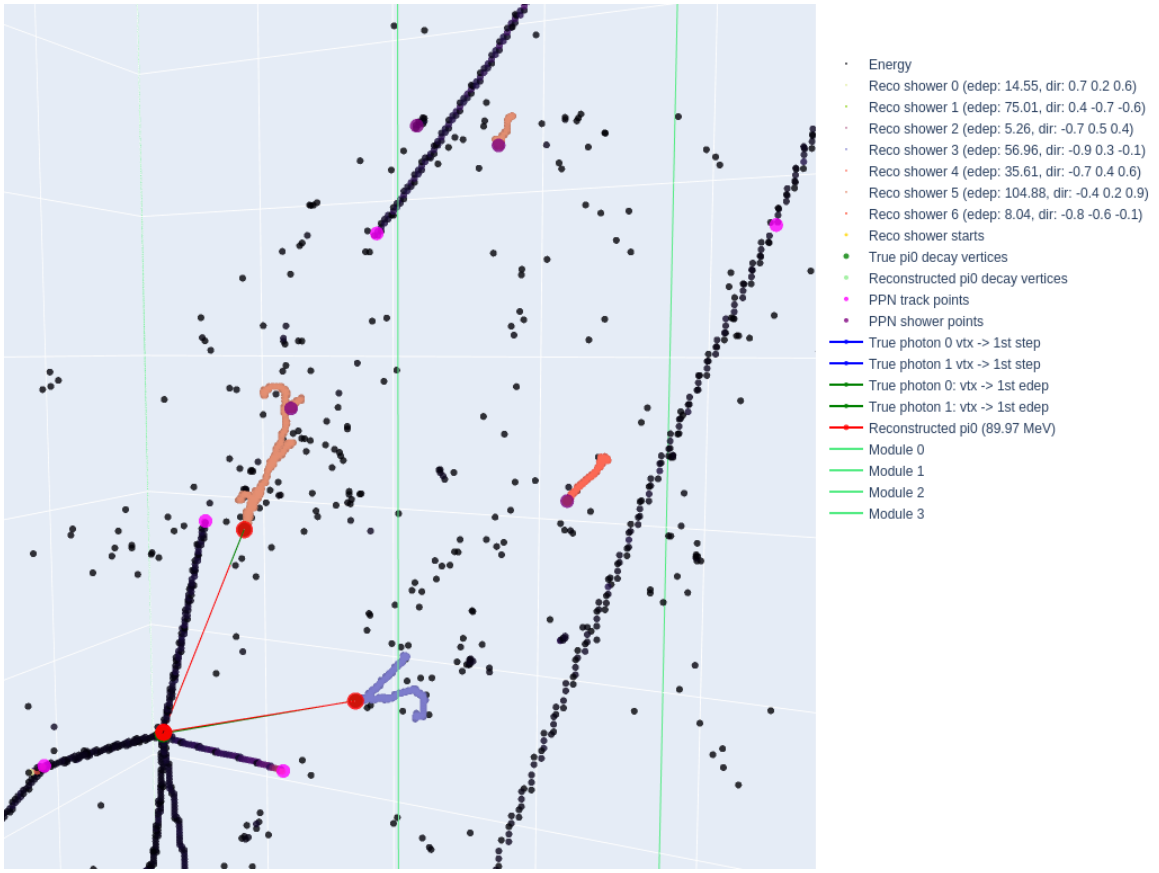

Figure 6: Event display with a correctly reconstructed π^0, event ID 3 from data sample number 4 (see Section 7.1.1). Energy depositions with a semantic class other than shower-like are drawn as black points. The coloured EDEPs correspond to the shower clusters, with the colour code representing the cluster number. Green lines indicate the module edges from the ArgonCube 2x2 Demonstrator (see Section 5.1.5). The π^0 mass has been reconstructed to 89.97 MeV (no Fudge factor applied yet).

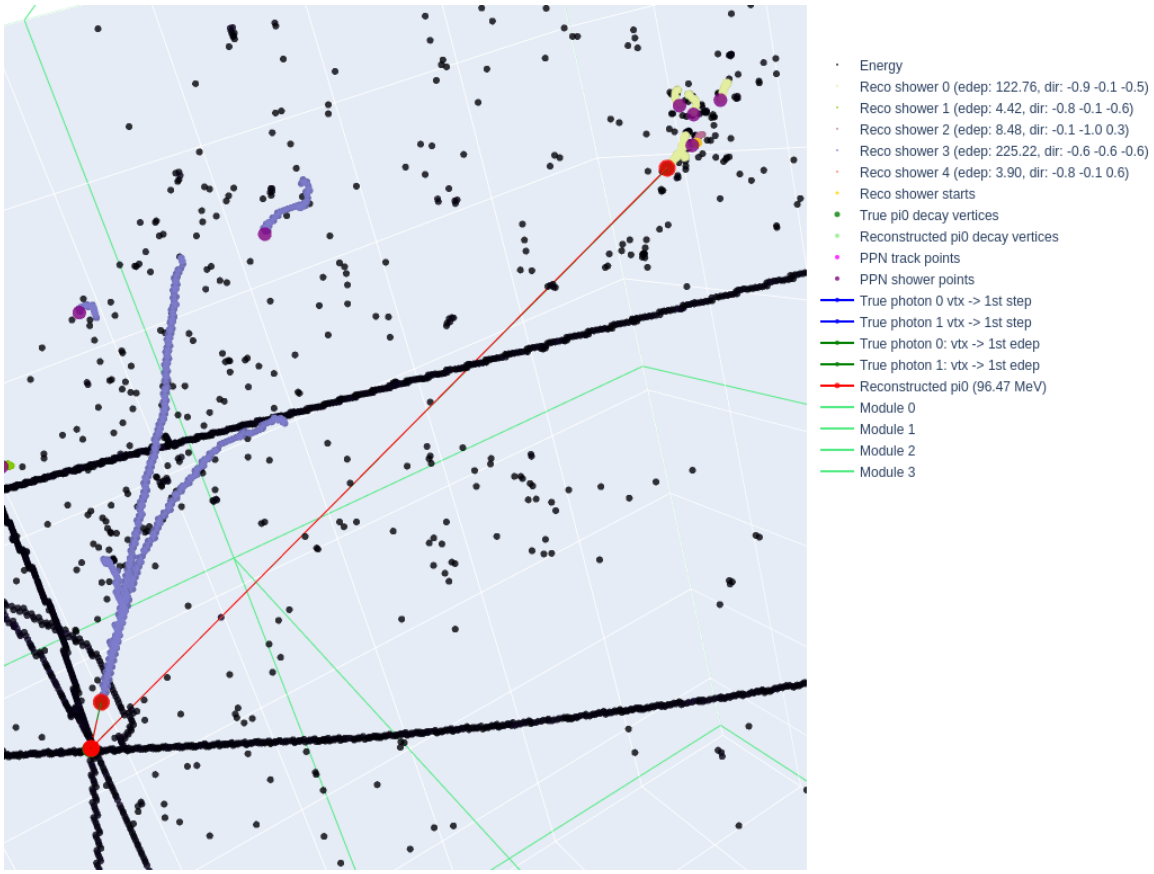

Figure 7: Event display with a correctly reconstructed π^0, event ID 5 from data sample number 4 (see Section 7.1.1). Energy depositions with a semantic class other than shower-like are drawn as black points. The coloured EDEPs correspond to the shower clusters, with the colour code representing the cluster number. Green lines indicate the module edges from the ArgonCube 2x2 Demonstrator (see Section 5.1.5). The π^0 mass has been reconstructed to 96.47 MeV (no Fudge factor applied yet).

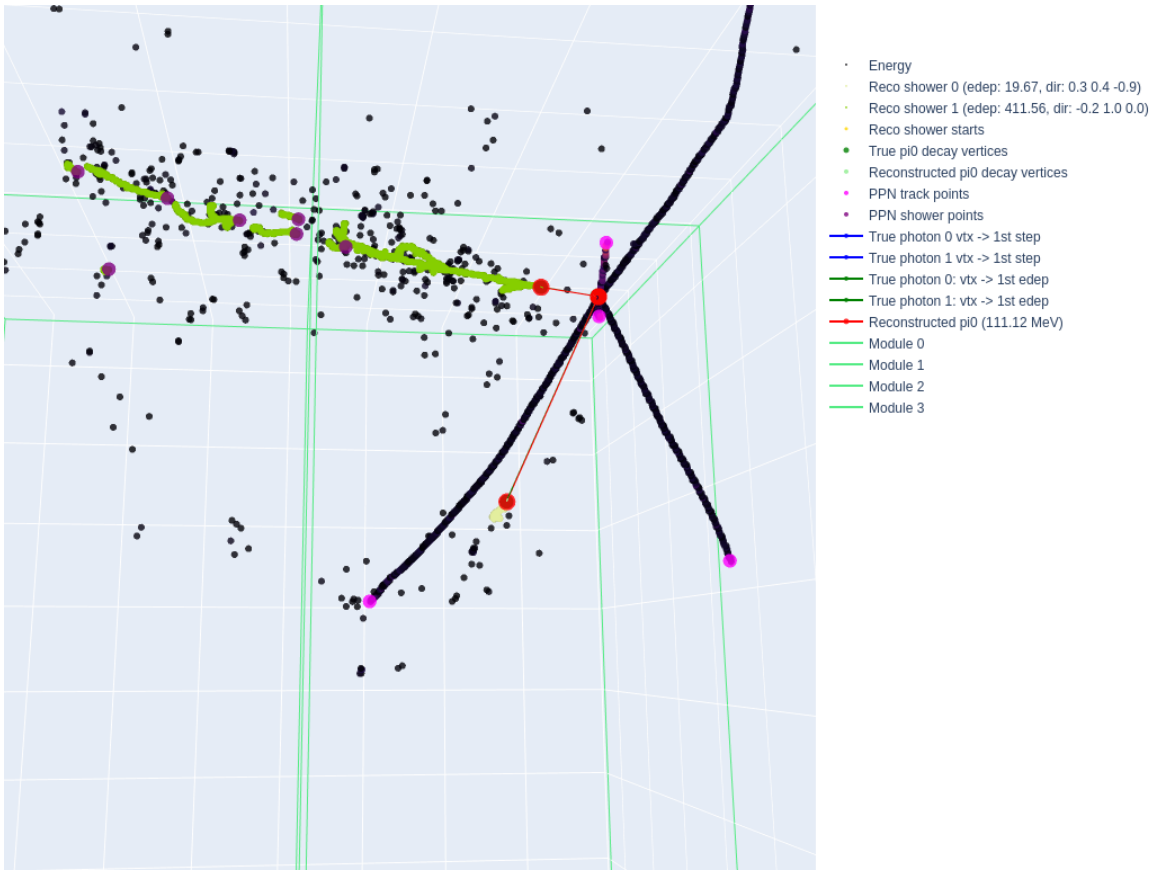

Figure 8: Event display with a correctly reconstructed π^0, event ID 6 from data sample number 4 (see Section 7.1.1). Energy depositions with a semantic class other than shower-like are drawn as black points. The coloured EDEPs correspond to the shower clusters, with the colour code representing the cluster number. Green lines indicate the module edges from the ArgonCube 2x2 Demonstrator (see Section 5.1.5). The π^0 mass has been reconstructed to 111.12 MeV (no Fudge factor applied yet).

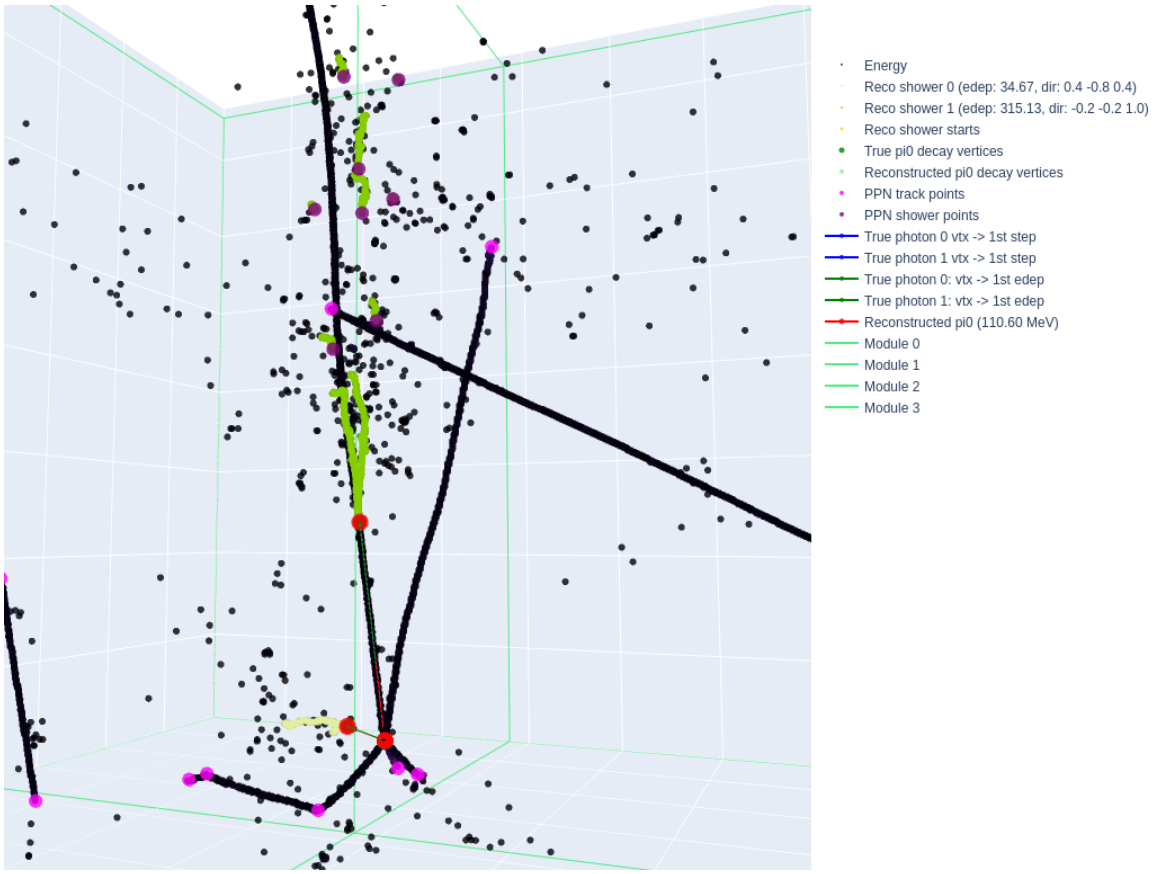

Figure 9: Event display with a correctly reconstructed π^0, event ID 13 from data sample number 4 (see Section 7.1.1). Energy depositions with a semantic class other than shower-like are drawn as black points. The coloured EDEPs correspond to the shower clusters, with the colour code representing the cluster number. Green lines indicate the module edges from the ArgonCube 2x2 Demonstrator (see Section 5.1.5). The π^0 mass has been reconstructed to 110.60 MeV (no Fudge factor applied yet).

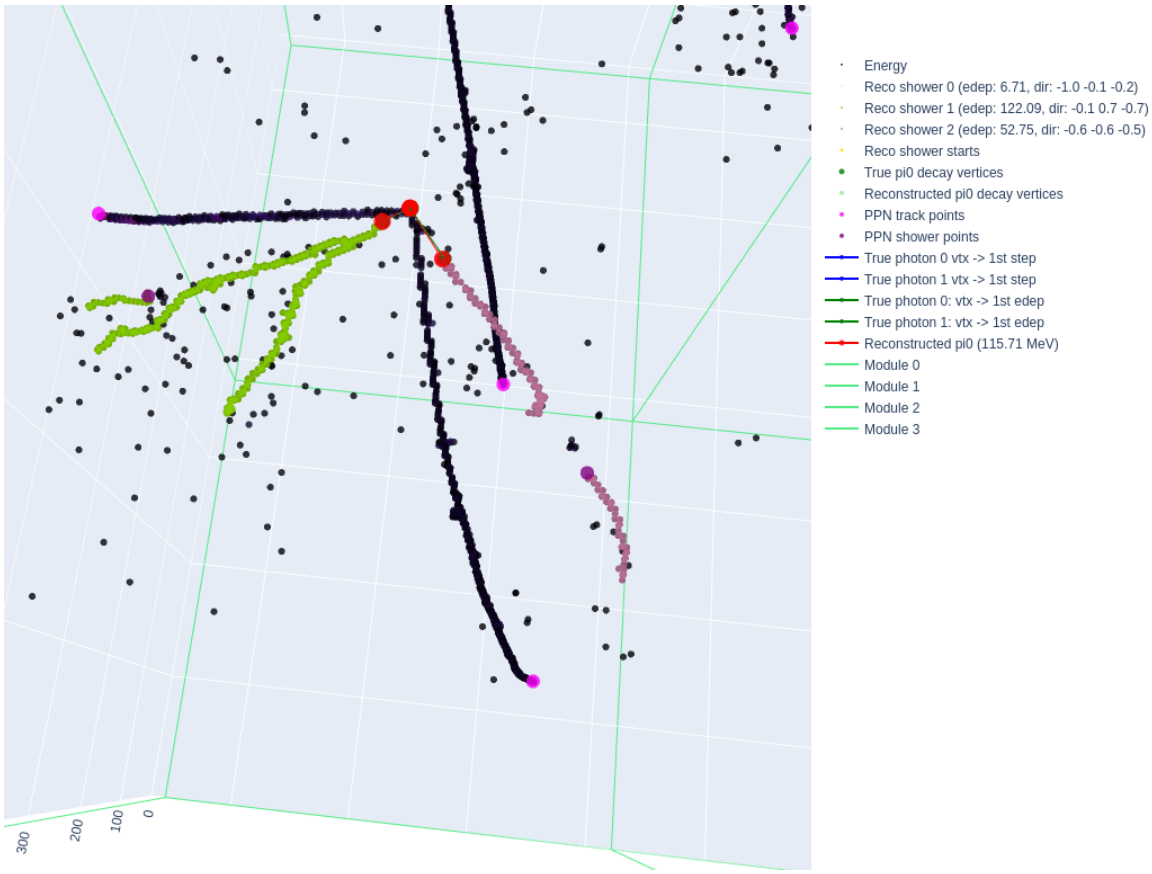

Figure 10: Event display with a correctly reconstructed π^0, event ID 15 from data sample number 4 (see Section 7.1.1). Energy depositions with a semantic class other than shower-like are drawn as black points. The coloured EDEPs correspond to the shower clusters, with the colour code representing the cluster number. Green lines indicate the module edges from the ArgonCube 2x2 Demonstrator (see Section 5.1.5). The π^0 mass has been reconstructed to 115.71 MeV (no Fudge factor applied yet).

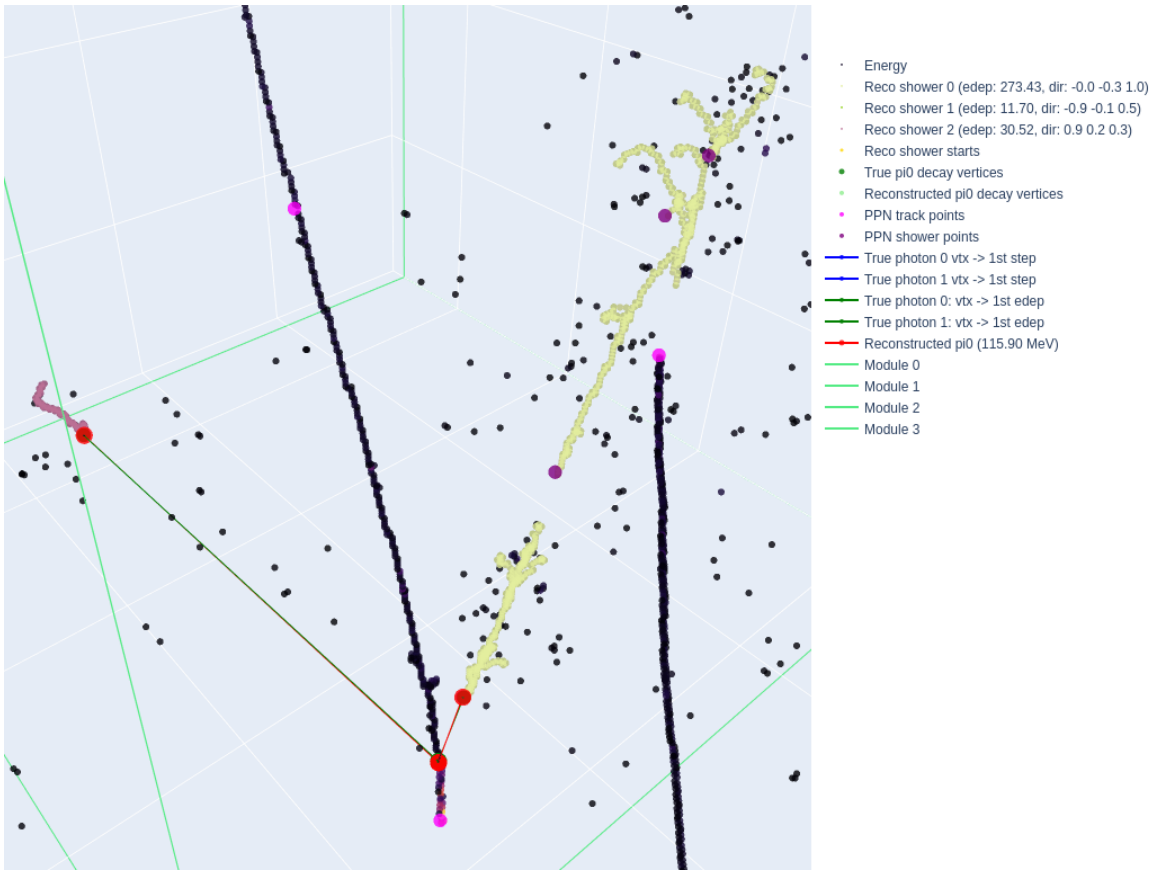

Figure 11: Event display with a correctly reconstructed π^0, event ID 19 from data sample number 4 (see Section 7.1.1). Energy depositions with a semantic class other than shower-like are drawn as black points. The coloured EDEPs correspond to the shower clusters, with the colour code representing the cluster number. Green lines indicate the module edges from the ArgonCube 2x2 Demonstrator (see Section 5.1.5). The π^0 mass has been reconstructed to 115.90 MeV (no Fudge factor applied yet).

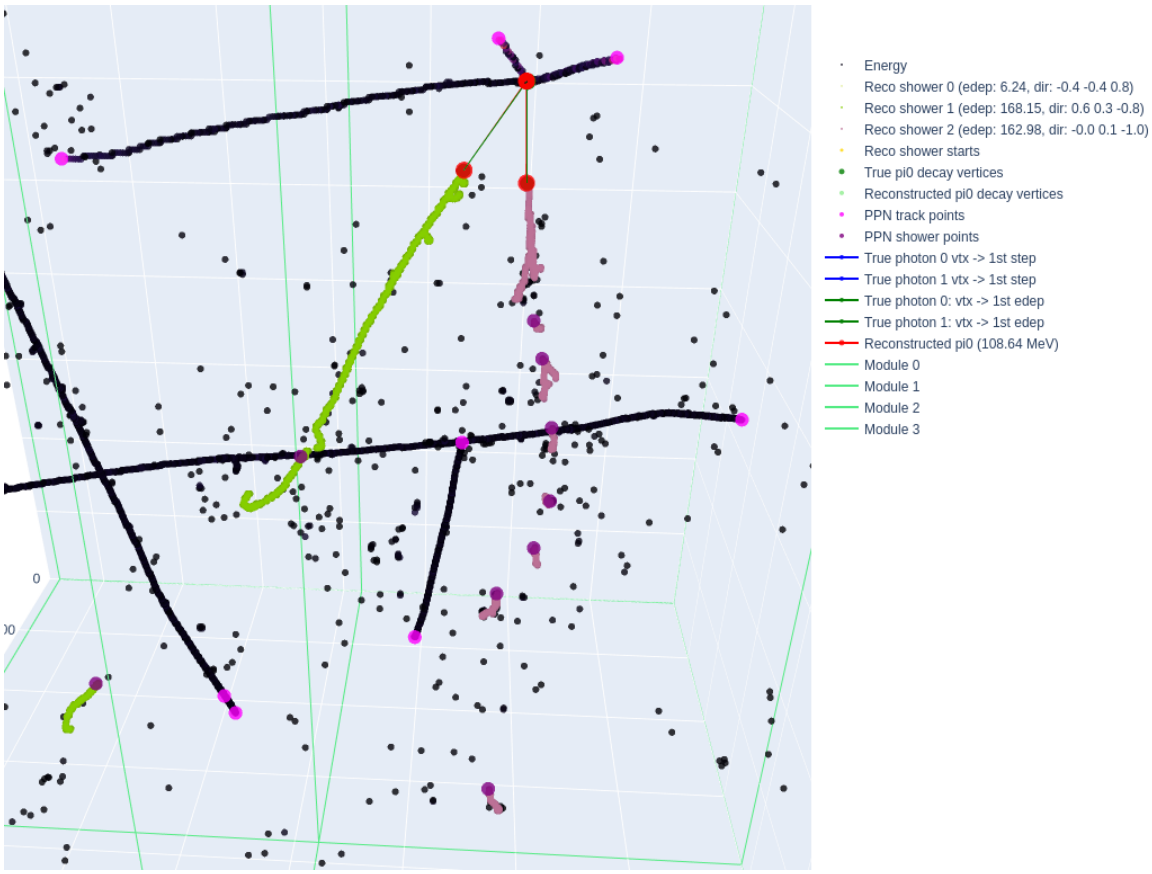

Figure 12: Event display with a correctly reconstructed π^0, event ID 21 from data sample number 4 (see Section 7.1.1). Energy depositions with a semantic class other than shower-like are drawn as black points. The coloured EDEPs correspond to the shower clusters, with the colour code representing the cluster number. Green lines indicate the module edges from the ArgonCube 2x2 Demonstrator (see Section 5.1.5). The π^0 mass has been reconstructed to 108.64 MeV (no Fudge factor applied yet).

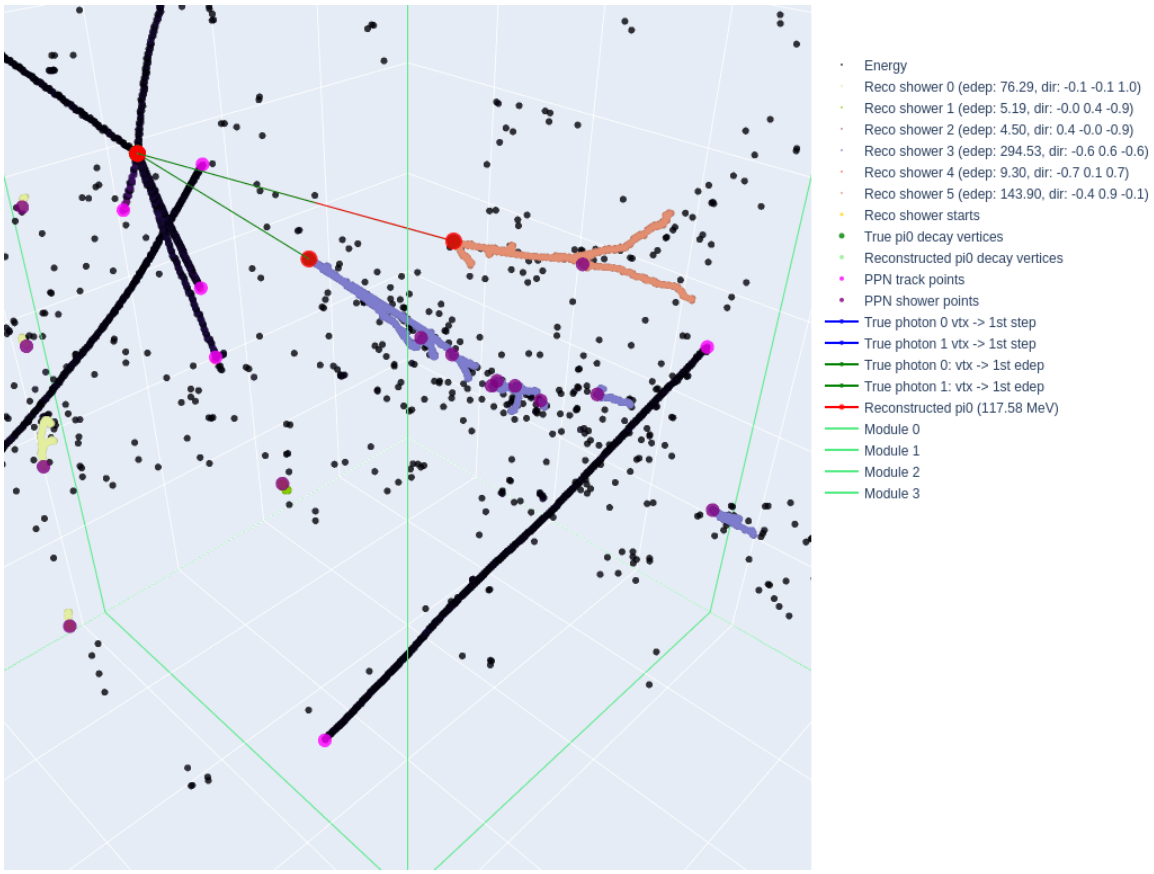

Figure 13: Event display with a correctly reconstructed π^0, event ID 23 from data sample number 4 (see Section 7.1.1). Energy depositions with a semantic class other than shower-like are drawn as black points. The coloured EDEPs correspond to the shower clusters, with the colour code representing the cluster number. Green lines indicate the module edges from the ArgonCube 2x2 Demonstrator (see Section 5.1.5). The π^0 mass has been reconstructed to 117.58 MeV (no Fudge factor applied yet).

References

[1] G. Aad et al. 'Observation of a new particle in the search for the Standard Model Higgs boson with the ATLAS detector at the LHC'. In: *Phys. Lett. B* 716 (2012), pp. 1–29. DOI: 10.1016/j.physletb.2012.08.020. arXiv: 1207.7214 [hep-ex] (cit. on p. 3).

[2] S. Chatrchyan et al. 'Observation of a New Boson at a Mass of 125 GeV with the CMS Experiment at the LHC'. In: *Phys. Lett. B* 716 (2012), pp. 30–61. DOI: 10.1016/j.physletb.2012.08.021. arXiv: 1207.7235 [hep-ex] (cit. on p. 3).

[3] Q. Ahmad et al. 'Direct evidence for neutrino flavor transformation from neutral current interactions in the Sudbury Neutrino Observatory'. In: *Phys. Rev. Lett.* 89 (2002), p. 011301. DOI: 10.1103/PhysRevLett.89.011301. arXiv: nucl-ex/0204008 (cit. on pp. 3, 8).

[4] A. D. Sakharov. 'Violation of CP Invariance, C asymmetry, and baryon asymmetry of the universe'. In: *Pisma Zh. Eksp. Teor. Fiz.* 5 (1967), pp. 32–35. DOI: 10.1070/PU1991v034n05ABEH002497 (cit. on p. 3).

[5] J. Chadwick. 'The intensity distribution in the magnetic spectrum of beta particles from radium (B + C)'. In: *Verh. Phys. Gesell.* 16 (1914), pp. 383–391 (cit. on p. 5).

[6] W. Pauli. 'Pauli letter collection: letter to Lise Meitner'. Typed copy. URL: https://cds.cern.ch/record/83282. (accessed: 11.06.2021) (cit. on p. 5).

[7] F. Perrin. 'Possibilité d'émission de particules neutres de masse intrinsèque nulle dans les radioactivités β'. In: *Comptes-Rendus* 197 (1933), pp. 1625–1627 (cit. on p. 5).

[8] E. Fermi. 'An attempt of a theory of beta radiation. 1.' In: *Z. Phys.* 88 (1934), pp. 161–177. DOI: 10.1007/BF01351864 (cit. on p. 5).

[9] H. Bethe and R. Peierls. 'The 'neutrino''. In: *Nature* 133 (1934), p. 532. DOI: 10.1038/133532a0 (cit. on p. 5).

[10] C. Cowan et al. 'Detection of the free neutrino: A Confirmation'. In: *Science* 124 (1956), pp. 103–104. DOI: 10.1126/science.124.3212.103 (cit. on p. 6).

[11] T. Lee and C.-N. Yang. 'Question of Parity Conservation in Weak Interactions'. In: *Phys. Rev.* 104 (1956), pp. 254–258. DOI: 10.1103/PhysRev.104.254 (cit. on p. 6).

[12] C. Wu et al. 'Experimental Test of Parity Conservation in β Decay'. In: *Phys. Rev.* 105 (1957), pp. 1413–1414. DOI: 10.1103/PhysRev.105.1413 (cit. on p. 6).

[13] T. Lee and C.-N. Yang. 'Parity Nonconservation and a Two Component Theory of the Neutrino'. In: *Phys. Rev.* 105 (1957). Ed. by G. Feinberg, pp. 1671–1675. DOI: 10.1103/PhysRev.105.1671 (cit. on p. 6).

[14] M. Goldhaber, L. Grodzins and A. Sunyar. 'Helicity of Neutrinos'. In: *Phys. Rev.* 109 (1958), pp. 1015–1017. DOI: 10.1103/PhysRev.109.1015 (cit. on p. 6).

[15] G. Danby et al. 'Observation of High-Energy Neutrino Reactions and the Existence of Two Kinds of Neutrinos'. In: *Phys. Rev. Lett.* 9 (1962), pp. 36–44. DOI: 10.1103/PhysRevLett.9.36 (cit. on p. 6).

[16] R. Davis Jr., D. S. Harmer and K. C. Hoffman. 'Search for neutrinos from the sun'. In: *Phys. Rev. Lett.* 20 (1968), pp. 1205–1209. DOI: 10.1103/PhysRevLett.20.1205 (cit. on p. 6).

[17] J. N. Bahcall, N. A. Bahcall and G. Shaviv. 'Present status of the theoretical predictions for the Cl-36 solar neutrino experiment'. In: *Phys. Rev. Lett.* 20 (1968), pp. 1209–1212. DOI: 10.1103/PhysRevLett.20.1209 (cit. on p. 7).

[18] M. L. Perl et al. 'Evidence for Anomalous Lepton Production in e+ - e- Annihilation'. In: *Phys. Rev. Lett.* 35 (1975), pp. 1489–1492. DOI: 10.1103/PhysRevLett.35.1489 (cit. on p. 7).

[19] K. S. Hirata et al. 'Experimental Study of the Atmospheric Neutrino Flux'. In: (1988). Ed. by J. Tran Thanh Van, pp. 235–246. DOI: 10.1016/0370-2693(88)91690-5 (cit. on p. 7).

[20] K. Hirata et al. 'Observation of B-8 Solar Neutrinos in the Kamiokande-II Detector'. In: *Phys. Rev. Lett.* 63 (1989), p. 16. DOI: 10.1103/PhysRevLett.63.16 (cit. on p. 7).

[21] D. Casper et al. 'Measurement of atmospheric neutrino composition with IMB-3'. In: *Phys. Rev. Lett.* 66 (1991), pp. 2561–2564. DOI: 10.1103/PhysRevLett.66.2561 (cit. on p. 7).

[22] J. N. Abdurashitov et al. 'Measurement of the solar neutrino capture rate with gallium metal'. In: *Phys. Rev. C* 60 (1999), p. 055801. DOI: 10.1103/PhysRevC.60.055801. arXiv: astro-ph/9907113 (cit. on p. 7).

[23] W. Hampel et al. 'GALLEX solar neutrino observations: Results for GALLEX IV'. In: *Phys. Lett. B* 447 (1999), pp. 127–133. DOI: 10.1016/S0370-2693(98)01579-2 (cit. on p. 7).

[24] D. Decamp et al. 'Determination of the Number of Light Neutrino Species'. In: *Phys. Lett. B* 231 (1989), pp. 519–529. DOI: 10.1016/0370-2693(89)90704-1 (cit. on pp. 7, 10).

[25] Y. Fukuda et al. 'Evidence for oscillation of atmospheric neutrinos'. In: *Phys. Rev. Lett.* 81 (1998), pp. 1562–1567. DOI: 10.1103/PhysRevLett.81.1562. arXiv: hep-ex/9807003 (cit. on p. 7).

[26] K. Kodama et al. 'Observation of tau neutrino interactions'. In: *Phys. Lett. B* 504 (2001), pp. 218–224. DOI: 10.1016/S0370-2693(01)00307-0. arXiv: hep-ex/0012035 (cit. on p. 8).

[27] Y. Abe et al. 'Indication of Reactor $\bar{\nu}_e$ Disappearance in the Double Chooz Experiment'. In: *Phys. Rev. Lett.* 108 (2012), p. 131801. DOI: 10.1103/PhysRevLett.108.131801. arXiv: 1112.6353 [hep-ex] (cit. on p. 8).

[28] K. Abe et al. 'Indication of Electron Neutrino Appearance from an Accelerator-produced Off-axis Muon Neutrino Beam'. In: *Phys. Rev. Lett.* 107 (2011), p. 041801. DOI: 10.1103/PhysRevLett.107.041801. arXiv: 1106.2822 [hep-ex] (cit. on p. 8).

[29] F. P. An et al. 'Observation of electron-antineutrino disappearance at Daya Bay'. In: *Phys. Rev. Lett.* 108 (2012), p. 171803. DOI: 10.1103/PhysRevLett.108.171803. arXiv: 1203.1669 [hep-ex] (cit. on p. 8).

[30] P. Ade et al. 'Planck 2013 results. XVI. Cosmological parameters'. In: *Astron. Astrophys.* 571 (2014), A16. DOI: 10.1051/0004-6361/201321591. arXiv: 1303.5076 [astro-ph.CO] (cit. on p. 8).

[31] M. Aker et al. 'First direct neutrino-mass measurement with sub-eV sensitivity'. In: (May 2021). arXiv: 2105.08533 [hep-ex] (cit. on p. 8).

[32] K. Abe et al. 'Observation of Electron Neutrino Appearance in a Muon Neutrino Beam'. In: *Phys. Rev. Lett.* 112 (2014), p. 061802. DOI: 10.1103/PhysRevLett.112.061802. arXiv: 1311.4750 [hep-ex] (cit. on p. 8).

[33] K. Abe et al. 'Improved constraints on neutrino mixing from the T2K experiment with $\mathbf{3.13 \times 10^{21}}$ protons on target'. In: *Phys. Rev. D* 103.11 (2021), p. 112008. DOI: 10.1103/PhysRevD.103.112008. arXiv: 2101.03779 [hep-ex] (cit. on pp. 8, 11, 27).

[34] S. F. King. 'Unified Models of Neutrinos, Flavour and CP Violation'. In: *Prog. Part. Nucl. Phys.* 94 (2017), pp. 217–256. DOI: 10.1016/j.ppnp.2017.01.003. arXiv: 1701.04413 [hep-ph] (cit. on p. 10).

[35] C. Giunti and C. W. Kim. *Fundamentals of Neutrino Physics and Astrophysics*. 2007. ISBN: 978-0-19-850871-7 (cit. on p. 10).

[36] P. A. Zyla et al. 'Review of Particle Physics'. In: *PTEP* 2020.8 (2020), p. 083C01. DOI: 10.1093/ptep/ptaa104 (cit. on pp. 12, 14, 19–21, 28, 35, 37, 45, 131, 157).

[37] L. Wolfenstein. 'Neutrino Oscillations in Matter'. In: *Phys. Rev. D* 17 (1978), pp. 2369–2374. DOI: 10.1103/PhysRevD.17.2369 (cit. on p. 12).

[38] B. Abi et al. 'Deep Underground Neutrino Experiment (DUNE), Far Detector Technical Design Report, Volume I Introduction to DUNE'. In: *JINST* 15.08 (2020), T08008. DOI: 10.1088/1748-0221/15/08/T08008. arXiv: 2002.02967 [physics.ins-det] (cit. on pp. 13, 27, 28, 30).

[39] A. Abed Abud et al. 'Deep Underground Neutrino Experiment (DUNE) Near Detector Conceptual Design Report'. In: (Mar. 2021). arXiv: 2103.13910 [physics.ins-det] (cit. on pp. 17, 53–55, 106, 107, 109, 110).

[40] B. Abi et al. 'Experiment Simulation Configurations Approximating DUNE TDR'. In: (Mar. 2021). arXiv: 2103.04797 [hep-ex] (cit. on p. 18).

[41] B. Gabioud et al. 'Measurement of Ionization Loss in the Relativistic Rise Region with the Time Projection Chamber'. In: *IEEE Trans. Nucl. Sci.* 30 (1983), pp. 63–66. DOI: 10.1109/TNS.1983.4332220 (cit. on pp. 21, 22, 32).

[42] K. Abe et al. 'Hyper-Kamiokande Design Report'. In: (May 2018). arXiv: 1805.04163 [physics.ins-det] (cit. on p. 27).

[43] K. Abe et al. 'The Hyper-Kamiokande Experiment - Snowmass LOI'. In: *2022 Snowmass Summer Study*. Sept. 2020. arXiv: 2009.00794 [physics.ins-det] (cit. on p. 27).

[44] B. Abi et al. 'Deep Underground Neutrino Experiment (DUNE), Far Detector Technical Design Report, Volume II: DUNE Physics'. In: (Feb. 2020). arXiv: 2002.03005 [hep-ex] (cit. on p. 27).

[45] B. Abi et al. 'Deep Underground Neutrino Experiment (DUNE), Far Detector Technical Design Report, Volume III: DUNE Far Detector Technical Coordination'. In: *JINST* 15.08 (2020), T08009. DOI: 10.1088/1748-0221/15/08/T08009. arXiv: 2002.03008 [physics.ins-det] (cit. on p. 27).

[46] B. Abi et al. 'Deep Underground Neutrino Experiment (DUNE), Far Detector Technical Design Report, Volume IV: Far Detector Single-phase Technology'. In: *JINST* 15.08 (2020), T08010. DOI: 10.1088/1748-0221/15/08/T08010. arXiv: 2002.03010 [physics.ins-det] (cit. on pp. 27, 111).

[47] J. Strait et al. 'Long-Baseline Neutrino Facility (LBNF) and Deep Underground Neutrino Experiment (DUNE): Conceptual Design Report, Volume 3: Long-Baseline Neutrino Facility for DUNE June 24, 2015'. In: (Jan. 2016). arXiv: 1601.05823 [physics.ins-det] (cit. on p. 28).

[48] B. Abi et al. 'Prospects for beyond the Standard Model physics searches at the Deep Underground Neutrino Experiment'. In: *Eur. Phys. J. C* 81.4 (2021), p. 322. DOI: 10.1140/epjc/s10052-021-09007-w. arXiv: 2008.12769 [hep-ex] (cit. on p. 30).

[49] G. Charpak et al. 'The Use of Multiwire Proportional Counters to Select and Localize Charged Particles'. In: *Nucl. Instrum. Meth.* 62 (1968), pp. 262–268. DOI: 10.1016/0029-554X(68)90371-6 (cit. on p. 31).

[50] D. R. Nygren. 'The Time Projection Chamber: A New 4 pi Detector for Charged Particles'. In: *eConf* C740805 (1974). Ed. by J. Kadyk et al., p. 58 (cit. on p. 31).

[51] D. R. Nygren. 'Origin and development of the TPC idea'. In: *Nucl. Instrum. Meth. A* 907 (2018), pp. 22–30. DOI: 10.1016/j.nima.2018.07.015 (cit. on p. 31).

[52] G. Charpak and F. Sauli. 'High-accuracy, two-dimensional read-out in multiwire proportional chambers'. In: *Nucl. Instrum. Meth.* 113 (1973), pp. 381–385. DOI: 10.1016/0029-554X(73)90503-X (cit. on p. 32).

[53] D. Fancher et al. 'Performance of a Time Projection Chamber'. In: *Nucl. Instrum. Meth.* 161 (1979), p. 383. DOI: 10.1016/0029-554X(79)90411-7 (cit. on pp. 32, 56).

[54] R. Z. Fuzesy, N. J. Hadley and P. R. Robrish. 'Design of the Multiwire Proportional Detectors for the {PEP}-4 Time Projection Chamber'. In: *Nucl. Instrum. Meth. A* 223 (1984), p. 40. DOI: 10.1016/0167-5087(84)90244-8 (cit. on p. 32).

[55] W. J. Willis and V. Radeka. 'Liquid Argon Ionization Chambers as Total Absorption Detectors'. In: *Nucl. Instrum. Meth.* 120 (1974), pp. 221–236. DOI: 10.1016/0029-554X(74)90039-1 (cit. on p. 32).

[56] C. Rubbia. 'The Liquid Argon Time Projection Chamber: A New Concept for Neutrino Detectors'. In: (May 1977) (cit. on p. 32).

[57] S. Amerio et al. 'Design, construction and tests of the ICARUS T600 detector'. In: *Nucl. Instrum. Meth. A* 527 (2004), pp. 329–410. DOI: 10.1016/j.nima.2004.02.044 (cit. on p. 32).

[58] E. Aprile et al. *Noble Gas Detectors*. Wiley, 2008. DOI: 10.1002/9783527610020 (cit. on pp. 34, 37).

[59] S. Kubota et al. 'Dynamical behavior of free electrons in the recombination process in liquid argon, krypton, and xenon'. In: *Phys. Rev. B* 20.8 (1979), p. 3486. DOI: 10.1103/PhysRevB.20.3486 (cit. on p. 34).

[60] R. Acciarri et al. 'Liquid Argon Dielectric Breakdown Studies with the MicroBooNE Purification System'. In: *JINST* 9.11 (2014), P11001. DOI: 10.1088/1748-0221/9/11/P11001. arXiv: 1408.0264 [physics.ins-det] (cit. on p. 36).

[61] C. Tegeler, R. Span and W. Wagner. 'A New Equation of State for Argon Covering the Fluid Region for Temperatures From the Melting Line to 700 K at Pressures up to 1000 MPa'. In: *Journal of Physical and Chemical Reference Data* 28.3 (1999), pp. 779–850. DOI: 10.1063/1.556037. eprint: https://doi.org/10.1063/1.556037. URL: https://doi.org/10.1063/1.556037. (accessed: 11.06.2021) (cit. on p. 37).

[62] R. L. Amey and R. H. Cole. 'Dielectric Constants of Liquefied Noble Gases and Methane'. In: *J. Chem. Phys.* 40.1 (Jan. 1964), pp. 146–148. DOI: 10.1063/1.1724850 (cit. on p. 37).

[63] T. Doke et al. 'Absolute Scintillation Yields in Liquid Argon and Xenon for Various Particles'. In: *Jap. J. Appl. Phys.* 41 (2002), pp. 1538–1545. DOI: 10.1143/JJAP.41.1538 (cit. on pp. 37, 40–42).

[64] A. Hitachi et al. 'Effect of ionization density on the time dependence of luminescence from liquid argon and xenon'. In: *Phys. Rev. B* 27 (1983), pp. 5279–5285. DOI: 10.1103/PhysRevB.27.5279 (cit. on pp. 37, 40, 41, 46).

[65] J. Calvo et al. 'Measurement of the attenuation length of argon scintillation light in the ArDM LAr TPC'. In: *Astropart. Phys.* 97 (2018), pp. 186–196. DOI: 10.1016/j.astropartphys.2017.11.009. arXiv: 1611.02481 [astro-ph.IM] (cit. on pp. 37, 46).

[66] N. Ishida et al. 'Attenuation length measurements of scintillation light in liquid rare gases and their mixtures using an improved reflection suppresser'. In: *Nuclear Instruments and Methods in Physics Research Section A: Accelerators, Spectrometers, Detectors and Associated Equipment* 384.2 (1997), pp. 380–386. ISSN: 0168-9002. DOI: https://doi.org/10.1016/S0168-9002(96)00740-1. URL: https://www.sciencedirect.com/science/article/pii/S0168900296007401 (cit. on pp. 37, 46).

[67] S. Kubota et al. 'Evidence of the existence of exciton states in liquid argon and exciton-enhanced ionization from xenon doping'. In: *Phys. Rev. B* 13.4 (1976), p. 1649. DOI: 10.1103/PhysRevB.13.1649 (cit. on p. 37).

[68] T. Doke et al. 'Estimation of Fano factors in liquid argon, krypton, xenon and xenon-doped liquid argon'. In: *Nucl. Instrum. Meth.* 134 (1976), pp. 353–357. DOI: 10.1016/0029-554X(76)90292-5 (cit. on p. 37).

[69] S. Amoruso et al. 'Study of electron recombination in liquid argon with the ICARUS TPC'. In: *Nucl. Instrum. Meth. A* 523 (2004), pp. 275–286. DOI: 10.1016/j.nima.2003.11.423 (cit. on p. 39).

[70] J. Thomas and D. A. Imel. 'Recombination of electron-ion pairs in liquid argon and liquid xenon'. In: *Phys. Rev. A* 36 (1987), pp. 614–616. DOI: 10.1103/PhysRevA.36.614 (cit. on p. 39).

[71] J. B. Birks. 'Scintillations from Organic Crystals: Specific Fluorescence and Relative Response to Different Radiations'. In: *Proc. Phys. Soc. A* 64 (1951), pp. 874–877. DOI: 10.1088/0370-1298/64/10/303 (cit. on p. 39).

[72] R. Berner et al. 'First Operation of a Resistive Shell Liquid Argon Time Projection Chamber: A New Approach to Electric-Field Shaping'. In: *Instruments* 3.2 (2019), p. 28. DOI: 10.3390/instruments3020028. arXiv: 1903.11858 [physics.ins-det] (cit. on pp. 43, 76).

[73] B. J. P. Jones et al. 'A Measurement of the Absorption of Liquid Argon Scintillation Light by Dissolved Nitrogen at the Part-Per-Million Level'. In: *JINST* 8 (2013). [Erratum: JINST 8, E09001 (2013)], P07011. DOI: 10.1088/1748-0221/8/07/P07011. arXiv: 1306.4605 [physics.ins-det] (cit. on pp. 43, 44).

[74] M. Zeller et al. 'Ionization signals from electrons and alpha-particles in mixtures of liquid Argon and Nitrogen: Perspectives on protons for Gamma Resonant Nuclear Absorption applications'. In: *JINST* 5 (2010), P10009. DOI: 10.1088/1748-0221/5/10/P10009. arXiv: 1008.4075 [physics.ins-det] (cit. on p. 44).

[75] Y. Li et al. 'Measurement of Longitudinal Electron Diffusion in Liquid Argon'. In: *Nucl. Instrum. Meth. A* 816 (2016), pp. 160–170. DOI: 10.1016/j.nima.2016.01.094. arXiv: 1508.07059 [physics.ins-det] (cit. on pp. 45, 46).

[76] G. M. Seidel, R. E. Lanou and W. Yao. 'Rayleigh scattering in rare gas liquids'. In: *Nucl. Instrum. Meth. A* 489 (2002), pp. 189–194. DOI: 10.1016/S0168-9002(02)00890-2. arXiv: hep-ex/0111054 (cit. on p. 46).

[77] E. Grace and J. A. Nikkel. 'Index of refraction, Rayleigh scattering length, and Sellmeier coefficients in solid and liquid argon and xenon'. In: *Nucl. Instrum. Meth. A* 867 (2017), pp. 204–208. DOI: 10.1016/j.nima.2017.06.031. arXiv: 1502.04213 [physics.ins-det] (cit. on p. 46).

[78] B. L. Henson. 'Mobility of Positive Ions in Liquefied Argon and Nitrogen'. In: *Phys. Rev.* 135 (4A Aug. 1964), A1002–A1008. DOI: 10.1103/PhysRev.135.A1002. URL: https://link.aps.org/doi/10.1103/PhysRev.135.A1002 (cit. on p. 47).

[79] A. Ereditato et al. 'A steerable UV laser system for the calibration of liquid argon time projection chambers'. In: *JINST* 9.11 (2014), T11007. DOI: 10.1088/1748-0221/9/11/T11007. arXiv: 1406.6400 [physics.ins-det] (cit. on p. 47).

[80] A. Ereditato et al. 'Design and operation of ARGONTUBE: a 5 m long drift liquid argon TPC'. In: *JINST* 8 (2013), P07002. DOI: 10.1088/1748-0221/8/07/P07002. arXiv: 1304.6961 [physics.ins-det] (cit. on p. 51).

[81] A. Blatter et al. 'Experimental study of electric breakdowns in liquid argon at centimeter scale'. In: *JINST* 9 (2014), P04006. DOI: 10.1088/1748-0221/9/04/P04006. arXiv: 1401.6693 [physics.ins-det] (cit. on pp. 51, 69).

[82] M. Auger et al. 'A method to suppress dielectric breakdowns in liquid argon ionization detectors for cathode to ground distances of several millimeters'. In: *JINST* 9 (2014), P07023. DOI: 10.1088/1748-0221/9/07/P07023. arXiv: 1406.3929 [physics.ins-det] (cit. on p. 51).

[83] M. Auger et al. 'On the Electric Breakdown in Liquid Argon at Centimeter Scale'. In: *JINST* 11.03 (2016), P03017. DOI: 10.1088/1748-0221/11/03/P03017. arXiv: 1512.05968 [physics.ins-det] (cit. on p. 51).

[84] B. Abi et al. 'The Single-Phase ProtoDUNE Technical Design Report'. In: (June 2017). arXiv: 1706.07081 [physics.ins-det] (cit. on p. 53).

[85] C. Rubbia et al. 'Underground operation of the ICARUS T600 LAr-TPC: first results'. In: *JINST* 6 (2011), P07011. DOI: 10.1088/1748-0221/6/07/P07011. arXiv: 1106.0975 [hep-ex] (cit. on p. 56).

[86] C. Anderson et al. 'The ArgoNeuT Detector in the NuMI Low-Energy beam line at Fermilab'. In: *JINST* 7 (2012), P10019. DOI: 10.1088/1748-0221/7/10/P10019. arXiv: 1205.6747 [physics.ins-det] (cit. on p. 56).

[87] R. Acciarri et al. 'Design and Construction of the MicroBooNE Detector'. In: *JINST* 12.02 (2017), P02017. DOI: 10.1088/1748-0221/12/02/P02017. arXiv: 1612.05824 [physics.ins-det] (cit. on p. 56).

[88] J. Joshi and X. Qian. 'Signal Processing in the MicroBooNE LArTPC'. In: *Meeting of the APS Division of Particles and Fields*. Nov. 2015. arXiv: 1511.00317 [physics.ins-det] (cit. on p. 56).

[89] G. De Geronimo et al. 'Front-end ASIC for a Liquid Argon TPC'. In: *IEEE Trans. Nucl. Sci.* 58 (2011), pp. 1376–1385. DOI: 10.1109/TNS.2011.2127487 (cit. on pp. 56, 74).

[90] D. A. Dwyer et al. 'LArPix: Demonstration of low-power 3D pixelated charge readout for liquid argon time projection chambers'. In: *JINST* 13.10 (2018), P10007. DOI: 10.1088/1748-0221/13/10/P10007. arXiv: 1808.02969 [physics.ins-det] (cit. on pp. 57, 69).

[91] C. Grace and D. Gnani. 'LArPix-v2 Datasheet'. Internal LBNL IC Group Design Note. 2019 (cit. on pp. 59, 60).

[92] A. A. Machado and E. Segreto. 'ARAPUCA a new device for liquid argon scintillation light detection'. In: *JINST* 11.02 (2016), p. C02004. DOI: 10.1088/1748-0221/11/02/C02004 (cit. on p. 62).

[93] L. Calivers. 'Development and Characterisation of a Novel Light Detector: ArCLight'. Master's thesis. Laboratory for High Energy Physics (LHEP), University of Bern, Jan. 2021 (cit. on pp. 62, 63, 65, 66).

[94] M. Auger et al. 'ArCLight—A Compact Dielectric Large-Area Photon Detector'. In: *Instruments* 2.1 (2018), p. 3. DOI: 10.3390/instruments2010003. arXiv: 1711.11409 [physics.ins-det] (cit. on p. 62).

[95] N. Anfimov et al. 'Development of the Light Collection Module for the Liquid Argon Time Projection Chamber (LArTPC)'. In: *JINST* 15.07 (2020), p. C07022. DOI: 10.1088/1748-0221/15/07/C07022 (cit. on p. 62).

[96] C. S. Chiu et al. 'Environmental Effects on TPB Wavelength-Shifting Coatings'. In: *JINST* 7 (2012), P07007. DOI: 10.1088/1748-0221/7/07/P07007. arXiv: 1204.5762 [physics.ins-det] (cit. on p. 65).

[97] B. J. P. Jones et al. 'Photodegradation Mechanisms of Tetraphenyl Butadiene Coatings for Liquid Argon Detectors'. In: *JINST* 8 (2013), P01013. DOI: 10.1088/1748-0221/8/01/P01013. arXiv: 1211.7150 [physics.ins-det] (cit. on p. 65).

[98] J. Asaadi et al. 'Emanation and bulk fluorescence in liquid argon from tetraphenyl butadiene wavelength shifting coatings'. In: *JINST* 14.02 (2019), P02021. DOI: 10.1088/1748-0221/14/02/P02021. arXiv: 1804.00011 [physics.ins-det] (cit. on p. 65).

[99] Y. Abraham et al. 'Wavelength-Shifting Performance of Polyethylene Naphthalate Films in a Liquid Argon Environment'. In: (Mar. 2021). arXiv: 2103.03232 [physics.ins-det] (cit. on p. 65).

[100] J. Asaadi et al. 'First Demonstration of a Pixelated Charge Readout for Single-Phase Liquid Argon Time Projection Chambers'. In: *Instruments* 4.1 (2020), p. 9. DOI: 10.3390/instruments4010009. arXiv: 1801.08884 [physics.ins-det] (cit. on p. 69).

[101] 3M Optical Systems. *Vikuiti Enhanced Specular Reflector (ESR)*. URL: http://multimedia.3m.com/mws/media/374730O/vikuiti-tm-esr-sales-literature.pdf?fn=ESR%5C%20ss2.pdf. (accessed: 29.09.2018) (cit. on p. 75).

[102] J. Mateski et al. *E974-MicroBooNE - Infrastructure Service Equiment, MicroBooNE Filter Inner Vessel*. Tech. rep. 2012 (cit. on p. 80).

[103] J. Kilmer et al. *E974-MicroBooNE - Infrastructure Service Equiment, MicroBooNE Sintered Metal Filter*. Tech. rep. 2012 (cit. on p. 80).

[104] P. Madigan. 'Performance of a PCB-based pixelated LArTPC anode (LArPix)'. In: *DUNE doc 22514* (Apr. 2021). URL: https://docs.dunescience.org/cgi-bin/private/ShowDocument?docid=22514. (accessed: 11.06.2021) (cit. on pp. 80, 82).

[105] DUNE collaboration. 'Physics analysis in a novel pixel-readout LArTPC'. Prepared for submission to JINST (cit. on pp. 91, 92).

[106] R. Berner. *RTD Resistance Temperature Detector*. 2019. URL: https://github.com/RomanMBerner/RTD_ResistanceTemperatureDetector. (accessed: 11.06.2021) (cit. on p. 96).

[107] R. Berner. *Pressure TPG252A*. 2019. URL: https://github.com/RomanMBerner/Pressure_TPG252A. (accessed: 11.06.2021) (cit. on p. 97).

[108] R. Berner. *Pressure TPG262*. 2019. URL: https://github.com/RomanMBerner/Pressure_TPG262. (accessed: 11.06.2021) (cit. on p. 97).

[109] R. Berner. *Pressure TPG362*. 2019. URL: https://github.com/RomanMBerner/Pressure_TPG362. (accessed: 11.06.2021) (cit. on p. 97).

[110] R. Berner. 'Levelmeters for a liquid xenon time projection chamber'. Bachelor's thesis. Laboratory for High Energy Physics (LHEP), University of Bern, Sept. 2016 (cit. on p. 97).

[111] R. Berner. *LAr Levelmeters*. 2020. URL: https://github.com/RomanMBerner/LAr_levelmeters. (accessed: 11.06.2021) (cit. on p. 97).

[112] R. Berner. *LAr Cryocamera*. 2020. URL: https://github.com/RomanMBerner/LAr_cryocamera. (accessed: 11.06.2021) (cit. on p. 99).

[113] K. Anderson et al. 'The NuMI Facility Technical Design Report'. In: (Oct. 1998). DOI: 10.2172/1156372 (cit. on p. 108).

[114] L. Aliaga et al. 'Design, Calibration, and Performance of the MINERvA Detector'. In: *Nucl. Instrum. Meth. A* 743 (2014), pp. 130–159. DOI: 10.1016/j.nima.2013.12.053. arXiv: 1305.5199 [physics.ins-det] (cit. on p. 108).

[115] J. Sinclair et al. 'ProtoDUNE-ND: proposal to place the ArgonCube 2x2 Demonstrator on-axis in NuMI'. In: *DUNE doc 12571* (Jan. 2019). URL: https://docs.dunescience.org/cgi-bin/private/ShowDocument?docid=12571. (accessed: 11.06.2021) (cit. on p. 108).

[116] D. Chesneanu. 'Neutrino-Argon Interaction with GENIE Event Generator'. In: *AIP Conf. Proc.* 1304.1 (2010). Ed. by L. Trache, S. Stoica and A. Smirnov, pp. 489–493. DOI: 10.1063/1.3527252 (cit. on p. 109).

[117] J. Asaadi et al. 'A New Concept for Kilotonne Scale Liquid Argon Time Projection Chambers'. In: *Instruments* 4.1 (2020), p. 6. DOI: 10.3390/instruments4010006. arXiv: 1908.10956 [physics.ins-det] (cit. on p. 111).

[118] F. Drielsma et al. 'Scalable, End-to-End, Deep-Learning-Based Data Reconstruction Chain for Particle Imaging Detectors'. In: *34th Conference on Neural Information Processing Systems*. Feb. 2021. arXiv: 2102.01033 [hep-ex] (cit. on p. 113).

[119] R. Berner. *LArTPC Machine Learning Reconstruction in 3D*. 2021. URL: https://github.com/RomanMBerner/lartpc_mlreco3d. (accessed: 11.06.2021) (cit. on p. 113).

[120] A. Aurisano et al. 'A Convolutional Neural Network Neutrino Event Classifier'. In: *JINST* 11.09 (2016), P09001. DOI: 10.1088/1748-0221/11/09/P09001. arXiv: 1604.01444 [hep-ex] (cit. on p. 114).

[121] L. Dominé and K. Terao. 'Scalable deep convolutional neural networks for sparse, locally dense liquid argon time projection chamber data'. In: *Phys. Rev. D* 102.1 (2020), p. 012005. DOI: 10.1103/PhysRevD.102.012005. arXiv: 1903.05663 [hep-ex] (cit. on pp. 114, 117).

[122] M. Ester et al. 'A density-based algorithm for discovering clusters in large spatial databases with noise'. In: AAAI Press, 1996, pp. 226–231 (cit. on p. 114).

[123] L. Dominé et al. 'Point Proposal Network for Reconstructing 3D Particle Endpoints with Sub-Pixel Precision in Liquid Argon Time Projection Chambers'. In: (June 2020). arXiv: 2006.14745 [hep-ex] (cit. on pp. 114, 118, 121).

[124] F. Drielsma et al. 'Clustering of Electromagnetic Showers and Particle Interactions with Graph Neural Networks in Liquid Argon Time Projection Chambers Data'. In: (July 2020). arXiv: 2007.01335 [physics.ins-det] (cit. on pp. 114, 123, 124, 126–128).

[125] C. Adams, K. Terao and T. Wongjirad. 'PILArNet: Public Dataset for Particle Imaging Liquid Argon Detectors in High Energy Physics'. In: (June 2020). arXiv: 2006.01993 [physics.ins-det] (cit. on pp. 115, 116).

[126] D. Collaboration. *LArTPC Event Generator*. 2020. URL: https://github.com/DeepLearnPhysics/LArTPCEventGenerator. (accessed: 15.06.2021) (cit. on p. 115).

[127] S. Agostinelli et al. 'GEANT4–a simulation toolkit'. In: *Nucl. Instrum. Meth. A* 506 (2003), pp. 250–303. DOI: 10.1016/S0168-9002(03)01368-8 (cit. on p. 115).

[128] L. Landau. 'On the energy loss of fast particles by ionization'. In: *J. Phys. (USSR)* 8 (1944), pp. 201–205 (cit. on p. 130).

[129] J. Moyal. 'Theory of ionization fluctuations'. In: *Phil. Mag. Ser. 7* 46.374 (1955), pp. 263–280. DOI: 10.1080/14786440308521076 (cit. on p. 130).

[130] R. Berner. *LArTPC Machine Learning Based Pi0 Reconstruction*. 2021. URL: https://github.com/RomanMBerner/pi0_reco. (accessed: 11.06.2021) (cit. on p. 135).

[131] R. Berner and F. Piastra. *Resistive Shell TPC - Analysis of the Electric Field Uniformity*. 2020. URL: https://github.com/RomanMBerner/RSTPC_FieldUniformityAnalysis. (accessed: 11.06.2021) (cit. on p. 157).

Publications

In the framework of this thesis, I was corresponding author of the following publication:

R. Berner et al. 'First Operation of a Resistive Shell Liquid Argon Time Projection Chamber: A New Approach to Electric-Field Shaping'. In: *Instruments* 3.2 (2019), p. 28. DOI: 10.3390/instruments3020028. arXiv: 1903.11858 [physics.ins-det].

Furthermore, I co-authored the following publications (ordered chronologically):

DUNE collaboration. 'Physics analysis in a novel pixel-readout LArTPC'. Prepared for submission to JINST.

A. Abud et al. 'Design, construction and operation of the ProtoDUNE-SP Liquid Argon TPC'. In: (Aug. 2021). arXiv: 2108.01902 [physics.ins-det].

A. Abud et al. 'Searching for Solar KDAR with DUNE'. In: (July 2021). arXiv: 2107.09109 [hep-ex].

A. Abud et al. 'Deep Underground Neutrino Experiment (DUNE) Near Detector Conceptual Design Report'. In: (Mar. 2021). arXiv: 2103.13910 [physics.ins-det].

B. Abi et al. 'Experiment Simulation Configurations Approximating DUNE TDR'. In: (Mar. 2021). arXiv: 2103.04797 [hep-ex].

B. Abi et al. 'Prospects for beyond the Standard Model physics searches at the Deep Underground Neutrino Experiment'. In: *Eur. Phys. J. C* 81.4 (2021), p. 322. DOI: 10.1140/epjc/s10052-021-09007-w. arXiv: 2008.12769 [hep-ex].

B. Abi et al. 'Supernova neutrino burst detection with the Deep Underground Neutrino Experiment'. In: *Eur. Phys. J. C* 81.5 (2021), p. 423. DOI: 10.1140/epjc/s10052-021-09166-w. arXiv: 2008.06647 [hep-ex].

N. Anfimov et al. 'Development of the Light Collection Module for the Liquid Argon Time Projection Chamber (LArTPC)'. In: *JINST* 15.07 (2020), p. C07022. DOI: 10.1088/1748-0221/15/07/C07022.

B. Abi et al. 'First results on ProtoDUNE-SP liquid argon time projection chamber performance from a beam test at the CERN Neutrino Platform'. In: *JINST* 15.12 (2020), P12004. DOI: 10.1088/1748-0221/15/12/P12004. arXiv: 2007.06722 [physics.ins-det].

B. Abi et al. 'Neutrino interaction classification with a convolutional neural network in the DUNE far detector'. In: *Phys. Rev. D* 102.9 (2020), p. 092003. DOI: 10.1103/PhysRevD.102.092003. arXiv: 2006.15052 [physics.ins-det].

B. Abi et al. 'Long-baseline neutrino oscillation physics potential of the DUNE experiment'. In: *Eur. Phys. J. C* 80.10 (2020), p. 978. DOI: 10.1140/epjc/s10052-020-08456-z. arXiv: 2006.16043 [hep-ex].

B. Abi et al. 'Deep Underground Neutrino Experiment (DUNE), Far Detector Technical Design Report, Volume IV: Far Detector Single-phase Technology'. In: *JINST* 15.08 (2020), T08010. DOI: 10.1088/1748-0221/15/08/T08010. arXiv: 2002.03010 [physics.ins-det].

B. Abi et al. 'Deep Underground Neutrino Experiment (DUNE), Far Detector Technical Design Report, Volume I Introduction to DUNE'. In: *JINST* 15.08 (2020), T08008. DOI: 10.1088/1748-0221/15/08/T08008. arXiv: 2002.02967 [physics.ins-det].

B. Abi et al. 'Deep Underground Neutrino Experiment (DUNE), Far Detector Technical Design Report, Volume II: DUNE Physics'. In: (Feb. 2020). arXiv: 2002.03005 [hep-ex].

B. Abi et al. 'Deep Underground Neutrino Experiment (DUNE), Far Detector Technical Design Report, Volume III: DUNE Far Detector Technical Coordination'. In: *JINST* 15.08 (2020), T08009. DOI: 10.1088/1748-0221/15/08/T08009. arXiv: 2002.03008 [physics.ins-det].

K. Abe et al. 'Measurement of the muon neutrino charged-current single π^+ production on hydrocarbon using the T2K off-axis near detector ND280'. In: *Phys. Rev. D* 101.1 (2020), p. 012007. DOI: 10.1103/PhysRevD.101.012007. arXiv: 1909.03936 [hep-ex].

J. Asaadi et al. 'A New Concept for Kilotonne Scale Liquid Argon Time Projection Chambers'. In: *Instruments* 4.1 (2020), p. 6. DOI: 10.3390/instruments4010006. arXiv: 1908.10956 [physics.ins-det].

K. Abe et al. 'Measurement of the ν_μ charged-current cross sections on water, hydrocarbon, iron, and their ratios with the T2K on-axis detectors'. In: *PTEP* 2019.9 (2019), p. 093C02. DOI: 10.1093/ptep/ptz070. arXiv: 1904.09611 [hep-ex].

R. Berner et al. 'First Operation of a Resistive Shell Liquid Argon Time Projection Chamber: A New Approach to Electric-Field Shaping'. In: *Instruments* 3.2 (2019), p. 28. DOI: 10.3390/instruments3020028. arXiv: 1903.11858 [physics.ins-det].

K. Abe et al. 'Search for heavy neutrinos with the T2K near detector ND280'. In: *Phys. Rev. D* 100.5 (2019), p. 052006. DOI: 10.1103/PhysRevD.100.052006. arXiv: 1902.07598 [hep-ex].

K. Abe et al. 'Search for light sterile neutrinos with the T2K far detector Super-Kamiokande at a baseline of 295 km'. In: *Phys. Rev. D* 99.7 (2019), p. 071103. DOI: 10.1103/PhysRevD.99.071103. arXiv: 1902.06529 [hep-ex].

K. Abe et al. 'Search for neutral-current induced single photon production at the ND280 near detector in T2K'. In: *J. Phys. G* 46.8 (2019), 08LT01. DOI: 10.1088/1361-6471/ab227d. arXiv: 1902.03848 [hep-ex].

B. Abi et al. 'The DUNE Far Detector Interim Design Report, Volume 2: Single-Phase Module'. In: (July 2018). arXiv: 1807.10327 [physics.ins-det].

B. Abi et al. 'The DUNE Far Detector Interim Design Report Volume 1: Physics, Technology and Strategies'. In: (July 2018). arXiv: 1807.10334 [physics.ins-det].

B. Abi et al. 'The DUNE Far Detector Interim Design Report, Volume 3: Dual-Phase Module'. In: (July 2018). arXiv: 1807.10340 [physics.ins-det].

K. Abe et al. 'Search for CP Violation in Neutrino and Antineutrino Oscillations by the T2K Experiment with 2.2×10^{21} Protons on Target'. In: *Phys. Rev. Lett.* 121.17 (2018), p. 171802. DOI: 10.1103/PhysRevLett.121.171802. arXiv: 1807.07891 [hep-ex].

K. Abe et al. 'Characterization of nuclear effects in muon-neutrino scattering on hydrocarbon with a measurement of final-state kinematics and correlations in charged-current pionless interactions at T2K'. In: *Phys. Rev. D* 98.3 (2018), p. 032003. DOI: 10.1103/PhysRevD.98.032003. arXiv: 1802.05078 [hep-ex].

K. Abe et al. 'Measurement of inclusive double-differential ν_μ charged-current cross section with improved acceptance in the T2K off-axis near detector'. In: *Phys. Rev. D* 98 (2018), p. 012004. DOI: 10.1103/PhysRevD.98.012004. arXiv: 1801.05148 [hep-ex].

A complete list of publications can be found here:
https://inspirehep.net/authors/1633523.

Declaration of consent

on the basis of Article 18 of the PromR Phil.-nat. 19

Name/First Name: Berner Roman

Registration Number: 10-177-798

Study program: PhD in Physics

Bachelor ☐ Master ☐ Dissertation ☑

Title of the thesis: ArgonCube - A Novel Concept for Liquid Argon Time Projection Chambers

Supervisor: Prof. Dr. Igor Kreslo

I declare herewith that this thesis is my own work and that I have not used any sources other than those stated. I have indicated the adoption of quotations as well as thoughts taken from other authors as such in the thesis. I am aware that the Senate pursuant to Article 36 paragraph 1 litera r of the University Act of September 5th, 1996 and Article 69 of the University Statute of June 7th, 2011 is authorized to revoke the doctoral degree awarded on the basis of this thesis.
For the purposes of evaluation and verification of compliance with the declaration of originality and the regulations governing plagiarism, I hereby grant the University of Bern the right to process my personal data and to perform the acts of use this requires, in particular, to reproduce the written thesis and to store it permanently in a database, and to use said database, or to make said database available, to enable comparison with theses submitted by others.

Place/Date

Signature